

5

Understanding giant vesicles: A theoretical perspective

Reinhard Lipowsky

As simple as possible but not simpler.

Albert Einstein

Contents

5.1	Introduction and Overview	74
5.2	Biomembranes and Giant Vesicles: Basic Aspects	75
5.2.1	Biomembranes Based on Lipid Bilayers	76
5.2.2	Semi-Permeability and Osmotic Conditions	76
5.2.3	Fluidity of Biomembranes	76
5.2.4	Remodeling of Composition and Shape	77
5.2.5	Stability of Bilayer Membranes	78
5.2.6	Polymorphism of Vesicles	78
5.3	Curvature of Membranes	79
5.3.1	Emergence of Curvature on Nanoscopic Scales	79
5.3.2	Mean and Gaussian Curvature	80
5.3.3	Sign of Membrane Curvature	80
5.3.4	Constant-Mean-Curvature Shapes	81
5.3.5	Local Curvature Generation and Spontaneous Curvature	81
5.4	Curvature Elasticity of Uniform Membranes	83
5.4.1	Spontaneous Curvature Model	84
5.4.2	Spontaneous Tension	85
5.4.3	Global and Local Parameters	85
5.4.4	Local Shape Equation and Energy Branches	87
5.4.5	Global Shape Equation	89
5.4.6	Vesicle Shapes with Membrane Necks	89
5.4.7	Area Difference Elasticity	92
5.5	Multi-Sphere Shapes of Uniform Membranes	93
5.5.1	Spherical Vesicles and Spherical Segments	93
5.5.2	Two-Sphere Vesicles	95
5.5.3	Modifications by Area Difference Elasticity	98
5.5.4	Effective Constriction Forces and Cleavage of Membrane Necks	100
5.5.5	Vesicle Shapes with Several Buds	101
5.5.6	N -Dependent Energy Landscape	105
5.6	Nanotubes of Uniform Membranes	107
5.6.1	Necklace-Like Nanotubes	107
5.6.2	Dominance of Spontaneous Tension	108
5.6.3	Morphological Complexity and Rugged Energy Landscape	110
5.6.4	Cylindrical Nanotubes	111
5.6.5	Shape Equations for Cylindrical Tubes	111
5.6.6	Spontaneous and Force-Induced Tubulation	112
5.6.7	Necklace-to-Cylinder Transformations	114

5.7	Adhesion of Vesicles	114
5.7.1	Interplay of Adhesion and Bending	115
5.7.2	Theory of Vesicle Adhesion	115
5.7.3	Vesicles Adhering to Planar Surfaces	116
5.7.4	More Complex Adhesion Geometries	119
5.7.5	Endocytosis of Nanoparticles	120
5.7.6	Ambience-Induced Segmentation	121
5.8	Membrane Phase Separation and Multi-Domain Vesicles	122
5.8.1	Budding of Intramembrane Domains	123
5.8.2	Theory of Two-Domain Vesicles	123
5.8.3	Domain-Induced Budding of Vesicles	126
5.8.4	Stable Multi-Domain Patterns	128
5.8.5	Membrane Phase Separation and Ambience-Induced Segmentation	129
5.9	Wetting of Membranes by Aqueous Droplets	130
5.9.1	Distinct In-Wetting Morphologies	131
5.9.2	Fluid-Elastic Molding of Membranes	132
5.9.3	Theory of Vesicle-Droplet Systems	132
5.9.4	Shape Equations and Matching Conditions	135
5.9.5	Three-Spherical-Cap Shapes	137
5.9.6	Shape Functional for Three Spherical Caps	139
5.9.7	Force Balance along Apparent Contact Line	141
5.9.8	Two-Droplet Vesicles with Closed Necks	143
5.9.9	Nucleation of Nanodroplets at Membranes	144
5.10	Topological Changes of Membranes	145
5.10.1	Free Energy Landscapes	145
5.10.2	Exergonic Fusion for Small m	145
5.10.3	Exergonic Fission for Large m	145
5.11	Summary and Outlook	146
	Acknowledgments	148
	Appendices	148
	Glossary of Symbols	162
	References	164

5.1 INTRODUCTION AND OVERVIEW

The architecture of biological membranes is characterized by a wide range of length scales. On the μm scale, these membranes exhibit a unique combination of properties: (i) They form closed surfaces without edges; (ii) They are highly flexible and, thus, can easily adapt their shape to external perturbations; (iii) In spite of this flexibility, they provide robust and stable barriers between the different aqueous compartments; and (iv) In the cell, these compartments are continuously remodeled via membrane fusion and fission (or scission).

These properties arise from the specific molecular structure of these membranes. When viewed on the nm scale, each biomembrane consists of a specific mixture of many different lipids and membrane proteins which reflects the biological functions of this membrane. However, in spite of this chemical complexity, all biomembranes are organized according to the same universal principle: their basic building block is provided by a *bilayer of lipid molecules*. The latter molecules are essentially *insoluble* in the aqueous solution which ensures the stability of the membrane. In addition, these lipid bilayers are maintained in a *fluid* state which enables the membranes to adapt to external perturbations by remodeling of membrane composition, shape, and topology.

Many of the fascinating remodeling processes that have been found for biological membranes can also be observed for giant unilamellar vesicles (GUVs) that are formed by membranes with a relatively small number of molecular components. The theory described here will typically be compared to experimental observations on lipid vesicles but the same theory applies to vesicle membranes that are composed of lipids and membrane proteins.

One intriguing example for the remodeling of membrane shape is provided by the formation of membrane necks via budding, a crucial step of all endo- and exocytotic processes. Another example is provided by the formation of membrane nanotubes, highly curved membrane structures that protrude from weakly curved membrane segments. As far as the remodeling of composition is concerned, we now have a variety of lipid mixtures that can phase separate into two fluid phases, a liquid-ordered and a liquid-disordered phase. When we study this membrane phase separation in giant vesicles, we often observe large intramembrane domains that partition the vesicle membrane into a few membrane compartments with a lateral extension in the micrometer range. In addition, multi-component membranes exposed to a heterogeneous environment form ambience-induced segments that can also differ

in their molecular composition. One example for this type of segmentation is provided by vesicle membranes exposed to aqueous two-phase systems or water-in-water emulsions which exhibit several wetting morphologies. The interplay between ambience-induced segmentation and membrane phase separation leads to the confinement of phase separation to single membrane segments which represents a generic mechanism to suppress the formation of large intramembrane domains or rafts in cellular membranes.

The present chapter is organized as follows. The next two Sections 5.2 and 5.3 are introductory in nature: they describe basic aspects of biomembranes and provide an elementary view of membrane curvature. The relation between local curvature generation and spontaneous curvature is explained in Section 5.3.5. Different molecular mechanisms for local curvature generation are described in Box 5.1. Section 5.4 describes the theory of curvature elasticity for uniform membranes.¹ This theory is based on the *local* curvature-elastic properties of the membranes, but also takes into account that the ultralow lipid solubility and the osmotic conditions lead to *global* constraints on the membrane area and the vesicle volume. In fact, what makes this theory both appealing and challenging is this interplay between local and global membrane properties.

We will focus on the spontaneous curvature model but also discuss the modifications arising from area-difference-elasticity. On the one hand, the spontaneous curvature model is particularly attractive from a theoretical point of view because it depends only on a small number of curvature-elastic parameters. In fact, for membranes with a laterally uniform composition, the spontaneous curvature model involves only two such parameters, (i) the bending rigidity κ which describes the resistance of the membrane against bending deformations and (ii) the spontaneous curvature which provides a quantitative measure for the bilayer asymmetry of the membranes. On the other hand, the spontaneous curvature model is also sufficient to obtain a quantitative description for the behavior of many membranes of interest. Indeed, this model applies to all membranes with (at least) one molecular component such as cholesterol that undergoes frequent flip-flops between the two leaflets of the bilayer. Area difference elasticity is only relevant in the absence of flip-flops, i.e., when the number of molecules is separately conserved in each leaflet.

One striking consequence of curvature elasticity is the formation of closed membrane necks that represent narrow funnel-like membrane structures between two larger membrane segments. The stability of these necks depends on the relative magnitude of the neck curvature and the spontaneous curvature, which may contain a nonlocal contribution from area-difference-elasticity. These stability conditions for closed membrane necks can be reinterpreted as effective constriction forces generated by spontaneous curvature. Simple estimates show that sufficiently large spontaneous curvatures lead to the cleavage of the membrane necks and thus to complete membrane fission. The different aspects of membrane necks are summarized in Box 5.2.

¹ Here and below, a ‘uniform membrane’ is ‘laterally uniform’ and a ‘uniform aqueous phase’ is ‘spatially uniform’.

Sections 5.5 and 5.6 are devoted to two striking morphologies formed by uniform membranes: (i) multi-sphere shapes that involve small spherical buds and (ii) membrane nanotubes that can be necklace-like or cylindrical. Section 5.7 describes the behavior of vesicles that interact with an adhesive and rigid surface. For simplicity, the latter section will focus on vesicle membranes with a laterally uniform composition but will also discuss adhesion of vesicles as an example for ambience-induced segmentation of membranes. A closely related subject, the behavior of adhesive nanoparticles in contact with membranes and vesicles, will be addressed in Chapter 8 of this book. The shapes and shape transformations of vesicles that contain two or multiple intramembrane domains are discussed in Section 5.8, and the wetting of membranes in contact with aqueous two-phase systems or water-in-water emulsions in Section 5.9. For partial wetting, the water-water interfaces exert capillary forces onto the membranes which then respond with strong shape deformations. On the nanometer scale, the membrane segments close to the three-phase contact line should be curved in a smooth manner and the capillary forces then lead to a complex force balance along this contact line which involves an intrinsic contact angle. On the micrometer scale, the membrane shapes exhibit kinks which define an apparent contact line and apparent contact angles. Experimental aspects of aqueous two-phase systems will be addressed in Chapter 29 of this book. Both membrane phase separation and membrane wetting leads to vesicle membranes that have a laterally nonuniform composition. At the end, we will briefly look at the consequences of curvature elasticity for membrane fusion and fission (or scission) of membranes, the two most important topological transformations of membranes.

Each of the different membrane systems discussed in Sections 5.7 through 5.9 involves one additional parameter: the adhesive strength W of substrate surfaces, the line tension λ of domain boundaries, and the interfacial tension $\Sigma_{\alpha\beta}$ between two different aqueous phases. Because all of these parameters can be measured or deduced from experimental observations, the theory leads to quantitative predictions. In fact, the theory described here leads to a large number of simple relationships between material parameters and geometric quantities which provide important checkpoints for the comparison between theory and experiment.

5.2 BIOMEMBRANES AND GIANT VESICLES: BASIC ASPECTS

Here and below, the term “biomembranes” will be used as an abbreviation for “biological and biomimetic membranes.” These two types of membranes differ primarily in their chemical complexity. Biological or cellular membranes usually contain hundreds or even thousands of different lipid species and a large number of different membrane proteins. Biomimetic membranes as considered here have a much simpler composition with only a few molecular components but share one crucial physical property with biological membranes, namely their fluidity, which enables both types of membranes to undergo analogous remodeling processes. The simplest biomimetic membranes are provided by one-component lipid bilayers which have a molecular structure as in Figure 5.1.

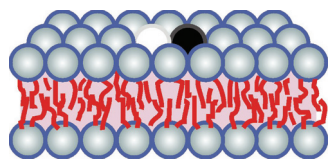


Figure 5.1 Lipid bilayer as the basic building block of all biomembranes: The lipid molecules are arranged into two monolayers or leaflets, with the lipid headgroups forming the two interfaces between the bilayer and the aqueous solutions. The thickness of the bilayer is 4 to 5 nm. For a *fluid* bilayer, each lipid molecule undergoes rapid lateral diffusion within the membrane. This diffusive process is based on the pairwise exchange of neighboring lipids (black and white) on the time scale of nanoseconds.

5.2.1 BIOMEMBRANES BASED ON LIPID BILAYERS

Essentially all biological membranes contain a single lipid bilayer as their basic building block. The importance of lipids was already realized by Langmuir and others at the beginning of the 20th century. This insight came from spreading experiments: the membranes were dissolved in a volatile organic solvent, the solution was spread on a water surface, and the solvent was evaporated. In this way, one obtains a lipid monolayer at the air–water interface. Such a technique was also used by Gorter and Grendel who extracted lipids from red blood cells (Gorter and Grendel, 1925; Robertson, 1960). They found that the area of the monolayer was approximately twice the area of the cell and proposed that the cell should be covered by a lipid bilayer. This proposal was confirmed, in the 1950s and 1960s, by imaging cross-sections of biomembranes via electron microscopy. Such electron microscopy images gave direct evidence that cell membranes are based upon a single bilayer and showed that these bilayers have a thickness of 4–5 nm (Robertson, 1959).

Electron microscopy studies also demonstrated that bilayers are already formed by a single species of phospholipid molecules (Bangham and Horne, 1964). Therefore, bilayers consisting of one or a few lipid components have become important model systems for biological membranes. Different bilayer systems have been developed and intensely studied, including multilamellar liposomes, black lipid membranes, solid-supported bilayers, and unilamellar vesicles. Giant unilamellar vesicles as considered here typically have a linear size of tens of micrometers and can be directly imaged in their fluid state using optical microscopy.

5.2.2 SEMI-PERMEABILITY AND OSMOTIC CONDITIONS

One basic function of biological membranes is that they partition space into separate aqueous compartments and represent effective barriers for the diffusion of ions and solute molecules from one compartment to another. These functions are also provided by lipid bilayers. When these bilayers form vesicles, they create an interior aqueous compartment that is well separated from the exterior solution. Indeed, the bilayers are permeable to small uncharged molecules such as H_2O , O_2 , and CO_2 as well as H_3O^+ and OH^- ions, but do not allow the permeation of other ions or larger water-soluble molecules such as glucose and

other monosaccharides. As a consequence, these solutes represent osmotically active “particles” and exert osmotic pressures onto the vesicle membranes. The experimental methods to measure the permeability of membranes are reviewed in [Chapter 20](#) of this book.

The osmotic pressures depend on the solute concentrations in the interior and exterior solutions. If a vesicle membrane is exposed to different interior and exterior concentrations, the resulting osmotic pressure difference causes water to move through the membrane into the compartment with the higher solute concentration. First, consider a higher solute concentration in the exterior solution which leads to osmotic deflation of the vesicle. In this case, the water outflux reduces the vesicle volume until the interior particle concentration matches the exterior one and the osmotic pressure difference is close to zero. On the other hand, if we start with a higher solute concentration in the interior compartment, the volume of the vesicle is increased by osmotic inflation. However, this volume increase is truncated by the limited ability of the vesicle membrane to increase its area by mechanical stretching. Indeed, when a lipid bilayer is mechanically stretched, its area can only be increased by a few percent before it ruptures. Therefore, once the inflated vesicle has attained a spherical shape, further influx of water increases the membrane tension up to a limiting value at which the membrane ruptures and forms pores. These pores then provide an alternative pathway for the reduction of the osmotic pressure difference.

5.2.3 FLUIDITY OF BIOMEMBRANES

Another universal aspect of biological membranes is that they are maintained in a fluid state which is characterized by fast lateral diffusion of the molecules along the membrane. This membrane fluidity became generally accepted at the beginning of the 1970s as a result of three parallel developments. First, the lateral diffusion was probed by spin-labeled lipids (Kornberg and McConnell, 1971; Devaux and McConnell, 1972) and steroids (Sackmann and Träuble, 1972; Träuble and Sackmann, 1972) which led to lateral diffusion constants of the order of $1 \mu\text{m}^2$ per second. Nowadays, the lateral diffusion of membrane molecules can be observed directly by fluorescence recovery after photobleaching (FRAP) (Almeida and Vaz, 1995) and by single particle tracking (Sako and Kusumi, 1994; Saxton and Jacobson, 1997; Fujiwara et al., 2002; Kusumi et al., 2005), two methods that have been applied to a large variety of biomimetic and biological membranes. These studies confirmed that the lateral diffusion constants of membrane molecules are indeed of the order of $1 \mu\text{m}^2$ per second. A detailed discussion of both FRAP and single particle tracking as well as tables with diffusion constants for a variety of lipids can be found in [Chapter 21](#) of this book.

Second, it has been realized that the observed shape transformations of red blood cells (Canham, 1970; Evans, 1974) and lipid vesicles (Helfrich, 1973; Deuling and Helfrich, 1976) are only possible if the membranes represent two-dimensional liquids. Indeed, these shape transformations change the curvature of the membranes in a smooth and continuous manner and would be impossible for solid-like or polymerized membranes. Particularly interesting shape changes are provided by budding processes in

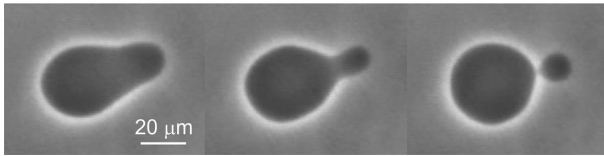


Figure 5.2 Formation of a spherical out-bud from a giant unilamellar vesicle (GUV) as observed by phase contrast microscopy. This budding process, which took about 5 s, proceeds in a smooth and continuous manner and provides direct evidence on the micrometer scale that the lipid membrane is in a fluid state on the molecular scale. (Reproduced with permission from Dimova, R. et al., A practical guide to giant vesicles: Probing the membrane nanoregime via optical microscopy, *J. Phys. Cond. Mat.*, 18, S1151–S1176, 2006, Institute of Physics)

which small spherical out- or in-buds are formed from larger mother vesicles. Out-buds point towards the exterior aqueous solution, in-buds towards the interior solution. One example for the formation of an out-bud is shown in Figure 5.2. Such a budding process provides direct evidence that the membrane is in a fluid state. The associated curvature elasticity of biomembranes has now been developed into a quantitative theory (Berndl et al., 1990; Seifert and Lipowsky, 1990; Seifert et al., 1991; Miao et al., 1991; Lipowsky, 1991; Miao et al., 1994; Döbereiner et al., 1997; Lipowsky, 2013; Liu et al., 2016; Lipowsky, 2018a) which will be described in this chapter.

Third, in 1972, a large body of observations on cellular membranes was integrated into the fluid mosaic model in which the membrane proteins are dispersed in a fluid bilayer of lipids (Singer and Nicolson, 1972). Whether the fluid mosaic model actually describes the supramolecular structure of cell membranes has been a matter of some debate. On the one hand, the endocytosis and exocytosis of cell membranes involves the formation of fluid domains that are enriched in membrane-anchored receptors and coat proteins and can be understood in terms of domain-induced budding (Lipowsky, 1992, 1993; Agudo-Canalejo and Lipowsky, 2015a).

On the other hand, it has also been proposed that cell membranes contain intramembrane domains, so-called rafts, that are enriched in certain lipids such as sphingomyelin and cholesterol (Simons and Ikonen, 1997). In spite of a large number of experimental studies, including superresolution microscopy methods such as stimulated emission depletion (STED) microscopy, it has not been possible to obtain direct evidence for such rafts in cellular membranes. If these lipid rafts exist in mammalian cells, their diameter does not exceed 20 nm (Eggeling et al., 2009). The different experimental techniques used to search for such rafts have been critically reviewed by (Klotzsch and Schütz, 2013). One generic mechanism that explains the difficulty to observe membrane phase separation in cellular membranes is ambient-induced segmentation by the heterogeneous environment to which these membranes are exposed (Lipowsky, 2014b) as discussed in Section 5.8.5 below.

5.2.4 REMODELING OF COMPOSITION AND SHAPE

In general, the fluidity of biomembranes implies that these membranes can easily adapt to changes in their environment by remodeling their composition, shape, and topology. This multi-responsive behavior includes shape transformations of GUVs,

membrane segmentation by laterally nonuniform environments such as adhesive surfaces, membrane phase separation, and the responses of GUVs to capillary forces arising from water-in-water droplets.

The remodeling of membrane composition in ternary lipid mixtures leads to the nucleation and growth of intramembrane domains that can be directly observed in the optical microscope, see Figure 5.3. Such domains, which demonstrate the coexistence of two (or more) lipid phases, have now been observed for a variety of membrane systems including giant vesicles (Dietrich et al., 2001; Veatch and Keller, 2003; Baumgart et al., 2003; Bacia et al., 2005; Riske et al., 2006; Dimova et al., 2007; Semrau et al., 2008), solid-supported membranes (Jensen et al., 2007; Garg et al., 2007; Kiessling et al., 2009), hole-spanning (or black lipid) membranes (Collins and Keller, 2008), as well as pore-spanning membranes (Orth et al., 2012). The phase diagrams of such three-component membranes have been determined using spectroscopic methods (David et al., 2009) as well as fluorescence microscopy of giant vesicles and X-ray diffraction of membrane stacks (Veatch et al., 2006; Vequi-Suplicy et al., 2010; Uppamoochikkal et al., 2010; Patariaia et al., 2014). The experimental aspects of lipid phase separation and domain formation are reviewed in more detail in Chapter 18 of this book.

Another particularly striking example for the remodeling of membrane shape that does not require membrane phase separation is provided by the spontaneous tubulation of GUVs (Li et al., 2011; Lipowsky, 2013; Liu et al., 2016). Two examples for the resulting pattern of nanotubes are displayed in Figure 5.4. In these examples, the vesicles respond to osmotic deflation by the formation of many nanotubes that emanate from the giant mother vesicle and protrude into the vesicle interior. As a result, highly curved membrane segments coexist with weakly curved segments even though the membrane has a laterally uniform composition. The nanotubes shown in Figure 5.4 were formed spontaneously, i.e., in the absence of external pulling forces. Another quite different mechanism for the formation of membrane

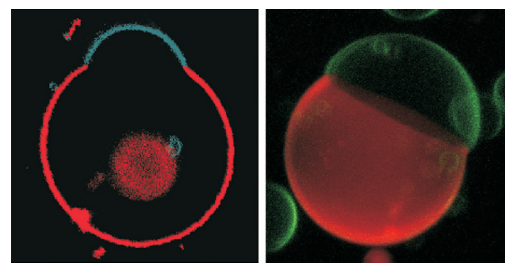


Figure 5.3 Remodeling of membrane composition can lead to domain-induced budding of vesicles as theoretically predicted in (Lipowsky, 1992, 1993; Jülicher and Lipowsky, 1993) and observed by fluorescence microscopy in (Baumgart et al., 2003; Riske et al., 2006): (left) Cross section through a vesicle that formed two domains after a decrease in temperature (Baumgart et al., 2003); and (right) Three-dimensional confocal scan of a two-domain vesicle that was formed by electrofusion. In both cases, the vesicle membrane is composed of dioleoyl phosphatidyl choline (DOPC), sphingomyelin, and cholesterol (see Appendix 1 of the book for structure and data on these lipids) together with small concentrations of two fluorescent probes. (Reproduced with permission from Riske, K.A. et al., *Biophys. Rev. Lett.*, 1, 387–400, 2006. Copyright (c) 2006 World Scientific Publishing.)

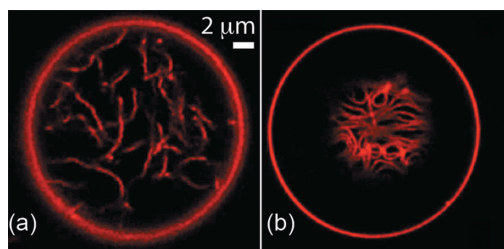


Figure 5.4 Remodeling of membrane shape can lead to complex patterns of flexible nanotubes. The nanotubes were formed by liquid-disordered membranes after the interior aqueous compartment separated into a PEG-rich and dextran-rich phase: (a) Disordered pattern corresponding to a vesicle membrane that is completely wetted by the PEG-rich phase; and (b) Layer of densely packed tubes corresponding to a membrane that is partially wetted by both aqueous phases. All tubes are connected to the outer vesicle membranes (red circles). In both images, the diameter of the tubes is below the diffraction limit of the confocal microscope but the tubes are theoretically predicted to be necklace-like and cylindrical in (a) and (b), respectively (Liu et al., 2016). (Reproduced with permission from Liu, Y. et al., *ACS Nano*, 10, 463–474, 2016. Copyright American Chemical Society.)

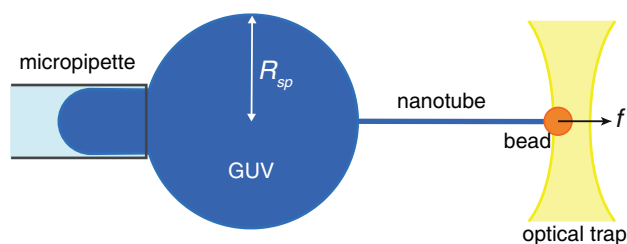


Figure 5.5 Pulling a membrane nanotube attached to a bead from a giant unilamellar vesicle (GUV) by an optical trap: The weakly curved GUV is aspirated by the micropipette, the right end of the strongly curved nanotube experiences the pulling force f arising from the optical trap. The latter force is typically of the order of 10 pN and can then generate tubes with a radius of 10–20 nm.

nanotubes is provided by external pulling forces that are locally applied to the membranes. A particularly instructive setup for the latter tubulation process is obtained if one aspirates a giant unilamellar vesicle in a micropipette and simultaneously applies a pulling force to a membrane-bound nanobead via magnetic tweezers (Heinrich and Waugh, 1996) or optical traps (Sorre et al., 2012), as schematically depicted in Figure 5.5.

The experimental methods that have been developed for GUVs composed of a few lipid components can also be applied to giant plasma membrane vesicles (GPMVs) or “blebs,” which contain a wide assortment of different lipids and proteins, all oriented in the same way as in the original cell membrane. In spite of their chemical complexity, the membranes of GPMVs were found to phase separate into coexisting lipid phases (Baumgart et al., 2007; Veatch et al., 2008), in close analogy to ternary lipid mixtures. One cellular process that has been elucidated using GPMVs is the molecular recognition of “self” during phagocytosis by macrophages. This recognition process involves the binding of the immunoglobulin CD47, a ubiquitous “marker of self” protein, to the macrophage receptor SIRP α (Sosale et al., 2015). The adhesion of GPMVs with CD47 to SIRP α immobilized on a substrate surface revealed that the two proteins bind in a cooperative

manner (Steinkühler et al., 2019), confirming previous theoretical studies (Weigl et al., 2009, 2016; Hu et al., 2013). Furthermore, it has also been observed that GPMVs form many nanotubes under deflation and that these tubulated vesicles exhibit rather unusual elastic properties (Steinkühler et al., 2018b).

5.2.5 STABILITY OF BILAYER MEMBRANES

In spite of their high flexibility, lipid membranes have a robust molecular architecture and maintain this architecture even under strong local deformations. One example is provided by force-induced tubulation as shown in Figure 5.5. Using this method, one can produce nanotubes or “tethers” with a radius of only 10 nm, which should be compared to the bilayer thickness of 4–5 nm (Sorre et al., 2012). Tubes of a similar width have also been generated by a slightly different setup in which the laser trap is replaced by another micropipette that grabs the nanobead (Hochmuth et al., 1982; Tian et al., 2009). However, in spite of the large curvature of these nanotubes, the tube membranes maintain their structural integrity and provide an efficient separation of the interior and exterior aqueous compartments. Detailed information about the experimental method to pull nanotubes from GUVs can be found in Chapter 16 of this book.

The stability of the bilayer structure reflects the ultralow solubility of phospholipids in water. One measure for this solubility is provided by the critical micelle concentration which represents both the concentration at which the lipids start to self-assemble into bilayers (instead of micelles) and the concentration of individual lipid molecules in the presence of bilayers. The critical micelle concentration of phospholipids decreases exponentially with their chain length, i.e., with the number of hydrocarbon groups per chain (Cevc and Marsh, 1987). The phospholipid dimyristoyl phosphatidyl choline (DMPC, see Appendix 1 of the book for structure and data on this and other lipids), for example, has the relatively short chain length of 14 hydrocarbon groups, but its critical micelle concentration is only $10^{-10.5}$ in mole fraction units or about 0.95 DMPC molecules per μm^3 . When this lipid forms a giant unilamellar vesicle with a radius of 10 μm , the vesicle membrane consists of about 4×10^9 lipid molecules whereas the interior aqueous compartment of the vesicle contains only about 4×10^3 such molecules. Most biologically relevant phospholipids have a chain length that exceeds 14 hydrocarbon groups which implies an even lower critical micelle concentration. As a consequence, one can usually ignore any exchange of phospholipids between the bilayer membrane and the aqueous solutions and assume that the membrane contains a fixed number of such lipids.

5.2.6 POLYMORPHISM OF VESICLES

Because biomembranes are fluid, one might expect that their shape can be understood by analogy with liquid droplets. However, in the absence of external forces or constraints, a liquid droplet of a given volume always attains a spherical shape in order to minimize its interfacial area and, thus, its interfacial free energy. In contrast to liquid droplets, lipid vesicles can attain a large variety of different shapes such as discocytes, stomatocytes, and dumbbells. Furthermore, the vesicle may undergo shape transformations as one changes the osmotic conditions or the temperature. Because the lipid molecules are practically insoluble in water, the total number of lipid molecules within

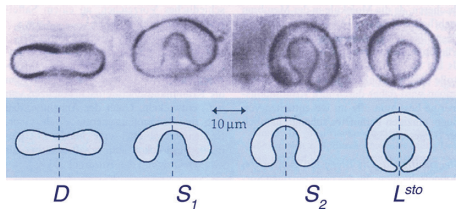


Figure 5.6 Temperature-induced shape transformation of a single vesicle: In this example, the vesicle starts from the initial shape of a discocyte (D) which is transformed, via the intermediate stomatocytes S_1 and S_2 , into the limit shape L^{sto} consisting of two spheres. The small sphere of L^{sto} forms an in-bud that is connected to the large sphere via a closed membrane neck. The generation of a smooth spherical bud without any membrane folds again demonstrates the fluidity of the membrane. The top row displays images of phase contrast microscopy, the bottom row theoretical shapes with minimal curvature energy. (From Berndt, K. et al., *Europhys. Lett.*, 13, 659–664, 1990.)

the membrane is conserved during such shape transformations. In addition, at any given temperature, each lipid molecule tries to occupy a certain optimal area within the membrane. Furthermore, when exposed to external forces or constraints, lipid bilayers hardly change their area before they rupture. Therefore, the area of the vesicle membrane is conserved, to a very good approximation, during isothermal shape transformations arising, e.g., from osmotic deflation and inflation. The latter processes change the vesicle volume for fixed membrane area. In general, the volume of a vesicle can become arbitrarily small but cannot exceed the volume of a sphere.

Shape transformations can also be induced by temperature changes reflecting the different thermal expansivities of the lipid bilayer and the aqueous solution. When we increase the temperature by ΔT , the initial membrane area A_0 increases by $\Delta A = \alpha_A \Delta T A_0$ with $\alpha_A \approx 2 \times 10^{-3}/\text{K}$ for lipid bilayers. At the same time, the initial water volume V_0 increases by $\Delta V = \alpha_V \Delta T V_0$ with $\alpha_V \approx 2 \times 10^{-4}/\text{K}$. When we apply these relations to a GUV, we find that an increase in temperature generates excess area of the membrane and reduces the volume-to-area ratio of the vesicle. One example for temperature-induced shape transformations is displayed in [Figure 5.6](#).

The multi-responsive behavior of GUVs as illustrated by [Figures 5.2](#) through [5.6](#) can be understood, in a quantitative manner, by the unusual curvature-elastic properties of the vesicle membranes. In the next two sections, we will first discuss the general concept of membrane curvature and then introduce the spontaneous curvature model for the description of curvature elasticity.

5.3 CURVATURE OF MEMBRANES

This section provides an elementary introduction into different aspects of curvature. It first emphasizes that membrane curvature emerges on nanoscopic scales and then describes basic concepts from differential geometry which include the two principal curvatures, the mean curvature, and the Gaussian curvature. Furthermore, one simple but important issue that is discussed in some detail is our convention for the sign of the principal curvatures, which can be positive or negative. At the end of this section, several molecular mechanisms for local curvature generation are briefly

discussed and summarized in [Box 5.1](#). Local curvature generation is intimately related to the preferred or spontaneous curvature of a membrane. The latter curvature can again be positive or negative. The present section is supplemented by [Appendix 5.A](#) on differential geometry.

5.3.1 EMERGENCE OF CURVATURE ON NANOSCOPIC SCALES

As shown in [Figure 5.3](#) and [Figure 5.6](#), vesicle shapes appear to be rather smooth when viewed under the optical microscope. Therefore, on the micrometer scale, membranes can be described as smoothly curved surfaces and then characterized by their curvature. However, this smoothness does not persist to molecular scales, i.e., when we resolve the molecular structure of a bilayer membrane as in [Figure 5.7](#).

Because membranes are immersed in liquid water, each lipid and protein molecule undergoes thermal motion with displacements both parallel and perpendicular to the membrane. The perpendicular displacements represent molecular protrusions that roughen the two interfaces bounding the membrane. Therefore, in order to characterize a lipid/protein bilayer by its curvature, one has to consider small membrane patches and average over the molecular conformations within these patches. The minimal lateral size of these patches can be determined from the analysis of the bilayer's shape fluctuations and was found, from molecular dynamics simulations of a one-component lipid bilayer, to be about 1.5 times the membrane thickness, see [Figure 5.7](#) (Goetz et al., 1999). For a membrane with a thickness of 4 nm, this minimal size is about 6 nm. Because such a membrane patch contains 80–100 lipid molecules, membrane curvature should be regarded as an emergent property arising from the collective behavior of a large number of lipid molecules.

The curvature just discussed applies to the midsurface of the bilayer membrane, i.e., to the surface between the two leaflets of the bilayer. Furthermore, for a membrane segment with mid-surface area A and bending rigidity κ , curved conformations as in [Figure 5.7](#) are only possible if the membrane is “tensionless” in the sense that the mechanical membrane tension is small compared to κ/A (Goetz and Lipowsky, 1998). For the example displayed in [Figure 5.7](#), the latter tension scale is found to be $\kappa/A = 0.08 \text{ mN/m}$.

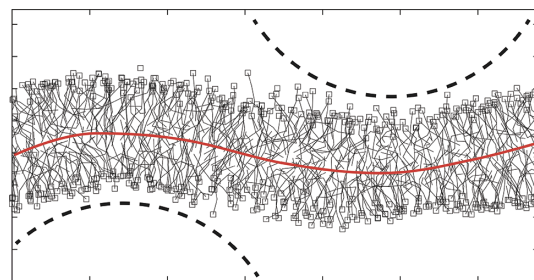


Figure 5.7 Emergence of membrane curvature on nanoscopic scales as observed in molecular dynamics simulations. The bilayer has a thickness of about 4 nm, the smallest curvature radius of its midsurface (red curve) is about 6 nm. For comparison, two circles (broken lines) with a radius of 6 nm are also displayed. (Reproduced from Goetz, R. et al., *Phys. Rev. Lett.*, 82, 221–224, 1999.)

5.3.2 MEAN AND GAUSSIAN CURVATURE

For each point on a smooth surface, we can construct a unit normal vector perpendicular to the membrane surface. Now, any plane that contains both the chosen point and this normal vector, defines a so-called normal section of the membrane surface, see Figure 5.8. The intersection between the surface and such a normal section defines a cross-sectional curve through the chosen point with a certain curvature C at this point. I will take this curvature to be positive if the cross-sectional curve bulges in the direction of the chosen normal vector as in Figure 5.8. This sign convention ensures that the cross-sectional curves on a sphere have positive curvature. Now, let us rotate the normal section around the normal vector. As a result of this rotation, the cross-sectional curve through the chosen point changes and so does the curvature C . As we change the rotation angle from 0 to 360 degrees, the latter curvature varies over a certain range as given by $C_{\min} \leq C \leq C_{\max}$. The two extremal values C_{\min} and C_{\max} define the principal curvatures, C_1 and C_2 , at the chosen point. These principal curvatures correspond to the eigenvalues of the negative curvature tensor, see Appendix 5.A. Furthermore, for $C_1 \neq C_2$, the normal sections that contain the cross-sectional curves with $C = C_1$ and $C = C_2$ are always orthogonal to each other.

For fluid membranes as considered here, the molecules diffuse laterally along the membrane, which implies that the membrane surface should be described in terms of geometric quantities that do not depend on the choice of the surface coordinates, i.e., that are invariant under a reparametrization of the surface. Such quantities are provided, apart from a possible change of sign, by the principal curvatures C_1 and C_2 or equivalently by the mean curvature

$$M \equiv \frac{1}{2}(C_1 + C_2) \quad (5.1)$$

and the Gaussian curvature

$$G \equiv C_1 C_2. \quad (5.2)$$

The mean curvature is proportional to the trace of the curvature tensor whereas the Gaussian curvature is equal to its determinant (Appendix 5.A). Note that $C_1 = M - \sqrt{M^2 - G}$ and $C_2 = M + \sqrt{M^2 - G}$. Both expressions are always real-valued because $M^2 \geq G$.² Indeed, the latter inequality is equivalent to

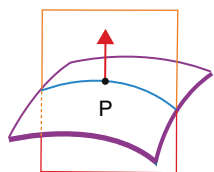


Figure 5.8 Normal section through membrane surface: Consider a point P of the membrane surface and the normal vector (arrow) at point P . A normal section is provided by any plane that contains both the point P and its normal vector. The intersection between the chosen normal section and the membrane surface defines a cross-sectional curve through point P . This curve has a certain curvature at point P . The latter curvature changes in a smooth manner as we rotate the normal section around the normal vector.

² The expressions for C_1 and C_2 imply that $C_1 = \dot{\psi}$ and $C_2 = \sin \psi / r$ for axisymmetric shapes parametrized by the tilt angle ψ and the radial coordinate r of the shape contour (Seifert et al., 1991).

$(C_1 - C_2)^2 \geq 0$ and, thus, holds for any shape of the membrane segment. The equality $M^2 = G$ applies to spherical segments with $C_1 = C_2$.

5.3.3 SIGN OF MEMBRANE CURVATURE

The mean curvature M is invariant under all orientation-preserving transformations of the surface coordinates, i.e., under all transformations that have a positive Jacobi determinant. The latter transformations do not affect the normal vectors of the membrane. However, we may also consider improper transformations of the surface coordinates which reverse the orientation of the normal vectors. A simple example of such an improper transformation A^1 is provided by a transposition of the two surface coordinates, i.e., by the transformation from (s^1, s^2) to $(\bar{s}^1 \equiv s^2, \bar{s}^2 \equiv s^1)$. The reversal of the normal vector implies that the principal curvatures change their sign and so does the mean curvature.

On the one hand, the reversal of the normal vectors provides a useful operation from a theoretical point of view because many physical properties of the membrane should not depend on our choice for the orientation of the normal vectors and must therefore be invariant under the reversal of these vectors. On the other hand, in order to avoid any ambiguity, we need a convention that always assigns a definite orientation to the normal vectors. For vesicle membranes as considered here, we can always distinguish between an interior and an exterior compartment and, thus, can always take the normal vectors to point towards the outer leaflet which is in contact with the exterior aqueous compartment, see Figure 5.9.

The sign of the mean curvature M depends on the sign of the principal curvatures C_1 and C_2 . As explained before, each principal curvature is obtained from a certain normal section and taken to be positive if the corresponding cross-sectional curve bulges in the direction of the normal vector. If all cross-sectional curves of the membrane bulge into the direction of the normal vector as in Figures 5.8 and 5.9a, both C_1 and C_2 are positive which implies that the mean curvature M is positive as well.³ Likewise, the mean

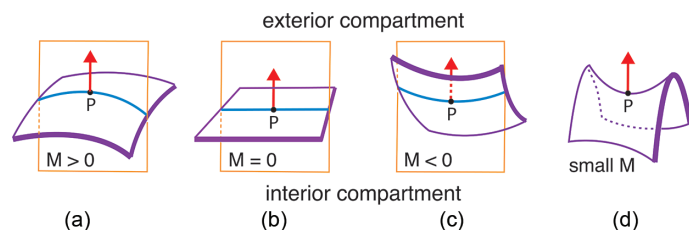


Figure 5.9 Sign convention for mean curvature M : (a) The mean curvature is *positive* if the membrane curves or bulges locally towards its outer leaflet in contact with the exterior compartment; (b) The mean curvature vanishes for a planar membrane; (c) The mean curvature is *negative* if the membrane curves or bulges locally towards its inner leaflet in contact with the interior compartment; and (d) If P is a saddle point, the two principal curvatures C_1 and C_2 have opposite sign and the mean curvature $M = \frac{1}{2}(C_1 + C_2)$ is small or even zero.

³ Choose local Cartesian coordinates (x, y, z) with the origin given by point $P = (0, 0, 0)$, normal vector $\hat{n} = (0, 0, 1)$, and the x -coordinate parallel to the normal section that contains the cross-sectional curve with the principal curvature $C_1 = C_{\min}$. The cross-sectional curves within the normal sections with $y = 0$ and $x = 0$ are then described by $z \approx -C_1 x^2$ and $z \approx -C_2 y^2$ for small values of x and y .

curvature M is *negative* if all cross-sectional curves of the membrane bulge into the direction of the negative normal vector, see [Figure 5.9c](#). At a saddle point of the membrane surface, the two principal curvatures have opposite signs and the mean curvature M can be positive or negative or even vanish, depending on the relative magnitude of the two principal curvatures, see [Figure 5.9d](#).

5.3.4 CONSTANT-MEAN-CURVATURE SHAPES

In general, the principal curvatures and the mean curvature M are local quantities that vary along the membrane surface. Some particularly simple shapes are, however, characterized by constant mean curvature, i.e., all points on the surface have the same mean curvature, see [Figure 5.10](#). Thus, a planar membrane has vanishing mean curvature, $M = 0$, whereas a sphere with radius R_{sp} has mean curvature $M = 1/R_{sp}$ and $M = -1/R_{sp}$ when its inner leaflet is in contact with the interior and the exterior solution, respectively. Likewise, a cylinder with radius R_{cy} has mean curvature $M = 1/(2R_{cy})$ when the enclosed volume of water belongs to the interior compartment and $M = -1/(2R_{cy})$ when this volume is connected to the exterior compartment. Another simple shape is a catenoid for which each point represents a saddle point with vanishing mean curvature $M = 0$ as depicted in [Figure 5.10c](#).

Cylinders represent possible shapes for membrane nanotubes. Another tube morphology that has been observed are necklace-like tubes as shown in [Figure 5.11a](#). The latter tubes consist of

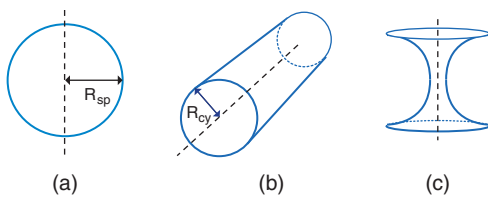


Figure 5.10 Simple membrane shapes with constant mean curvature M : (a) Sphere with radius R_{sp} and mean curvature $M = \pm 1/R_{sp}$; (b) Cylinder with radius R_{cy} and mean curvature $M = \pm 1/(2R_{cy})$; and (c) Catenoid with mean curvature $M = 0$. For spheres and cylinders, the sign of the mean curvature depends on whether the inner leaflet is in contact with the interior or exterior aqueous solution.

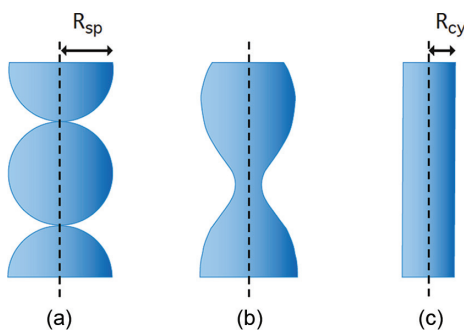


Figure 5.11 Three membrane tubes with different morphologies but the same constant mean curvature M : (a) Necklace-like tube consisting of identical spheres with radius $R_{sp} = 1/|M|$. The spheres are connected by closed membrane necks; (b) Unduloid with lemon-like bulges connected by open necks. The neck radius R_{ne} and the bulge radius R_{bu} are related to $|M|$ via $|M| = 1/(R_{ne} + R_{bu})$; and (c) Cylindrical tube with radius $R_{cy} = 1/(2|M|)$. (Reproduced from Lipowsky, R. *Biol. Chem.* 395, 253–274, 2014b. With permission of Walter de Gruyter GmbH & CO.KG.)

identical spheres connected by closed membrane necks. For spheres with radius R_{sp} , the necklace-like tube has mean curvature $M = 1/R_{sp}$ and $M = -1/R_{sp}$ when the enclosed volume of the tube is connected to the interior and exterior solution, respectively. A necklace-like tube consisting of spheres with radius R_{sp} can be continuously transformed into a cylindrical tube with radius $R_{cy} = \frac{1}{2} R_{sp}$, thereby preserving the value of the mean curvature. This transformation proceeds via a family of intermediate unduloids, all of which have the same mean curvature as the necklace-like and the cylindrical tube. The unduloids consist of lemon-like bulges connected by open necks, see the example in [Figure 5.11b](#). Thus, during the constant-mean-curvature transformation, the closed necks of the necklace-like tube open up and the bulges of the necklace retract until the necks and the bellies have the same radius and form a cylindrical tube.

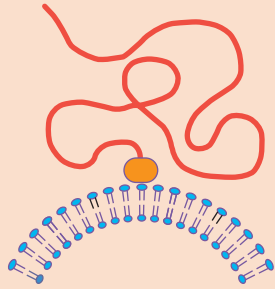
5.3.5 LOCAL CURVATURE GENERATION AND SPONTANEOUS CURVATURE

The simulation snapshot in [Figure 5.7](#) displays a symmetric bilayer consisting of two leaflets that have the same molecular composition and are exposed to the same aqueous environment. Likewise, the cartoons in [Figure 5.9](#) did not indicate any asymmetry between the two leaflets. In real systems, such symmetric bilayers are somewhat exceptional, but they provide a useful reference system because their elastic properties are governed by a single elastic parameter, the bending rigidity κ that provides the basic energy scale of membranes. For phospholipid bilayers, the latter scale is of the order of 10^{-19} J, which is about $20k_B T$ at room temperature. For different lipid bilayers, the measured values of the bending rigidity vary by about an order of magnitude, see the corresponding tables in [Chapters 11, 14, and 15](#) of this book.

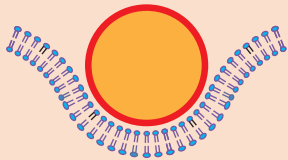
Real bilayer membranes are typically asymmetric. This asymmetry can arise from a different lipid composition of the two leaflets as found in all biological membranes (van Meer et al., 2008; Fadeel and Xue, 2009). One prominent example is provided by the ganglioside GM1, a glycolipid that is abundant in all mammalian neurons (Aureli et al., 2016) and plays an important role in many neuronal processes and diseases (Schengrund, 2015). Furthermore, GM1 acts as a membrane anchor for various toxins, bacteria, and viruses such as the simian virus 40 (Ewers et al., 2010). The curvature generated by different leaflet concentrations of GM1 has been recently studied, both experimentally for giant vesicles (Bhatia et al., 2018; Dasgupta et al., 2018) and by simulations of molecular bilayers (Dasgupta et al., 2018; Sreekumari and Lipowsky, 2018; Miettinen and Lipowsky, 2019). Likewise, membrane proteins in biological membranes have a preferred orientation, which also contributes to their asymmetry. In addition, membranes can acquire such an asymmetry from their environment as provided by the exterior and interior aqueous compartments. Indeed, the membranes become asymmetric when these two compartments contain different concentrations of ions, small solutes such as sugar molecules, and/or proteins that form adsorption or depletion layers on the two leaflets of the bilayer membranes (Lipowsky and Döbereiner, 1998; Lipowsky, 2013; Rozycki and Lipowsky, 2015, 2016; Liu et al., 2016; Karimi et al., 2018; Ghosh et al., in preparation). Examples for mechanisms of local generation of membrane curvature are given in [Box 5.1](#). Local curvature generation by proteins is reviewed in [Chapter 23](#) of this book.

Box 5.1 Local generation of membrane curvature

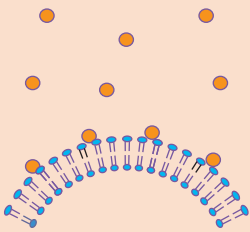
Bilayer asymmetry and spontaneous curvature can be generated by a variety of molecular mechanisms as illustrated in this Box.



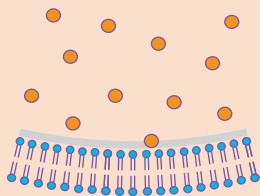
- A simple example is provided by a flexible polymer that is anchored with one of its ends to the membrane (Lipowsky, 1995; Nikolov et al., 2007).
- Such an anchored polymer generates curvature in order to increase its configurational entropy.



- Adhesive nanoparticles that are partially engulfed by the membrane act as scaffolds and impose their curvature onto this membrane, (Lipowsky and Döbereiner, 1998; Deserno, 2004; Agudo-Canalejo and Lipowsky, 2015a) see [Chapter 8](#) of this book.

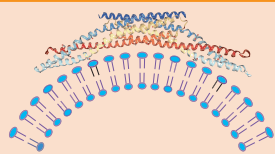


- Small adhesive solutes generate a substantial spontaneous curvature m as predicted theoretically (Lipowsky and Döbereiner, 1998; Lipowsky, 2013) and observed in molecular simulations (Rozycki and Lipowsky, 2015). For particles with a diameter of 1 nm and a concentration difference of 100 mM, adsorption leads to $m = \frac{1}{77nm}$.



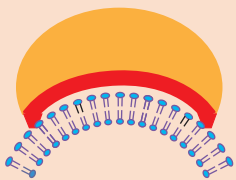
- Depletion layers of solutes induce a spontaneous curvature m of the opposite sign (Lipowsky and Döbereiner, 1998). This prediction has also been confirmed by recent molecular simulations (Rózycki and Lipowsky, 2016). For particles with a diameter of 1 nm and a concentration difference of 100 mM, depletion leads to $m = -\frac{1}{270nm}$.

The case of divalent ions is controversial because two recent experimental studies on Ca^{2+} ions (Simunovic et al., 2015; Baumgart et al., 2017) led to different conclusions about the sign of the ion-induced spontaneous curvature.

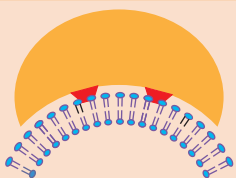


- N-BAR proteins such as amphiphysin (Takei et al., 1999; Peter et al., 2004) and endophilin (Farsad et al., 2001), F-BAR proteins such as pacsin/syndapin (Wang et al., 2009), and other proteins involved in endocytosis such as epsin (Ford et al., 2002) can bind to membranes and impose their curvature onto these membranes.

Membrane-binding proteins that act as scaffolds for the membrane shape are usually quite rigid. They can be regarded as adhesive nanoparticles with two characteristic properties: (i) their shape is typically nonspherical and often banana-like or convex-concave; and (ii) their surface contains a more or less complex pattern of adhesive and nonadhesive surface domains. Thus membrane-binding proteins that impose their shape onto the membrane can be regarded as nonspherical Janus-like nanoparticles.



- If the *planar* membrane can bind to some of the adhesive surface domains (red) of the particle, the particle generates membrane curvature via an induced-fit mechanism.



- If the adhesive surface domains (red) can only be reached by an appropriately *curved* membrane, the particle generates membrane curvature via conformational selection (Lipowsky, 2014b).

On length scales that exceed about twice the membrane thickness, the bilayer asymmetry can be described in terms of another curvature-elastic parameter, the spontaneous curvature m . In order to define the sign of m in an unambiguous manner, we use the same sign convention as for the mean curvature M , see Figure 5.9. Thus, we distinguish an interior from an exterior aqueous compartment and take the spontaneous curvature to be positive and negative if the membrane prefers to bulge towards the exterior and interior compartment, respectively. Note that, under the reversal of the normal vectors, the spontaneous curvature transforms in the same way as the mean curvature and, thus, changes sign.

If the membrane is decorated by many bound “particles,” it will acquire a certain spontaneous curvature that depends both on the local particle-induced curvature and on the particle coverages for the two leaflets of the bilayer membrane (Breidenich et al., 2000; Lipowsky, 2002). Thus, if a single particle that is bound to the outer leaflet of an asymptotically flat bilayer generates the local, position-dependent mean curvature $M_{si}(s^1, s^2)$, the spontaneous curvature m is given by

$$m = I_{M,si}(\Gamma_{ex} - \Gamma_{in}) \quad (5.3)$$

with the integrated mean curvature

$$I_{M,si} \equiv \int dA M_{si}(s^1, s^2) \quad (5.4)$$

and the coverages Γ_{ex} and Γ_{in} which are equal to the numbers of particles bound to the outer and inner leaflets per unit area (Breidenich et al., 2000). In contrast to other elastic membrane parameters such as the bending rigidity or the area compressibility modulus, the spontaneous curvature can vary over more than three orders of magnitude, from the inverse size of giant vesicles, which is of the order of $1/(50 \mu\text{m})$, to half the inverse membrane thickness, which is of the order of $1/(10 \text{ nm})$.

Inspection of the relationship Eq. 5.3 shows that the sign of the spontaneous curvature m is determined (i) by the sign of the integrated mean curvature $I_{M,si}$ induced by a single particle bound to the outer leaflet of the bilayer and (ii) by the sign of the difference $\Gamma_{ex} - \Gamma_{in}$ between the coverages of the outer and inner leaflets. Depending on the molar particle concentrations in the exterior and interior aqueous compartments, the sign of $\Gamma_{ex} - \Gamma_{in}$ can be positive or negative. Likewise, the sign of the integrated curvature $I_{M,si}$ can be positive or negative as well, reflecting different molecular interactions between the bound particle and the membrane. An anchored polymer, for example, generates a positive value of $I_{M,si}$ but this value becomes negative when all monomers of the polymer are strongly adsorbed onto the membrane (Breidenich et al., 2001, 2005). A negative sign of $I_{M,si}$ also applies if the particle is large and partially engulfed by the membrane.

As explained previously, we use two related conventions in order to define the sign of the local mean curvature of the membrane in an unambiguous manner. The first convention is that the normal vector of the membrane is taken to point towards the exterior compartment. The second convention is that we take the local mean curvature of the membrane to be positive if the membrane

bulges in the direction of the normal vector. Therefore, the spontaneous curvature is taken to be positive as well if the membrane prefers to bulge towards the exterior solution, i.e., in the direction of the normal vector.

The intuitive notion that asymmetric membranes have a preferred curvature was originally discussed by Bancroft for surfactant monolayers in water-oil emulsions (Bancroft, 1913; Bancroft and Tucker, 1927) and was included by Frank as the so-called “splay term” in the curvature elasticity of liquid crystals (Frank, 1958). In the context of lipid bilayers, spontaneous curvature was first considered by Helfrich (1973), who introduced it in analogy to the splay term for liquid crystals. The corresponding curvature energy of the membrane is now known as the spontaneous curvature model (Seifert et al., 1991) which will be presented in the next section.

5.4 CURVATURE ELASTICITY OF UNIFORM MEMBRANES

This chapter describes the theoretical framework that has been crucial in order to understand the morphology of giant vesicles. This framework is based on membrane curvature and the associated elastic energy contributions. The theory also takes into account that the low lipid solubility and the osmotic conditions lead to important constraints on the membrane area and the vesicle volume. In fact, what makes this theory both appealing and challenging is the interplay between local and global membrane properties.

On the one hand, the shape of a membrane can be described locally by its mean and Gaussian curvatures. On the other hand, in the absence of topological transformations such as membrane fusion and fission, both the membrane area and the vesicle volume are essentially fixed which has a direct and strong influence on the local membrane behavior. The connection between local and global properties is provided by two quantities, the mechanical tension Σ within the membrane and the pressure difference ΔP across this membrane. For free vesicles, these two quantities cannot be measured experimentally. However, the theory described in this chapter provides explicit relations between Σ and ΔP and those quantities that are directly accessible to experimental observations.

Another intriguing aspect of the morphology of giant vesicles is the frequent observation of membrane necks that connect two larger membrane segments. One example is provided by the neck that connects the spherical bud to the mother vesicle in Figure 5.2, another example is provided by the shape L^{sto} in Figure 5.6. Theoretically, these necks were first discovered by numerical energy minimization (Seifert et al., 1991; Miao et al., 1991; Berndl et al., 1990) of vesicles with uniform membranes as considered in this section. The necks are interesting from a conceptual point of view because they lead to *local* relations between (i) geometric quantities that can be directly observed in the optical microscope and (ii) curvature-elastic parameters such as the spontaneous curvature.

This section focuses on the spontaneous curvature model which is theoretically appealing because it depends on a relatively small number of parameters. Indeed, uniform vesicle membranes involve two geometric quantities, the vesicle volume

V and the membrane area A , as well as two material parameters, the bending rigidity κ and the spontaneous curvature m introduced in Section 5.3.5. In fact, as shown below, the vesicle shapes depend only on two dimensionless parameters, the volume-to-area ratio proportional to $V/A^{3/2}$, also known as the reduced volume, and the dimensionless spontaneous curvature proportional to $mA^{1/2}$.

The spontaneous curvature model is based on an expansion in powers of the principal curvatures and should be reliable as long as these curvatures are small compared to the inverse membrane thickness. In addition, the spontaneous curvature model implicitly assumes that the area difference between the two leaflets can change via flip-flops of lipid molecules. While a phospholipid molecule may stay in the same leaflet for hours, a cholesterol molecule will, on average, flip-flop from one leaflet to the other within one second. Therefore, the spontaneous curvature model should provide a reliable description for bilayer membranes that contain cholesterol or another sterol. The latter membranes are of particular interest because they undergo phase separation into liquid-disordered and liquid-ordered phases, see Section 5.8 below and Chapter 18 of this book.

If all membrane components undergo relatively slow flip-flops, one should extend the spontaneous curvature model by adding a nonlocal term that depends on the quenched area difference between the two leaflets. This extension leads to the area-difference-elasticity model and to an effective spontaneous curvature as described at the end of this section.

The present section is supplemented by three appendices: Appendix 5.B on different topologies of vesicles; Appendix 5.D which explains the identity of the mechanical tension with the Lagrange multiplier for membrane area; and Appendix 5.E which describes the different variants of curvature models.

5.4.1 SPONTANEOUS CURVATURE MODEL

Curvature expansion of local curvature energy

Within the spontaneous curvature model, the curvature energy functional $\mathcal{E}_{\text{cu}}\{S\}$ of a certain membrane shape S is provided by the area integral⁴

$$\mathcal{E}_{\text{cu}}\{S\} = \int dA \varepsilon_{\text{cu}}(\underline{s}) \quad (5.5)$$

where $\varepsilon_{\text{cu}}(\underline{s})$ represents a local energy density that varies smoothly with the two-dimensional surface coordinates $\underline{s} \equiv (s^1, s^2)$ used to parametrize the membrane surface via the three-dimensional vector $\vec{X}(\underline{s})$. When expressed in terms of these coordinates, the area element dA depends on the metric tensor g_{ij} , see Appendix 5.A, and has the form

$$dA = ds^1 ds^2 \sqrt{g} \quad \text{with} \quad g \equiv \det(g_{ij}) = g_{11}g_{22} - g_{12}g_{21}. \quad (5.6)$$

The local density ε_{cu} of the curvature energy should only depend on the principal curvatures C_1 and C_2 . In addition,

at any given point P of the membrane surface, this energy density must remain unchanged when we rotate the surface coordinates by $\pi/2$ which implies $\varepsilon_{\text{cu}}(C_2, C_1) = \varepsilon_{\text{cu}}(C_1, C_2)$. An expansion of ε_{cu} up to second order in the principal curvatures then leads to⁵

$$\varepsilon_{\text{cu}}(C_1, C_2) \approx a_0 + a_1(C_1 + C_2) + a_2(C_1^2 + C_2^2) + a_3 C_1 C_2. \quad (5.7)$$

When this relation is expressed in terms of the mean curvature M and the Gaussian curvature G , we obtain

$$\varepsilon_{\text{cu}} \approx 2\kappa(M - m)^2 + \kappa_G G \quad (5.8)$$

with the bending rigidity κ , the spontaneous curvature m , and the Gaussian curvature modulus κ_G .⁶ As a result, the curvature energy functional has the form (Helfrich, 1973; Seifert et al., 1991)

$$\mathcal{E}_{\text{cu}}\{S\} = \int dA [2\kappa(M(\underline{s}) - m)^2 + \kappa_G G(\underline{s})] \quad (5.9)$$

which defines the spontaneous curvature model.

Vesicles without bilayer edges or pores

For a closed vesicle without bilayers edges or pores, the Gauss-Bonnet theorem of differential geometry implies

$$\int dA G = 2\pi\chi = 2\pi(2 - 2g) \quad (5.10)$$

with the Euler characteristic χ and the topological genus g , which counts the number of handles, see Appendix 5.B. Thus, for a closed vesicle shape S and a uniform vesicle membrane, the spontaneous curvature model is defined by the curvature energy functional

$$\mathcal{E}_{\text{cu}}\{S\} = \mathcal{E}_{\text{be}}\{S\} + 2\pi\chi\kappa_G \quad (5.11)$$

with the bending energy functional

$$\mathcal{E}_{\text{be}}\{S\} = 2\kappa \int dA (M - m)^2. \quad (5.12)$$

When we evaluate the functionals \mathcal{E}_{cu} and \mathcal{E}_{be} for a certain shape S_o , we obtain the corresponding curvature and bending energies $E_{\text{cu}} = \mathcal{E}_{\text{cu}}\{S_o\}$ and $E_{\text{be}} = \mathcal{E}_{\text{be}}\{S_o\}$ for which we use normal capital letters E .

It is instructive to consider the behavior of the bending energy functional Eq. 5.12 under the reversal of the normal vectors. Thus, consider a certain shape S_o and map it onto another shape S'_o by reversing all normal vectors of its membrane surface. The mean curvature M of shape S_o is then transformed into the mean curvature $M'(\underline{s}) = -M(\underline{s})$ of shape S'_o which implies

⁴ Here and below, large calligraphic letters such as \mathcal{E} and \mathcal{F} are used for functionals that map shapes into real numbers.

⁵ Here and below, the symbol \approx stands for 'asymptotically equal' in a certain limit

⁶ The constant term $a_0 - a_1^2/(4a_2)$ has been omitted.

$$\mathcal{E}_{\text{be}}(\{S'_o\}, m') = \mathcal{E}_{\text{be}}(\{S_o\}, m) \quad \text{for } m' = -m, \quad (5.13)$$

i.e., the bending energy functional is invariant under a reversal of the normal vectors provided we reverse the spontaneous curvature m as well.

The bending energy functional $\mathcal{E}_{\text{be}}\{S\} \sim \int dA M^2$ of symmetric membranes with $m = 0$ has a long history in the calculus of variations. The quadratic expression in the mean curvature was first studied at the beginning of the 19th century by the French mathematician Germain in her theory of vibrating plates (Dalmédico, 1991). About a hundred years later, this expression played a prominent role in the work of the German mathematician Blaschke and his students, who were particularly interested in its invariance properties under conformal transformations. In the 1960s, the subject was studied in a systematic manner by the British mathematician Willmore, and the shapes that minimize $\int dA M^2$ are often referred to as Willmore surfaces (Willmore, 1982).

Separation of length scales

As described above, the spontaneous curvature model is based on the expansion of the curvature energy density in powers of the principal curvatures and includes all terms up to second order in these curvatures. This truncation of the curvature expansion at second order is clearly appropriate as long as the principal curvatures are much smaller than the inverse membrane thickness $1/\ell_{\text{mc}} \simeq 1/(4 \text{ nm})$ as follows from the discussion in Section 5.3.1. Thus, the spontaneous curvature model should provide a reliable description for the shapes of giant vesicles as observed in the (conventional) optical microscope, which resolves membrane curvatures below $1/(300 \text{ nm})$. In fact, as explained in Appendix 5.C.1, the spontaneous curvature model is expected to be quite reliable up to principal curvatures of about $1/(80 \text{ nm})$. For more strongly curved membrane segments, third-order curvature terms may become important which involve two additional curvature-elastic parameters, see Appendix 5.C.1.

5.4.2 SPONTANEOUS TENSION

The bending energy functional as given by Eq. 5.12 attains its minimal value, $\mathcal{E}_{\text{be}} = 0$, when we consider shapes for which the mean curvature M is equal to the spontaneous curvature m . The expression Eq. 5.12 also implies that the bending rigidity κ represents a “spring constant” for deviations of the

actual mean curvature M from the spontaneous curvature m of the membrane.

Real membranes experience a variety of constraints that necessarily lead to such deviations of M from m . One important constraint is provided by the size of the membrane. If the membrane area A is large compared to $4\pi/m^2$, which is the surface area of a sphere with radius $1/|m|$, the membrane cannot adapt its curvature to the spontaneous curvature by forming a single sphere but can do so, to a large extent, by forming a long cylinder with radius $R_{\text{cy}} = 1/(2m)$. Another important constraint arises from the osmotic conditions that determine the vesicle volume and, thus, the volume-to-area ratio, also known as the reduced volume. If the vesicle volume is increased by osmotic inflation, it will eventually attain a spherical shape with mean curvature $M = 1/R_{\text{sp}}$ that usually differs from the spontaneous curvature m of the vesicle membrane. In fact, for a giant spherical vesicle, the mean curvature $M = 1/R_{\text{sp}}$ can be very small compared to the absolute value $|m|$ of the spontaneous curvature. Likewise, supported lipid bilayers with $M = 0$ can have a large spontaneous curvature with magnitude $|m| \gg 0$. Whenever a large membrane segment of area A is forced to attain a mean curvature that is much smaller than the spontaneous curvature, the contribution of this segment to the bending energy obtained from Eq. 5.12 has the form $E_{\text{be}} \approx A\sigma$ with the spontaneous tension (Lipowsky, 2013)

$$\sigma \equiv 2\kappa m^2. \quad (5.14)$$

This tension represents the only tension scale that can be defined, apart from a dimensionless multiplicative factor, by the two parameters κ and m . Therefore, the spontaneous tension σ may be viewed as the intrinsic tension of curvature elasticity. If the membrane has a bending rigidity of about 10^{-19} J , a spontaneous curvature of $1/(20 \mu\text{m})$ leads to a spontaneous tension of about 10^{-6} mN/m while a spontaneous curvature of $1/(20 \text{ nm})$ leads to a spontaneous tension of about 1 mN/m . Thus, in real membrane systems, the spontaneous tension can vary over six orders of magnitude, see the examples in Table 5.1.

5.4.3 GLOBAL AND LOCAL PARAMETERS

Volume and area as global control parameters

As explained in Section 5.2.2, lipid bilayers are permeable to water and small gas molecules but essentially impermeable to ions and solute molecules, see also Chapter 20 of this book. As a consequence, the vesicle volume is primarily determined

Table 5.1 Spontaneous (or preferred) curvature m in units of $1/\mu\text{m}$ and associated spontaneous tension $\sigma = 2\kappa m^2$ in units of 2 mN/m for four different membrane systems where the bending rigidity was taken to have the typical value $\kappa \simeq 10^{-19} \text{ J}$.

	SUGAR SOLUTIONS ^a	DNA STRANDS ^b	PEG/DEXTRAN SOLUTIONS ^c	BAR-DOMAIN PROTEINS ^d
$m [1/\mu\text{m}]$	0.01–0.1	0.1–1	3–10	10–50
$\sigma [2 \text{ mN/m}]$	10^{-8} – 10^{-6}	10^{-6} – 10^{-4}	10^{-3} – 10^{-2}	10^{-2} –0.5

^a Döbereiner, H.G. et al., *Eur. Biophys. J.*, 28, 174–178, 1999.

^b Nikolov, V. et al., *Biophys. J.*, 92, 4356–4368, 2007.

^c Li, Y. et al., *Proc. Nat. Acad. Sci. USA*, 108, 4731–4736, 2011; Liu, Y. et al., *ACS Nano*, 10, 463–474, 2016.

^d Peter, B.J. et al., *Science*, 303, 495–499, 2004; McMahon, H.T. and Gallop, J.L. *Nature*, 438, 590–596, 2005.

by the osmotic conditions and the temperature. Therefore, one convenient procedure to change the vesicle volume at constant temperature is via osmotic inflation and deflation. Osmotic deflation is limited by the attractive intermolecular forces that start to become important when different membrane segments come into close proximity. Thus, at very small volumes, different segments of the vesicle membrane may start to fold back onto themselves or to form local membrane stacks. On the other hand, osmotic inflation is limited by the available membrane area. Indeed, for a given membrane area A and the corresponding vesicle size

$$R_{\text{ve}} = \sqrt{A/(4\pi)}, \quad (5.15)$$

the vesicle volume V attains its maximal value when the vesicle has a spherical shape. Therefore, the vesicle volume satisfies the inequality

$$V \leq \frac{4\pi}{3} R_{\text{ve}}^3 = \frac{4\pi}{3} \left(\frac{A}{4\pi} \right)^{3/2}. \quad (5.16)$$

For constant temperature and lipid composition, the area A of the vesicle membrane is primarily determined by the number of lipid molecules within the membrane. Indeed, in the absence of external forces or constraints, the lipids attain a certain molecular area corresponding to their optimal packing density. In principle, the membrane area can be changed by a mechanical tension that acts to stretch the membrane. In practice, such a tension can increase the membrane area only by a few percent because the membrane starts to rupture for larger extensions of its area. Therefore, as long as the membrane does not rupture, the membrane area A should attain a constant value to a very good approximation.

For giant unilamellar vesicles, one can directly measure the vesicle volume V and the membrane area A . It is therefore rather natural from an experimental point of view to regard V and A as basic geometric parameters that determine the vesicle shape.

Dimensionless parameters of spontaneous curvature model

For closed vesicles, the Gaussian curvature modulus contributes a constant term to the curvature energy functional \mathcal{E}_{cu} which is independent of the vesicle shape. We are then left with the bending energy functional \mathcal{E}_{be} that depends on four (dimensionful) parameters: two material parameters, namely bending rigidity κ and spontaneous curvature m , as well as two geometric parameters, vesicle volume V and membrane area A . Furthermore, we can choose a basic energy and length scale. One convenient choice for these two scales is provided by the bending energy κ and the vesicle size R_{ve} as defined by Eq. 5.15.

For the latter choice, the dimensionless bending energy E_{be}/κ depends only on two dimensionless parameters: (i) the volume-to-area ratio or reduced volume of the vesicle

$$v \equiv \frac{V}{\frac{4\pi}{3} R_{\text{ve}}^3} = 6\sqrt{\pi} V/A^{3/2} \quad (5.17)$$

and (ii) the rescaled and dimensionless spontaneous curvature

$$\bar{m} \equiv m R_{\text{ve}} = m \sqrt{A/(4\pi)}. \quad (5.18)$$

In the following, we will often discuss the behavior of vesicles with a certain, fixed membrane area and, thus, with a fixed length scale R_{ve} . Deflation and inflation processes are then described by changes in the volume v for a certain value of the spontaneous curvature \bar{m} . Likewise, adsorption and desorption processes which affect the bilayer asymmetry are described by changes of the spontaneous curvature \bar{m} for a fixed value of the volume v .

Scale transformations of vesicle shapes

The conclusions of the previous subsection can be understood from a somewhat different perspective if we study the behavior of the energy functional in Eq. 5.12 under scale transformations. As mentioned, the vesicle shape S can be described by a vector-valued function $\vec{X}(\underline{s})$ that depends on the two-dimensional surface coordinate \underline{s} . A scale transformation from the shape S to the new shape S' is then described by

$$\vec{X}(\underline{s}) \rightarrow \vec{X}'(\underline{s}) \equiv \zeta \vec{X}(\underline{s}) \quad \text{with a scale factor } \zeta > 0 \quad (5.19)$$

which implies the scale transformations

$$V \rightarrow V' = \zeta^3 V \quad \text{and} \quad A \rightarrow A' = \zeta^2 A \quad (5.20)$$

of vesicle volume and membrane area.

The bending energy functional \mathcal{E}_{be} in Eq. 5.12 remains invariant under the scale transformation Eq. 5.19, i.e., $\mathcal{E}_{\text{be}}\{S'\} = \mathcal{E}_{\text{be}}\{S\}$ if we combine this transformation with the rescaling

$$m \rightarrow m' \equiv m/\zeta \quad (5.21)$$

of the spontaneous curvature.

Now, assume that we have minimized the energy functional and found the shape S_0 of minimal bending energy for a certain set of the (dimensionful) parameters V , A , κ , and m . Any slightly deformed shape, say S_1 , will have a larger bending energy, i.e., $\mathcal{E}_{\text{be}}\{S_1\} > \mathcal{E}_{\text{be}}\{S_0\}$. This property remains valid if we compare the bending energies of the shapes S'_0 and S'_1 as obtained by rescaling both S_0 and S_1 with the same scale factor ζ , i.e., $\mathcal{E}_{\text{be}}\{S'_1\} > \mathcal{E}_{\text{be}}\{S'_0\}$ for any small deformation of S'_0 , provided we also rescale the spontaneous curvature according to Eq. 5.21. Therefore, the rescaled shape S'_0 represents the shape of minimal bending energy for the parameters $\zeta^3 V$, $\zeta^2 A$, κ , and m/ζ .

The same conclusion can be drawn from the dimensionless parameters introduced in the previous subsection. Indeed, the dimensionless bending energy E_{be}/κ depends only (i) on the volume-to-area ratio $v \propto VA^{3/2}$ and (ii) on the spontaneous curvature $\bar{m} = m R_{\text{ve}}$, both of which remain invariant under the combined scale transformation Eqs 5.20 and 5.21.

It is often instructive to consider the special case of a symmetric membrane with vanishing spontaneous curvature, $m = 0$. In this case, the energy functional Eq. 5.12 is invariant under

the scale transformation of the vesicle geometry as described by Eq 5.20 and does not involve the rescaling of any material parameter. Thus, for $m = 0$, large and small vesicles have the same bending energy if they have the same shape.

5.4.4 LOCAL SHAPE EQUATION AND ENERGY BRANCHES

Constrained energy minimization

If we take the vesicle volume and the membrane area as control parameters, we are thus faced with the problem of minimizing the curvature energy functional as given by Eq. 5.11 for a given vesicle volume V and membrane area A . In principle, there are a variety of ways to tackle this minimization problem numerically.

Numerical minimization typically involves a discretization of the vesicle shape into a triangular mesh of membrane patches. Furthermore, in order to model the fluidity of the membrane, one has to choose a dynamic triangulation. The advantage of numerical minimization is that we do not have to make any simplifying assumptions about the vesicle shape. The disadvantage of such a numerical procedure is that we can only explore a limited region of the parameter space. Furthermore, numerical minimization methods becomes difficult whenever the vesicle shape involves narrow membrane necks or long tubes. As we will see further below, such somewhat exotic shapes are quite common for vesicle membranes.

In order to apply analytical approaches to the constrained minimization, we will now incorporate the area and volume constraints via Lagrange multipliers Σ and ΔP and consider the shape functional

$$\mathcal{F}\{S\} = -\Delta P \mathcal{V}\{S\} + \Sigma \mathcal{A}\{S\} + \mathcal{E}_{\text{bc}}\{S\} \quad (5.22)$$

where we have omitted the shape-independent term arising from the integrated Gaussian curvature. The two Lagrange multipliers have to be chosen in such a way that the volume functional \mathcal{V} and the area functional \mathcal{A} attain the values $\mathcal{V}\{S\} = V$ and $\mathcal{A}\{S\} = A$. Note that we again denote the functionals \mathcal{F} , \mathcal{V} , and \mathcal{A} by large calligraphic letters and their numerical values for a certain shape by normal capital letters F , V , and A .

As shown in Appendix 5.D, the Lagrange multiplier Σ can be identified with the mechanical tension experienced by the uniform membrane. The latter identity can be derived by defining the overall elastic energy of the membrane to be the sum of its bending and stretching energy and by minimizing this overall elastic energy (Lipowsky, 2014a).

Euler-Lagrange or local shape equation

The first variation of the shape functional $\mathcal{F}\{S\}$ leads to the Euler-Lagrange equation

$$\Delta P = 2\Sigma M - 2\kappa \nabla_{\text{LB}}^2 M - 4\kappa [M - m][M(M + m) - G] \quad (5.23)$$

with the Laplace-Beltrami operator ∇_{LB}^2 and the (local) Gaussian curvature G . When expressed in terms of the surface coordinates \underline{s} , the action of this operator onto a scalar function $f(\underline{s})$ has the explicit form

$$\nabla_{\text{LB}}^2 f = \frac{1}{\sqrt{g}} \frac{\partial}{\partial s^k} \left(\sqrt{g} g^{kj} \frac{\partial}{\partial s^j} f \right) \quad (5.24)$$

with the inverse metric tensor $(g^{ij}) \equiv (g_{ij})^{-1}$ and an implicit summation over repeated indices (do Carmo, 1976). Note that the Euler-Lagrange Eq. 5.23 provides an explicit relation between the Lagrange multipliers ΔP and Σ with the mean and Gaussian curvatures, M and G , which describe the membrane shape locally. Therefore, the Euler-Lagrange equation represents a *local* shape equation.

The Euler-Lagrange Eq. 5.23 is equivalent to

$$\Delta P = 2\hat{\Sigma}M - 2\kappa \nabla_{\text{LB}}^2 M - 4\kappa mM^2 - 4\kappa [M - m][M^2 - G] \quad (5.25)$$

with the total membrane tension

$$\hat{\Sigma} \equiv \Sigma + 2\kappa m^2 = \Sigma + \sigma \quad (5.26)$$

which represents the sum of the mechanical tension Σ and the spontaneous tension σ , where we identified the Lagrange multiplier Σ with the mechanical tension, see Appendix 5.D. Therefore, the only tension that enters the solution of the Euler-Lagrange equation is the total tension $\hat{\Sigma}$ that contains the spontaneous tension σ defined in Eq. 5.14.

For spontaneous curvature $m = 0$, the Euler-Lagrange Eq 5.23 assumes the simplified form

$$\Delta P = 2\Sigma M - 2\kappa \nabla_{\text{LB}}^2 M - 4\kappa M[M^2 - G] \quad (m = 0) \quad (5.27)$$

which was derived by several mathematicians as reviewed in the monograph of Willmore (Willmore, 1982). It seems that the variation of the more general case with $m \neq 0$ was first considered by (Jenkins, 1977) who included both normal and tangential displacements of the membrane surface.⁷ However, in order to derive the Euler-Lagrange Eq. 5.23, it is sufficient to include only normal displacements as shown by (Ou-Yang and Helfrich, 1989).

Energy branches of stationary shapes

The solutions of the Euler-Lagrange Eq. 5.23 represent the stationary shapes corresponding to local minima, saddle points, or local maxima of the bending energy. The physically relevant shapes are the local minima, which represent (meta)stable states, and the saddle points which provide the activation barriers between different (meta)stable states.

In practice, the combination of the Laplace-Beltrami operator and the nonlinearities in the principal curvatures C_1 and C_2 , arising from the second and third power of the mean curvature $M = \frac{1}{2}(C_1 + C_2)$ and from the Gaussian curvature $G = C_1 C_2$, make the Euler-Lagrange Eq. 5.23 rather difficult to solve. As explained further below, much insight can be obtained for special shapes such as spheres, cylinders, and combinations

⁷ The final result of the variational calculation by (Jenkins, 1977) contains one term that is cancelled by another, missing term.

thereof. For axisymmetric shapes, the partial differential Eq 5.23 is equivalent to a set of ordinary differential equations that can be solved numerically, e.g., by shooting methods. In this way, the regime of relatively small spontaneous curvatures m with $|\bar{m}| = |m| R_{ve} \lesssim 2$ has been studied in a systematic manner (Seifert et al., 1991).

These numerical solutions have shown that the stationary shapes form, in general, several branches for the same set of parameters as illustrated in Figure 5.12.⁸ The latter figure displays the branches for vanishing spontaneous curvature $m = 0$. The different branches will now be labeled by the index j and the corresponding stationary shapes by S^j . Along branch j , the bending energy function

$$E_{bc}(V, A; \kappa, m; j) = \mathcal{E}_{bc}\{S^j\} \quad (5.28)$$

varies in a continuous manner as one changes one of the control parameters. When expressed in terms of the dimensionless parameters v and $\bar{m} = m R_{ve}$ as defined in Eqs 5.17 and 5.18, one obtains

$$E_{bc}(V, A; \kappa, m; j) = 8\pi\kappa \bar{E}(v, \bar{m}; j), \quad (5.29)$$

see Figure 5.12. The corresponding shapes of minimal energy are displayed in Figure 5.13.

Pressure difference and membrane tension

In order to get further insight into the two Lagrange multipliers ΔP and Σ , it is useful to consider the shape energy

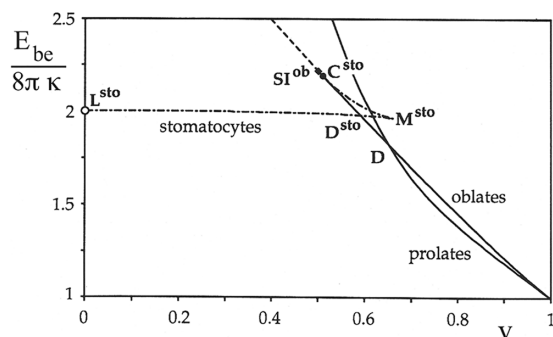


Figure 5.12 Dimensionless bending energy $\bar{E}_{bc} = E_{bc}/(8\pi\kappa)$ as a function of volume-to-area ratio v for spontaneous curvature $m = 0$: The sphere corresponds to the largest possible volume-to-area ratio $v = 1$. In the limit of small v , we obtain the limit shape L^{sto} of a stomatocyte consisting of two concentric spheres of (almost) equal size connected by a closed membrane neck. The two full lines emanating from the sphere correspond to (meta)stable prolates and oblates. The dashed-dotted line connecting the limit shape L^{sto} with the transition point D^{sto} corresponds to stable stomatocytes, the one between D^{sto} and M^{sto} to metastable stomatocytes, and the dashed-dotted line between M^{sto} and C^{sto} to the activation barriers between the oblates and the stomatocytes. (Reproduced from Seifert, U. et al., *Phys. Rev. A*, 44, 1182–1202, 1991.)

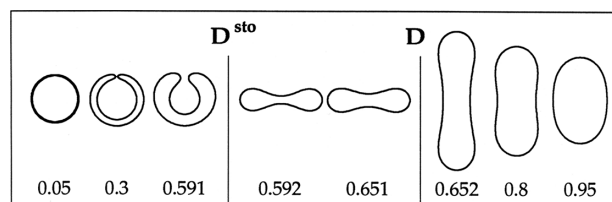


Figure 5.13 Axisymmetric shapes of a vesicle with constant area A and variable volume V as expressed in terms of the dimensionless volume v (bottom row) for spontaneous curvature $\bar{m} = 0$. (Reproduced from Seifert, U. et al., *Phys. Rev. A*, 44, 1182–1202, 1991.)

$$F(\Delta P, \Sigma; \kappa, m; j) \equiv -\Delta P V + \Sigma A + E_{bc}(V, A; \kappa, m; j) \quad (5.30)$$

along a certain branch j of stationary shapes and to interpret this expression as the Legendre-transformed energy from the extensive variables V and A to the intensive variables ΔP and Σ . The formal structure of such a Legendre transformation, which plays an important role in thermodynamics, implies (Svetina and Zeks, 1989; Seifert et al., 1991; Miao et al., 1991; Seifert, 1997)

$$\Delta P = \left(\frac{dE_{bc}(V, A; \kappa, m; j)}{dV} \right)_A \quad (5.31)$$

and

$$\Sigma = - \left(\frac{dE_{bc}(V, A; \kappa, m; j)}{dA} \right)_V. \quad (5.32)$$

When we have several branches of stationary shapes for the same values of V and A , the derivatives on the right hand side of these relations will depend on the branch index j and so will the values of ΔP and Σ , compare Figure 5.12.

The relation Eq. 5.31 implies that the Lagrange multiplier ΔP is the pressure conjugate to the vesicle volume V and can, thus, be identified with the difference

$$\Delta P = P_{in} - P_{ex} \quad (5.33)$$

between the pressures P_{in} and P_{ex} within the interior and exterior compartments. In practise, these pressures are usually osmotic pressures but may also include hydrostatic pressures as imposed by a micropipette. The pressure difference ΔP is usually orders of magnitude smaller than the individual osmotic pressures P_{in} and P_{ex} . The relation Eq. 5.32 implies that the Lagrange multiplier Σ is the tension conjugate to the membrane area A . In fact, as previously mentioned, this tension can be identified with the mechanical tension experienced by the uniform membrane as shown in Appendix 5.D (Lipowsky, 2014a).

When expressed in terms of the dimensionless bending energy $\bar{E}_{bc} = E_{bc}/(8\pi\kappa)$, the general relations Eqs 5.31 and 5.32 for the pressure difference and the membrane tension can be rewritten in the form

$$\frac{\Delta P}{8\pi\kappa} = \left(\frac{dv}{dV} \right)_A \frac{\partial \bar{E}_{bc}}{\partial v} = 6\sqrt{\pi} \frac{1}{A^{3/2}} \frac{\partial \bar{E}_{bc}}{\partial v} \quad (5.34)$$

⁸ The ‘branches’ are really two-dimensional sheets over the (v, \bar{m}) -plane.

or

$$\frac{\Delta P R_{ve}^3}{\kappa} = 6 \frac{\partial \bar{E}_{bc}}{\partial v} \quad (5.35)$$

and

$$\frac{\Sigma}{8\pi\kappa} = 9\sqrt{\pi} \frac{V}{A^{5/2}} \frac{\partial \bar{E}_{bc}}{\partial v} - \frac{1}{4\sqrt{\pi}} \frac{m}{A^{1/2}} \frac{\partial \bar{E}_{bc}}{\partial \bar{m}} \quad (5.36)$$

or

$$\frac{\Sigma R_{ve}^2}{\kappa} = 3v \frac{\partial \bar{E}_{bc}}{\partial v} - \bar{m} \frac{\partial \bar{E}_{bc}}{\partial \bar{m}}. \quad (5.37)$$

For vanishing spontaneous curvature, $\bar{m} = m = 0$, the second term in Eqs 5.37 and 5.36 vanishes which implies that both ΔP and Σ become proportional to the partial derivative $\partial \bar{E}_{bc} / \partial v$. Inspection of Figure 5.12 shows that this derivative is negative along the prolate and oblate branch but close to zero along the stomatocyte branch. Thus, as we reduce the volume of a spherical vesicle with $m = 0$, the pressure difference ΔP and the membrane tension Σ are both negative along the prolate and oblate branches. A negative pressure difference $\Delta P = P_{in} - P_{ex}$ implies that the exterior osmotic pressure exceeds the interior one and that the pressure difference acts to compress the vesicle volume. A negative tension Σ implies that the membrane is slightly compressed compared to its optimal packing density. Along the stomatocyte branch, on the other hand, both the pressure difference and the membrane tension are close to zero.

A combination of the two relations Eqs 5.34 and 5.36 leads to

$$3\Delta P V - 2\Sigma A = 4\sqrt{\pi} \frac{\kappa m}{A^{1/2}} \frac{\partial \bar{E}_{bc}}{\partial \bar{m}}, \quad (5.38)$$

independent of the derivative $\partial \bar{E}_{bc} / \partial v$ which cancels out from this special combination of ΔP and Σ . In the absence of a spontaneous curvature, we then obtain the simple relation

$$3\Delta P V = 2\Sigma A \quad (m = 0). \quad (5.39)$$

We will see in the next subsection that the same relation also follows from special deformations (or variations) of the stationary shapes as provided by infinitesimal scale transformations.

5.4.5 GLOBAL SHAPE EQUATION

Now, consider a certain stationary shape S^j of the shape functional \mathcal{F} as given by Eq. 5.22. The pressure difference ΔP and the tension Σ then have specific values as obtained from the partial derivatives in Eqs 5.31 and 5.32 along the corresponding branch that includes the chosen shape S^j . Small deformations of this shape can be described by membrane displacements $\bar{u}(\underline{s})$ which define the deformed shape S' via

$$\bar{X}(\underline{s}) \rightarrow \bar{X}'(\underline{s}) = \bar{X}(\underline{s}) + \varepsilon \bar{u}(\underline{s}) \quad \text{with} \quad |\varepsilon| \ll 1. \quad (5.40)$$

Because the shape S^j represents a local minimum or saddle point of the shape functional F , we know that

$$\mathcal{F}\{S^i\} - \mathcal{F}\{S^j\} = O(\varepsilon^2) \quad \text{or} \quad \left. \frac{d\mathcal{F}\{S^i\}}{d\varepsilon} \right|_{\varepsilon=0} = 0. \quad (5.41)$$

A particular shape deformation is provided by the choice $\bar{u}(\underline{s}) = \bar{X}(\underline{s})$ which leads to the infinitesimal scale transformation

$$\bar{X}(\underline{s}) \rightarrow \bar{X}'(\underline{s}) = (1 + \varepsilon) \bar{X}(\underline{s}). \quad (5.42)$$

This scale transformation implies that the area A and the volume V are transformed according to $A \rightarrow A' = (1 + \varepsilon)^2 A$ and $V \rightarrow V' = (1 + \varepsilon)^3 V$. Likewise the integrated mean curvature

$$I_M = \mathcal{I}_M\{S\} \equiv \int dA M \quad (5.43)$$

transforms according to

$$I_M = \mathcal{I}_M\{S\} \rightarrow I'_M = \mathcal{I}_M\{S'\} = (1 + \varepsilon) I_M \quad (5.44)$$

while the integral $\int dA M^2$ remains unchanged. When applied to the explicit form of the shape functional \mathcal{F} , the condition Eq 5.41 leads to

$$-3\Delta P V + 2\hat{\Sigma} A - 4\kappa m I_M = 0 \quad (5.45)$$

with the total membrane tension $\hat{\Sigma} = \Sigma + 2\kappa m^2$ as in Eq. 5.26. For any stationary shape S^j , this equation provides an explicit connection between ΔP , $\hat{\Sigma}$ and the global geometric quantities V , A , and I_M . Therefore, Eq. 5.45 represents a *global* shape equation.

For $m = 0$, the global shape equation reduces to the relation Eq. 5.39. Furthermore, a combination of Eq. 5.45 with Eq. 5.38 leads to the expression

$$\frac{\partial \bar{E}_{bc}}{\partial \bar{m}} = 2\bar{m} - \frac{I_M}{\sqrt{\pi} A} \quad (5.46)$$

for the partial derivative of the dimensionless bending energy $\bar{E}_{bc}(v, \bar{m})$ with respect to the spontaneous curvature $\bar{m} = m R_{ve}$. Note that the integrated mean curvature I_M depends on the stationary shape S^j and, thus, on the spontaneous curvature \bar{m} .

5.4.6 VESICLE SHAPES WITH MEMBRANE NECKS

The numerical solutions of the Euler-Lagrange equations for axisymmetric shapes revealed that these shapes develop narrow membrane necks in certain regions of the parameter space and that these shapes approach limit shapes with closed necks. These necks provide information about the spontaneous curvature m as will be explained in the following subsections, see also Box 5.2 for a summary of necks for vesicle membranes with laterally uniform composition.

Neck closure condition

Let us consider a branch of stationary shapes S^{st} that represent local minima of the bending energy and, thus, solutions of the Euler-Lagrange Eq. 5.23. These shapes are smooth in the sense

that the shape variable $\bar{X}(s)$ is twice differentiable with respect to the surface coordinates and that the mean curvature varies continuously along an arbitrary path on the membrane surface. For any point P on this surface and for any path through this point, we can thus define two mean curvature values, M_{P+} and M_{P-} , which represent the limiting values of the mean curvature as we approach the point P from the “left” and from the “right” along the chosen path. The continuous variation of M then implies that

$$M_P = \frac{1}{2}(M_{P+} + M_{P-}). \quad (5.47)$$

For a smooth surface, we could also use the more general expression $M_P = \zeta M_{P+} + (1 - \zeta)M_{P-}$ with $0 \leq \zeta \leq 1$ corresponding to different weights for the left-sided and the right-sided limit. However, because the assignment of “left” and “right” is completely arbitrary, we want the expression to remain unchanged when we interchange “left” and “right,” which implies $\zeta = 1/2$. We now interpret the expression Eq. 5.47 as an interpolation formula and extend it to closed necks, i.e., to points on the membrane surface at which the mean curvature develops a discontinuity. Thus, if the two membrane segments, 1 and 2, adjacent to the closed neck have the mean curvatures M_1 and M_2 , we define the effective curvature of the closed neck by

$$M_{\text{ne}} \equiv \frac{1}{2}(M_1 + M_2). \quad (5.48)$$

This definition is analogous to the value $H(0) = \frac{1}{2}$ of the Heaviside step function $H(x)$ as obtained from smooth approximations for $H(x)$.

The numerical studies of membrane necks also showed that the neck closure makes no contributions to the bending energy. Because the energy density at the neck is given by

$$\varepsilon_{\text{bc}}(M_{\text{ne}}) \equiv 2\kappa[M_{\text{ne}} - m]^2, \quad (5.49)$$

we conclude that the neck closes in such a way that

$$M_{\text{ne}} = \frac{1}{2}(M_1 + M_2) = m \quad (\text{neck closure}). \quad (5.50)$$

It follows from this condition that the two membrane segments 1 and 2 have the same bending energy density, i.e., that

$$\varepsilon_{\text{bc}}(M_1) = \varepsilon_{\text{bc}}(M_2). \quad (5.51)$$

In fact, we could also start from the requirement that the bending energy density is continuous across the closed neck which leads to $M_1 - m = \pm(M_2 - m)$. For the root with the plus sign, we obtain the relation $M_1 = M_2$, i.e., a continuous variation of M and, thus, no neck but, for the root with the minus sign, we recover the neck closure condition Eq. 5.50.

The neck closure condition Eq. 5.50 has been confirmed for a large number of axisymmetric shapes as obtained by minimizing the bending energy numerically (Seifert et al., 1991). So far, necks

between non-axisymmetric membrane segments have not been studied in a systematic manner but the continuity arguments given above also apply to such non-axisymmetric situations and then lead to the same closure condition.

Neck closure of membrane buds

It is instructive to apply the condition Eq. 5.50 to the neck closure of membrane buds as frequently observed in experiments. Two cases can be distinguished corresponding to in- and out-buds that point towards the interior and exterior compartment, respectively, see Figure 5.14.

First, consider spherical out-buds as shown in Figure 5.14a–c. For such a bud with radius R_2 , the bud membrane adjacent to the neck has positive mean curvature $M_2 = 1/R_2$. The 1-segment on the other side of the neck must satisfy $M_1 \geq -M_2$ because the two membrane segments cannot intersect each other. Combining this geometric constraint with the neck closure condition Eq. 5.50, we obtain the inequality

$$m = \frac{1}{2}(M_1 + M_2) \geq 0 \quad (\text{neck closure of out-bud}) \quad (5.52)$$

for the spontaneous curvature m . Thus, whenever we observe the neck closure of an out-bud, we can conclude that the spontaneous curvature must be positive or zero. Furthermore, for $m = 0$, neck closure of an out-bud implies $M_1 = -M_2$, i.e., the 1-segment partially engulfs the bud membrane in the vicinity of the neck. Therefore, for a 1-segment with mean curvature $M_1 > -M_2 = -1/R_2$, neck closure of an *out-bud* implies a *positive* spontaneous curvature.

Next, consider spherical in-buds as shown in Figure 5.14d–f. For a spherical in-bud with radius R_2 , the bud membrane adjacent to the neck has negative mean curvature $M_2 = -1/R_2$. The 1-segment on the other side of the neck must satisfy $M_1 \leq -M_2 = |M_2|$ because the two membrane segments should not intersect each other.

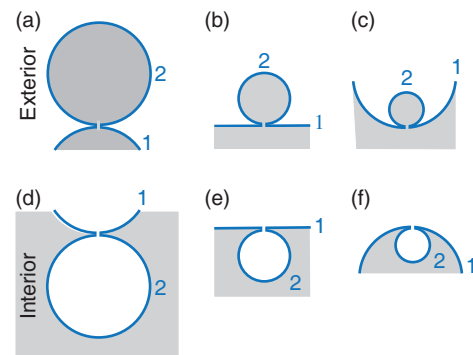


Figure 5.14 (a–c) Out-buds with closed necks, formed as limit shapes by a membrane with *positive* spontaneous curvature: The out-buds are filled with interior medium (gray) and point towards the exterior medium (white). The three membranes (blue) in (a–c) have the same spontaneous curvature $m > 0$ but differ in the mean curvatures of the 1- and 2-segments; (d–f) In-buds with closed necks, formed as limit shapes by a membrane with *negative* spontaneous curvature: The in-buds are filled with exterior medium (white) and point towards the interior medium (gray). The three membranes (blue) in (d–f) have the same spontaneous curvature $m < 0$ but differ in the mean curvatures of the two membrane segments. The two segments have mean curvature $M_1 = m$ and $M_2 = m$ in (a) and (d), $M_1 = 0$ and $M_2 = 2m$ in (b) and (e), and $M_1 = -m$ and $M_2 = 3m$ in (c) and (f).

A combination of the latter inequality with the neck closure condition Eq. 5.50 now leads to the condition

$$m = \frac{1}{2}(M_1 + M_2) \leq 0 \quad (\text{neck closure of in-bud}) \quad (5.53)$$

for the spontaneous curvature m . Thus, whenever we observe the neck closure of an in-bud, we can conclude that the spontaneous curvature must be negative or zero. For $m = 0$, neck closure of an in-bud now implies $M_1 = -M_2 = |M_2|$ as for the limit shape L^{sto} in Figure 5.12. Therefore, for a 1-segment with mean curvature $M_1 < |M_2| = 1/R_2$, neck closure of an *in-bud* implies a *negative* spontaneous curvature.

Stability of closed necks

The neck closure condition Eq. 5.50 applies to limit shapes as obtained from smooth solutions of the local shape Eq. 5.23 or the corresponding set of ordinary differential equations for axisymmetric shapes. One may also consider a closed neck and ask under what conditions this neck is locally stable. This problem has been addressed for axisymmetric vesicles consisting of two almost spherical vesicles that are connected by a narrow neck with radius R_{nc} . More precisely, these vesicle shapes consist of two spherical caps which are connected by two unduloid segments which form a membrane neck of radius R_{nc} . The shapes are parametrized in such a way that one can study the closure of the neck keeping the total membrane area constant. For vanishing neck radius R_{nc} , the shapes approach the two-sphere shapes Θ^{out} and Θ^{in} .⁹ The two-sphere shape Θ^{out} consists of a sphere with radius R_1 and mean curvature $M_1 = 1/R_1$ connected, via a closed neck, to a spherical out-bud with radius $R_2 \leq R_1$ and mean curvature $M_2 = 1/R_2$ as in Figure 5.14a. The two-sphere shape Θ^{in} again consists of a sphere of radius R_1 and mean curvature $M_1 = 1/R_1$ but now connected, via a closed membrane neck, to a spherical in-bud with radius $R_2 \leq R_1$ and mean curvature $M_2 = -1/R_2$ as in Figure 5.14f. For small but nonzero R_{nc} , the bending energy of these vesicle shapes can then be expanded in powers of the neck radius R_{nc} .

If the two membrane segments 1 and 2 adjacent to the neck have positive mean curvatures as in Figure 5.14a, the bending energy is found to behave as (Fourcade et al., 1994)

$$E_{\text{bc}}(R_{\text{nc}}) \approx E_{\text{bc}}(0) - 4\pi\kappa(M_1 - m + M_2 - m)R_{\text{nc}} \quad \text{for small } R_{\text{nc}}. \quad (5.54)$$

On the other hand, if the 1-segment has positive mean curvature whereas the 2-segment has negative mean curvature as in Figure 5.14f, the bending energy has the asymptotic behavior (Lipowsky, 2014a)

$$E_{\text{bc}}(R_{\text{nc}}) \approx E_{\text{bc}}(0) + 4\pi\kappa(M_1 - m + M_2 - m)R_{\text{nc}} \quad \text{for small } R_{\text{nc}} \quad (5.55)$$

⁹ In the next Section 5.5 we will study such two-sphere vesicles in a systematic manner and distinguish limit shapes from persistent shapes. The two-sphere shapes Θ^{out} then correspond to the limit shapes L^{pea} and L^{out} as well as to the persistent shapes Φ^{pea} . Likewise, the two-sphere shapes Θ^{in} represent both the limit shapes L^{sto} and L^{in} as well as the persistent shapes Φ^{sto} .

with a plus instead of a minus sign in front of the linear term. In both cases, the bending energy $E_{\text{bc}}(0)$ of the two-sphere shapes Θ^{out} and Θ^{in} , which are characterized by vanishing neck radius $R_{\text{nc}} = 0$, does not involve any contribution from the neck itself.

The asymptotic behavior as given by Eq. 5.54 implies that the closed neck in Figure 5.14a, corresponding to an out-bud, is stable provided the average neck curvature M_{nc} satisfies

$$M_{\text{nc}} = \frac{1}{2}(M_1 + M_2) \leq m \quad \text{with } M_1 > 0 \text{ and } M_2 > 0 \quad (5.56)$$

but opens up if $M_{\text{nc}} > m$. The marginal case with $M_{\text{nc}} = m$ corresponds to the neck closure condition Eq. 5.52 with *positive* spontaneous curvature. Therefore, when a membrane with $m > 0$ forms a closed neck with $M_1 > 0$ and $M_2 > 0$ as in Figure 5.14a, this neck remains closed if the effective neck curvature M_{nc} decreases below the spontaneous curvature m .

On the other hand, the small R_{nc} -behavior in Eq. 5.55 implies that the closed neck of the in-bud in Figure 5.14f is stable provided

$$M_{\text{nc}} = \frac{1}{2}(M_1 + M_2) \geq m \quad \text{with } M_1 > 0 \text{ and } M_2 < 0 \quad (5.57)$$

but opens up if $M_{\text{nc}} < m$. Now, the marginal case with $M_{\text{nc}} = m$ corresponds to the neck closure condition Eq. 5.53 with *negative* spontaneous curvature. Therefore, when a membrane with $m < 0$ forms a closed neck with $M_1 > 0$ and $M_2 < 0$ as in Figure 5.14f, this neck remains stable if the effective neck curvature M_{nc} increases above the spontaneous curvature m , i.e., if the absolute value $|M_{\text{nc}}|$ of the effective neck curvature decreases below the absolute value $|m|$ of the spontaneous curvature.

The stability of a closed neck must not depend on our choice for the direction of the normal vectors. When we reverse the normal vectors, we change both the sign of the mean curvatures and the sign of the spontaneous curvature. Let us first apply this transformation to the neck configuration in Figure 5.14a which leads to the neck configuration in Figure 5.14d. The corresponding stability relation now becomes

$$M_{\text{nc}} = \frac{1}{2}(M_1 + M_2) \geq m \quad \text{with } M_1 < 0, M_2 < 0, \text{ and } m < 0. \quad (5.58)$$

Furthermore, if we reverse the normal vectors of the neck configuration in Figure 5.14f, we obtain the neck configuration in Figure 5.14c and the associated stability relation

$$M_{\text{nc}} = \frac{1}{2}(M_1 + M_2) \leq m \quad \text{with } M_1 < 0, M_2 > 0, \text{ and } m > 0. \quad (5.59)$$

In summary, we obtain essentially two different stability relations for the closed necks depicted in Figure 5.14. Closed necks with *non-negative* neck curvature M_{nc} can only exist for non-negative spontaneous curvature $m \geq 0$ and the neck curvature can then attain a value within the interval

$$0 \leq M_{\text{nc}} \leq m \quad (\text{out-bud, spontaneous curvature } m \geq 0) \quad (5.60)$$

which includes the neck configurations in Figure 5.14(a–c). The limiting case $M_{\text{ne}} = 0$ applies to an out-bud that is partially enclosed by the adjacent 1-segment of the mother vesicle whereas the equality $M_{\text{ne}} = m$ corresponds to the neck closure condition of the limit shape. An example for $M_{\text{ne}} = 0$ is provided by a discocyte with a membrane neck that connects the discocyte's north pole with mean curvature $M_1 < 0$ to a spherical out-bud with mean curvature $M_2 = -M_1 > 0$.

Closed necks with *non-positive* neck curvature M_{ne} , on the other hand, can only exist for non-positive spontaneous curvature $m \leq 0$ and the neck curvature can then have a value within the interval

$$0 \geq M_{\text{ne}} \geq m \quad (\text{in-bud, spontaneous curvature } m \leq 0) \quad (5.61)$$

which includes the neck configurations in Figure 5.14(d–f). Now, the neck closure condition $M_{\text{ne}} = m$ and the enclosed bud condition $M_{\text{ne}} = 0$ provide lower and upper bounds for the range of possible M_{ne} -values.

Mismatch between neck curvature and spontaneous curvature

For a stably closed neck that satisfies the inequalities $M_{\text{ne}} < m$ and $m < M_{\text{ne}}$ in Eqs 5.60 and 5.61, the bending energy density $\varepsilon_{be} = 2\kappa[M_{\text{ne}} - m]^2$ as given by Eq. 5.49 does not vanish. The closed neck may just be considered as a curvature “defect” as discussed in Appendix 5.C.2. In the continuum description used here, this defect is point-like and has vanishing area which implies that its bending energy vanishes as well. The latter property is explicitly borne out in the derivation of the relations Eqs 5.54 and 5.55 because the energies $E_{\text{bc}}(0)$ obtained for vanishing neck radius $R_{\text{ne}} = 0$ do not contain any contribution from the neck.

However, a large mismatch between the neck curvature and the spontaneous curvature as obtained for stable necks with $0 < M_{\text{ne}} = m$ and $m = M_{\text{ne}} < 0$ does have an important consequence for the morphology of the vesicle. Indeed, a sufficiently large mismatch leads to an effective, curvature-induced constriction force that cleaves the membrane neck and thus leads to membrane fission, see Section 5.5.4 below.

5.4.7 AREA DIFFERENCE ELASTICITY

As mentioned at the beginning of this section, the spontaneous curvature model provides a quantitative description for the morphology of vesicles as long as the membrane curvatures are large compared to the inverse membrane thickness. Thus, highly curved membrane structures such as nanobuds or nanotubes may involve higher order curvature terms as discussed in Appendix 5.E. In addition, the spontaneous curvature model implicitly assumes that the area difference between the two bilayer leaflets can change via fast flip-flops of at least one molecular membrane component. If flip-flops can be ignored on the experimentally relevant time scales, the spontaneous curvature model should be supplemented by an additional energy term as described in this subsection.

Nonlocal energy term for preferred area difference

The bending energy functional Eq. 5.12 represents the area integral over a *local* energy density. In general, the bending of a bilayer membrane consisting of two leaflets may be constrained in a *nonlocal* or *global* manner. Indeed, if the membrane molecules

cannot undergo flip-flops between the two leaflets, the number of molecules are fixed within each leaflet and the quenched difference between these two numbers leads to a preferred area difference between these leaflets. This constraint was originally considered by Evans (1974), incorporated into the bilayer-coupling model by (Svetina and Zeks, 1989; Seifert et al., 1991), and generalized in terms of the area-difference-elasticity model (Miao et al., 1994; Döbereiner et al., 1997; Seifert, 1997).

The area difference ΔA between the area of the outer leaflet and the area of the inner leaflet is given by

$$\Delta A = 2d_{\text{mo}}I_M \quad (5.62)$$

with the molecular length scale d_{mo} , which corresponds to the distance between the neutral surfaces of the two monolayers or leaflets, and the integrated mean curvature $I_M = \int dA M$ as in Eq 5.43. The area-difference-elasticity model is defined by the energy functional

$$\mathcal{E}_{\text{ADE}}\{S\} = \mathcal{E}_{\text{bc}}\{S\} + \mathcal{D}_{\text{ADE}}\{S\} \quad (5.63)$$

with the local energy functional $\mathcal{E}_{\text{bc}}\{S\}$ as defined by Eq. 5.12 corresponding to the spontaneous curvature model and the nonlocal area-difference-elasticity term (Miao et al., 1994; Döbereiner et al., 1997)

$$\begin{aligned} \mathcal{D}_{\text{ADE}}\{S\} &= \frac{\pi\kappa_{\Delta}}{2Ad_{\text{mo}}^2} (\Delta\mathcal{A}\{S\} - \Delta A_0)^2 \\ &= \frac{2\pi\kappa_{\Delta}}{A} (\mathcal{I}_M\{S\} - I_{M,0})^2 \end{aligned} \quad (5.64)$$

where $\Delta\mathcal{A}\{S\}$ represents the area difference of the vesicle shape S and $\mathcal{I}_M\{S\}$ the integrated mean curvature of this shape. The additional energy term \mathcal{D}_{ADE} introduces two new parameters, the second bending rigidity κ_{Δ} and the integrated mean curvature $I_{M,0} = \Delta A_0/2d_{\text{mo}}$, corresponding to optimal molecular areas in both leaflets (Seifert, 1997). These molecular areas are, however, not accessible to current experimental methods and depend on the mechanical membrane tension. If the leaflets of a large spherical vesicle with radius R_{ve} had optimal molecular areas, we would obtain

$$I_{M,0} = \int dA \frac{1}{R_{\text{ve}}} = 4\pi R_{\text{ve}}. \quad (5.65)$$

Local and nonlocal spontaneous curvature

The stationary shapes with fixed membrane area A and fixed vesicle volume V are now more difficult to calculate because of the nonlocal character of the area-elasticity-difference but can be obtained using a two-step variational procedure, see Appendix 5.E. This procedure shows that all stationary shapes of the area-difference-elasticity model are also stationary shapes of the spontaneous curvature model with the shape functional $\mathcal{F}\{S\}$ as given by Eq. 5.22 and the effective spontaneous curvature (Döbereiner et al., 1997)

$$m_{\text{eff}} \equiv m + m_{\text{nlo}} \quad (5.66)$$

with the spontaneous curvature m , which is determined locally by the molecular interactions as considered in the previous subsections, and the nonlocal spontaneous curvature

$$m_{\text{nlo}} \equiv \pi \frac{\kappa_{\Delta}}{\kappa} \frac{I_{M,0} - \mathcal{I}_M\{S^j\}}{\mathcal{A}} \quad (5.67)$$

which depends on the stationary shape S^j via the integrated mean curvature $\mathcal{I}_M\{S^j\}$.

As mentioned before, area-difference-elasticity is only relevant if the membrane contains no molecular components that undergo flip-flops on the experimentally relevant time scales. Therefore, as far as the effective spontaneous curvature m_{eff} is concerned, we need to distinguish two cases: (i) For relatively fast flip-flops of some membrane components such as cholesterol, we can ignore the nonlocal spontaneous curvature m_{nlo} which implies that the effective spontaneous curvature m_{eff} becomes equal to the spontaneous curvature m , i.e., the area-difference-elasticity model reduces to the spontaneous curvature model; and (ii) For relatively slow flip-flops of all molecular membrane components, we will, in general, have a nonlocal spontaneous curvature m_{nlo} contributing to the effective spontaneous curvature $m_{\text{eff}} = m + m_{\text{nlo}}$. In order to examine whether this nonlocal spontaneous curvature m_{nlo} is relevant for a given vesicle shape, we need to determine its magnitude and to compare it with the local spontaneous curvature m .

Generalized stability relations for membrane necks

The latter approach can be applied, in particular, to two-sphere shapes with closed membrane necks. The stability of these necks can also be examined for the area-difference-elasticity model using the shape parametrization described in Section 5.4.6. Thus, we again consider axisymmetric shapes with membrane necks, parametrized in such a way that they approach the two-sphere shapes Θ^{out} and Θ^{in} in the limit of small neck radii. As before, the two-sphere shape Θ^{out} consist of a sphere with a spherical out-bud and the two-sphere shape Θ^{in} of a sphere with a spherical in-bud. We now use the energy functional Eq. 5.63 of the area-difference-elasticity model to calculate the elastic energy of the vesicle shapes up to first order in the neck radius R_{nc} . One then finds that closed necks with positive curvature M_{nc} are stable if

$$0 < M_{\text{nc}} \leq m_{\text{eff}} = m + \pi \frac{\kappa_{\Delta}}{\kappa} \frac{I_{M,0} - I_M\{\Theta^{\text{out}}\}}{\mathcal{A}} \quad (5.68)$$

(stable Θ^{out} shapes)

and necks with negative curvature M_{nc} are stable if

$$0 \geq M_{\text{nc}} \geq m_{\text{eff}} = m + \pi \frac{\kappa_{\Delta}}{\kappa} \frac{I_{M,0} - I_M\{\Theta^{\text{in}}\}}{\mathcal{A}} \quad (5.69)$$

(stable Θ^{in} shapes).

These stability conditions involve three different types of quantities: (i) the neck curvature, a purely geometric quantity that can be directly deduced from the two-sphere shapes; (ii) the local spontaneous curvature m , a material parameter determined by the molecular interactions, and (iii) the non-local spontaneous curvature m_{nlo}

that depends both on the geometry of the shape via the integrated mean curvature and on the bending rigidity ratio κ_{Δ}/κ . In subsection 5.5.3 further below, we will discuss the consequences of the stability conditions Eqs 5.68 and 5.69 for multi-sphere vesicles.

5.5 MULTI-SPHERE SHAPES OF UNIFORM MEMBRANES

In this section, we will consider a variety of multi-sphere shapes for vesicles with uniform membranes, i.e., membranes that have laterally uniform compositions and curvature-elastic properties. This section should be considered as a case study which nicely illustrates the polymorphism and multi-responsive behavior of giant vesicles.

We will focus on multi-component membranes that contain at least one membrane component such as cholesterol that undergoes relatively fast flip-flops. As mentioned, these membranes are appealing from a theoretical point of view because we can study their shapes within the spontaneous curvature model which depends only on two dimensionless parameters, the volume-to-area ratio (or reduced volume) v and the (local) spontaneous curvature \bar{m} . These two parameters can be controlled experimentally, e.g., by the osmotic conditions and by the adsorption of small solutes. In addition, three-component membranes with cholesterol have been of particular interest recently because they can form liquid-ordered and liquid-disordered phases. For both types of intramembrane phases, multi-sphere shapes have indeed been observed experimentally (Liu et al., 2016).

We will start with the Euler-Lagrange equations for spherical shapes which reveal the coexistence of two different sphere radii. When combined with the stability relations for the individual spheres and for the closed necks, we obtain multi-sphere vesicles that consist of several spheres with two different radii. We first consider two-sphere shapes and show that these shapes can be found in extended regions of the (v, \bar{m}) -plane and that these regions are bounded by two types of limit shapes. We also examine the changes of the morphology diagram when area difference elasticity is taken into account. We conclude that these changes are negligible both for large spontaneous curvatures and for small bud sizes.

Multi-sphere shapes consisting of more than two spheres will also be discussed. One interesting example is provided by one sphere with radius R_1 and N spherical buds with radius R_2 , all connected by closed necks that have the same neck curvature. For $N > 1$, the morphology diagram exhibits a more complex bifurcation structure with two bifurcation points and three types of limit shapes. The multi-sphere shapes with $N > 1$ buds described in this section are intimately related to the necklace-like tubes with $N > 1$ spherules as considered in the next Section 5.6.

5.5.1 SPHERICAL VESICLES AND SPHERICAL SEGMENTS

We now specify the local shape Eq. 5.23, which represents the Euler-Lagrange equation of the bending energy functional, and the global shape Eq. 5.45, which follows from the invariance of the bending energy under infinitesimal scale transformations,

to a spherical membrane segment with constant mean curvature $M = M_{\text{sp}}$. It turns out that *both shape equations lead to the same quadratic equation* for M_{sp} as given by

$$\Delta P = P_{\text{in}} - P_{\text{ex}} = 2\hat{\Sigma}M_{\text{sp}} - 4\kappa mM_{\text{sp}}^2 \quad (5.70)$$

with the total membrane tension $\hat{\Sigma} = \Sigma + \sigma$. For a symmetric bilayer membrane with $m = 0$, the relation Eq. 5.70 further simplifies and becomes

$$\Delta P = 2\Sigma M_{\text{sp}} \quad (m = 0) \quad (5.71)$$

which has the same form as the Laplace equation for liquid droplets. The Euler-Lagrange Eq. 5.70 can be derived in a more intuitive manner if one parametrizes the spherical shape by its radius R_{sp} and minimizes the shape energy with respect to R_{sp} (Lipowsky, 2013).

It follows from Eqs 5.70 and 5.71 that each value of $M_{\text{sp}} = \pm 1/R_{\text{sp}}$ defines a straight M_{sp} -line in the $(\Sigma, \Delta P)$ -plane. For $m = 0$, these M_{sp} -lines cover the whole $(\Sigma, \Delta P)$ -plane. For $m \neq 0$, on the other hand, the straight M -lines do not cover the whole $(\hat{\Sigma}, \Delta P)$ -plane as follows from the solution of the quadratic Eq. 5.70 which has the form

$$M_{1/2} = \frac{\hat{\Sigma}}{4\kappa m} \pm \left[\left(\frac{\hat{\Sigma}}{4\kappa m} \right)^2 - \frac{\Delta P}{4\kappa m} \right]^{1/2}. \quad (5.72)$$

Because the mean curvature must be real-valued, spherical segments are not possible for those values of $\hat{\Sigma}$ and ΔP for which the expression under the square root (or discriminant) becomes negative. Therefore, a certain choice of $\hat{\Sigma}$ and ΔP leads to spherical segments if

$$\Delta P \geq -\frac{\hat{\Sigma}^2}{4\kappa|m|} \quad \text{for } m < 0 \quad (5.73)$$

and if

$$\Delta P \leq \frac{\hat{\Sigma}^2}{4\kappa m} \quad \text{for } m > 0. \quad (5.74)$$

Along the parabolic boundaries $\Delta P = \hat{\Sigma}^2 / (4\kappa m)$ of these regions, we have only one solution as given by

$$M_1 = M_2 = \frac{\hat{\Sigma}}{4\kappa m} = \frac{\Sigma + 2\kappa m^2}{4\kappa m}. \quad (5.75)$$

For all other possible values of $\hat{\Sigma}$ and ΔP , we have two different solutions as in Eq. 5.72 with $M_1 \neq M_2$, corresponding to two different spherical segments. In general, the mean curvatures M_1 and M_2 may be positive or negative depending on the signs of the pressure difference ΔP , the membrane tension Σ , and the spontaneous curvature m .

Coexistence of two spherical segments

The two solutions M_1 and M_2 are characterized by the same values of the pressure difference ΔP and the mechanical tension Σ .

Therefore, the two membrane segments can coexist for these values of ΔP and Σ . Vice versa, when we observe the coexistence of

two spherical membrane segments with mean curvatures M_1 and M_2 , we can use the two Euler-Lagrange equations to conclude that the membrane tension is given by

$$\Sigma = 2\kappa m(M_1 + M_2) - 2\kappa m^2 \quad (5.76)$$

and the pressure difference by

$$\Delta P = 4\kappa m M_1 M_2. \quad (5.77)$$

The coexistence of two spherical shapes is indeed observed when out- and in-buds are formed from larger mother vesicles as shown in Figure 5.2 through Figure 5.6 and discussed in more detail in the next subsection.

On the other hand, the coexistence of more than two spherical segments with pair-wise different mean curvatures M_i and M_j is not possible for a uniform membrane. Indeed, if $N \geq 3$ different types of spherical segments coexisted on the same vesicle, we would have N Euler-Lagrange equations of the form Eq. 5.70. When we now choose a pair of spherical segments with mean curvatures M_i and M_j , we obtain the relations Eqs 5.76 and 5.77 with M_1 and M_2 replaced by M_i and M_j . For fixed i , we can choose $N - 1$ different values for j and obtain $N - 1$ different relations of the form Eqs 5.76 and 5.77. These relations immediately imply that all mean curvatures M_j must be identical. Because we can repeat this procedure for each value of i , we conclude that the shape equations for spherical segments allow only two different values of the mean curvature to coexist for uniform membranes.

Multi-component membranes can lead to the coexistence of several lipid phases and several types of intramembrane domains that differ in their composition, see Section 5.8 below. For two types of domains, the membrane can form coexisting spherical segments with four different mean curvatures. In general, a membrane with K types of domains can form coexisting spherical segments with $2K$ different mean curvatures as follows from the Euler-Lagrange equations for the different membrane domains. This morphological complexity remains to be explored.

Stability of individual spheres

Now, consider a single sphere which experiences the pressure difference $P_{\text{sp}} = P_{\text{sp,in}} - P_{\text{sp,ex}}$ where $P_{\text{sp,in}}$ is the osmotic pressure acting within the volume enclosed by the sphere. The second variation of the shape functional shows that a sphere with radius R_{sp} and mean curvature $M = 1/R_{\text{sp}}$ is (locally) stable provided this pressure difference P_{sp} satisfies (Ou-Yang and Helfrich, 1989; Seifert et al., 1991; Miao et al., 1991)

$$P_{\text{sp}} > P_{\text{sp}}^{*+} \equiv \frac{4\kappa}{R_{\text{sp}}^3} (mR_{\text{sp}} - 3) \quad (M_{\text{sp}} = 1/R_{\text{sp}}) \quad (5.78)$$

When we reverse the normal vector of the sphere, we change the signs of both the mean curvature M and the spontaneous curvature m . For such an inverted sphere, we obtain the stability condition

$$P_{\text{sp}} > P_{\text{sp}}^{*-} \equiv \frac{4\kappa}{R_{\text{sp}}^3} (-mR_{\text{sp}} - 3) \quad (M_{\text{sp}} = -1/R_{\text{sp}}). \quad (5.79)$$

One example for an inverted sphere in real systems is provided by an in-bud protruding into a giant vesicle which is a possible shape for negative spontaneous curvature $m < 0$. The in-bud with radius $R_{sp} = R_2$ and mean curvature $M_2 = -1/R_2$ is attached to a spherical mother vesicle with radius $R_{sp} = R_1 \geq R_2$ and mean curvature $M_1 = 1/R_1$. In this case, the volume enclosed by the in-bud is a subvolume of the exterior solution. Therefore, the membrane of the in-bud experiences the pressure difference $P_{sp} = -\Delta P$ whereas the membrane of the mother vesicle is exposed to $P_{sp} = \Delta P$.

Because the mother vesicle and the in-bud experience two different pressure differences, the two spherical membrane segments are then governed by two different stability conditions. Indeed, using the stability relations Eqs 5.78 and 5.79 as well as the general expression Eq. 5.77 for ΔP , the spherical shape of the mother vesicle is found to be stable if

$$\Delta P = -\frac{4\kappa m}{R_1 R_2} > \frac{4\kappa}{R_1^3}(mR_1 - 3) \quad \text{or} \quad \frac{m}{R_2} < \frac{3 - mR_1}{R_1^2} \quad (5.80)$$

whereas the stability condition for the spherical in-bud has the form

$$-\Delta P = \frac{4\kappa m}{R_1 R_2} > \frac{4\kappa}{R_2^3}(-mR_2 - 3) \quad \text{or} \quad \frac{m}{R_1} > \frac{-mR_2 - 3}{R_2^2} \quad (5.81)$$

At the critical pressures $P_{sp} = P_{sp}^{*\pm}$, the spherical shape undergoes a bifurcation which generates the branches of prolate and oblate shapes. For conventional spheres with $M_{sp} > 0$, the prolate shape has the lowest bending energy for small $|m|/M_{sp}$ -values whereas the oblate shape represents the lower energy shape for sufficiently large negative values of m/M_{sp} , see the morphology diagram in Figure 5.16 (Seifert et al., 1991).

5.5.2 TWO-SPHERE VESICLES

Giant vesicles frequently form shapes that consist of two spheres connected by a narrow membrane neck. Within the spontaneous curvature model, such shapes arise quite naturally and can be reached by deflation of smoothly curved shapes. Two such limit shapes have been obtained from a systematic numerical study of axisymmetric shapes (Berndl, 1990; Seifert et al., 1991): the limit shapes L^{pea} with a spherical out-bud and the limit shapes L^{sto} with a spherical in-bud. These limit shapes represent two-sphere shapes and have the geometries displayed in Figure 5.15. The limit shapes L^{pea} are reached, for positive spontaneous curvature, by the deflation of pear-like vesicles, the limit shapes L^{sto} for negative spontaneous curvature by the deflation of stomatocytes, see the morphology diagram in Figure 5.16. Inspection of this diagram shows that these limit shapes are found along two lines within the (v, \bar{m}) -plane.

Closer inspection of this morphology diagram also reveals that the deflation of a spherical vesicle with $v = 1$ and $\bar{m} > 0$ leads to a prolate-pear bifurcation before the limit shape L^{pea} is reached. Because the latter bifurcation is discontinuous and exhibits hysteresis, the experimental observation of the true limit shape will be facilitated if one studies both the deflation and the subsequent inflation of the GUV. Likewise, the deflation of a spherical vesicle with $v = 1$ and $\bar{m} < 0$ leads to an oblate-stomatocyte bifurcation

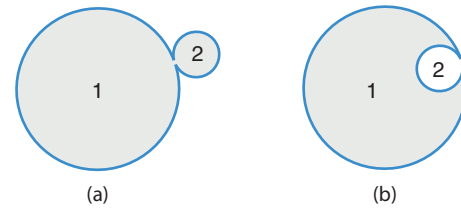


Figure 5.15 Geometry of shapes consisting of two spheres with radii $r_1 = R_1/R_{ve}$ and $r_2 = R_2/R_{ve} \leq r_1$ connected by a closed neck: (a) Two-sphere shape Θ^{out} with an out-bud and positive neck curvature $M_{ne} = \frac{1}{2}(\frac{1}{r_1} + \frac{1}{r_2}) > 0$ which can only form for positive spontaneous curvature $\bar{m} \geq \sqrt{2}$ and (b) Two-sphere shape Θ^{in} with an in-bud and non-positive neck curvature $M_{ne} = \frac{1}{2}(\frac{1}{r_1} - \frac{1}{r_2}) \leq 0$ which can only form for non-positive spontaneous curvature $\bar{m} \leq 0$. The stability of the membrane neck in (a) and (b) is governed by Eqs 5.60 and 5.61, respectively. $M_{ne} = \bar{m}$, the shape Θ^{out} in (a) represents a limit shape L^{pea} as obtained by neck closure from a stationary pear-like shape of the Euler-Lagrange equation while it represents a persistent shape Φ^{pea} with a stably closed neck for $M_{ne} < \bar{m}$. Likewise, the shape Θ^{in} may represent a limit shape L^{sto} as obtained by neck closure from a stationary stomatocyte or a persistent shape Φ^{sto} . The limit shapes are found along certain lines within the (v, \bar{m}) -plane whereas the persistent shapes are stable within two-dimensional regions of this plane, see the morphology diagrams in Figures 5.16 and 5.17.

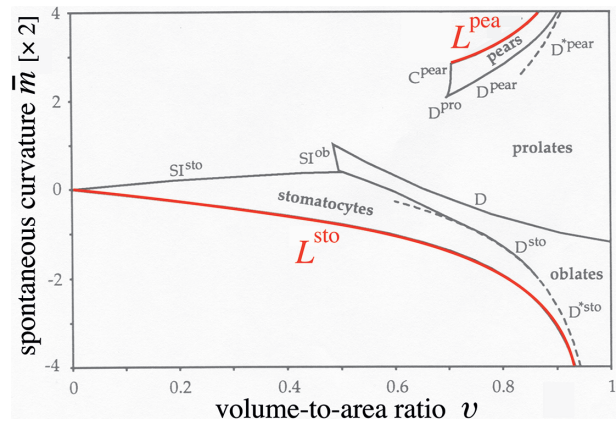


Figure 5.16 Morphology diagram as a function of volume-to-area ratio v and spontaneous curvature $c_0 \equiv 2\bar{m}$ which exhibits two lines of limit shapes. The limit shapes L^{pea} with an out-bud as in Figure 5.15a are found for $\bar{m} \geq \sqrt{2}$ along the upper line which is truncated at the end point $(v^+, \bar{m}^+) = (1/\sqrt{2}, \sqrt{2})$ corresponding to two equal spheres. As we move along the L^{pea} -line by increasing the spontaneous curvature \bar{m} and the volume-to-area-ratio v , the out-bud becomes smaller and smaller until the whole membrane area is taken up by the larger sphere. The limit shapes L^{sto} with an out-bud, see Figure 5.15b, are found for $\bar{m} \leq 0$ along the lower line which is truncated at the end point $(v^-, \bar{m}^-) = (0, 0)$ corresponding to two nested spheres of equal size. As we move along the L^{sto} -line by decreasing $\bar{m} < 0$ and increasing v , the in-bud becomes smaller and smaller until the vesicle forms a single sphere with $v = 1$ (Berndl, 1990). (Reproduced from Seifert, U. et al., *Phys. Rev. A*, 44, 1182–1202, 1991; Berndl, K. *Formen Von Vesikeln Diplomarbeit*, Ludwig-Maximilians-Universität München, 1990.)

before the limit shape L^{sto} is reached. The latter bifurcation is again discontinuous (Seifert et al., 1991).

The following analysis of two-sphere vesicles involves several steps (Lipowsky, 2018b). First, the geometric properties of the two-sphere shapes lead to other types of limit shapes, $L_{=}$ and

L_{\pm}^{in} , consisting of two identical spheres. Second, the neck closure condition determines the limit shapes L^{pea} and L^{sto} . Finally, we must examine the stability of the two individual spheres in order to find instability lines at which the two-sphere vesicles transform into other types of shapes. We will also emphasize two-sphere vesicles with buds that have zero bending energy and consider the two-sphere limit shapes obtained in the presence of area difference elasticity.

Geometric properties

The geometry of any two-sphere vesicle is determined by the radii R_1 and R_2 of the two spheres. In the following, we will consider vesicles with fixed area A and vesicle size $R_{\text{ve}} = \sqrt{A/(4\pi)}$ but variable volume V as controlled by the osmotic conditions. We then measure the radii of the two spheres in units of R_{ve} and define the dimensionless radii

$$r_1 \equiv R_1 / R_{\text{ve}} \quad \text{and} \quad r_2 \equiv R_2 / R_{\text{ve}}. \quad (5.82)$$

These two radii satisfy the implicit equations

$$r_1^2 + r_2^2 = \frac{A}{4\pi R_{\text{ve}}^2} = 1 \quad (5.83)$$

and

$$r_1^3 \pm r_2^3 = \frac{V}{4\pi R_{\text{ve}}^3} = v \quad (5.84)$$

where the plus and minus sign in Eq. 5.84 correspond to two-sphere shapes with an out- and in-bud, respectively. Therefore, the geometry of any two-sphere vesicle is determined by its area A and its volume V and depends only on the volume-to-area ratio v . As in Figure 5.15, we use the notation Θ^{out} and Θ^{in} for two-sphere shapes for which we have not examined the stability of their necks.

For a two-sphere vesicle with an in-bud, the radius r_2 of this bud must satisfy $r_2 \leq r_1$ because the membrane segments of the two spheres should not intersect. For a two-sphere vesicle with an out-bud, the shapes for $r_1 < r_2$ are identical with the shapes for $r_1 > r_2$. In order to avoid this degeneracy, we will impose the restriction $r_2 \leq r_1$ for out-buds as well. Because $r_1^2 + r_2^2 = 1$ as in Eq 5.83, the inequality $r_1 \geq r_2 = \sqrt{1 - r_1^2}$ implies

$$r_1 \geq \frac{1}{\sqrt{2}} \quad \text{and} \quad r_2 \leq \frac{1}{\sqrt{2}}. \quad (5.85)$$

The limiting cases with $r_2 = r_1 = 1/\sqrt{2}$ corresponds to two spheres with the same size and defines two other types of limit shapes, denoted by L_{\pm}^{out} and L_{\pm}^{in} . The limit shape L_{\pm}^{out} consists of two equal spheres with positive mean curvature whereas the limit shape L_{\pm}^{in} consists of two nested spheres which have the same size but opposite mean curvatures. In addition, these limit shapes have the smallest possible volume of two-sphere vesicles as given by

$$\min(v) = v_{\pm}^{\text{out}} \equiv 1/\sqrt{2} \quad \text{for } L_{\pm}^{\text{out}} \quad (5.86)$$

and

$$\min(v) = v_{\pm}^{\text{in}} \equiv 0 \quad \text{for } L_{\pm}^{\text{in}}. \quad (5.87)$$

A related property of these limit shapes is that their neck curvatures have the smallest absolute values. When expressed in terms of the dimensionless neck curvature

$$\bar{M}_{\text{nc}} \equiv M_{\text{nc}} R_{\text{ve}} = \frac{1}{2} \left(\frac{1}{r_1} \pm \frac{1}{r_2} \right), \quad (5.88)$$

these minimal neck curvatures have the values

$$\min(\bar{M}_{\text{nc}}) = \sqrt{2} \quad \text{for } L_{\pm}^{\text{out}} \quad (5.89)$$

and

$$\min(|\bar{M}_{\text{nc}}|) = \max(\bar{M}_{\text{nc}}) = 0 \quad \text{for } L_{\pm}^{\text{in}}. \quad (5.90)$$

Neck closure and neck stability

A necessary prerequisite for a stable two-sphere vesicle is the stability of the closed neck connecting the two spheres. The stability of closed necks was already studied in subsection 5.4.6 where we distinguished neck closure from closed neck conditions. The closure condition has the dimensionless form

$$\bar{M}_{\text{nc}} = \frac{1}{2} \left(\frac{1}{r_1} \pm \frac{1}{r_2} \right) = \bar{m} \quad (\text{neck closure}) \quad (5.91)$$

where the plus and minus sign again corresponds to two-sphere shapes with out- and in-buds, respectively. In addition, the closed neck condition is given by

$$0 < \bar{M}_{\text{nc}} = \frac{1}{2} \left(\frac{1}{r_1} + \frac{1}{r_2} \right) < \bar{m} \quad \text{for out-buds} \quad (5.92)$$

and by

$$0 > \bar{M}_{\text{nc}} = \frac{1}{2} \left(\frac{1}{r_1} - \frac{1}{r_2} \right) > \bar{m} \quad \text{for in-buds.} \quad (5.93)$$

Limit shapes related to neck closure

The combination of the geometric relations Eqs 5.83 and 5.84 with the neck closure condition Eq. 5.91 determines the limit shapes L^{pea} and L^{sto} . When we eliminate the two radii from these three equations, we obtain the functional relationships

$$v = v^{\text{pea}}(\bar{m}) \quad \text{for the line of } L^{\text{pea}} \text{ shapes} \quad (5.94)$$

and

$$v = v^{\text{sto}}(\bar{m}) \quad \text{for the line of } L^{\text{sto}} \text{ shapes.} \quad (5.95)$$

The function $v^{\text{pea}}(\bar{m})$ has the explicit form (Seifert et al., 1991)

$$v = v^{\text{pea}}(\bar{m}) \equiv -\frac{1}{4\bar{m}^3} + \left(1 - \frac{1}{2\bar{m}^2}\right) \sqrt{1 + \frac{1}{4\bar{m}^2}} \quad \text{for } \bar{m} \geq \sqrt{2}, \quad (5.96)$$

which behaves as

$$v^{\text{pea}}(\bar{m}) \approx 1 - \frac{3}{8\bar{m}^2} \quad \text{for large } \bar{m}. \quad (5.97)$$

The function $v^{\text{sto}}(\bar{m})$ has the same \bar{m} -dependence as $v^{\text{pea}}(\bar{m})$ but applies to $\bar{m} \leq 0$.

Both lines of limit shapes L^{pea} and L^{sto} extend down to the smallest possible volumes which they reach when both spheres have the same size. The corresponding values of the spontaneous curvature \bar{m} are given by

$$\min(\bar{m}) = \bar{m}_{=}^{\text{out}} \equiv \sqrt{2} \quad \text{for } L^{\text{pea}} \quad (5.98)$$

and by

$$\max(\bar{m}) = \bar{m}_{=}^{\text{in}} \equiv 0 \quad \text{for } L^{\text{sto}}, \quad (5.99)$$

see the L^{pea} and L^{sto} lines in Figure 5.16. In the following subsection, the region of the morphology diagram with $\bar{m} > 0$, which contains the limit shapes L^{pea} and $L_{=}^{\text{out}}$, will be discussed in more detail.

Buds with zero bending energy

It is useful to distinguish another special case of budded vesicle shapes, denoted by Z^{out} and Z^{in} . The spherical buds of these shapes have radius $r_2 = 1/|\bar{m}|$ and thus zero bending energy. Because of the inequality $r_2 \leq 1/\sqrt{2}$ as in Eq. 5.85, we then have

$$r_2 = \frac{1}{|\bar{m}|} \leq \frac{1}{\sqrt{2}} \quad \text{and} \quad r_1 = \sqrt{1 - \frac{1}{\bar{m}^2}} \geq \frac{1}{\sqrt{2}}. \quad (5.100)$$

Both relations lead to the same inequality $|\bar{m}| \geq \sqrt{2}$ which implies

$$\bar{m} \geq \sqrt{2} \quad \text{for out-buds} \quad (5.101)$$

and

$$\bar{m} \leq -\sqrt{2} \quad \text{for in-buds}. \quad (5.102)$$

For these vesicles, the buds have vanishing bending energy and the whole bending energy is provided by the bending energy of the mother vesicle with radius r_1 . The neck mean curvature is then given by

$$\bar{M}_{\text{nc}} = \bar{M}_{\text{nc}}^0(\bar{m}) \equiv \frac{1}{2} \left(\frac{1}{\sqrt{1 - 1/\bar{m}^2}} + \bar{m} \right) \quad (5.103)$$

which satisfies

$$\bar{M}_{\text{nc}}^0(\bar{m}) \leq \bar{m} \quad \text{for out-buds with } \bar{m} \geq \sqrt{2} \quad (5.104)$$

and

$$\bar{M}_{\text{nc}}^0(\bar{m}) \geq \bar{m} \quad \text{for in-buds with } \bar{m} \leq -\sqrt{2}. \quad (5.105)$$

Comparison with the stability relations as given by Eqs 5.92 and 5.93 then shows that the closed necks between the zero-energy buds and the mother vesicles are stable for both positive and negative spontaneous curvatures. For out-buds, the equality $\bar{M}_{\text{nc}} = \bar{M}_{\text{nc}}^0(\bar{m}) = \bar{m}$ describes the neck closure condition and applies to $r_1 = r_2 = 1/\bar{m}$, i.e., to the case of two identical spheres. This special morphology represents a limit shape for which the whole bending energy vanishes.

The volume of the two-sphere vesicles Z^{out} and Z^{in} with zero-energy buds is given by

$$v = v^{\text{zcb}} \equiv \left(1 - \frac{1}{\bar{m}^2}\right)^{3/2} \pm \frac{1}{\bar{m}^3} \quad (5.106)$$

where the plus and minus sign applies to out- and in-buds, respectively. This volume behaves as

$$v^{\text{zcb}} \approx 1 - \frac{3}{2\bar{m}^2} \quad \text{for large } |\bar{m}| \quad (5.107)$$

which applies to both out-buds with $\bar{m} > 0$ and in-buds with $\bar{m} < 0$.

Morphology diagram for positive spontaneous curvature

As displayed in Figure 5.17, the morphology diagram for positive spontaneous curvature contains two lines of limit shapes, L^{pea} and $L_{=}^{\text{out}}$, that have a common end point at

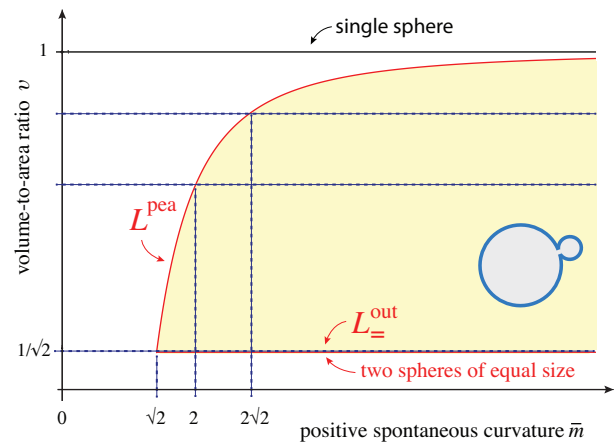


Figure 5.17 Morphology diagram for two-sphere vesicles with an out-bud (inset) and positive spontaneous curvature: Such vesicles have positive neck curvature and can be formed for spontaneous curvature $\bar{m} \geq \sqrt{2}$ as well as reduced volume v in the interval $1/\sqrt{2} \leq v \leq v^{\text{pea}}(\bar{m})$ corresponding to the shaded (yellow) region. The lower boundary of this region (horizontal line) is provided by the limit shapes $L_{=}^{\text{out}}$ that consist of two identical spheres and have the volume $v_{=}^{\text{out}} = 1/\sqrt{2}$, the upper boundary (curved line) by the limit shapes L^{pea} as described by $v = v^{\text{pea}}(\bar{m})$ in Eq. 5.96. The two boundary lines have a common end point at $(\bar{m}_{=}^{\text{out}}, v_{=}^{\text{out}}) = (\sqrt{2}, 1/\sqrt{2})$. When a limit shape L^{pea} is deflated for constant spontaneous curvature $\bar{m} > \sqrt{2}$, the larger sphere shrinks whereas the smaller sphere (or out-bud) grows transforming the limit shape L^{pea} into a persistent shape Φ^{pea} with neck curvature $\bar{M}_{\text{nc}} < \bar{m}$. The closed neck persists during further deflation until the lower limit shape $L_{=}^{\text{out}}$ with two identical spheres is reached. All two-sphere vesicles with the same volume v (broken horizontal lines) have the same neck curvature and the same shape but differ in their bending energy, see text. The upper broken line corresponds to the two-sphere geometry with $v = 0.941$ and $\bar{M}_{\text{nc}} = 2\sqrt{2}$, the intermediate broken line to $v = 0.871$ and $\bar{M}_{\text{nc}} = 2$.

$(\bar{m}, v) = (\bar{m}_{\pm}^{\text{out}}, v_{\pm}^{\text{out}}) = (\sqrt{2}, 1/\sqrt{2})$. Thus, the limit shapes L^{pea} are located at

$$v = v^{\text{pea}}(\bar{m}) \quad \text{and} \quad \bar{m} \geq \bar{m}_{\pm}^{\text{out}} = \sqrt{2} \quad (5.108)$$

while the L_{\pm}^{out} shapes are located at

$$v = v_{\pm}^{\text{out}} = 1/\sqrt{2} \quad \text{and} \quad \bar{m} \geq \bar{m}_{\pm}^{\text{out}} = \sqrt{2}. \quad (5.109)$$

Note that all L_{\pm}^{out} shapes have the same geometry but differ in their bending energy which has the \bar{m} -dependent form

$$\bar{E}_{\text{bc}}\{L_{\pm}^{\text{out}}\} = \frac{E_{\text{bc}}\{L_{\pm}^{\text{out}}\}}{8\pi\kappa} = 2(1 - \eta\bar{m})^2 \quad \text{with} \quad \eta = 1/\sqrt{2}. \quad (5.110)$$

which vanishes for $\bar{m} = \bar{m}_{\pm}^{\text{out}} = \sqrt{2}$ and increases as $\sim \bar{m}^2$ for large \bar{m} .

Inspection of Figure 5.17 shows that the two lines of limit shapes enclose an extended region of two-sphere shapes, Φ^{pea} , with stably closed necks. This region can be entered by deflation of the L^{pea} shapes, by inflation of the L_{\pm}^{out} shapes, and by increasing the spontaneous curvature of the L^{pea} shapes. All Φ^{pea} shapes that are produced by one of these processes are persistent in the sense that their necks remain stably closed during both deflation and inflation as well as under small changes of the spontaneous curvature.

Stability of individual spheres

A second requirement for the stability of two-sphere vesicles is the shape stability of both spheres. Thus, in order to examine the stability of the individual spheres, we now use the stability criterion Eq. 5.78 together with the pressure difference $P_{\text{sp}} = \Delta P$ and ΔP as given by Eq. 5.77. We then conclude that the spherical mother vesicle with radius R_1 is stable if

$$\Delta P = \frac{4\kappa m}{R_1 R_2} > \frac{4\kappa}{R_1^3} (m R_1 - 3) \quad \text{or} \quad \frac{\bar{m}}{r_2} > \frac{\bar{m}\eta - 3}{r_1^2} \quad (5.111)$$

whereas the out-bud with radius R_2 is stable if

$$\Delta P = \frac{4\kappa m}{R_1 R_2} > \frac{4\kappa}{R_2^3} (m R_2 - 3) \quad \text{or} \quad \frac{\bar{m}}{r_1} > \frac{\bar{m}r_2 - 3}{r_2^2}. \quad (5.112)$$

Because the two radii $r_1 = R_1/R_c$ and $r_2 = R_2/R_c$ satisfy the geometric relation $r_1^2 + r_2^2 = 1$, we can express both stability relations in terms of a single radius, say r_2 . One then finds that both individual spheres are stable for all limit shapes L^{pea} and L_{\pm}^{out} as well as for the shapes Z^{out} with zero-energy buds. Furthermore, the larger sphere of the intermediate persistent shapes Φ^{pea} is always stable whereas the spherical out-bud may become unstable for sufficiently large values of the spontaneous curvature and a certain range of v -values. More precisely, the spherical out-bud with radius r_2 is stable if

$$r_2 - \frac{r_2^2}{\sqrt{1-r_2^2}} < \frac{3}{\bar{m}} \quad (5.113)$$

and unstable if

$$r_2 - \frac{r_2^2}{\sqrt{1-r_2^2}} > \frac{3}{\bar{m}}. \quad (5.114)$$

Therefore, the instability line between the stable and unstable out-buds follows from the solutions of the equation

$$r_2 - \frac{r_2^2}{\sqrt{1-r_2^2}} = \frac{3}{\bar{m}}. \quad (5.115)$$

This equation has no solution for $\bar{m} < \bar{m}_{\text{ss}} = 13.29$, one solution for $\bar{m} = \bar{m}_{\text{ss}}$ and two solutions for $\bar{m} > \bar{m}_{\text{ss}}$.

Therefore, the out-buds of the persistent shapes Φ^{pea} are stable for $\bar{m} < \bar{m}_{\text{ss}}$ but become unstable for $\bar{m} \geq \bar{m}_{\text{ss}}$ and a certain \bar{m} -dependent range of v -values. At $\bar{m} = \bar{m}_{\text{ss}}$, the instability consists of the single point $(\bar{m}_{\text{ss}}, v_{\text{ss}}) = (13.29, 0.8259)$ which opens up into a parabola-like curve for $\bar{m} > \bar{m}_{\text{ss}}$. For large \bar{m} , the upper and lower branches of the parabola-like curve approach the Z^{out} line and the L_{\pm}^{out} line, respectively. Because $\bar{m}_{\text{ss}} = 13.29$, this bifurcation structure is located outside of the (\bar{m}, v) -region displayed in Figure 5.17.

Thus, we conclude that two-sphere vesicles with out-buds can be found in a large region of the morphology diagram for $\bar{m} > 0$. In particular, when we deflate a limit shape L^{pea} for $\sqrt{2} < \bar{m} < \bar{m}_{\text{ss}} \simeq 13.29$, we obtain a family of stable persistent shapes Φ^{pea} with decreasing neck curvatures \bar{M}_{ne} until we reach the limit shape L_{\pm}^{out} with the smallest possible neck curvature $\bar{M}_{\text{ne}} = \bar{m}^{\pm} = \sqrt{2}$. Further deflation of the limit shape L_{\pm}^{out} leads back to a dumbbell-like shape with an open neck.

5.5.3 MODIFICATIONS BY AREA DIFFERENCE ELASTICITY

So far, two-sphere vesicles have been discussed in the context of the spontaneous curvature model which depends on the locally generated spontaneous curvature m and assumes that one molecular component of the bilayer membrane can undergo frequent flip-flops between the two bilayer leaflets. It is instructive to see how the morphology diagram is changed when we consider bilayer membranes with slow flip-flops between the leaflets. In the latter situation, the area difference ΔA between the two leaflets is constrained as described by the nonlocal energy term in the area-difference-elasticity model, see the nonlocal expression in Eq. 5.64 that contributes to the energy functional Eq. 5.63 of this model.

As explained in Section 4.7.1, the shapes that minimize this energy functional also minimize the energy functional of the spontaneous curvature model as in Eq. 5.12, provided we use the effective spontaneous curvature $m_{\text{eff}} \equiv m + m_{\text{nlo}}$ as given by Eq. 5.66 which represents the sum of the local spontaneous curvature m and the nonlocal spontaneous curvature

$$m_{\text{nlo}} \equiv \pi \frac{\kappa_{\Delta}}{\kappa} \frac{I_{M,0} - \mathcal{I}_M\{S\}}{A}$$

as in Eq. 5.67. If the leaflets of a sphere with radius R_{ve} have optimal molecular areas, one has $I_{M,0} = 4\pi R_{ve}$ and the geometric factor of the nonlocal spontaneous curvature becomes

$$\frac{I_{M,0} - \mathcal{I}_M\{S\}}{A} = \frac{4\pi R_{ve} - \mathcal{I}_M\{S\}}{4\pi R_{ve}^2}. \quad (5.116)$$

Now, consider again the two-sphere vesicles Θ^{out} and Θ^{in} with radii R_1 and R_2 connected by a closed membrane neck as shown in Figure 5.15. The integrated mean curvature \mathcal{I}_M of these shapes is given by

$$\mathcal{I}_M\{\Theta^{\text{out}}\} = 4\pi(R_1 + R_2) \quad \text{and} \quad \mathcal{I}_M\{\Theta^{\text{in}}\} = 4\pi(R_1 - R_2) \quad (5.117)$$

which leads to the geometric factors

$$\frac{4\pi R_{ve} - \mathcal{I}_M\{S\}}{4\pi R_{ve}^2} = \frac{1}{R_{ve}}(1 - \eta \mp r_2) \quad (5.118)$$

and to the nonlocal spontaneous curvatures

$$\bar{m}_{\text{nlo}} = m_{\text{nlo}} R_{ve} = \pi \frac{\kappa_{\Delta}}{\kappa} (1 - \eta \mp r_2) \quad (5.119)$$

where the minus and plus sign applies to out- and in-buds, respectively. The nonlocal spontaneous curvature involves the geometric factor

$$1 - \eta \mp r_2 = 1 - \eta \mp \sqrt{1 - \eta^2} \quad (5.120)$$

where we used the area relation $\eta^2 + r_2^2 = 1$. For the shape Θ^{out} with an out-bud, this expression is negative and bounded by

$$1 - \sqrt{2} \leq 1 - \eta - \sqrt{1 - \eta^2} \leq 0 \quad \text{for } 0 \leq \eta \leq 1 \text{ (out-bud)}. \quad (5.121)$$

For the shape Θ^{in} with an in-bud, on the other hand, the corresponding expression is positive and satisfies the bounds

$$0 \leq 1 - \eta + \sqrt{1 - \eta^2} \leq \sqrt{2} + 1 \quad \text{for } 0 \leq \eta \leq 1 \text{ (in-bud)}. \quad (5.122)$$

Therefore, the absolute value of the nonlocal spontaneous curvature satisfies the bounds

$$|\bar{m}_{\text{nlo}}| \leq \pi(\sqrt{2} - 1) \frac{\kappa_{\Delta}}{\kappa} \quad \text{for } \Theta^{\text{out}} \quad (5.123)$$

and

$$|\bar{m}_{\text{nlo}}| \leq \pi(\sqrt{2} + 1) \frac{\kappa_{\Delta}}{\kappa} \quad \text{for } \Theta^{\text{in}}. \quad (5.124)$$

These bounds can be used to estimate the relative magnitude of the nonlocal and local contributions to the spontaneous curvature, see further below.

When we include area-difference-elasticity, the stability conditions for the closed neck are given by Eqs 5.68 and 5.69 which imply the neck closure condition

$$\bar{M}_{\text{nc}} = \frac{1}{2} \left(\frac{1}{r_1} \pm \frac{1}{r_2} \right) = \bar{m} + \bar{m}_{\text{nlo}} = \bar{m} + \pi \frac{\kappa_{\Delta}}{\kappa} (1 - \eta \mp r_2) \quad (5.125)$$

where the last equality follows from Eq. 5.119. In order to determine the location of the limit shapes L^{pea} and L^{sto} in the (ν, \bar{m}) -plane, we must now combine the neck closure relation Eq 5.125 with the geometric relations $r_1^2 + r_2^2 = 1$ and $r_1^3 \pm r_2^3 = \nu$. In general, the κ_{Δ} -term will shift the L^{pea} - and L^{sto} -lines in the (ν, \bar{m}) -plane, a shift that can be easily calculated for any value of κ_{Δ}/κ . For positive spontaneous curvature, for example, one then finds that the lines of limit shapes L^{pea} are shifted towards higher \bar{m} -values as we increase the rigidity ratio κ_{Δ}/κ . Furthermore, when we describe the shifted L^{pea} lines by $\bar{m}^{\text{pea}} = f(\nu)$, the function $f(\nu)$ develops a minimum for $\kappa_{\Delta}/\kappa > 1$.

In addition, we can draw some general conclusions about the morphology diagram when we include the area-difference-elasticity term proportional to κ_{Δ} . First, the limit shapes L_{\pm}^{out} and L_{\pm}^{in} , consisting of two spheres with the same radius, are again located at $\nu = \nu_{\pm}^{\text{out}} = 1/\sqrt{2}$ for $\bar{m} > 0$ and at $\nu = \nu_{\pm}^{\text{in}} = 0$ for $\bar{m} < 0$ as follows from the two geometric relations alone. Therefore, the morphology diagram in the (ν, \bar{m}) -plane will always contain extended regions with (meta)stable two-sphere shapes as in Figure 5.17, irrespective of the value of κ_{Δ}/κ .

Second, we can conclude from the neck closure condition in Eq. 5.125 and from the bounds provided by Eqs 5.123 and 5.124 that the nonlocal contributions \bar{m}_{nlo} arising from area difference elasticity can be neglected for sufficiently large local contributions \bar{m} . More precisely, we obtain from Eqs 5.125 and 5.123 that the nonlocal spontaneous curvature can be ignored for the shape Θ^{out} if the local spontaneous curvature is sufficiently large and positive with

$$\bar{m} \gg \pi(\sqrt{2} - 1) \frac{\kappa_{\Delta}}{\kappa} \quad \text{(out-bud)}. \quad (5.126)$$

Likewise, combining Eq. 5.125 with Eq. 5.124, we conclude that the nonlocal contribution can be ignored for the shape Θ^{in} if the local spontaneous curvature is large and negative with

$$\bar{m} \ll -\pi(\sqrt{2} + 1) \frac{\kappa_{\Delta}}{\kappa} \quad \text{(in-bud)}. \quad (5.127)$$

The ratio κ_{Δ}/κ of the bending rigidities is expected to be of the order of one (Döbereiner et al., 1997). Therefore, both for out- and for in-buds, the nonlocal contribution can be ignored compared to the local one if $|\bar{m}| \gg 1$ or $|m| \gg 1/R_{ve}$.

Finally, assume that we were able to measure the radii r_1 and r_2 of a vesicle during neck closure. We can then use the neck closure condition in Eq. 5.125 to estimate the local spontaneous curvature \bar{m} via

$$\bar{m} = \frac{1}{2} \left(\frac{1}{r_1} \pm \frac{1}{r_2} \right) + \pi \frac{\kappa_{\Delta}}{\kappa} (\eta \pm r_2 - 1) \quad (5.128)$$

where the plus and minus sign applies to an out- and in-bud, respectively. For small bud radius r_2 , the radius $\eta = \sqrt{1 - r_2^2} \approx 1 - r_2^2$. When we use this asymptotic equality in Eq. 5.128, we obtain the local spontaneous curvature which implies

$$\bar{m} \approx \frac{1}{2} \left(\frac{1}{r_1} \pm \frac{1}{r_2} \right) \pm \pi \frac{\kappa_\Delta}{\kappa} r_2 \quad \text{for small buds with } r_2 \ll 1. \quad (5.129)$$

The asymptotic behavior as given by Eq. 5.129 implies that the κ_Δ -term can also be ignored for sufficiently small buds. This behavior for small buds is consistent with the behavior for large spontaneous curvatures \bar{m} because large \bar{m} implies limit shapes with small buds.

The influence of area difference elasticity on two-sphere vesicles has been recently studied for giant vesicles that contained lipids with photoresponsive F-Azo groups and underwent light-induced budding (Georgiev et al., 2018). A theoretical analysis of the experimental data based on Eq. 5.128 showed that the spontaneous curvature can indeed be decomposed into a local and a nonlocal contribution, that all vesicles were governed by the same rigidity ratio κ_Δ/κ , and that the local spontaneous curvature $m = \bar{m}R_{ve}$ was about $1/(2.5 \mu\text{m})$.

5.5.4 EFFECTIVE CONSTRICTION FORCES AND CLEAVAGE OF MEMBRANE NECKS

As explained in the previous subsections, the persistent shapes Φ^{pea} have the same geometry, for a given volume v , as the limit shapes L^{pea} but an increased spontaneous curvature \bar{m} compared to the spontaneous curvature of L^{pea} . When expressed in terms of dimensionful variables, the spontaneous curvature m then satisfies the stability condition $m > M_{ne} = \frac{1}{2}(M_1 + M_2)$ for the closed necks of out-buds as in Eqs 5.60 and 5.92. Now, consider an explicit constriction force f that acts on the neck radius R_{ne} , which we take into account by adding the term fR_{ne} to the bending energy in Eq. 5.54.¹⁰ We then obtain the generalized condition

$$f - 4\pi\kappa(M_1 + M_2 - 2m) > 0 \quad (5.130)$$

for a closed membrane neck which may be rewritten in the form

$$f + f_{eff}^{out} > 0 \quad (5.131)$$

with the effective constriction force

$$f_{eff}^{out} \equiv 4\pi\kappa(2m - M_1 - M_2) \geq 0 \quad (\text{out-buds with } m > 0). \quad (5.132)$$

This constriction force vanishes when the neck satisfies the neck closure condition $M_1 + M_2 = 2m$.

Now, let us consider a persistent shape Φ^{pea} close to the line of limit shapes $L_{=}^{out}$ which consist of two identical spheres. These persistent shapes have a volume $v \gtrsim 1/\sqrt{2}$ and are characterized by two spheres with small mean curvatures M_1 and M_2 , both of which are of the order of $\sqrt{2}/R_{ve}$. Furthermore, the individual spheres of these persistent shapes are stable up to fairly high m -values because the individual spheres of the limit shapes $L_{=}^{out}$ are stable for all values of m . If the spontaneous curvature m

is large compared to both M_1 and M_2 , the expression for the curvature-induced constriction force as given by Eq. 5.132 simplifies and becomes asymptotically equal to

$$f_{eff}^{out} \approx f_m^{out} \quad \text{with} \quad f_m^{out} \equiv 8\pi\kappa m \quad \text{for } 2m \gg M_1 + M_2, \quad (5.133)$$

where f_m^{out} represents the curvature-induced constriction force. Thus, for the bending rigidities $\kappa = 10^{-19}$ J and $\kappa = 4 \times 10^{-19}$ J, the spontaneous curvature $m = 1/(100\text{nm})$ generates the constriction forces $f_m^{out} \simeq 25$ pN and $f_m^{out} \simeq 100$ pN, respectively.

In the absence of flip-flops between the bilayer leaflets, we should include the effects of area-difference-elasticity as discussed in the previous subsection. In this case, the effective constriction force has the form

$$f_{eff}^{out} \equiv 4\pi\kappa(2m + 2m_{nlo}^{out} - M_1 - M_2) \geq 0 \quad (5.134)$$

with the nonlocal spontaneous curvature

$$m_{nlo}^{out} = \pi \frac{\kappa_\Delta}{\kappa} \frac{I_{M,0} - \mathcal{I}_M\{\Theta^{out}\}}{A} = \pi \frac{\kappa_\Delta}{\kappa} \frac{1 - \eta - r_2}{R_{ve}} \quad (5.135)$$

as in Eq. 5.119. This term is negative, see Eq. 5.121, which implies that area-difference-elasticity acts to weaken the curvature-induced constriction forces for out-buds.

In-buds with closed necks are formed for negative spontaneous curvatures. In the latter case, we obtain the effective constriction force

$$f_{eff}^{in} \equiv 4\pi\kappa(M_1 + M_2 - 2m) > 0 \quad (\text{in-buds with } m < 0) \quad (5.136)$$

which behaves as $f_{eff}^{in} \approx f_m^{in}$ with the curvature-induced constriction force

$$f_m^{in} \equiv -8\pi\kappa m \quad \text{for } 2m \ll M_1 + M_2 < 0. \quad (5.137)$$

In the absence of molecular flip-flops between the bilayer leaflets, the effective constriction force is

$$f_{eff}^{in} \equiv 4\pi\kappa(M_1 + M_2 - 2m - 2m_{nlo}^{in}) \quad (5.138)$$

with the nonlocal spontaneous curvature

$$m_{nlo}^{in} = \pi \frac{\kappa_\Delta}{\kappa} \frac{I_{M,0} - \mathcal{I}_M\{\Theta^{in}\}}{A} = \pi \frac{\kappa_\Delta}{\kappa} \frac{1 - \eta + r_2}{R_{ve}} \quad (5.139)$$

as in Eq. 5.119. This term is positive, see Eq. 5.122, which implies that area-difference-elasticity also acts to weaken the effective constriction forces for in-buds.

In the curvature models, a closed membrane neck is described by a point-like discontinuity of the membrane curvature. Because of the finite membrane thickness ℓ_{me} , the radius R_{ne} of the membrane neck is necessarily restricted to $R_{ne} \gtrsim \ell_{me}$. Therefore, strictly speaking, the above derivation of the effective constriction forces f_{eff}^{out} and f_{eff}^{in} implicitly assumed that $R_{ne} \gtrsim \ell_{me}$. However, we will now argue that these constriction forces may also be used to obtain a simple criterion for the cleavage of the membrane neck.

¹⁰The same approach has been used for the endocytosis and exocytosis of nanoparticles in (Agudo-Canalejo and Lipowsky, 2016).

Neck cleavage represents a topological transformation from a budded vesicle that has the same topology as a single sphere to a cleaved state with the topology of two spheres. The free energy difference between the budded and the cleaved state involves a contribution from the Gaussian curvature modulus κ_G , see Section 5.10 at the end of this chapter. Furthermore, this free energy difference depends strongly on the magnitude of the spontaneous curvature. For large values of $|m|$, the fission process is exergonic and reduces the free energy of the vesicle as explained in Section 5.10.3. Therefore, in the presence of a large spontaneous curvature, thermodynamics allows fission to occur spontaneously, i.e., without any free energy input from a chemical reaction such as ATP hydrolysis. How fast this exergonic process occurs depends, however, on the free energy barrier between the budded and the cleaved state of the vesicle membrane.

In order to cleave the membrane neck, we have to create two bilayer edges. For a neck with radius R_{ne} , these two bilayer edges have the combined length $4\pi R_{\text{ne}}$. The associated edge energy E_{ed} depends on the edge tension λ_{ed} and has the form

$$E_{\text{ed}} = 4\pi R_{\text{ne}} \lambda_{\text{ed}} \quad \text{with } R_{\text{ne}} \gtrsim \ell_{\text{me}} \quad (5.140)$$

where the latter inequality reminds us that the neck radius should exceed the membrane thickness ℓ_{me} . The edge energy provides a simple estimate for the free energy barrier between the budded and the cleaved state of the vesicle membrane. This barrier has to be overcome by the mechanical work $f_m R_{\text{ne}}$ expended by the curvature-induced constriction force $f_m = f_m^{\text{out}}$ or f_m^{in} from $R_{\text{ne}} = \ell_{\text{me}}$ to $R_{\text{ne}} = 0$. Therefore, we obtain the cleavage criterion $f_m R_{\text{ne}} \gg E_{\text{ed}}$ which is equivalent to

$$|m| \gg |m^{\text{cl}}| \equiv \frac{\lambda_{\text{ed}}}{2\kappa} \quad \text{for large } |m|. \quad (5.141)$$

This criterion predicts that the membrane neck is cleaved and undergoes fission if the absolute value $|m|$ of the spontaneous curvature is sufficiently large and exceeds the threshold value $|m^{\text{cl}}| = \lambda_{\text{ed}}/(2\kappa)$.

The main contribution to the edge tension λ_{ed} comes from the interface between the hydrophobic core of the bilayer and the aqueous solution. The corresponding interfacial tension Σ_{hc} may be reduced by a rearrangement of the head groups along the bilayer edge or by the adsorption of edge-active molecules. For an interfacial tension $\Sigma_{\text{hc}} \gtrsim 1$ mN/m and a thickness $\ell_{\text{hc}} \simeq 2$ nm of the hydrophobic core, we obtain the estimate $\lambda_{\text{ed}} = \Sigma_{\text{hc}} \ell_{\text{hc}} \gtrsim 2$ pN. Using the typical bending rigidity $\kappa = 10^{-19}$ J, neck cleavage requires the spontaneous curvature m to exceed the threshold value $|m^{\text{cl}}| \gtrsim 1/(100 \text{ nm})$. As we will see in Section 7.5 below, neck cleavage is further facilitated by the adhesion of membranes to solid substrates and nanoparticles.

Curvature-induced budding and fission has been recently observed in molecular dynamics simulations of nanovesicles (Ghosh et al., in preparation). In this case, the spontaneous curvature was generated by the adsorption of small solute particles. Combined budding and fission has also been observed experimentally for giant vesicles exposed to polyhistidine-tagged GFP proteins that were bound to certain lipid components within the vesicle membranes (Steinkühler et al., in preparation).

5.5.5 VESICLE SHAPES WITH SEVERAL BUDS

Let us now consider multi-sphere vesicles that consist of more than two spheres connected by more than one closed neck, see also Box 5.2. The Euler-Lagrange Eq. 5.70, which applies to all membrane segments of such a multi-sphere vesicle apart from the closed necks, implies that at most two different types of spheres with two distinct radii, $r_1 = R_1/R_{\text{ve}}$ and $r_2 = R_2/R_{\text{ve}}$, can coexist on the same vesicle.

These two radii are determined by the membrane area $A = 4\pi R_{\text{ve}}^2$, by the vesicle volume $V = v(4\pi/3)R_{\text{ve}}^3$, and by the numbers N_1 and N_2 of the two types of spheres. If both types of spheres have a positive mean curvature, the two radii r_1 and r_2 satisfy the geometric relations

$$N_1 r_1^2 + N_2 r_2^2 = 1 \quad (5.142)$$

and

$$N_1 r_1^3 + N_2 r_2^3 = v \quad (\bar{M}_1 > 0 \text{ and } \bar{M}_2 > 0). \quad (5.143)$$

If we define the volumes v_1 and v_2 of the individual spheres via

$$\frac{4\pi}{3} R_1^3 = v_1 \frac{4\pi}{3} R_{\text{ve}}^3 \quad \text{and} \quad \frac{4\pi}{3} R_2^3 = v_2 \frac{4\pi}{3} R_{\text{ve}}^3, \quad (5.144)$$

the relation Eq. 5.143 can be rewritten in the form

$$N_1 v_1 + N_2 v_2 = v. \quad (5.145)$$

Simple examples for such multi-sphere shapes with $N_1 = 1$ are shown in Figure 5.18a–c. If the r_1 - and r_2 -spheres have positive and negative mean curvature, respectively, multi-sphere shapes with $N_1 > 1$ are impossible because they would require different types of necks with positive and negative neck curvature. Therefore, we are left with $N_1 = 1$, i.e., one large sphere with N_2 in-buds as illustrated in Figure 5.18d. In the latter case, the second geometric relation Eq. 5.143 is replaced by

$$r_1^3 - N_2 r_2^3 = v_1 - N_2 v_2 = v \quad (\bar{M}_1 > 0 \text{ and } \bar{M}_2 < 0). \quad (5.146)$$

In contrast to these geometric relations, the stability relations for the membrane necks are local and do not depend on the sphere

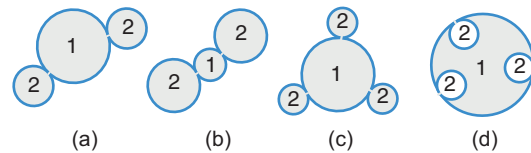


Figure 5.18 (a–c) Examples for vesicles consisting of 1 + N spheres with positive neck curvature: (a) Large r_1 -sphere with two smaller r_2 -spheres; (b) Small r_1 -sphere with two larger r_2 -spheres as observed in (Lipowsky and Dimova, 2003); (c) Large r_1 -sphere with three smaller r_2 -spheres; and (d) Example for a vesicle consisting of 1 + 3 spheres with negative neck curvature. For simplicity, all membrane necks have been placed in the plane of the figure. The positions of these necks are, however, arbitrary and can be shifted along the surface of the large sphere as long as the buds do not intersect each other.

numbers N_1 and N_2 . Therefore, both the neck closure condition Eq. 5.91 as well as the closed neck conditions Eqs 5.92 and 5.93 are valid for arbitrary numbers N_1 and N_2 of r_1 - and r_2 -spheres, where we implicitly assume that these spheres do not intersect each other.

However, a multi-sphere vesicles built up from several r_1 -spheres and r_2 -spheres may exhibit different types of closed necks. Indeed, we can distinguish necks between two r_1 -spheres from necks between two r_2 -spheres and from necks between an r_1 - and an r_2 -sphere. These three types of necks have different neck curvatures \bar{M}_{nc} as long as $r_1 \neq r_2$. In this section, we will focus on the simplest case in which all necks have the same curvature as in Figure 5.18 and again focus on the case with out-buds. Multi-sphere shapes with two types of necks will be discussed in the next section in the context of necklace-like tubes.

Multi-sphere vesicles with N out-buds

The simplest multi-sphere shapes with more than two spheres consist of one r_1 -sphere and N r_2 -spheres which are connected by N closed necks with the same neck curvature \bar{M}_{ve} . All examples in Figure 5.18 belong to this category. If the neck curvature is positive, the r_2 -spheres form N out-buds of the r_1 -sphere as in Figure 5.18a–c. The latter shapes lead to a morphology diagram with two bifurcation points B_*^+ and B_\diamond^+ as displayed in Figure 5.19.

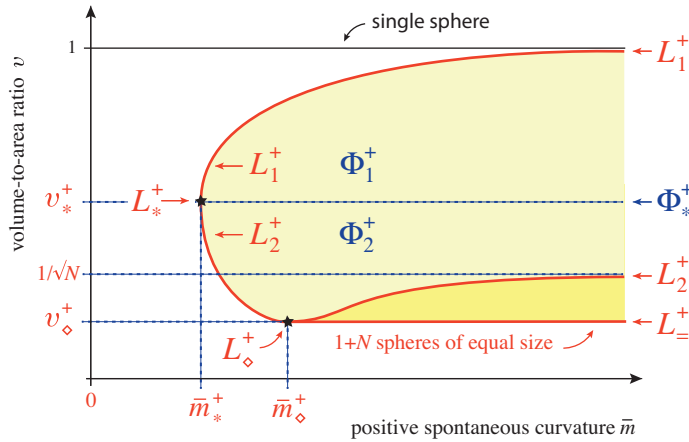


Figure 5.19 Morphology diagram for $(1 + N)$ -sphere vesicles with positive spontaneous curvature: The vesicles consist of one r_1 -sphere and N r_2 -spheres as illustrated in Figure 5.18a–c. These vesicles are (meta)stable within the yellow (dark and light) parameter region bounded by three types of limit shapes (red lines), denoted by L_1^+ , L_2^+ , and L_*^+ . The limit shapes L_1^+ and L_2^+ have variable neck curvature $\bar{M}_{ne} = \bar{m}$ whereas the limit shapes L_*^+ have the constant neck curvature $\bar{M}_{ne} = \sqrt{1+N}$. The limit shapes involve two types of bifurcation points (black stars). At the bifurcation point B_*^+ with coordinates $(\bar{m}, v) = (\bar{m}_*^+, v_*^+)$ as given by Eqs 5.147 and 5.148, the limit shape L_*^+ bifurcates into the shapes L_1^+ and L_2^+ . The limit shape L_*^+ has a balanced geometry in the sense that the volume of the r_1 -sphere is equal to the combined volume of all r_2 -spheres. The same geometry applies to the persistent shapes Φ_1^+ along the horizontal broken line (blue) that emanates from the bifurcation point B_*^+ . At the bifurcation point B_\diamond^+ with $(\bar{m}, v) = (\bar{m}_\diamond^+, v_\diamond^+) = (\sqrt{1+N}, 1/\sqrt{1+N})$ corresponding to the limit shape L_\diamond^+ , the limit shapes L_\diamond^+ bifurcate off from the line of L_2^+ shapes. The limit shapes L_\diamond^+ and L_*^+ consist of $1 + N$ spheres with the same size. The region between the L_\diamond^+ -line and the L_2^+ -line with $\bar{m} > \bar{m}_\diamond^+$ (dark yellow) is special because two different Φ_2^+ shapes can be formed at each point within this region: one of these shapes is characterized by $r_1 > r_2$, the other by $r_1 < r_2$. Both shapes can be reached by inflation of the limit shape L_\diamond^+ as illustrated in Figure 5.20 for $N = 3$.

Bifurcation of L_1^+ and L_2^+ shapes

Inspection of Figure 5.19 reveals that membranes with sufficiently small spontaneous curvatures do not form stable multi-sphere shapes. As we increase the spontaneous curvature, we encounter the bifurcation points B_*^+ at which a single multi-sphere shape, L_*^+ , appears with spontaneous curvature

$$\bar{m} = \bar{m}_*^+(N) \equiv \frac{1}{2}(1 + N^{1/3})^{3/2} \quad (5.147)$$

and volume

$$v = v_*^+(N) \equiv \frac{2}{(1 + N^{1/3})^{3/2}}. \quad (5.148)$$

It is interesting to note that $\bar{m}_*^+(N)v_*^+(N) = 1$ for all values of N . The limit shape L_*^+ has a balanced volume in the sense that

$$v_1 = r_1^3 = Nr_2^3 = Nv_2 \quad (\text{balanced volume}). \quad (5.149)$$

i.e., the volume of the r_1 -sphere is equal to the combined volume of all r_2 -spheres.

For $\bar{m} > \bar{m}_*^+(N)$, the limit shape L_*^+ bifurcates into two different branches of limit shapes, L_1^+ and L_2^+ , as shown in Figure 5.19. For the upper branch with the limit shapes L_1^+ , the volume v_1 of the r_1 -sphere exceeds the combined volume Nv_2 of the r_2 -spheres. For the lower branch with the limit shapes L_2^+ , on the other hand, the r_2 -spheres dominate in the sense that $Nv_2 > v_1$. Thus, the volume ratio

$$\rho_1 \equiv \frac{v_1}{Nv_2} > 1 \quad \text{for the } L_1^+ \text{ shapes} \quad (5.150)$$

but

$$\rho_1 < 1 \quad \text{for the } L_2^+ \text{ shapes.} \quad (5.151)$$

As we move along the line of L_1^+ -shapes by increasing the spontaneous curvature \bar{m} , both the total volume v and the volume ratio ρ_1 increase monotonically until the r_1 -sphere has taken up the whole volume in the limit of large \bar{m} . More precisely, the volume $\mathcal{V}\{L_1^+\}$ of the L_1^+ -shapes increases monotonically with increasing spontaneous curvature \bar{m} and behaves as

$$\mathcal{V}\{L_1^+\} \approx \frac{4\pi}{3} R_{ve}^3 \left[1 - \frac{3N}{8\bar{m}^2} - \frac{N}{4\bar{m}^3} \right] \quad \text{for large } \bar{m}. \quad (5.152)$$

On the other hand, we can also move along the lower branch of the L_2^+ -shapes by increasing L_2^+ which leads to a monotonic decay of the volume ratio ρ_1 until the N r_2 -spheres have taken up the whole volume and $v \approx Nr_2^3 \approx 1/\sqrt{1+N}$, see Figure 5.19.

As a consequence, the two limit shapes L_1^+ and L_2^+ look rather different for large \bar{m} . In this limit, the L_1^+ -shapes consist of a large r_1 -sphere and N small r_2 -spheres with radii

$$r_1 \approx 1 \quad \text{and} \quad r_2 \approx \frac{1}{2\bar{m}} \quad (L_1^+, \text{ large } \bar{m}). \quad (5.153)$$

In contrast, the L_2^\pm -shapes consist of a small r_1 -sphere and N large r_2 -spheres with radii

$$r_1 \approx \frac{1}{2\bar{m}} \quad \text{and} \quad r_2 \approx \frac{1}{\sqrt{N}} \quad (L_2^\pm, \text{ large } \bar{m}). \quad (5.154)$$

For $N = 2$, these two limit shapes are illustrated in [Figure 5.18a,b](#).

Bifurcation of L_\pm^\pm from L_2^\pm shapes

When we inspect the morphology diagram in [Figure 5.19](#) more closely, we discover an additional complication related to the L_2^\pm -branch. In contrast to the volume ratio ρ_1 that decreases monotonically along this branch, the total volume $\mathcal{V}\{L_2^\pm\}$ of the L_2^\pm -shapes exhibits a minimum as a function of \bar{m} . At this minimum, the L_2^\pm -shape consists of $1 + N$ spheres of equal size with $r_1 = r_2 = 1/\sqrt{1+N}$, and provides the end point for the line of limit shapes L_\diamond^\pm , see [Figure 5.19](#). Therefore, the limit shape L_\diamond^\pm with

$$\bar{m} = \bar{m}_\diamond^\pm(N) \equiv \sqrt{1+N} \quad \text{and} \quad v = v_\diamond^\pm(N) \equiv \frac{1}{\sqrt{1+N}} \quad (5.155)$$

represents a second bifurcation point, B_\diamond^\pm , at which the L_\pm^\pm shapes split off from the L_2^\pm shapes. Note that the limit shape L_\diamond^\pm is built up from $1 + N$ spheres of equal size with radius $r_1 = r_2 = 1/\sqrt{1+N} = 1/\bar{m}_\diamond^\pm$. As a consequence, the bending energy vanishes for each of these spheres and, thus, for the whole limit shape L_\diamond^\pm .

For $\bar{m} > \bar{m}_\diamond^\pm(N)$, the volume $\mathcal{V}\{L_2^\pm\}$ increases again and behaves as

$$\mathcal{V}\{L_2^\pm\} \approx \frac{4\pi}{3} R_{vc}^3 \left[\frac{1}{\sqrt{N}} - \frac{3}{8\sqrt{N}\bar{m}^2} + \frac{1}{8\bar{m}^3} \right] \quad \text{for large } \bar{m}. \quad (5.156)$$

In contrast, all L_\pm^\pm shapes have the same geometry and, thus, the same volume $\mathcal{V}\{L_\pm^\pm\} = (4\pi/3)R_{vc}^3/\sqrt{1+N}$. The latter shapes are distinguished by their bending energies which depend on \bar{m} . It is again interesting to note that $\bar{m}_\diamond^\pm(N)v_\diamond^\pm(N) = 1$ for all values of N .

As shown in [Figure 5.19](#), the lines of limit shapes L_1^\pm , L_2^\pm , and L_\pm^\pm enclose an extended region of two-sphere shapes Φ^+ with stably closed necks. This region can be entered by deflation of L_1^\pm or L_2^\pm shapes, by inflation of L_2^\pm or L_\pm^\pm shapes, and by increasing the spontaneous curvature of L_1^\pm or L_2^\pm shapes. All Φ^+ shapes that are produced by one of these processes are persistent in the sense that their neck remains stably closed during both deflation and inflation as well as under small changes of the spontaneous curvature.

It is interesting to note that all bifurcation points B_\star^\pm and B_\diamond^\pm are located on the line $v = 1/\bar{m}$ within the (\bar{m}, v) -plane. Indeed, it follows from Eqs 5.147 and 5.148 that $v_\star^\pm(N) = 1/\bar{m}_\star^\pm(N)$ and from Eq. 5.155 that $v_\diamond^\pm(N) = 1/\bar{m}_\diamond^\pm(N)$ for all values of N . Furthermore, for large N , the \bar{m} -coordinates behave as $\bar{m}_\star^\pm(N) \approx \frac{1}{2}N^{1/2}$ for the bifurcation points B_\star^\pm and as $\bar{m}_\diamond^\pm(N) \approx N^{1/2}$ for the bifurcation points B_\diamond^\pm which implies that the points B_\diamond^\pm are more widely spaced compared to the points B_\star^\pm .

Stability of individual spheres

When we apply the stability criterion Eq. 5.78 to examine the stability of the individual spheres, we find that both spheres are stable for all limit shapes L_1^\pm , L_2^\pm , and L_\pm^\pm . Furthermore, the larger sphere of the intermediate persistent shapes Φ^+ is always stable whereas the smaller sphere becomes unstable for sufficiently large values of the spontaneous curvature. The corresponding instability lines now follow from the solutions of the equation

$$r_2 - \frac{r_2^2}{\sqrt{1-Nr_2^2}} = \frac{3}{\bar{m}} \quad (5.157)$$

This equation has no solution for $\bar{m} < \bar{m}_{ss}(N)$, one solution for $\bar{m} = \bar{m}_{ss}(N)$ and two solutions for $\bar{m} > \bar{m}_{ss}(N)$. The critical value $\bar{m}_{ss}(N)$ for the instability of the small spheres is found to be $\bar{m}_{ss} = 14.3, 15.2, \text{ and } 19.6$ for $N = 2, 3, 10$, respectively.

For large \bar{m} , the right hand side of Eq. 5.157 becomes small which implies the two asymptotic solutions

$$r_2 \approx \frac{3}{\bar{m}} \quad \text{and} \quad r_2 \approx \frac{1}{\sqrt{1+N}} \quad (\text{large } \bar{m}) \quad (5.158)$$

for the bud radius r_2 . In the same limit, the reduced volume

$$v = r_1^3 + Nr_2^3 = (1 - Nr_2^2)^{3/2} + Nr_2^3 \quad (5.159)$$

behaves as

$$v \approx 1 - \frac{27}{2} \frac{N}{\bar{m}^2} + 27 \frac{N}{\bar{m}^3} \quad \text{for } r_2 \approx 3/\bar{m} \quad (5.160)$$

and as

$$v \approx \frac{1}{\sqrt{1+N}} = v_\diamond^\pm \quad \text{for } r_2 \approx 1/\sqrt{1+N}. \quad (5.161)$$

Therefore, the two branches of the instability line approach the straight lines $v = 1$ and $v = v_\diamond^\pm$ corresponding to a single sphere and to a multi-sphere consisting of $(1 + N)$ spheres of equal size, respectively, compare [Figure 5.19](#).

Along the instability line that approaches $v = v_\diamond^\pm = 1/\sqrt{1+N}$ for large \bar{m} , the N buds are smaller than or equal to the central sphere, i.e., $r_2 \leq r_1$, as illustrated in [Figure 5.18a](#) and [Figure 5.20a](#). In contrast, the shapes along the L_2^\pm line with $\bar{m} > \bar{m}_\diamond^\pm$ are characterized by N buds that are larger than the central sphere, i.e., $r_2 > r_1$, as illustrated in [Figure 5.18b](#) and [Figure 5.20c](#). As a consequence, the instability line that approaches $v = v_\diamond^\pm = 1/\sqrt{1+N}$ for large \bar{m} does not cross the L_2^\pm line obtained for $\bar{m} > \bar{m}_\diamond^\pm$. Indeed, for the dark yellow region in [Figure 5.19](#), we obtain a stack of two different sheets of $(1 + N)$ -spheres, the two sheets being connected via the L_\pm^\pm line. This bifurcation structure will be discussed in more detail in the next paragraphs.

Persistent shapes and deflation behavior

As for two-sphere vesicles, the geometry of the persistent shapes Φ^+ is fully determined by the volume v . Thus, if we consider any point (\bar{m}_o, v_o) within the region bounded by the limit shapes, see the yellow region in Figure 5.19, the persistent shape at this point has the same geometry as the limit shape with the same volume $v = v_o$, i.e., as the limit shape obtained by projecting the point (\bar{m}_o, v_o) parallel to the \bar{m} -axis onto the line of limit shapes. Using this constant-volume projection, we can then distinguish persistent shapes Φ_1^+ , Φ_*^+ , and Φ_2^+ which have the same geometry as the limit shapes L_1^+ , L_*^+ , and L_2^+ , respectively.

Now, consider a point (\bar{m}_o, v_o) within the region between the L_{\pm}^+ -line and the L_2^+ -line with $\bar{m} > \bar{m}_\diamond^+$, corresponding to the dark yellow region in Figure 5.19. The constant-volume projection of this point onto the lines of limit shapes leads to two such shapes. One of these L_2^+ shapes is located at $\bar{m} < \bar{m}_\diamond^+$ and characterized by $r_1 > r_2$ whereas the other L_2^+ shape is located at $\bar{m} > \bar{m}_\diamond^+$ which implies $r_1 < r_2$. As a consequence, for each point (\bar{m}_o, v_o) within the dark yellow region in Figure 5.19, we obtain two different persistent shapes Φ_2^+ with $r_2 < r_1$ and $r_2 > r_1$, respectively. Therefore, the dark yellow region in Figure 5.19 is characterized by a stack of two different sheets of shapes, two sheets that merge along the line of limit shapes L_{\pm}^+ .

This two-sheet structure of the morphology diagram has interesting consequences for the deflation and inflation behavior of the multi-sphere vesicles considered here. Starting from a “balanced” persistent shape Φ_*^+ , deflation eventually leads to a limit shape L_{\pm}^+ , consisting of $1 + N$ spheres of equal size. Further deflation of the latter shape will open up the necks of the L_{\pm}^+ -shapes. However, inflation of the L_{\pm}^+ -shape will not necessarily lead back to the Φ_*^+ -shapes that were obtained by deflation of the balanced Φ_*^+ -shapes. Indeed, the whole L_{\pm}^+ -line should be regarded as another bifurcation line from which two sheets of Φ_2^+ -shapes emanate, both of which are accessible via inflation of the L_{\pm}^+ -shapes. Inflation along one of these two sheets leads back to the balanced Φ_*^+ -shapes, inflation along the other sheet leads to the limit shapes L_2^+ with $\bar{m} > \bar{m}_\diamond^+$. This behavior is illustrated in Figure 5.20 for $N = 3$.

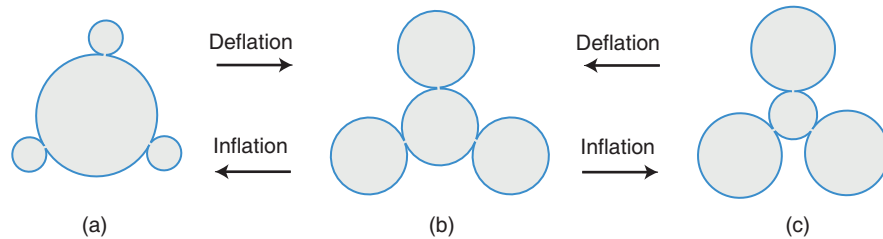


Figure 5.20 Three multi-sphere vesicles that can be transformed into each other by deflation or inflation. All three vesicles consist of a single r_1 -sphere and three r_2 -spheres: (a) Persistent shape Φ_1^+ with one large r_1 -sphere with volume v_1 and $N = 3$ smaller r_2 -spheres with combined volume $3v_2 < v_1$; (b) Limit shape L_3^+ for which the r_1 -sphere and the three r_2 -spheres have the same size; and (c) Persistent shape Φ_2^+ with a small r_1 -sphere and three larger r_2 -spheres. Deflation of Φ_1^+ in (a) leads, via an intermediate shape Φ_2^+ , to L_3^+ as in (b) but inflation of L_3^+ can lead either back to (a) or to (c). Such deflation and inflation processes are possible for $\bar{m} > \bar{m}_\diamond^+(3) = 2$, see Figure 5.19.

Out-buds with zero bending energy

The persistent shapes Φ^+ include the special shapes Z_N^{out} with N out-buds that have radius $r_2 = 1/\bar{m}$ and, thus, vanishing bending energy. The reduced volume of these latter shapes is given by

$$v = \left(1 - \frac{N}{\bar{m}^2}\right)^{3/2} + \frac{N}{\bar{m}^3} \approx 1 - \frac{3}{2} \frac{N}{\bar{m}^2} + \frac{N}{\bar{m}^2} \quad \text{for large } \bar{m}. \quad (5.162)$$

Therefore, the line of special shapes Z_N^{out} with zero-energy buds also approaches the straight line $v = 1$ for a single sphere. Comparison with Eqs 5.152 and 5.160 shows that the line of Z_N^{out} shapes is located between the line of limit shapes L_1^+ as described by Eq. 5.152 and the upper branch of the instability line for individual spheres as given by Eq. 5.160. As a consequence, the special shapes Z_N^{out} are stable for large \bar{m} . Furthermore, the line of Z_N^{out} shapes with zero-energy buds includes the limit shape L_\diamond^+ , see Figure 5.19, because

$$v = \left(1 - \frac{N}{\bar{m}^2}\right)^{3/2} + \frac{N}{\bar{m}^3} = \frac{1}{\sqrt{1+N}} = v_\diamond^+ \quad \text{for } \bar{m} = \bar{m}_\diamond^+ = \sqrt{1+N}. \quad (5.163)$$

In the latter case, the N out-buds have the same size as the mother vesicle which implies that the whole limit shape L_\diamond^+ has vanishing bending energy as mentioned previously. Therefore, the Z_N^{out} shapes with zero-energy buds have stably closed necks connecting stable individual spheres, and the corresponding Z_N^{out} line in the morphology diagram emanates from the limit shape L_\diamond^+ with $\bar{m} = \bar{m}_\diamond^+ = \sqrt{1+N}$ and approaches the straight line $v = 1$, corresponding to a single sphere, for large \bar{m} .

Corrections arising from area-difference-elasticity

When we include area-difference-elasticity, the shapes with a large mother vesicle of radius r_1 and N spherical out-buds of radius r_2 generate the nonlocal spontaneous curvature

$$\bar{m}_{\text{nlc}} = \pi \frac{\kappa_\Delta}{\kappa} (1 - \eta - Nr_2) = \pi \frac{\kappa_\Delta}{\kappa} \left(1 - \eta - \sqrt{N(1 - \eta^2)}\right) \quad (5.164)$$

which generalizes Eq. 5.119 from $N = 1$ to $N \geq 1$. The last equality in Eq. 5.164 follows from the area relation $\eta_1^2 + Nr_2^2 = 1$. The geometric factor in Eq. 5.164 is negative and bounded by

$$1 - \sqrt{1+N} \leq 1 - \eta_1 - \sqrt{N(1-\eta_1^2)} \leq 0 \quad (5.165)$$

which implies that the absolute value of the nonlocal spontaneous curvature satisfies

$$|\bar{m}_{\text{nlo}}| \leq \pi \left(\sqrt{1+N} - 1 \right) \frac{\kappa_\Delta}{\kappa}. \quad (5.166)$$

The neck closure condition is now given by

$$\bar{M}_{\text{nc}} = \frac{1}{2} \left(\frac{1}{\eta_1} + \frac{1}{r_2} \right) = \bar{m} + \bar{m}_{\text{nlo}} = \bar{m} + \pi \frac{\kappa_\Delta}{\kappa} (1 - \eta_1 - Nr_2) \quad (5.167)$$

Using the inequality in Eq. 5.166, we can ignore the nonlocal contribution \bar{m}_{nlo} in the neck closure condition as given by Eq 5.167 for

$$\bar{m} \gg \pi \left(\sqrt{1+N} - 1 \right) \frac{\kappa_\Delta}{\kappa} \quad (5.168)$$

which generalizes Eq. 5.126 for two-sphere shapes with $N = 1$ to arbitrary values of N .

Alternatively, we can consider the limit of small out-buds and, thus, small bud radii r_2 . In this limit, the radius r_1 of the mother vesicle behaves as $\eta_1 \approx 1 - \frac{1}{2}Nr_2^2$ for small Nr_2^2 as follows from the area relation $\eta_1^2 + Nr_2^2 = 1$. As a consequence, the neck closure condition in Eq. 5.167 leads to the local spontaneous curvature

$$\bar{m} \approx \frac{1}{2} \left(\frac{1}{\eta_1} + \frac{1}{r_2} \right) + \pi \frac{\kappa_\Delta}{\kappa} Nr_2 \quad \text{for small buds with } r_2 \ll 1/\sqrt{N} \quad (5.169)$$

which shows that we can ignore the κ_Δ term arising from area-difference-elasticity for small $r_2 \ll 1/\sqrt{N}$.

Mutual exclusion of out-buds

Because all out-buds or r_2 -spheres are attached to the r_1 -sphere, they may become closely packed when they reach a certain size. For $N = 2$ as shown in Figures 5.18a, b, the two r_2 -spheres can become arbitrarily large without getting into contact. Therefore, mutual exclusion of the two r_2 -spheres does not affect the morphology diagram in Figure 5.19. For $N = 3$, mutual exclusion of the three r_2 -spheres starts to play a role when the radius of the r_2 -spheres becomes sufficiently large compared to the radius of the r_1 -sphere, compare Figure 5.20c. Indeed, the three r_2 -spheres come into contact when $r_2 = \frac{\sqrt{3}}{2-\sqrt{3}}r_1 = 6.46r_1$ corresponding to the contact volume $v_{\text{co}}^+ = 0.5712$ for $N = 3$. As a consequence, $(1 + 3)$ -sphere shapes with $r_2 > r_1$ can no longer be formed for the volume range $0.5712 < v < 1/\sqrt{3} = 0.5774$.

In general, the mutual exclusion of the r_2 -spheres acts to reduce the parameter region in which $(1 + N)$ -sphere shapes can be formed for all $N \geq 3$. The corresponding contact volume $v_{\text{co}}^+(N)$ decreases with increasing N . For $N = 12$, the r_2 -spheres

come into contact along the L_{\pm}^+ -line where the r_2 -spheres have the same size as the r_1 -sphere. The corresponding contact volume $v_{\text{co}}^+(12) = v_{\text{co}}^+(12) = 1/\sqrt{13} = 0.2774$. As a consequence, $(1 + 12)$ -sphere shapes, for which each r_2 -sphere is larger than the r_1 -sphere can no longer be formed when we take mutual exclusion of the r_2 -spheres into account. On the other hand, we can also conclude that the morphology diagram exhibits both bifurcation points B_1^+ and B_0^+ as well as the limit shapes L_1^+ , L_2^+ with $r_1 > r_2$, and L_{\pm}^+ up to bud number $N = 11$. Thus, for $3 \leq N \leq 11$, the mutual exclusion of the out-buds will only affect the $(1 + N)$ -spheres for which the bud radius r_2 exceeds the radius r_1 of the central sphere, as illustrated in Figure 5.20c for $N = 3$.

5.5.6 N-DEPENDENT ENERGY LANDSCAPE

Optimal bud number

In the previous subsections, we focused on the stability of different multi-sphere shapes and found certain stability regions within the (\bar{m}, v) -plane for each of these shapes. When we vary the spontaneous curvature \bar{m} and the volume v within such a stability region, the bending energy of the corresponding multi-sphere shape changes smoothly and defines an energy surface over this region. Because the different stability regions overlap with each other in the (\bar{m}, v) -plane, we often find many energy surfaces stacked above one another, when we consider the vicinity of a certain point in the (\bar{m}, v) -plane. These energy surfaces of the multi-sphere shapes should be regarded as partial branches that supplement the branches of stationary solutions obtained from the Euler-Lagrange equations. Therefore, the overall energy landscape of the vesicle shapes is rather complex.

In order to determine the shape of lowest bending energy for given values of \bar{m} and v , we need to compare the different branches of shapes. As an example, let us again consider multi-sphere shapes with N out-buds which have the dimensionless bending energy

$$\bar{E}_{\text{be}} = (1 - mR_1)^2 + N(1 - mR_2)^2 = 1 + N + \bar{m}^2 - 2\bar{m}(\eta_1 + Nr_2) \quad (5.170)$$

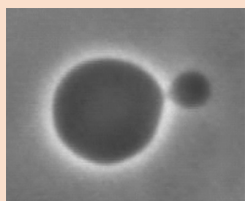
where the radii r_1 and r_2 satisfy the geometric relations in Eqs 5.142 and 5.143 with $N_1 = 1$ and $N_2 = N$. When we minimize this bending energy with respect to N , we find the optimal bud number

$$N_{\text{opt}} \approx \frac{2(1-v)}{3} \bar{m}^2 \quad \text{for large } \bar{m}. \quad (5.171)$$

For $N = N_{\text{opt}}$, the radius of the out-buds has the value $r_2 \approx 1/\bar{m}$ which implies that shapes with an optimal bud number are identical with the shapes Z_N^{out} possessing N zero-energy out-buds. The asymptotic equality as given by Eq. 5.171 implies that the optimal number $N = N_{\text{opt}}$ of out-buds increases with the spontaneous curvature \bar{m} when we consider a fixed volume $v < 1$ as obtained by the osmotic deflation of a single sphere. The actual shape transition from a shape with N out-buds to a shape with $N + 1$ out-buds necessarily involves smooth vesicle shapes with open necks. For small values of N , the corresponding bifurcations have been calculated by numerical energy minimization in (Seifert et al., 1991; Liu et al., 2016). For large values of N , we need to consider sufficiently large GUVs with radius $r_1 \gg r_2 = 1/\bar{m}_1$ so that we can ignore the mutual exclusion of the out-buds.

Box 5.2 Membrane necks of vesicles with laterally uniform composition

Membrane necks are funnel-like membrane structures that connect two different membrane compartments. The mean curvatures, M_1 and M_2 , of the two membrane segments adjacent to the neck define the neck curvature $M_{ne} = \frac{1}{2}(M_1 + M_2)$ as introduced in Eq. 5.48.



- GUV and out-bud connected by a narrow membrane neck (from Figure 5.2). The mother vesicle has the radius $R_1 = 19 \mu\text{m}$, the out-bud has the radius $R_2 = 7.2 \mu\text{m}$. The neck curvature M_{ne} then has the positive value $M_{ne} = \frac{1}{2}(\frac{1}{R_1} + \frac{1}{R_2}) = \frac{1}{10.4 \mu\text{m}}$.



- GUV and in-bud connected by a narrow membrane neck (from Figure 5.6). The mother vesicle has the radius $R_1 = 10.4 \mu\text{m}$, the in-bud has the radius $R_2 = 4.7 \mu\text{m}$, which leads to the negative neck curvature $M_{ne} = \frac{1}{2}(\frac{1}{R_1} - \frac{1}{R_2}) = -\frac{1}{8.6 \mu\text{m}}$.

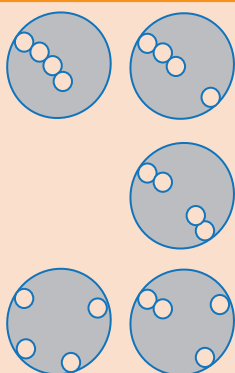
When we observe the closure of a neck, the neck curvature M_{ne} is equal to the spontaneous curvature m_{eff} , which may include a non-local contribution from area-difference-elasticity as in Eq. 5.68. Thus, the observation of neck closure leads to an estimate for m_{eff} . Furthermore, sufficiently large values of m_{eff} lead to the cleavage of the membrane neck and thus to complete membrane fission, see Section 5.5.4.



- A spherical vesicle may form several spherical buds with closed membrane necks. In equilibrium, all buds must have the same mean curvature as follows from the Euler-Lagrange Eq. 5.70 for spherical membrane segments. Therefore, the necks of all buds must have the same neck curvature M_{ne} .
- (Top) A vesicle with four out-buds and positive neck curvature.
- (Bottom) A vesicle with four in-buds and negative neck curvature.



- (Top) A vesicle membrane with positive spontaneous curvature forming a necklace-like out-tube consisting of four out-beads with the same positive mean curvature.
- (Bottom) A vesicle membrane with negative spontaneous curvature forming a necklace-like in-tube consisting of four in-beads with the same negative mean curvature.
- In both cases, the neck curvature M_{ne} attains two different values (i) for the necks connecting the necklace-like tube with the mother vesicle and (ii) for the necks between two neighboring beads within the tube.



- Five different morphologies of a vesicle with four in-beads or in-buds of equal size. All five morphologies have the same membrane area, the same vesicle volume, the same integrated mean curvature, and the same bending energy. This degeneracy illustrates the morphological complexity of membranes, see Section 6.4 further below.
- Apart from the 4-bud morphology, all morphologies involve two types of necks that differ in their neck curvature.

GUVs with buds and necklace-like tubes stabilized by membrane necks have some interesting properties. On the one hand, they provide aqueous subcompartments that could be used for the confinement of nanoparticles or microspheres. The closed necks represent diffusion barriers that can, however, be removed relatively easily, e.g., by osmotic inflation which leads to neck opening for all morphologies displayed in this box. On the other hand, the formation of many buds and necklace-like tubes provides an area reservoir to the mother vesicle which increases the vesicle's robustness against mechanical perturbation as shown by micropipette aspiration (Bhatia et al., 2018). The stability of membrane necks can be further enhanced by adhesion and constriction forces (Agudo-Canalejo and Lipowsky, 2016), see Chapter 8 of this book.

5.6 NANOTUBES OF UNIFORM MEMBRANES

Giant vesicles can spontaneously form long nanotubes that emanate from the vesicle membrane. Such a tubulation process provides direct evidence that the vesicle membrane has a relatively large spontaneous curvature m . In-tubes pointing towards the interior of the vesicle are formed for large negative m -values, see Figure 5.21, out-tubes pointing towards the exterior solution for large positive values of m . Therefore, a uniform membrane with constant spontaneous curvature will form either in-tubes or out-tubes but not both types of tubes simultaneously.

In general, in- and out-tubes differ in several important aspects. First, the in- and out-tubes are connected to different volume reservoirs: the in-tubes exchange volume with the exterior aqueous compartment, which represents an effectively unlimited volume reservoir, whereas the out-tubes exchange aqueous solution with the interior vesicle compartment. Second, the membranes of out- and in-tubes experience different osmotic pressure differences: the membrane of an out-tube is subject to the same pressure difference ΔP as the membrane of the large spherical segment whereas an in-tube feels the opposite pressure difference $-\Delta P$. Third, the membrane segments that form in- and out-tubes differ in the sign of their mean curvature which is negative for in-tubes and positive for out-tubes.

As shown in Figure 5.21, membrane nanotubes can have two different morphologies: necklace-like tubes consisting of small quasi-spherical beads connected by closed membrane necks as well as cylindrical tubes. From a theoretical point of view, necklace-like tubes represent multi-sphere vesicles with two types of necks whereas cylinders are governed by different shape equations. For cylindrical tubes, we include a pulling force that is applied locally to the tip of the tubes. For both tube morphologies, the mechanical tension is relatively small, reflecting the large area reservoir provided by the tubes, and the total membrane tension is dominated by the spontaneous tension, $\sigma = 2\kappa m^2$ (Lipowsky, 2013). At the end, we briefly discuss the transformation of necklace-like tubes into cylindrical ones, a transformation that occurs when the tube length has reached a certain critical value.

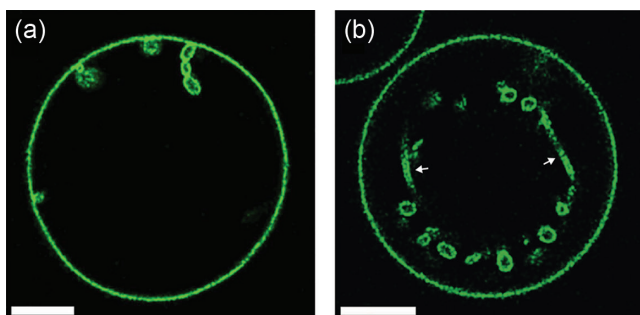


Figure 5.21 Giant vesicles with in-tubes, i.e., with membrane nanotubes that point towards the vesicle interior: (a) one necklace-like tube and several buds and (b) several necklace-like tubes and two cylindrical tube segments (white arrows). (Reproduced with permission from Liu, Y. et al., *ACS Nano*, 10, 463–474, 2016.)

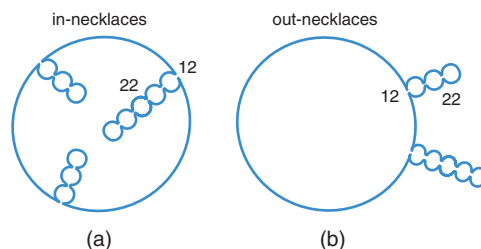


Figure 5.22 Necklace-like nanotubes consisting of spherules with radius r_2 emanating from a giant spherical vesicle with radius r_1 . These shapes involve two different types of closed necks, 12-necks and 22-necks, that differ in their neck curvatures: (a) Necklace-like in-tubes with negative neck curvatures M_{12} and $M_{22} < M_{12}$ are formed for negative spontaneous curvature; and (b) Necklace-like out-tubes with positive neck curvatures M_{12} and $M_{22} > M_{12}$ require a membrane with positive spontaneous curvature.

5.6.1 NECKLACE-LIKE NANOTUBES

Necklace-like nanotubes as observed experimentally consist of identical quasi-spherical beads that are connected by closed membrane necks. One such necklace consisting of three beads is visible in Figure 5.21a. If one ignores thermally excited fluctuations, such a necklace can be described, in the context of curvature models, by a multi-sphere vesicle with two different types of closed necks as shown in Figure 5.22. Indeed, we now have to distinguish the necks between the large sphere and a necklace from the necks between two small spheres within the same necklace. In the following, we will use three terms for the sake of clarity. First, we will distinguish “buds” that are directly connected to the mother vesicle from “beads” that are connected to buds or other beads. Second, both buds and beads will be collectively called “spherules.”

Necklace geometry and neck stability

Geometry of vesicle with necklace-like nanotubes. Consider a GUV consisting of a large spherical mother vesicle and one or several necklace-like nanotubes as displayed in Figure 5.22. The tubes contain a total number N of spherules. For a vesicle membrane with area A , we will again use the vesicle size

$R_{ve} = \sqrt{A/(4\pi)}$ as the basic length scale and use the rescaled radii $r_1 = R_1/R_{ve}$ and $r_2 = R_2/R_{ve} < r_1$ of the mother vesicle and the spherules. These radii satisfy the relations

$$r_1^2 + Nr_2^2 = 1 \quad (5.172)$$

corresponding to the total membrane area A and

$$r_1^3 \pm Nr_2^3 = v \quad (5.173)$$

corresponding to the vesicle volume V where the plus and minus sign applies to out- and in-necklaces. Note that the same geometric relations apply to a GUV with N out- or in-buds as described in Section 5.5.

Stability of membrane necks. As mentioned, each necklace connected to a giant vesicle is characterized by two types of necks, 12- and 22-necks, see Figure 5.22. These two necks have two different neck curvatures as given by

$$M_{12} = \frac{1}{2}(M_1 + M_2) \quad (5.174)$$

and

$$M_{22} = \frac{1}{2}(M_2 + M_2) = M_2. \quad (5.175)$$

We will now examine the stability of these two types of necks. Out-necklaces require positive spontaneous curvature $m > 0$ and are characterized by positive mean curvature $M_2 = 1/R_2$ of the spherules. For such a necklace, the 22-necks connecting two neighboring spherules, see Figure 5.22, are stable if the neck curvature M_{22}

$$0 < M_{22} = M_2 \leq m \quad (\text{stable 22-neck of out-necklace}). \quad (5.176)$$

Furthermore, the stability condition for the 12-necks, connecting the mother vesicle with the out-necklace, has the form

$$M_1 + M_2 \leq 2m \quad (5.177)$$

which follows from the stability condition Eq. 5.176 for the 22-necks because

$$M_1 + M_2 < 2M_2 \leq 2m. \quad (5.178)$$

In-necklaces, on the other hand, can form for negative spontaneous curvature $m < 0$ and are characterized by negative mean curvature $M_2 = -1/R_2$ of the spherules. The stability condition for the 22-necks is now given by

$$m \leq M_{22} = M_2 < 0 \quad (\text{stable 22-neck of in-necklace}). \quad (5.179)$$

Furthermore, the stability condition for the 12-necks, connecting the mother vesicle with the out-necklace, has the form

$$M_1 + M_2 \geq 2m \quad (5.180)$$

which follows from the stability condition Eq. 5.179 for the 22-necks because

$$M_1 + M_2 > 2M_2 \geq 2m. \quad (5.181)$$

Necklaces of zero-energy spherules

We now consider necklaces that consist of zero-energy spherules with radius $R_2 = 1/|m| \ll R_1$ and denote the shapes with N zero-energy spherules by L_N^{in} and L_N^{out} .¹¹ In contrast to the persistent shapes Z_N^{in} and Z_N^{out} with N zero-energy in- and out-buds as discussed in Section Multi-sphere vesicles with N out-buds, the shapes L_N^{in} and L_N^{out} are limit shapes because the closed 22-necks between neighboring spherules fulfill the neck closure condition $M_{22} = m$, compare Eqs 5.176 and 5.179.

For the limit shapes L_N^{in} and L_N^{out} with spherules of radius $r_2 = 1/|m| \ll 1$, the mother vesicle has the radius

$$r_1 = r_1(N) = \sqrt{1 - \frac{N}{\bar{m}^2}} \quad (5.182)$$

and the volume is given by

$$v = v(N) = \left[1 - \frac{N}{\bar{m}^2} \right]^{3/2} \mp \frac{N}{|\bar{m}|^3}, \quad (5.183)$$

where the minus and plus sign applies to in- and out-necklaces, respectively.

Because the spherules have the radius $r_2 = 1/|\bar{m}|$, the in- and out-necklaces do not contribute to the bending energies of the L_N^{in} and L_N^{out} shapes. The latter energies are then equal to the bending energies of the mother vesicle with radius r_1 and mean curvature $\bar{M}_1 = 1/r_1$. These bending energies have the form

$$E_{\text{bc}}(\eta) = 8\pi\kappa(1 - \bar{m}\eta)^2 \quad \text{for both in- and out-necklaces} \quad (5.184)$$

corresponding to $\bar{m} < 0$ and $\bar{m} > 0$, respectively. Using Eq. 5.182, the latter bending energy can be rewritten as

$$\bar{E}_{\text{bc}}(\eta) = \frac{E_{\text{bc}}(\eta)}{8\pi\kappa} = 1 + \bar{m}^2 - 2\bar{m}\sqrt{1 - \frac{N}{\bar{m}^2}} - N \quad (5.185)$$

which behaves as

$$\bar{E}_{\text{bc}}(\eta) \approx (1 - \bar{m})^2 - N \left(1 - \frac{1}{\bar{m}} \right) \quad \text{for large } |\bar{m}|. \quad (5.186)$$

The first term of this expression represents the bending energy of a single sphere with spontaneous curvature \bar{m} . The second term proportional to N is negative for $\bar{m} < 0$ or $\bar{m} > 1$. Thus, for large negative or positive values of \bar{m} , the bending energies of the two limit shapes L_N^{in} and L_N^{out} decrease with increasing N . Therefore, these limit shapes provide possible low-energy pathways for the osmotic deflation of giant vesicles with large negative and large positive spontaneous curvatures, respectively.

The low-energy pathway provided by the sequence of L_N^{in} shapes has been studied in detail by numerical minimization of the shape functional $\mathcal{F}\{S\}$ in Eq. 5.22 (Liu et al., 2016). As a result, it was found that each limit shape L_N^{in} belongs to a different branch of (meta)stable shapes. When we start from such a limit shape with a certain value of N , an increase in vesicle volume via osmotic inflation leads to an opening of the necks and the necklaces then resemble unduloids as shown in Figure 5.23b, compare also Figure 5.28 further below. On the other hand, decreasing the vesicle volume by osmotic deflation does not open the closed necks connecting neighboring spherules but increases the radius of the spherules to $r_2 > 1/|\bar{m}|$, see Figure 5.23b. The corresponding metastable branch extends up to $r_2 = 3/|\bar{m}|$ at which point the spherules become unstable and undergo a sphere-prolate bifurcation.

5.6.2 DOMINANCE OF SPONTANEOUS TENSION

The mechanical equilibrium between the spherical mother vesicle and the spherules implies the two shape equations

$$\Delta P = 2\hat{\Sigma}M_{\text{sp}} - 4\kappa m M_{\text{sp}}^2 \quad \text{with } M_{\text{sp}} = M_1 = \frac{1}{R_1} \text{ or } M_2 = \pm \frac{1}{R_2}$$

¹¹In (Liu et al., 2016), the shapes L_N^{in} have been denoted by L^{in} .

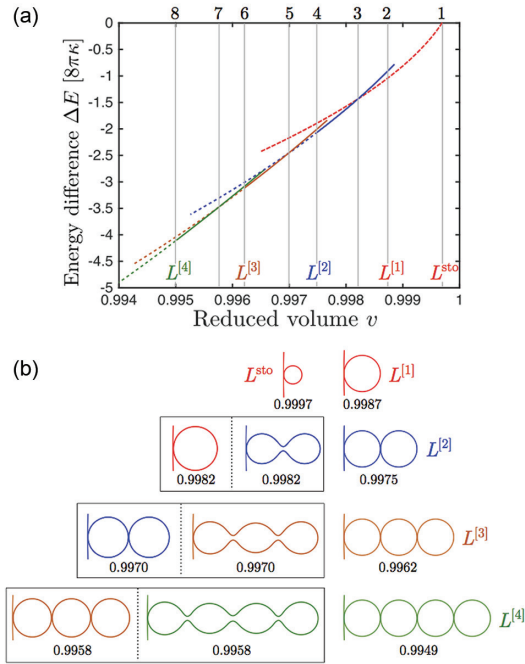


Figure 5.23 Osmotic deflation and inflation of a lipid vesicle with size $R_{ve} = 20.7 \mu\text{m}$ and spontaneous curvature $m = -1/(599\text{nm})$: (a) Energy landscape of the vesicle as a function of the reduced volume v with the limit shapes $L^{[N]} \equiv L_N^{\text{in}}$. The energy difference ΔE describes the deflation-induced reduction in bending energy compared to the initial spherical vesicle, in units of $8\pi\kappa$. The eight vertical lines labeled from 1 to 8 (top) correspond to eight v -values obtained via eight discrete deflation steps; and (b) Tube shapes for the global energy minima at these eight v -values. The short vertical line on the left end of the tubes represents a short segment of the mother vesicle which is connected to each tube by a closed membrane neck. As we deflate the initial vesicle with $v = 1$, we move along the 1-necklace branch (red) that begins at the limit shape L^{sto} with bud radius $R_2 \approx 1/(2|m|)$ and $v = 0.9997$. After passing the shape $L^{[1]} = L_1^{\text{in}}$ with $R_2 = 1/|m|$ and $v = 0.9987$, we reach the reduced volume $v = 0.9982$ at which the 1-necklace branch crosses the 2-necklace branch (blue). For the latter v -value, a bud with radius $R_2 > 1/|m|$ coexists with a 2-necklace that has an open 2-neck. Further deflation leads to the 2-necklace $L^{[2]} = L_2^{\text{in}}$ with a closed neck at $v = 0.9975$ and, subsequently, to the 3-necklace branch (orange) and the 4-necklace branch (green). The dashed and solid segments of the free energy landscape in panel (a) correspond to tubes with closed and open necks, respectively. (Reproduced with permission from Liu, Y. et al., ACS Nano, 10, 463–474, 2016.)

as in Eq. 5.70 with the total membrane tension $\hat{\Sigma} = \Sigma + 2\kappa m^2$. Combining these two equations to eliminate the pressure difference ΔP , we obtain the mechanical tension

$$\Sigma = 2\kappa m(M_1 + M_2) - 2\kappa m^2 = 4\kappa m M_{12} - 2\kappa m^2 \quad (5.187)$$

where the first equality is equal to Eq. 5.76 and the second equality follows from the mean curvature M_{12} of the 12-neck as given by Eq. 5.174. Therefore, the mechanical tension Σ depends on the neck curvature M_{12} whereas the stability of the multi-sphere shape is determined by the neck curvature M_{22} of the 22-necks.

For the limit shapes L_N^{in} and L_N^{out} , the spherules have the mean curvature $M_2 = m$ and the mean curvature of the 12-necks is given by $M_{12} = \frac{1}{2}(M_1 + m)$. As a consequence, the mechanical tension in Eq. 5.187 becomes

$$\Sigma = 2\kappa m M_1 = \frac{\sigma}{m R_1} = \mp \frac{R_2}{R_1} \sigma \quad (5.188)$$

where the minus and plus sign applies to the limit shapes L_N^{in} and L_N^{out} , respectively. Because the radius R_1 of the mother vesicle is much larger than the radius $R_2 = 1/|m|$ of the spherules, the absolute value $|\Sigma|$ of the mechanical tension in Eq. 5.188 is much smaller than the spontaneous tension $\sigma = 2\kappa m^2$.

The limit shapes L_N^{in} and L_N^{out} represent the equilibrium shapes of the tubulated vesicle for certain vesicle volumes or, equivalently, for certain values of the membrane area

$$A_{\text{nt}} = A_{\text{nt},N} \equiv N4\pi/m^2 \quad (\text{limit shapes } L_N^{\text{in}} \text{ and } L_N^{\text{out}}) \quad (5.189)$$

stored in the tubes (Liu et al., 2016; Bhatia et al., 2018). Each of these limit shapes belongs to a whole branch of shapes, as illustrated for in-necklaces by the energy branches in Figures 5.23 and 5.24. The latter figure displays the bending energy landscape E_{nt} for the necklace-like tubes that grow as we reduce the volume of the GUV. The deflation process decreases the membrane area A_1 of the mother vesicle and increases the area A_{nt} stored in the tubes, for fixed total area $A = A_1 + A_{\text{nt}}$. The bending energy of the tubulated GUV is equal to $E_1 + E_{\text{nt}}$ where the bending energy E_1 of the mother vesicle is a monotonically decreasing function

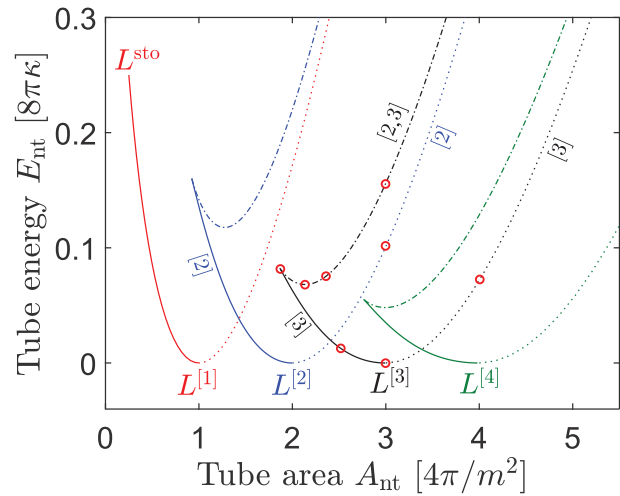


Figure 5.24 Energy landscape E_{nt} of a necklace-like nanotube protruding into a GUV as a function of membrane area A_{nt} stored in the tube. The size of the GUV is much larger than the width of the nanotube. The energy landscape is built up from a discrete set of $[N]$ -branches with $N \geq 1$. The different branches are distinguished by different colors. Each $[N]$ -branch attains its energy minimum for the limit shape $L^{[N]} = L_N^{\text{in}}$ which consists of N spherules with radius $R_2 = 1/|m|$ and area $4\pi/m^2$. When we deflate the limit shape $L^{[N]}$, i.e., when we reduce the vesicle volume for fixed membrane area, we move towards larger values of the tube area A_{nt} along the dotted lines which represent necklace-like tubes with N small spheres of radius $R_2 > 1/|m|$ and $N - 1$ closed necks. When R_2 reaches the limiting value $R_2 = 3/|m|$, the spherules undergo a sphere-prolate bifurcation (outside of the figure). When we inflate the limit shape $L^{[N]} = L_N^{\text{in}}$, we move towards smaller values of A_{nt} along the full lines that represent necklace-like tubes with N bellies and $N - 1$ open necks. The dash-dotted lines represent unstable necklace-like tubes corresponding to transition states $[N, N + 1]$ between the (meta)stable $[N]$ and $[N + 1]$ states. The red circles mark the nanotube morphologies displayed in Figure 5.25. (From Bhatia, T. et al., ACS Nano, 12, 4478–4485, 2018.)

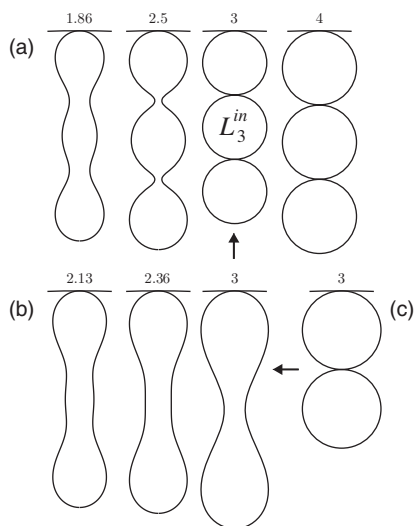


Figure 5.25 Morphologies of necklace-like nanotubes corresponding to the red circles in Figure 5.24. The number at the top of each tube represents the tube area A_{nt} in units of $4\pi/m^2$: (a) Four shapes along the (meta)stable [3]-branch. The shape with $A_{nt} = 1.86$ represents the bifurcation point between the [3]-branch and the unstable [2, 3]-branch of transition states. The shape with $A_{nt} = 3$ is the limit shape L_3^{in} ; (b) Three shapes along the unstable [2, 3]-branch of transition states. The shape with $A_{nt} = 2.13$ is located at the energy minimum of the [2, 3]-branch, see Figure 5.24, the shape with $A_{nt} = 2.36$ separates transition states with three from those with two bellies; and (c) Metastable shape of the [2]-branch that decays into the limit shape $L^{[3]} = L_3^{in}$ via the rightmost transition state in (b) with $A_{nt} = 3$ (two arrows). (From Bhatia, T. et al., *ACS Nano*, 12, 4478–4485, 2018.)

of A_{nt} . Examples for the morphologies of the necklace-like tubes along several branches of the energy landscape are displayed in Figure 5.25.

Inspection of the energy landscape in Figure 5.24 reveals that the equilibrium shapes with the lowest bending energy E_{nt} are provided by short segments of the $[N]$ -branches as obtained by slight deflation and slight inflation of the limit shapes L_N^{in} . Slight deflation of L_N^{in} reduces the vesicle volume and increases the area A_{nt} of the necklace-like tubes until we reach the intersection point of the $[N]$ -branch with the $[N + 1]$ -branch at tube area $A_{nt} = (N + \varepsilon_N)4\pi/m^2$ with a dimensionless coefficient ε_N that satisfies $0 < \varepsilon_N < 1$. We now consider the increase in tube area as given by

$$A_{nt} - A_{nt,N} \equiv \delta_N \frac{4\pi}{m^2} \quad \text{with } 0 \leq \delta_N \leq \varepsilon_N \quad (5.190)$$

which leads to the mean curvature

$$M_2 = \frac{m}{\sqrt{1 + \delta_N/N}} \approx m \left(1 - \frac{\delta_N}{2N} \right) \quad \text{for large } N. \quad (5.191)$$

The number N of spherules is directly related to the length L_{nt} of the necklace-like nanotubes via $L_{nt} = 2NR_2 = 2N/|M_2|$ which implies

$$M_2 \approx m + \frac{\delta_N}{L_{nt}} \quad \text{for large } L_{nt} \gg R_2, \quad (5.192)$$

i.e., for a tube length L_{nt} that is large compared to the radius R_2 of the spherules, with $0 < \delta_N < 1$. Using again the general expression for the mechanical tension Σ of necklace-like tubes as given by Eq. 5.187, we obtain

$$\Sigma \approx 2\kappa m \left(M_1 + \frac{\delta_N}{L_{nt}} \right) = \left(\frac{1}{mR_1} + \frac{\delta_N}{mL_{nt}} \right) \sigma \quad (5.193)$$

Therefore, the absolute value $|\Sigma|$ of a necklace-like tube is much smaller than the spontaneous tension σ if both the mother vesicle radius R_1 and the tube length L_{nt} are much larger than the small sphere radius $R_2 \approx 1/|m|$. In such a situation, the total membrane tension $\hat{\Sigma} = \Sigma + \sigma$ of a GUV with necklace-like nanotubes becomes

$$\hat{\Sigma} = \Sigma + \sigma \approx \left(\frac{1}{mR_1} + \frac{\delta_N}{mL_{nt}} \right) \sigma + \sigma \approx \sigma \quad (\text{large } |m|) \quad (5.194)$$

and is, thus dominated by the spontaneous tension σ . The small mechanical tension reflects the large area reservoirs as provided by the nanotubes. Indeed, when the tubulated vesicle is exposed to external forces or constraints, it can adapt to these perturbations, for fixed vesicle volume and membrane area, by simply shortening the nanotubes. This increased robustness of tubulated vesicles has been recently demonstrated by micropipette aspiration of tubulated GUVs (Bhatia et al., 2018).

5.6.3 MORPHOLOGICAL COMPLEXITY AND RUGGED ENERGY LANDSCAPE

As previously mentioned, the limit shapes L_N^{in} displayed in Figure 5.23 provide a low-energy pathway for the growth of a single necklace-like tube. The elongation of this tube from $L^{[N]}$ to $L^{[N+1]}$ proceeds via a sphere-prolate bifurcation. Inspection of the microscopy images displayed in Figure 5.21 and Figure 5.4 reveals however that giant vesicles can form much more complex shapes consisting of many buds and tubes. This morphological complexity emerges from the presence of a second low-energy pathway provided by the nucleation of another bud via an oblate-stomatocyte bifurcation (Liu et al., 2016). The competition of these two pathways—elongation of an existing bud or necklace and nucleation of another bud—can lead to many different morphologies (Lipowsky, 2018b).

In order to illustrate the morphological complexity, let us consider a monodisperse batch of vesicles with a certain spontaneous curvature m . These vesicles are now osmotically deflated by the same deflation steps as in Figures 5.23–5.25. As a result, we obtain the same sequence of vesicle volumes V_N that lead to the limit shapes L_N^{in} , but let us now include the possibilities (i) that the vesicle membrane can also form, at each step, a new bud and (ii) that the same deflation step can elongate any of the existing buds and necklaces. As a result, we obtain a complex sequence of morphologies as shown in Figure 5.26.

In Figure 5.26, all morphologies with the same number N of spherules have the same bending energy (Lipowsky, 2014a; Liu et al., 2016) and represent, in fact, the states of lowest bending energy for given area A and volume V_N . The N -bead morphologies

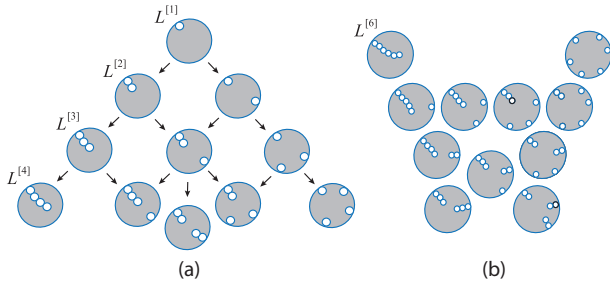


Figure 5.26 (a) The deflation of the limit shape $L^{[1]} = L^{[n]}$ in with a single in-bud (top) can lead to the shape $L^{[2]} = L^{[2]}$ with a necklace consisting of two spherules or to another shape with two in-buds. Further deflation steps (arrows) lead to an increasing number $|\Omega|$ of distinct N -bead morphologies which all have the same area, volume, and bending energy and represent, in fact, the states of lowest bending energy. Note that we have $|\Omega| = 5$ distinct morphologies with $N = 4$ spherules; and (b) For $N = 6$, the vesicle can attain $|\Omega| = 11$ different morphologies, all having the same volume, area, and bending energy as $L^{[6]} = L^{[6]}$. Neighboring morphologies differ in the location of only one bead and can be obtained by a “cut and paste” operation (Lipowsky, 2014a). In both (a) and (b), all contact zones between two spherical membrane segments contain a closed membrane neck which implies that all beads are filled with exterior solution (white).

differ, however, in the detailed arrangement of the spherules and belong to different energy branches that cross each other at volume $V = V_N$. Note also that all spherules connected to the same mother vesicle must have the same size. The latter feature follows directly from the Euler-Lagrange equation for uniform membranes because this equation allows only spherical segments with two different radii to coexist on the same vesicle.

What happens when we continue to deflate the vesicles displayed at the bottom of Figure 5.26a? It turns out that the number $|\Omega|$ of distinct N -spherule morphologies grows quite rapidly for $N > 4$. This is illustrated in Figure 5.26b by the $|\Omega| = 11$ distinct states of lowest bending energy for $N = 6$. Each of these 11 states has again the same area, volume, and bending energy. Therefore, we have 11 different branches of shapes that cross each other at volume $V = V_6$. For even larger values of N , the number $|\Omega|$ of distinct N -spherule morphologies grows exponentially with \sqrt{N} as follows from known results about partitions in the sense of mathematical number theory. Furthermore, when we reach a certain volume V_N after the N th deflation step, many n -spherule morphologies with $n < N$ can still exist as metastable states with larger spherule sizes. As a consequence, the energy landscape becomes more and more rugged as the volume decreases and the largest possible bead number N increases.

The morphological complexity described above has been recently studied experimentally by optical microscopy of giant vesicles (Bhatia et al., in preparation). These vesicles were exposed to aqueous solutions of two monosaccharides, sucrose and glucose. Varying the two sugar concentrations, one can independently change the volume-to-area ratio v and the spontaneous curvature m . As a result, a large variety of different morphologies has been observed, in agreement with the theoretical predictions.

5.6.4 CYLINDRICAL NANOTUBES

As shown in Figure 5.21b, the spontaneous tubulation of giant vesicles can also lead to cylindrical nanotubes. Cylindrical shapes

are described by two shape equations, both of which differ from the shape equation for spherical shapes. In the next subsection, we will first derive the shape equations for cylinders. In the subsequent subsection, we will then combine the shape equations for cylinders and spheres in order to describe giant vesicles with cylindrical nanotubes.

5.6.5 SHAPE EQUATIONS FOR CYLINDRICAL TUBES

A cylindrical membrane segment is characterized by constant mean curvature $M = M_{cy}$ and vanishing Gaussian curvature $G = 0$. It then follows from the Euler-Lagrange Eq. 5.23 that the mean curvature M_{cy} satisfies the cubic equation

$$\Delta P = 2\Sigma M_{cy} - 4\kappa M_{cy}(M_{cy}^2 - m^2) = 2\hat{\Sigma}M_{cy} - 4\kappa M_{cy}^3 \quad (5.195)$$

with the total membrane tension $\hat{\Sigma} = \Sigma + 2\kappa m^2$ as before. In contrast to spherical shapes, an infinitesimal scale transformation of cylindrical shapes leads to a global shape Eq. 5.45 that differs from the Euler-Lagrange Eq. 5.195. Indeed, the global shape equation has the form

$$3\Delta P = 8\hat{\Sigma}M_{cy} - 16\kappa m M_{cy}^2 \quad (5.196)$$

for both in- and out-tubes. The Euler-Lagrange Eq. 5.195 and the global shape Eq. 5.196 can be derived in a more intuitive manner if one parametrizes the cylindrical shape by its radius R_{cy} and its length L_{cy} and minimizes the corresponding shape energy both with respect to R_{cy} and with respect to L_{cy} (Lipowsky, 2013).

We can now eliminate the term proportional to $\hat{\Sigma}$ by a combination of Eqs 5.195 and 5.196 which leads to the pressure difference

$$\Delta P = 16\kappa M_{cy}^2 (m - M_{cy}). \quad (5.197)$$

When we insert the latter equation into Eq. 5.195, we obtain the total tension

$$\hat{\Sigma} = 8\kappa m M_{cy} - 6\kappa M_{cy}^2 \quad (5.198)$$

and the mechanical tension

$$\Sigma = \hat{\Sigma} - 2\kappa m^2 = -6\kappa (M_{cy} - m)(M_{cy} - \frac{1}{3}m) \quad (5.199)$$

as a function of mean curvature M_{cy} .

The two relations in Eqs 5.197 and 5.199 have two immediate consequences: (i) For fixed curvature-elastic parameters κ and \bar{m} , each possible value of M_{cy} leads to unique values of ΔP and Σ . Thus, as we vary the value of M_{cy} , we move along a certain line in the $(\Sigma, \Delta P)$ -plane; and (ii) Vice versa, for each point in the $(\Sigma, \Delta P)$ -plane, we find only a single solution for M_{cy} . Taken separately, both the cubic relationship Eq. 5.197 between the pressure difference ΔP and the mean curvature M_{cy} as well as the quadratic

relationship Eq. 5.199 between the mechanical tension Σ and M_{cy} can lead to several solutions for M_{cy} . However, one cannot find two different values for M_{cy} that satisfy both relationships simultaneously. Therefore, these equations do not allow the coexistence of two cylinders with different radii.

5.6.6 SPONTANEOUS AND FORCE-INDUCED TUBULATION

To proceed, let us now consider a vesicle as shown in Figures 5.5 and 5.27 that has the shape of a large sphere with radius R_{sp} and a cylindrical tube with radius R_{cy} and length L_{cy} . As in the case of necklace-like tubes, we must distinguish cylindrical in-tubes as in Figure 5.27a from cylindrical out-tubes as in Figure 5.27b. To study the interplay of spontaneous and force-induced tubulation, a locally applied external force will be included that acts at the tip of the cylinder as shown in Figure 5.27. The force f is taken to be positive and negative if it points towards the exterior and interior aqueous solution, respectively, see Figure 5.27 (this convention is different from the one used in (Lipowsky, 2013), where f described the absolute value of the pulling force for both pulling directions). As shown in (Lipowsky, 2013), minimization with respect to R_{cy} and L_{cy} then leads to two equations that have the same form as Eqs 5.197 and 5.199 but with the spontaneous curvature m replaced by the composite curvature

$$m_{com} \equiv m + \frac{f}{4\pi\kappa} \quad (5.200)$$

which represents the superposition of the spontaneous curvature m and the rescaled pulling force $f/(4\pi\kappa)$.

Next, we take into account that the cylindrical tubes emanate from a giant spherical vesicle as in Figure 5.27. The different membrane segments that form the tubes and the giant vesicle experience the same pressure difference ΔP and the same membrane tension $\hat{\Sigma}$. These two quantities are related to the mean curvature of the giant vesicle via the Euler-Lagrange equation

$$\Delta P = 2\hat{\Sigma}M_{sp} - 4\kappa m M_{sp}^2$$

as given by Eq. 5.70 with $M_{sp} = 1/R_{sp}$.

If we insert the expressions Eqs 5.197 and 5.199 for the cylinder, with m replaced by m_{com} , into the Euler-Lagrange Eq. 5.70 for

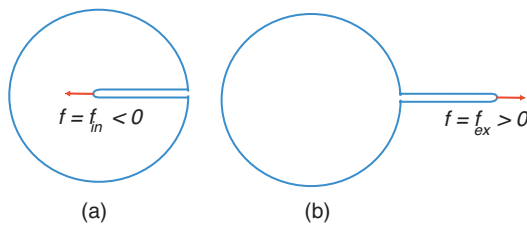


Figure 5.27 Giant vesicles with cylindrical nanotubes formed by spontaneous or force-induced tubulation: (a) Cylindrical in-tube in the presence of a pulling force $f = f_{in}$ that points towards the interior solution; and (b) Cylindrical out-tube in the presence of a pulling force $f = f_{ex}$ that points towards the exterior solution. The pulling forces f_{in} and f_{ex} are taken to be negative and positive, respectively.

the sphere, we obtain a cubic equation for the mean curvature M_{cy} which has the form (Lipowsky, 2013)

$$g(M_{cy}) = 0 \quad (5.201)$$

with the polynomial

$$g(x) \equiv 4x^3 - (4m_{com} + 3M_{sp})x^2 + 4m_{com}M_{sp}x - mM_{sp}^2. \quad (5.202)$$

A cylindrical nanotube that emanates from a large mother vesicle must have a radius R_{cy} that is much smaller than the radius R_{sp} of the large mother vesicle. This separation of length scales is corroborated by the experimental observations, compare Figure 5.21b, and implies that the curvature $|M_{cy}| = 1/(2R_{cy})$ of the cylindrical tube is much larger than the curvature $M_{sp} = 1/R_{sp}$ of the giant vesicle. In this limit, the cubic equation Eq. 5.201 has the solution

$$M_{cy} \approx m_{com} - \frac{1}{4R_{sp}} = m + \frac{f}{4\pi\kappa} - \frac{1}{4R_{sp}} \quad \text{for } R_{sp} \gg R_{cy}. \quad (5.203)$$

Therefore, to leading order, the mean curvature of the cylindrical nanotube is equal to the composite curvature $m_{com} = m + f/(4\pi\kappa)$. For spontaneous tubulation with $f = 0$, the relation Eq. 5.203 also implies that the limit of large R_1/R_{cy} is equivalent to the limit of large $|m|R_1$ which is of the same order of magnitude as $|\bar{m}| = |m|R_{ve}$.

Composite curvature and total membrane tension

Alternatively, we may also combine the Euler-Lagrange Eq 5.70 for the large sphere with the Euler-Lagrange Eq. 5.195 for the cylindrical nanotube to eliminate only the pressure difference. In the limit of giant vesicles, we then obtain the asymptotic equality

$$M_{cy} \approx \pm \sqrt{\hat{\Sigma}/(2\kappa)} - \frac{1}{2R_{sp}} \quad \text{for } |m| \gg 1/R_{sp} \quad (5.204)$$

with the total membrane tension $\hat{\Sigma} = \Sigma + \sigma = \Sigma + 2\kappa m^2$ as in Eq. 5.26, where the plus and minus sign in Eq. 5.204 applies to out- and in-tubes, respectively. Note that the latter relation does not depend explicitly on the locally applied force f . A combination of the two asymptotic equalities Eqs 5.203 and 5.204 then leads to the relation

$$m_{com} = m + \frac{f}{4\pi\kappa} \approx \pm \sqrt{\hat{\Sigma}/(2\kappa)} - \frac{1}{4R_{sp}} \quad \text{for } R_{sp} \gg R_{cy} \quad (5.205)$$

between the spontaneous curvature m , the locally applied force f , and the total membrane tension $\hat{\Sigma} = \Sigma + \sigma$ which includes the spontaneous tension $\sigma = 2\kappa m^2$ and, thus, depends on the spontaneous curvature m as well.

It is also possible to pull both out- and in-tubes via an optical trap from the same aspirated GUV (Dasgupta and Dimova, 2014; Dasgupta et al., 2018). One can then measure the two forces f_{ex} and f_{in} that generate out- and in-tubes for the same aspiration

pressure and, thus, for the same mechanical membrane tension Σ . Both cases are described by Eq. 5.205 with f replaced by f_{ex} for the plus sign and by f_{in} for the minus sign. The sum of these two relations leads to the simple expression

$$m \approx -\frac{f_{\text{ex}} + f_{\text{in}}}{8\pi\kappa} - \frac{1}{4R_{\text{sp}}} \quad (R_{\text{sp}} \gg R_{\text{cy}}) \quad (5.206)$$

for the spontaneous curvature m . The term $-1/(4R_{\text{sp}})$ represents again a small correction term because $|m| \gg 1/R_{\text{sp}}$ as in Eq. 5.204. Therefore, one can determine the spontaneous curvature m by measuring the forces f_{ex} and f_{in} , irrespective of the membrane tension. For symmetric bilayers as studied in (Dasgupta and Dimova, 2014), the spontaneous curvature vanishes and the relation Eq. 5.206 implies that $f_{\text{in}} = -f_{\text{ex}}$. For GUVs containing a binary mixture of POPC and GM1, on the other hand, the out- and in-pulling forces, f_{ex} and f_{in} , were observed to have different magnitudes, i.e., $f_{\text{in}} \neq -f_{\text{ex}}$ which implies a nonzero spontaneous curvature (Dasgupta et al., 2018).

Total membrane tension and aspiration tension

The relationship between the composite curvature and the total membrane tension as given by Eq. 5.205 depends on the total membrane tension $\hat{\Sigma}$. In some experimental studies of force-induced out-tubes, (Sorre et al., 2012; Simunovic et al., 2015) the relation in Eq. 5.205 was used with the total membrane tension $\hat{\Sigma}$ replaced by the aspiration tension Σ_{asp} as obtained from the spherical end cap of the membrane tongue within the micropipette. Thus, consider the membrane tongue of a GUV that is aspirated by a cylindrical micropipette with radius R_{pip} . The spherical end cap of this tongue has the mean curvature $M_{\text{to}} \leq 1/R_{\text{pip}}$ which increases initially from the value $M_{\text{to}} = 1/R_{\text{ve}}$, i.e., the mean curvature of the initial mother vesicle, up to $M_{\text{to}} = 1/R_{\text{pip}}$ and then remains constant during further aspiration. Thus, it is useful to distinguish *initial* aspiration with $1/R_{\text{ve}} < M_{\text{to}} < 1/R_{\text{pip}}$ from *prolonged* aspiration with $M_{\text{to}} = 1/R_{\text{pip}}$.

If the pressures within the interior vesicle compartment and within the pipette are denoted by P_{in} and P_{pip} , the spherical end cap of the tongue is then described by the shape equation

$$P_{\text{in}} - P_{\text{pip}} = 2\hat{\Sigma}M_{\text{to}} - 4\kappa mM_{\text{to}}^2 \quad (5.207)$$

as follows from Eq. 5.70 for spherical segments with M_{sp} replaced by M_{to} . In addition, the spherical mother vesicle with curvature radius R_{sp} and mean curvature $M_{\text{sp}} = 1/R_{\text{sp}}$ leads to the second shape equation

$$P_{\text{in}} - P_{\text{ex}} = 2\hat{\Sigma}M_{\text{sp}} - 4\kappa mM_{\text{sp}}^2$$

as in Eq. 5.70. Subtracting the latter equation from Eq. 5.207, we obtain the suction pressure

$$P_{\text{ex}} - P_{\text{pip}} = 2[M_{\text{to}} - M_{\text{sp}}] \left[\hat{\Sigma} - 2\kappa m(M_{\text{to}} + M_{\text{sp}}) \right]. \quad (5.208)$$

Note that the suction pressure $P_{\text{ex}} - P_{\text{pip}}$ vanishes for $M_{\text{to}} = M_{\text{sp}}$ which corresponds to the initial contact between GUV and pipette.

Solving Eq. 5.208 for the total membrane tension $\hat{\Sigma}$, we obtain

$$\hat{\Sigma} = \Sigma_{\text{asp}} + \Delta\hat{\Sigma} \quad (5.209)$$

with the aspiration tension

$$\Sigma_{\text{asp}} \equiv \frac{P_{\text{ex}} - P_{\text{pip}}}{2(M_{\text{to}} - M_{\text{sp}})} \quad \text{for } M_{\text{to}} > M_{\text{sp}} \quad (5.210)$$

and the additional tension term

$$\Delta\hat{\Sigma} \equiv 2\kappa m(M_{\text{sp}} + M_{\text{to}}). \quad (5.211)$$

When the mean curvature M_{to} of the tongue's end cap has reached its maximal value $1/R_{\text{pip}}$, the aspiration tension and the additional tension term become

$$\Sigma_{\text{asp}} = \frac{(P_{\text{ex}} - P_{\text{pip}})R_{\text{pip}}}{2(1 - R_{\text{pip}}/R_{\text{sp}})} \quad (5.212)$$

and

$$\Delta\hat{\Sigma} = 2\kappa m(M_{\text{sp}} + 1/R_{\text{pip}}). \quad (5.213)$$

The expression in Eq. 5.212 has been widely used to obtain the aspiration tension from micropipette experiments by controlling the suction pressure $P_{\text{ex}} - P_{\text{pip}}$ and by measuring the pipette radius R_{pip} as well as the radius R_{sp} of the mother vesicle by optical microscopy. The approximation used in (Sorre et al., 2012; Simunovic et al., 2015; Dasgupta et al., 2018) was to ignore the additional tension term $\Delta\hat{\Sigma}$ and to replace the total tension $\hat{\Sigma}$ in Eq. 5.205 by the aspiration tension Σ_{asp} as given by Eq. 5.212.

The accuracy of this approximation depends on the magnitude of the suction pressure and of the spontaneous curvature. As an example, let us consider a GUV membrane with bending rigidity $\kappa = 10^{-19}$ J and spontaneous curvature $m = \tilde{m}/\mu\text{m}$ and let us assume that the GUV is aspirated by a micropipette of radius $R_{\text{pip}} = 3 \mu\text{m}$ and then forms a larger spherical segment of radius $R_{\text{sp}} = 6 \mu\text{m}$. The additional tension term $\Delta\hat{\Sigma}$ then has the magnitude $2\kappa m(M_{\text{sp}} + 1/R_{\text{pip}}) = 0.1\tilde{m} \mu\text{N}/\text{m}$ which is equal to $1 \mu\text{N}/\text{m}$ for $\tilde{m} = 10$ or $m = 1/(100 \text{ nm})$. This inaccuracy should be compared to the smallest values of the aspiration tension which are also of the order of $1 \mu\text{N}/\text{m}$ for the considered geometry, corresponding to the smallest accessible suction pressures of about 1 Pa. Therefore, we conclude that the additional tension term $\Delta\hat{\Sigma}$ should *not* be neglected if the spontaneous curvature is large and/or if the suction pressure is small.

Dominance of spontaneous tension

In the absence of locally applied pulling forces, the total tension $\hat{\Sigma} = \Sigma + \sigma$ of a cylindrical nanotube is given by the relation Eq. 5.198, which depends on the bending rigidity κ , the spontaneous curvature m , and the tube's mean curvature M_{cy} . Inserting the asymptotic equality Eq. 5.203 for M_{cy} with $f = 0$ into Eq. 5.198, the total tension becomes

$$\hat{\Sigma} \approx 2\kappa m^2 + \frac{\kappa m}{R_{sp}} = \sigma \left(1 + \frac{1}{mR_{sp}} \right) \quad \text{for large } |m| R_{sp} \quad (5.214)$$

with the spontaneous tension $\sigma = 2\kappa m^2$. It then follows that the total membrane tension is again dominated by the spontaneous tension and that the mechanical tension $\Sigma = \hat{\Sigma} - \sigma$ behaves as (Lipowsky, 2013)

$$\Sigma \approx \frac{\kappa m}{R_{sp}} = \frac{1}{2mR_{sp}} \sigma = \pm \frac{R_{cy}}{R_{sp}} \sigma \quad \text{for large } |m| R_{sp} \quad (5.215)$$

where the plus and minus sign applies to out- and in-tubes, respectively. Thus, in the limit of large R_{sp}/R_{cy} or large $R_{sp} |m| \simeq |\bar{m}|$ corresponding to large spherical segments or narrow tubes, the total tension $\hat{\Sigma}$ approaches the spontaneous tension σ whereas the mechanical tension goes to zero as $\Sigma \approx \kappa m/R_{sp}$.

It is interesting to note that the relation Eq. 5.215 is equivalent to $1/R_{sp} \approx \Sigma/(\kappa m)$. A combination of this latter relation with Eq 5.203 leads to

$$M_{cy} \approx m - \frac{\Sigma}{4\kappa m} \quad \text{for } R_{sp} \gg R_{cy} \text{ and } f = 0. \quad (5.216)$$

Thus, for fixed values of the curvature-elastic parameters κ and m , an increase in the mechanical membrane tension Σ leads to a reduction of $|M_{cy}|$ and, thus, to an increase in the tube radius R_{cy} . This conclusion, which applies to both $m > 0$ and $m < 0$, is somewhat counterintuitive but also follows from the quadratic expression Eq. 5.199 for the mechanical tension Σ as a function of M_{cy} . A closer look at this latter expression reveals that cylindrical tubes do not exist for

$$\Sigma > \Sigma_{\max} \equiv \frac{2}{3} \kappa m^2 = \frac{\sigma}{3} \quad (\text{no cylindrical tubes}). \quad (5.217)$$

Furthermore, starting from a cylinder with $M_{cy} = m$, corresponding to $\Sigma = 0$ and zero bending energy, an increase in the mechanical tension Σ decreases the mean curvature $|M_{cy}|$ and increases the cylinder radius $R_{cy} = 1/(2|M_{cy}|)$ until we reach $\Sigma = \Sigma_{\max} = \sigma/3$ corresponding to a cylindrical tube with mean curvature $M_{cy} = 2|m|/3$ and radius $R_{cy} = 3/(4|m|)$.

5.6.7 NECKLACE-TO-CYLINDER TRANSFORMATIONS

As shown in Figure 5.21b, necklace-like and cylindrical nanotubes have been observed to coexist on the same vesicle. These observations can be understood from the competition of different energy contributions which favor necklace-like tubes below a certain critical tube length but cylindrical tubes above this length (Lipowsky, 2013; Liu et al., 2016). At the critical tube length, the necklace-like tube transforms into a cylindrical one. Such a transformation can proceed in a continuous manner *via* intermediate unduloids as shown in Figure 5.28.

The existence of a critical tube length can be understood intuitively from the following simple argument (Lipowsky, 2013). If the membrane has spontaneous curvature m , a necklace-like

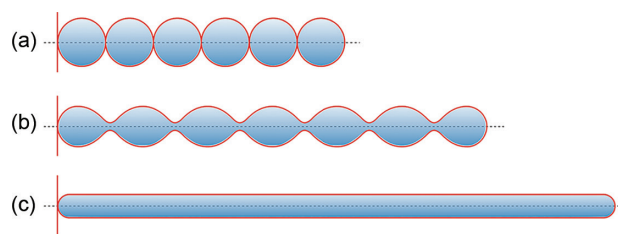


Figure 5.28 Low energy transformation of a necklace-like tube into a capped cylinder: All three tubes have the same surface area and, apart from the end caps, the same mean curvature M which is equal to the spontaneous curvature m . (a) Necklace-like tube L_0^0 with vanishing bending energy consisting of six spherules connected by closed membrane necks. The spherules have the radius $R_2 = 1/|m|$ and mean curvature $M = -1/R_2 = m$; (b) Capped unduloid with neck radius R_{ne} , bulge radius R_{bu} , and mean curvature $M = -1/(R_{ne} + R_{bu}) = m$; and (c) Capped cylinder with radius $R_{cy} = 1/(2|m|)$ and mean curvature $M = -1/(2R_{cy}) = m$. The transformation of the sphere-necklace into the cylinder proceeds via a continuous family of intermediate unduloids. During this transformation, the tube volume is reduced by a factor 3/4. If we ignore the end caps of the unduloids in (b) and the cylinder in (c), both types of tubes have zero bending energy as does the necklace-like tube in (a). (Reproduced with permission from Liu, Y. et al., ACS Nano, 10, 463–474, 2016.)

tube consisting of spherules with radius $R_2 = 1/|m|$ connected by closed membrane necks has vanishing bending energy. For a cylindrical tube with radius $R_{cy} = 1/(2|m|)$, the main body of the cylinder also has vanishing bending energy but such a tube must be closed by two end caps which have the finite bending energy $2\pi\kappa$. Therefore, the bending energy of the end caps disfavors the cylindrical tube. On the other hand, the necklace-like tube has a larger volume compared to the cylindrical one and the osmotic pressure difference across the membranes acts to compress the tubes when they protrude into the interior solution within the vesicles. Therefore, such a tube can lower its free energy by reducing its volume which favors the cylindrical tube. The volume work is proportional to the tube length whereas the bending energy of the end caps is independent of this length. The competition between these two energies then implies that short tubes are necklace-like whereas long tubes are cylindrical.

The same conclusion is obtained by minimizing the bending energy of the whole vesicle membrane (Liu et al., 2016). One then finds that, for fixed vesicle volume and membrane area, the mother vesicle has a smaller bending energy when it forms a cylindrical tube and that this energy decrease of the mother vesicle overcompensates the bending energy increase from the end caps of the cylinder when the tube is sufficiently long. The critical tube length at which the necklace-like tube transforms into a cylindrical one is about three times the vesicle radius.

5.7 ADHESION OF VESICLES

When a vesicle is in contact with an adhesive substrate surface as in Figure 5.29, it can gain adhesion energy by spreading onto this surface but must then increase its bending energy to adapt its shape to the adhesive surface. For large vesicles, the adhesion energy must dominate because it is proportional to the contact area of the vesicle and thus grows quadratically with the size of the vesicle whereas the increased bending energy is concentrated

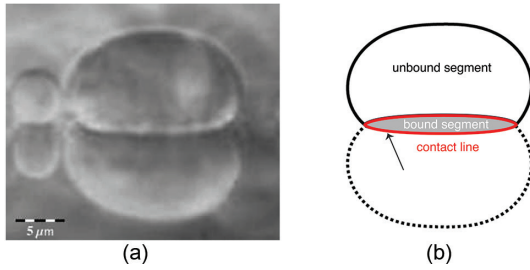


Figure 5.29 (a) Optical micrograph of two vesicles adhering to a pure glass surface that reflects the light and creates two mirror images; and (b) Shape of the larger vesicle consisting of a bound (gray region) and an unbound (white region) membrane segment. The two segments join along the contact line (red) which represents the boundary of the bound membrane segment. (Reproduced with permission from Gruhn, T. et al., *Langmuir*, 23, 5423–5429, 2007. Copyright 2007 American Chemical Society.)

along the contact line of the vesicle with the surface and thus grows only linearly with the size of the vesicle.

Within the contact area, the membrane experiences a variety of molecular forces. In order to study the overall shape of the adhering vesicle, one may ignore the molecular details and focus on the adhesive strength $|W|$ of the membrane-surface interactions which corresponds to the adhesion (free) energy per area (Seifert and Lipowsky, 1990). This coarse-grained description of the membrane-surface interactions in terms of the single parameter $|W|$ is consistent with the separation of length scales that has been used to construct the different curvature models.

Because the bound and the unbound membrane segments are exposed to different environments and, thus, to different molecular interactions, they can differ in their molecular composition and, thus, in their curvature-elastic properties (Rouhiparkouhi et al., 2013; Lipowsky et al., 2013; Lipowsky, 2014b). In order to reduce the number of parameters, we will first assume that this ambience-induced segmentation of the vesicle membranes can be ignored and that the bound and unbound membrane segments have the same curvature-elastic properties. Adhesion-induced segmentation of multi-component membranes will be discussed at the end of this section and at the end of Section 5.8.

Furthermore, we will again focus on the spontaneous curvature model which depends on only two dimensionless parameters, the volume v and the spontaneous curvature \bar{m} . When we parametrize the adhesion energy in terms of the dimensionless adhesive strength $|w|$ proportional to $|W|/\kappa$, vesicles adhering to planar surfaces are described by only three parameters. On the one hand, this parametrization is convenient from a theoretical point of view because it allows us to explore large regions of the parameter space. On the other hand, the additional parameter $|W|$ can be directly deduced from experimental observations of adhering vesicles. At the end of this section, more complex adhesion geometries will be briefly discussed corresponding to curved and/or chemically patterned substrate surfaces. The extension of the theory described here to the interactions of membranes with adhesive nanoparticles is described in Chapter 8 of this book. The experimental methods used to study the adhesion of GUVs are reviewed in Chapter 17.

5.7.1 INTERPLAY OF ADHESION AND BENDING

First, let us consider a planar substrate surface and focus on the competition between bending rigidity κ and adhesive strength $|W|$ for the simple case of a vesicle that is free to adapt its volume, corresponding to the osmotic pressure difference $\Delta P = 0$, and is bounded by a symmetric membrane with vanishing spontaneous curvature, $m = 0$. We are then left with only three dimensionful parameters, the membrane area A , the bending rigidity κ , and the adhesive strength $|W|$.

The non-adhering or free vesicle forms a spherical shape S_{fr} with bending energy $\mathcal{E}_{bc}\{S_{fr}\} = 8\pi\kappa$. When the vesicle membrane spreads onto an adhesive surface, the vesicle attains the shape S_{ad} with contact area A_{bo} of the bound membrane segment and gains the adhesion energy

$$E_{ad} \equiv -|W| A_{bo}. \quad (5.218)$$

For a planar surface, this adhesion energy is the only energy contribution from the bound membrane segment. The unbound membrane segment, on the other hand, has to adapt its shape to the presence of the substrate surface which leads to the bending energy increase

$$\Delta E_{bc} = \mathcal{E}_{bc}\{S_{ad}\} - \mathcal{E}_{bc}\{S_{fr}\} = 8\pi\kappa \Delta \bar{E}_{bc}. \quad (5.219)$$

Adhesion is favored if

$$E_{ad} + \Delta E_{bc} < 0 \quad \text{or} \quad 8\pi\kappa \Delta \bar{E}_{bc} < |W| A_{bo}. \quad (5.220)$$

Because $\Delta \bar{E}_{bc}$ is a dimensionless number, we can immediately conclude from this relation that the vesicle adheres to the surface if the adhesive strength $|W|$ is sufficiently large or if the bending rigidity κ is sufficiently small.

In general, the adhesion of vesicles involves three additional parameters: the osmotic conditions that determine the volume-to-area ratio, the spontaneous curvature m of asymmetric bilayers, and the mean curvature M_{bo} of the bound membrane segment arising from a curved adhesive surface. In order to take these additional parameters into account, we need a systematic theory based on an appropriate energy functional.

5.7.2 THEORY OF VESICLE ADHESION

The shape S of a vesicle that adheres to a rigid substrate surface can be decomposed into two membrane segments, a bound segment with shape S_{bo} in contact with the surface and an unbound segment with shape S_{un} not in contact with this surface. The total membrane area A can then be decomposed according to

$$A = A_{bo} + A_{un} = \mathcal{A}\{S_{bo}\} + \mathcal{A}\{S_{un}\} \quad (5.221)$$

where $A_{bo} = \mathcal{A}\{S_{bo}\}$ and $A_{un} = \mathcal{A}\{S_{un}\}$ are the partial areas of the bound and unbound membrane segments S_{bo} and S_{un} , respectively. In general, the two partial areas also depend on the shape of the adhesive surface. The combined bending and adhesion energy of the vesicle leads to the energy functional (Seifert and Lipowsky, 1990)

$$\mathcal{E}_{AV}\{\mathcal{S}\} = 2\kappa \int dA (M - m)^2 + \mathcal{E}_{ad}\{\mathcal{S}\} \quad (5.222)$$

with the adhesion (free) energy functional

$$\mathcal{E}_{ad}\{\mathcal{S}\} = -|W| \mathcal{A}\{\mathcal{S}_{bo}\} \quad (5.223)$$

where the subscript “AV” stands for “adhering vesicle.” The first term on the right hand side of Eq. 5.222, which represents the bending energy functional of the spontaneous curvature model, can be decomposed into the bending energies of the unbound and the bound membrane segments according to

$$\mathcal{E}_{be}\{\mathcal{S}\} = 2\kappa \int dA_{un} (M - m)^2 + 2\kappa \int dA_{bo} (M_{bo} - m)^2 \quad (5.224)$$

where the mean curvature M_{bo} of the bound segment is imposed onto the latter segment by the shape of the rigid substrate.

The stationary states of the adhering vesicle are then obtained by minimizing the shape functional

$$\mathcal{F}_{AV}\{\mathcal{S}\} = -\Delta P \mathcal{V}\{\mathcal{S}\} + \Sigma \mathcal{A}\{\mathcal{S}\} + \mathcal{E}_{AV}\{\mathcal{S}\} \quad (5.225)$$

with the constraints that $\mathcal{V}\{\mathcal{S}\} = V$ and $\mathcal{A}\{\mathcal{S}\} = A$ where V and A are the prescribed vesicle volume and membrane area as before. It is important to note that the value of the contact area A_{bo} of the bound membrane segment is not prescribed here which implies that the contact line is not pinned but free to find its optimal position.

Additional parameters related to adhesion

As before, it is again convenient to choose the vesicle size $R_{ve} = \sqrt{A/(4\pi)}$ as the basic length scale and the bending rigidity κ as the basic energy scale. The shape of the adhering vesicle then depends on the dimensionless volume $v = 6\sqrt{\pi}V/A^{3/2}$ and on the dimensionless spontaneous curvature $\bar{m} = mR_{ve}$, both of which also determine the shape of free vesicles. In addition, the adhering shape also depends on the dimensionless adhesion strength

$$|w| \equiv |W| R_{ve}^2 / \kappa \quad (5.226)$$

and on the dimensionless curvatures $\bar{M}_{bo} = M_{bo}R_{ve}$ that the substrate surface imposes on the bound membrane segment.

The simplest substrate geometry is provided by a planar surface with $M_{bo} = 0$ which reduces the parameter space to the three dimensionless parameters v , \bar{m} , and $|w|$. The next-to-simplest substrate geometry is obtained for constant-mean-curvature surfaces such as spherical surfaces or cavities. In the latter case, the mean curvature \bar{M}_{bo} of the bound membrane segment is constant and the parameter space becomes four-dimensional. In the following subsections, we will first discuss the planar case and subsequently summarize the modifications arising from spherical surfaces and cavities.

5.7.3 VESICLES ADHERING TO PLANAR SURFACES

Contact curvature and contact mean curvature

For a planar substrate surface as in Figure 5.29, the bound membrane segment of the adhering vesicle is planar as well. We require the bound and the unbound membrane segments to join along

the contact line in a smooth manner, i.e., that the two membrane segments have a common tangent plane or, equivalently, that the normal vector of the unbound membrane segment is also normal to the planar substrate along the contact line. In other words, the membrane shape should not exhibit any kink along the contact line. This geometric requirement is equivalent to the condition that the membrane has a finite bending energy (Seifert and Lipowsky, 1990).

Because the normal vector is required to vary continuously across the contact line, the principal curvature $C_{\parallel co}$ tangential to the contact line vanishes. In addition, the principal curvature $C_{\perp co}$ of the unbound membrane segment perpendicular to the contact line is given by

$$C_{\perp co} = \sqrt{2|W|/\kappa} \quad (5.227)$$

as follows from the first variation of the shape functional Eq 5.225, both for axisymmetric (Seifert and Lipowsky, 1990) and for non-axisymmetric (Deserno et al., 2007) shapes. Therefore, the contact mean curvature becomes

$$M_{co} = \frac{1}{2}(C_{\parallel co} + C_{\perp co}) = \frac{1}{2}C_{\perp co} = \sqrt{|W|/(2\kappa)} \quad (\text{planar substrate}). \quad (5.228)$$

Because the mean curvature of the bound segment vanishes, the mean curvature of the membrane jumps from $M = M_{co}$ to $M = 0$ when we cross the planar contact line.

It is interesting to note that the contact mean curvature M_{co} does not depend on the spontaneous curvature m , which is somewhat counterintuitive. This m -independence also applies when the vesicle adheres to a curved surface, see further below. However, the shape and the contact area of an adhering vesicle do depend quite significantly on the spontaneous curvature (Agudo-Canalejo and Lipowsky, in preparation).

One should also note that the principal curvature $C_{\perp co}$ jumps along the contact line from $C_{\perp co} = 0$ within the bound membrane segment to $C_{\perp co} = \sqrt{2|W|/\kappa}$ within the unbound segment. Likewise, as mentioned, the mean curvature jumps from $M = 0$ within the bound membrane segment to $M = M_{co}$ within the unbound segment. In the following sections, we will see that analogous curvature discontinuities are also present along domain boundaries separating two intramembrane domains and along three phase contact lines arising from membrane wetting.

Adhesion length

The contact mean curvature $M_{co} = \sqrt{|W|/(2\kappa)}$ as given by Eq 5.228 is a material parameter that directly encodes the competition between membrane bending as governed by the bending rigidity κ and membrane-surface adhesion as described by the adhesive strength $|W|$. For planar substrate surfaces as considered here, the inverse of the contact mean curvature is equal to the adhesion length

$$R_W \equiv \sqrt{2\kappa/|W|} = \sqrt{2/|w|} R_{ve}. \quad (5.229)$$

Table 5.2 Five combinations of lipid bilayers and adhesive materials, with estimates of the bending rigidity κ , the adhesive strength $|W|$, and the adhesion length R_W ; see Appendix 1 of the book for structure and data on the lipids

ADHESION REGIME	LIPID BILAYER	ADHESIVE MATERIAL	κ [10^{-19} J]	$ W $ [mJ/m ²]	R_W [nm]
Strong	DMPC	Silica	0.8 ^a	0.5–1 ^b	13–18
Strong	EggPC	Glass	$\simeq 1$	0.15 ^c	26
Intermediate	DMPC	Receptor-ligand	0.8 ^a	0.03 ^d	73
Weak	DOPC/DOPG	Coated glass	0.4 ^e	3×10^{-4} ^e	510
Ultraweak	DOPC/DOPG	Glass	0.4 ^e	10^{-5} ^e	2800

^a Brüning, B.A. et al., *Biochim. Biophys. Acta*, 1838, 2412–2419, 2014.

^b Anderson, T.H. et al., *Langmuir*, 25, 6997–7005, 2009.

^c Schönherr, H. et al., *Langmuir*, 20, 11600–11606, 2004.

^d Moy, V.T. et al., *Biophys. J.*, 76, 1632–1638, 1999.

^e Gruhn, T. et al., *Langmuir*, 23, 5423–5429, 2007.

Depending on the lipid composition of the bilayer membrane and on the adhesive material, the adhesion length R_W can vary between about 10 nanometers for strong adhesion and a few micrometers for ultraweak adhesion as illustrated by the examples in Table 5.2. For the adhering vesicle displayed in Figure 5.29, the adhesion length was estimated to be $2.8 \mu\text{m}$ corresponding to the ultra-weak adhesion regime, see bottom row of Table 5.2. In this case, the contact curvature radius

$$R_{\perp\text{co}} \equiv 1/C_{\perp\text{co}} = \frac{1}{2}R_W = \sqrt{\kappa / (2|W|)} \quad (5.230)$$

can be directly read off from the optical image displayed in Figure 5.29a.

When the adhesion length becomes of the order of 10 nanometer as in the first two rows of Table 5.2, we start to “see” the molecular structure of the lipid bilayers. As a consequence, higher-order curvature terms as discussed in Section C.1 may start to play a role. On the other hand, the estimates in the latter section also imply that we can certainly ignore such terms for $R_W \gtrsim 80 \text{ nm}$.

Shapes of adhering vesicles

The shape of the unbound membrane segment of the adhering vesicle is obtained by solving the Euler-Lagrange Eq. 5.23 with the boundary condition as given by Eq. 5.228. If the shape is axisymmetric with respect to the normal vector of the planar surface, the Euler-Lagrange equation leads to a set of ordinary differential equations that can be solved numerically, see the examples in Figure 5.30 (Seifert and Lipowsky, 1990). In all panels of this figure, the membrane has the same area and the same bending rigidity as well as vanishing spontaneous curvature. In Figure 5.30a, we see the shapes of five vesicles that can freely adapt their volume corresponding to $\Delta P = 0$. The five vesicle shapes are obtained for five different values of the adhesive strength $|w|$.

Inspection of Figure 5.30a shows that the contact area of the bound membrane segment increases with increasing $|w|$ as one would expect intuitively. However, as we decrease the adhesive strength $|w|$, the contact area vanishes already at the threshold value

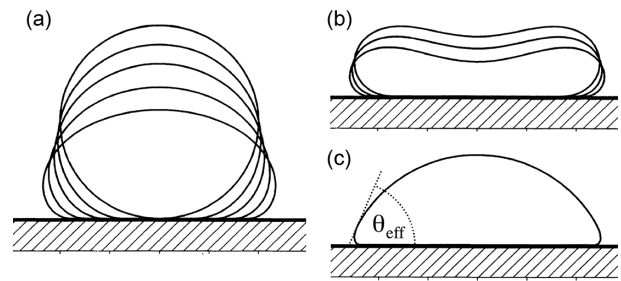


Figure 5.30 Vesicles with identical membrane area and vanishing spontaneous curvature adhering to substrate surfaces (shaded) with variable adhesive strength: (a) Vesicle shapes and five different values of the adhesive strength, $|w| = 2, 2.9, 4.1, 6.4,$ and 10.2 , in the absence of a volume constraint, corresponding to pressure difference $\Delta P = 0$. As $|w|$ decreases, so does the contact area of the bound membrane segment. The spherical shape with vanishing contact area is obtained for the finite value $|w| = 2$; (b) Adhering discocyte vesicles for different values of the adhesive strength $|w|$ and the pressure difference $\Delta P < 0$; and (c) In the strong adhesion regime with $|w| \gg 2$, the vesicle shape approaches a spherical cap, characterized by the effective (or apparent) contact angle θ_{eff} . (Reproduced from Seifert, U. and Lipowsky, R., *Phys. Rev., A* 42, 4768–4771, 1990.)

$$|w| = |w_{\text{ad}}| = 2 \quad (\Delta P = 0), \quad (5.231)$$

corresponding to the spherical shape in Figure 5.30a. Thus, the vesicle starts to spread over the substrate surface provided (Seifert and Lipowsky, 1990)

$$|w| = |W| R_{\text{ve}}^2 / \kappa > |w_{\text{ad}}| = 2 \quad \text{for } \Delta P = 0. \quad (5.232)$$

The relation $|w| > 2$ is equivalent to the intuitive relations

$$R_{\text{ve}} > R_W \quad \text{or} \quad A|W| > 8\pi\kappa \quad (\Delta P = 0), \quad (5.233)$$

i.e., the membrane starts to spread over the substrate surface when the vesicle size R_{ve} exceeds the adhesion length R_W . The latter criterion directly reflects the competition between the adhesive strength $|W|$ and the bending rigidity κ which favors and disfavors the onset of spreading, respectively.

The shapes in Figure 5.30a have been obtained for spontaneous curvature $m = 0$ but the threshold value $|w_{\text{ad}}| = 2$

or $|W_{ad}| = 2\kappa / R_{ve}^2$ should apply as long as the spherical shape of the free vesicle remains stable. Because a sphere with $\Delta P = 0$ is stable for $m < 3/R_{ve}$, the threshold value $|w_{ad}| = 2$ for the onset of spreading is expected to apply for this range of m -values as well. This expectation is confirmed by numerical energy minimization for axisymmetric shapes (Agudo-Canalejo and Lipowsky, in preparation). The latter calculations also show that the contact area increases with increasing spontaneous curvature $m > 0$ even though the contact mean curvature M_{co} does not depend on m .

If the vesicle volume is constrained by the osmotic conditions, the spreading of the vesicle membrane onto the adhesive surface sets in for (Lipowsky and Seifert, 1991)

$$|W| > |w_{ad}(v)|\kappa / R_{ve}^2 \quad (5.234)$$

where the dimensionless parameter $|w_{ad}|$ depends on the dimensionless volume v , approaches the value $|w_{ad}(v)| \approx 2$ for small $1 - v$, and stays of order one for arbitrary values of v . For an ensemble of vesicles with different sizes, the relation Eq. 5.234 implies that large vesicles with

$$R_{ve} > \sqrt{|w_{ad}(v)|\kappa / |W|} \quad (\text{bound vesicle}) \quad (5.235)$$

adhere to the adhesive surface whereas small vesicles do not. This difference in the size distribution of bound and free vesicles should be accessible to experiment.

General criterion for the onset of adhesion

The contact mean curvature M_{co} characterizes the membrane shape along the contact line between the bound and unbound membrane segment as described by Eq. 5.228. It turns out that this curvature also provides a general stability criterion for the onset of adhesion, i.e., for the initial spreading of the membrane onto the adhesive surface. This criterion is based on the comparison between the contact mean curvature M_{co} and the mean curvature M_{ms} of the membrane segment that comes initially into contact with the adhesive surface. Indeed, the membrane segment starts to spread onto the adhesive surface if (Agudo-Canalejo and Lipowsky, 2015a,b)

$$M_{ms} < M_{co} \quad (\text{onset of adhesion}), \quad (5.236)$$

i.e., if the mean curvature M_{ms} of the adjacent membrane segment is smaller than the contact mean curvature M_{co} .

For a spherical vesicle with radius R_{ve} , all membrane segments have the same mean curvature, $M_{ms} = 1/R_{ve}$. Furthermore, for a planar surface as considered here, the contact mean curvature is given by $M_{co} = \sqrt{|W|} / (2\kappa)$ as in Eq 5.228. The general criterion Eq. 5.236 then assumes the form $|W| > 2\kappa / R_{ve}^2$ or $|w| > 2$ in agreement with the inequality Eq. 5.232. The general criterion for the onset of adhesion as given by Eq. 5.236 will be discussed further below for the adhesion of vesicles to spherical beads and cavities, and plays a prominent role for the engulfment of nanoparticles, see Chapter 8 of this book.

Strong adhesion regime and effective contact angle

The strong adhesion regime corresponds to the situation in which the adhesion length R_W is much smaller than the vesicle size, i.e.,

$$R_{ve} \gg R_W \quad \text{or} \quad |W|A \gg 8\pi\kappa \quad \text{or} \quad |w| \gg 2. \quad (5.237)$$

For a given value of the adhesion strength $|W|$, the strong adhesion regime corresponds to the limit of small bending rigidity κ . Thus, the limiting case $R_W/R_{ve} = 0$ can be obtained for a hypothetical membrane with vanishing bending rigidity $\kappa = 0$. In this limit, the shape functional Eq. 5.225 for the adhering vesicle reduces to

$$\mathcal{F}_{AV}\{S\} = -\Delta P V\{S\} + \Sigma \mathcal{A}\{S\} - |W| \mathcal{A}\{S_{bo}\} \quad (5.238)$$

with the bound membrane segment S_{bo} . The shape functional in (5.238) is identical with the shape functional of a liquid droplet in contact with a planar surface (Lipowsky et al., 2005). This shape functional for $\kappa = 0$ is minimized by vesicle shapes which correspond to spherical caps in complete analogy to liquid droplets.

For $\kappa = 0$, the contact curvature radius R_{co} vanishes, and the vesicle forms a sharp “microscopic” contact angle with the surface along the contact line. For $\kappa > 0$ but small R_{co}/R_{ve} , the shape of the vesicle consists of a spherical cap, a strongly curved membrane segment along the contact line, and a bound membrane segment with area $A_{bo} < \frac{1}{2}A$. The strongly curved membrane segment has a mean curvature of the order of $M_{co} = (|W|/2\kappa)^{1/2}$ and provides the connection between the unbound spherical cap and the bound membrane segment. On length scales which are large compared to $1/M_{co}$, the adhering vesicle can be characterized by an effective (or apparent) contact angle θ_{eff} as in Figure 5.30c (Seifert and Lipowsky, 1990). The effective contact angle does not represent a material parameter but is determined by the spherical cap geometry and the volume-to-area ratio v via the geometric relation

$$v = 2 \frac{[1 - \cos(\theta_{eff})]^{1/2} [2 + \cos(\theta_{eff})]}{[3 + \cos(\theta_{eff})]^{3/2}}. \quad (5.239)$$

Furthermore, in the strong adhesion regime corresponding to the limit of large $|w|$, the combined bending and adhesion energy $\bar{E}_{AV} \equiv E_{AV} / (8\pi\kappa)$ of the vesicle can be expanded in powers of the dimensionless adhesive strength $|w|$ (Lipowsky and Seifert, 1991; Tordeux et al., 2002; Steinkühler et al., 2016). One then finds

$$\bar{E}_{AV} \approx -\frac{1 + \cos\theta_{eff}}{2(3 + \cos\theta_{eff})} |w| + 2 \frac{1 - \sin(\theta_{eff}/2)}{\sqrt{3 + \cos\theta_{eff}}} \sqrt{|w|} \quad \text{for large } |w|. \quad (5.240)$$

When we rewrite this expression in terms of dimensionful parameters, we obtain

$$E_{AV} \approx -A_{bo} |W| + 8\sqrt{\pi} \frac{1 - \sin(\theta_{eff}/2)}{\sqrt{3 + \cos\theta_{eff}}} \sqrt{\kappa |W| A}. \quad (5.241)$$

The first-order term represents the adhesion energy of the bound membrane segment with area

$$A_{\text{bo}} = \frac{1 + \cos \theta_{\text{eff}}}{3 + \cos \theta_{\text{eff}}} A. \quad (5.242)$$

The second-order term in Eq. 5.241 is proportional to

$$\sqrt{\kappa |W| A} \sim R_{\perp \text{co}} \sqrt{A_{\text{bo}}} \kappa M_{\text{co}}^2 \quad (5.243)$$

where the right hand side represents an estimate for the bending energy of the strongly curved membrane segment close to the contact line because this segment has an area of the order of $R_{\perp \text{co}} \sqrt{A_{\text{bo}}}$ and the mean curvature M_{co} . Therefore, the second-order term can be regarded as a line energy term that depends, however, on the effective contact angle θ_{eff} and, thus, on the volume-to-area ratio ν via the relation Eq. 5.239. In the absence of a volume constraint, i.e., for pressure difference $\Delta P = 0$, the strong adhesion regime leads to a pancake-like shape with $\theta_{\text{eff}} = 0$ and $A_{\text{bo}} = \frac{1}{2} A$. In this case, the expression Eq. 5.241 for the combined bending and adhesion energy simplifies and becomes

$$E_{\text{AV}} \approx -\frac{1}{2} A |W| + 4\sqrt{\pi} \sqrt{\kappa |W| A} \quad (5.244)$$

$$\text{for large } |w| = |W| R_{\text{vc}}^2 / \kappa.$$

5.7.4 MORE COMPLEX ADHESION GEOMETRIES

In the present subsection, we will discuss the contact mean curvature M_{co} for more complex adhesion systems as provided by curved surfaces and chemically patterned substrates.

Adhesion of vesicle to large spherical particle

When the vesicle adheres to a large spherical particle with radius R_{pa} , the bound membrane segment has the mean curvature $M_{\text{bo}} = -1/R_{\text{pa}}$ which implies the membrane curvature $C_{\parallel \text{co}} = -1/R_{\text{pa}}$ parallel to the contact line. Within the unbound membrane segment, the second principal curvature $C_{\perp \text{co}}$ perpendicular to the contact line is given by

$$C_{\perp \text{co}} = \sqrt{2|W|/\kappa} - 1/R_{\text{pa}} \quad (5.245)$$

as obtained by minimization of the bending energy (Seifert and Lipowsky, 1990). As a consequence, the contact mean curvature has the form

$$M_{\text{co}} = \frac{1}{2} (C_{\parallel \text{co}} + C_{\perp \text{co}}) = \left(\frac{|W|}{2\kappa} \right)^{1/2} - \frac{1}{R_{\text{pa}}} \quad (5.246)$$

or

$$M_{\text{co}} = \frac{1}{R_W} - \frac{1}{R_{\text{pa}}} \quad (\text{spherical particle of radius } R_{\text{pa}}) \quad (5.247)$$

where we used the definition of the adhesion length R_W as given by Eq. 5.229. The general criterion Eq. 5.236 for the onset of

membrane adhesion now assumes the form (Agudo-Canalejo and Lipowsky, 2015a)

$$M_{\text{ms}} < M_{\text{co}} = \frac{1}{R_W} - \frac{1}{R_{\text{pa}}} \quad (\text{adhesion to spherical particle}) \quad (5.248)$$

where M_{ms} is the mean curvature of the membrane segment that comes initially in contact with the particle. The contact mean curvature is positive for large particles with $R_{\text{pa}} > R_W$ and negative for small particles with $R_{\text{pa}} < R_W$.¹²

Note that the principal curvature $C_{\perp \text{co}}$ and the mean curvature M are again discontinuous along the contact line. The principal curvature $C_{\perp \text{co}}$ jumps from the value $C_{\perp \text{co}} = -1/R_{\text{pa}}$ within the bound membrane segment to the value $C_{\perp \text{co}} = \sqrt{2|W|/\kappa} - 1/R_{\text{pa}}$ within the unbound membrane segment. In fact, the curvature discontinuity as given by $\sqrt{2|W|/\kappa}$ is independent of the particle size and thus applies also to the limit of a large R_{pa} corresponding to a planar surface. Likewise, as we move across the contact line, the mean curvature jumps from $M = -1/R_{\text{pa}}$ within the bound membrane segment to $M = M_{\text{co}} = 1/R_W - 1/R_{\text{pa}}$. Therefore, the discontinuity of the mean curvature is always equal to the inverse adhesion length, irrespective of the particle size R_{pa} .

Adhesion of vesicle to large spherical cavity

When the vesicle adheres to a large spherical cavity with radius R_{cav} , the bound membrane segment has the mean curvature $M_{\text{bo}} = 1/R_{\text{cav}}$ which also applies to the membrane curvature $C_{\parallel \text{co}}$ parallel to the contact line. The membrane curvature $C_{\perp \text{co}}$ perpendicular to the contact line is given by

$$C_{\perp \text{co}} = \sqrt{2|W|/\kappa} + 1/R_{\text{cav}} \quad (5.249)$$

as obtained by minimization of the energy functional. As a consequence, the contact mean curvature now has the form

$$M_{\text{co}} = \frac{1}{2} (C_{\parallel \text{co}} + C_{\perp \text{co}}) = \left(\frac{|W|}{2\kappa} \right)^{1/2} + \frac{1}{R_{\text{cav}}} \quad (\text{spherical cavity of radius } R_{\text{cav}}). \quad (5.250)$$

It now follows from the general adhesion criterion Eq. 5.236 that a membrane segment with mean curvature M_{ms} starts to adhere to the cavity wall if

$$M_{\text{ms}} < M_{\text{co}} = \frac{1}{R_W} + \frac{1}{R_{\text{cav}}} \quad (\text{adhesion to a spherical cavity}) \quad (5.251)$$

with the adhesion length R_W as defined by Eq. 5.229. Therefore, as we move across the contact line, the mean curvature now jumps from $M = 1/R_{\text{cav}}$ within the bound membrane segment to $M = M_{\text{co}} = 1/R_W + 1/R_{\text{cav}}$ within the unbound membrane segment, with the curvature discontinuity being again equal to $1/R_W$.

¹² The limiting case with $M_{\text{ms}} = M_{\text{co}}$ can be further elucidated for nanoparticles with $R_{\text{pa}} \ll R_{\text{vc}}$, see Eq. 5.257 below.

Adhesion of vesicle to chemically patterned surface

Finally, let us consider the adhesion of vesicles to a planar but chemically structured surface which contains two types of surface domains, D_1 and D_2 . These two types of domains are characterized by two different adhesive strengths, W_1 and W_2 , with $|W_2| < |W_1|$, i.e., the D_2 domain is less adhesive than the D_1 domain.

If the contact line of an adhering vesicle is located *within* the D_1 domain, the contact mean curvature is given by

$$M_{\text{co}}^{[1]} = \left(\frac{|W_1|}{2\kappa} \right)^{1/2}. \quad (5.252)$$

Likewise, for a contact line within the D_2 domain, the contact mean curvature is

$$M_{\text{co}}^{[2]} = \left(\frac{|W_2|}{2\kappa} \right)^{1/2} < M_{\text{co},1}. \quad (5.253)$$

On the other hand, if a contact line segment (CLS) of the vesicle is pinned to the boundary between the two surface domains, the contact curvature radius $M_{\text{co}} = M_{\text{co}}^{\text{pin}}$ is not fixed but can vary within the range (Lipowsky et al., 2005)

$$M_{\text{co}}^{[2]} \leq M_{\text{co}}^{\text{pin}} \leq M_{\text{co}}^{[1]} \quad (\text{pinned CLS}). \quad (5.254)$$

This freedom of the contact mean curvature $M_{\text{co}}^{\text{pin}}$ along the boundaries of surface domains leads to transitions between different shapes of adhering vesicles (Lipowsky et al., 2005). One example is provided by a vesicle on a striped surface domain that is strongly adhesive and surrounded by another surface domain that is non-adhesive or only weakly adhesive. When the volume-to-area ratio ν is close to a sphere, the adhering vesicle has a fairly compact shape and a relatively small contact area. During deflation, the vesicle then undergoes a morphological transition from this compact shape to a thin tube-like state with a large contact area.

5.7.5 ENDOCYTOSIS OF NANOPARTICLES

The adhesion of nanoparticles to cell membranes represents the first step for the process of endocytosis which is essential for the cellular uptake of such particles, see [Chapter 8](#) of this book. In general, the endocytosis of a nanoparticle that comes into contact with the outer leaflet of the membrane consists of three steps: Onset of particle adhesion, spreading of the membrane over the particle surface until the particle is completely engulfed by the membrane, and cleavage (or scission) of the membrane neck connecting the completely engulfed particle with the mother membrane.

Completely engulfed particle

When a particle in contact with the outer leaflet becomes completely engulfed, the membrane forms a limit shape with a closed membrane neck. For this limit shape, the mean curvature M'_{ms} of the unbound membrane segment adjacent to the membrane neck satisfies the neck closure condition (Agudo-Canalejo and Lipowsky, 2015a)

$$M'_{\text{ms}} + M_{\text{co}} = M'_{\text{ms}} + \frac{1}{R_{\text{W}}} - \frac{1}{R_{\text{pa}}} = 2m \quad (5.255)$$

with the contact mean curvature M_{co} as given by Eq. 5.247. Comparison with the neck closure condition for spherical in- and out-buds as described by Eq. 5.50 and [Figure 5.14](#) shows that the mean curvature of the bud is now replaced by the contact mean curvature M_{co} of the adhesive nanoparticle. Furthermore, the closed neck is stable provided

$$M'_{\text{ms}} + M_{\text{co}} - 2m \geq 0 \quad (\text{stable neck, endocytosis}). \quad (5.256)$$

in close analogy to the case of an in-bud with a stably closed neck as described by Eq. 5.61.

The presumably simplest way to derive the neck closure condition in Eq. 5.255 is to require that the bending energy density of the membrane as given by $2\kappa(M - m)^2$, see Eq. 5.12, is continuous across the neck. The latter requirement implies $(M_{\text{co}} - m)^2 = (M'_{\text{ms}} - m)^2$ or $M_{\text{co}} - m = \pm(M'_{\text{ms}} - m)$. The root with the plus sign leads to $M_{\text{co}} = M'_{\text{ms}}$ and thus to a continuous variation of the mean curvature. The root with the minus sign, on the other hand, is equivalent to the neck closure condition in Eq. 5.255. In (Agudo-Canalejo and Lipowsky, 2016), the two relations in Eqs 5.255 and 5.256 have been derived in a systematic manner by calculating the free energy of certain membrane shapes with small neck radii R_{ne} and taking the limit of zero R_{ne} .

Energy landscape for small particles

In the limit of small particles with $R_{\text{pa}} \ll R_{\text{ve}}$, one can identify the mean curvature M'_{ms} of the unbound membrane segment adjacent to the closed neck for the completely engulfed particle with the mean curvature M_{ms} of the membrane segment that comes initially into contact with the particle, see Eq. 5.248 (Agudo-Canalejo and Lipowsky, 2015b). One can then explicitly calculate the local (free) energy landscape E as a function of the area fraction q of the particle surface that is covered by the vesicle membrane. The physically meaningful range of q -values corresponds to $0 \leq q \leq 1$. For small particles, the energy landscape is then found to have the simple quadratic form (Agudo-Canalejo and Lipowsky, 2017)

$$E(q) = E(0) + 16\pi\kappa R_{\text{pa}} [(M - M_{\text{co}})q + (m - M)q^2] \quad (5.257)$$

which depends on three parameters: the local mean curvature $M = M_{\text{ms}} = M'_{\text{ms}}$, the contact mean curvature M_{co} , and the spontaneous curvature m .

Local conditions for adhesion plus engulfment

Complete engulfment with a stable membrane neck corresponds to an energy landscape $E(q)$ that has a boundary minimum at $q = 1$. The latter criterion is equivalent to the stability condition in Eq. 5.256. Furthermore, the completely engulfed particle state represents the *global* minimum of this energy landscape when the three curvatures satisfy the inequalities

$$M_{\text{co}} \geq M \geq 2m - M_{\text{co}}. \quad (5.258)$$

The first inequality corresponds to the local criterion for the onset of adhesion, the second inequality to a completely engulfed particle with a stable membrane neck. Therefore, the inequalities in Eq. 5.258 imply both adhesion and complete engulfment of the nanoparticle.

Effective constriction forces

The stability relation as given by Eq. 5.256, which applies to a stably closed neck for the complete engulfment of a nanoparticle, can be generalized by including an external force $f > 0$ that acts to constrict the membrane neck. Such a force contributes the term fR_{ne} to the energy of the vesicle-particle system which is proportional to the neck radius R_{ne} (Agudo-Canalejo and Lipowsky, 2016). One then finds the stability relation

$$\frac{f}{4\pi\kappa} + M'_{ms} + M_{co} - 2m \geq 0 \quad (5.259)$$

which defines the effective constriction force

$$f_{\text{eff}}^{\text{in}} \equiv 4\pi\kappa(M'_{ms} + M_{co} - 2m) \quad \text{for endocytosis.} \quad (5.260)$$

For small M'_{ms} , i.e., for a weakly curved membrane of the mother vesicle, the effective constriction force behaves as

$$f_{\text{eff}}^{\text{in}} \approx f_{\mathcal{W}}^{\text{in}} + f_m^{\text{in}} \quad (5.261)$$

with the adhesion-induced constriction force

$$f_{\mathcal{W}}^{\text{in}} \equiv 4\pi\kappa \left(\frac{1}{R_{\mathcal{W}}} - \frac{1}{R_{\text{pa}}} \right) \quad (5.262)$$

and the curvature-induced constriction force

$$f_m^{\text{in}} \equiv -8\pi\kappa m, \quad (5.263)$$

where f_m^{in} has the same form as in Eq. 5.137.

The final step of endocytosis corresponds to the cleavage (or scission) of the membrane neck. As explained in Section 5.4, the cleavage of a neck with radius R_{ne} leads to two bilayer edges and to a free energy barrier of the order of $4\pi R_{ne}\lambda_{ed}$ which depends on the edge tension λ_{ed} . To overcome this barrier, the effective constriction force must be sufficiently large and satisfy

$$f_{\text{eff}}^{\text{in}} \approx f_{\mathcal{W}}^{\text{in}} + f_m^{\text{in}} \gg 4\pi\lambda_{ed}. \quad (5.264)$$

Inspection of Eq. 5.262 for the adhesion-induced constriction force $f_{\mathcal{W}}^{\text{in}}$ shows that this force facilitates neck cleavage for strong adhesion with $1/R_{\mathcal{W}} \gg 1/R_{\text{pa}}$. Thus, even for a symmetric membrane with $m = 0$ and $f_m^{\text{in}} = 0$, strong adhesion with

$$f_{\mathcal{W}}^{\text{in}} \gg 4\pi\lambda_{ed} \quad \text{or} \quad R_{\mathcal{W}} \ll \frac{\kappa}{\lambda_{ed}} \quad (5.265)$$

leads to neck cleavage and, thus, to the release of the membrane-enclosed nanoparticle from the mother membrane. Using the typical value $\kappa = 10^{-19}$ J for the bending rigidity and the estimate

$\lambda_{ed} \gtrsim 1$ pN for the edge tension, the inequality in Eq. 5.265 predicts neck cleavage for an adhesion length $R_{\mathcal{W}}$ that is small compared to 100 nm.

5.7.6 AMBIENCE-INDUCED SEGMENTATION

The membranes considered in the previous sections were taken to have a laterally uniform composition which implies laterally uniform curvature-elastic properties even if they contained several molecular components. However, when a multi-component membrane is in contact with an adhesive surface, different membrane components will typically experience different molecular interactions with this surface, which implies that the membrane-surface interactions can lead to an enrichment or depletion of the different components within the bound segment of the vesicle membrane. As a consequence, the bound membrane segment will, in general, differ in its composition from the unbound segment of the membrane which provides an example for ambience-induced segmentation of membranes as displayed in Figure 5.31a (Rouhiparkouhi et al., 2013; Lipowsky et al., 2013; Lipowsky, 2014b). For two-component membranes, this kind of segmentation has been theoretically studied in some detail, see Appendix 5.G.

The adhesion geometry in Figure 5.31a corresponds to a chemically uniform substrate surface which leads to only two membrane segments, one bound and one unbound segment. If the substrate surface is chemically patterned as in Figure 5.31b and consists of two chemically distinct surface domains, both of which are adhesive but differ in their adhesive strengths, the vesicle membrane is partitioned into three different segments, corresponding to two different bound segments and one unbound segment. An even more complex geometry is depicted in Figure 5.31c: three vesicle membranes that differ in their overall

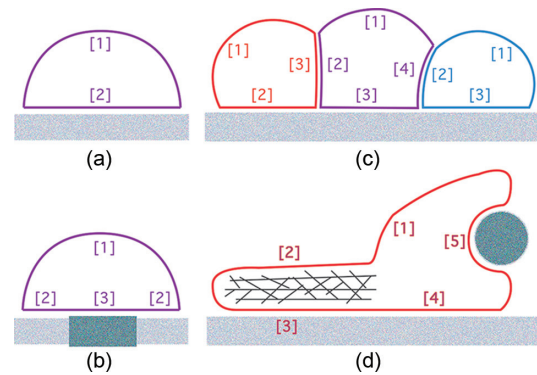


Figure 5.31 Ambience-induced segmentation of membranes that are exposed to different local environments: (a) Vesicle adhering to a planar, chemically uniform substrate surface; (b) Vesicle adhering to a planar and chemically patterned surface; (c) Cluster of three vesicles adhering to a planar, chemically uniform surface and to each other; and (d) Cartoon of a macrophage that moves along a solid surface and engulfs a small particle. The colors of the membranes represent their overall compositions. For each membrane, the numbers $[k] = [1], [2]$, etc indicate the different ambience-induced membrane segments. Because of the different molecular interactions between the membrane components and the different environments, each membrane segment will, in general, have a molecular composition that differs from the overall composition. (From Lipowsky, R. *Biol. Chem.*, 395, 253–274, 2014.)

compositions and interact both with the solid support and with other membranes. In addition, Figure 5.31d displays, in a rather schematic manner, the outer cell membrane of a macrophage that moves along a solid surface, contains some cytoskeletal filaments, and engulfs a microparticle.

In all examples displayed in Figure 5.31, the different membrane segments, labeled by $[k] = 1, 2, \dots, K$, can differ in their molecular composition which implies that they can also differ in their curvature-elastic properties. We are then led to consider membrane segments with different bending rigidities $\kappa^{[k]}$ and different spontaneous curvatures $m^{[k]}$. This approach has been recently applied to clathrin-dependent endocytosis which involves two membrane segments, corresponding to the presence and absence of the clathrin-containing protein coat (Agudo-Canalejo and Lipowsky, 2015a). The latter process is discussed in more detail in Chapter 8 of this book.

Ambience-induced segmentation of vesicle membranes has been recently observed for giant vesicles that adhere to planar electrodes (Steinkühler et al., 2016). The vesicles contained anionic lipids and adhered to the positively charged electrode at the bottom of the chamber. Using fluorescence quenching assays, the bound membrane segment was observed to have a different composition than the unbound segment, but, in contrast to naive expectations, only the outer leaflet of the bilayer membrane was affected and the bound segment of this latter segment was depleted of anionic lipids.

Ambience-induced segmentation will play an important role in the next two sections on membrane phase separation (Section 5.8) and membrane wetting (Section 5.9). Indeed, the interplay of ambience-induced segmentation and membrane phase separation (Section 5.8.5) confines the phase transition, for a given composition, to one of the membrane segments and each of these phase transitions occurs for a reduced range of compositions. In the case of wetting, the membranes are exposed to different aqueous phases that provide different local environments for these membranes, in close analogy to the adhesive substrate surfaces that have been discussed in the present section.

5.8 MEMBRANE PHASE SEPARATION AND MULTI-DOMAIN VESICLES

Biological and biomimetic membranes are fluid, contain several molecular components, and represent two-dimensional systems. As a consequence, the membranes should be able to undergo phase separation into two different liquid phases, in close analogy to phase separation of liquid mixtures in three dimensions. Membrane phase separation proceeds via the formation of intramembrane domains that differ in their molecular composition from the surrounding membrane matrix. The presence of domains implies the appearance of a new parameter, the line tension, which acts to shorten the domain boundaries (Lipowsky, 1992).

In the context of liquid droplets, the tension of the three-phase contact line, which was already considered by Gibbs, represents a relatively small correction term to the interfacial free energies that can be completely ignored on the micrometer scale. In contrast, the line tension associated with intramembrane domains has a rather strong effect on the

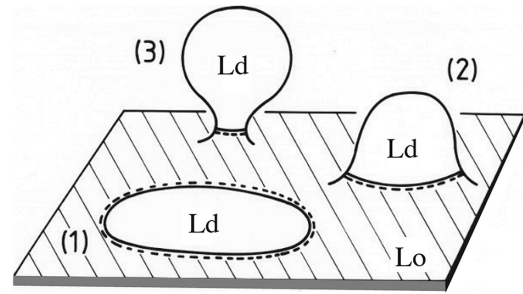


Figure 5.32 Domain-induced budding of a growing liquid-disordered (Ld) domain within an liquid-ordered (Lo) matrix: (1) Essentially flat Ld domain; (2) Partial Ld bud; and (3) Complete Ld bud. During the time evolution from (1) to (3) the domain boundary between the Ld domain and the Lo matrix shortens and the line energy of this boundary decreases continuously. In the following, the letters *a* and *b* will be used to indicate two coexisting fluid phases within the membranes. These membrane phases can be pure lipid phases or involve membrane proteins as well. (With kind permission Springer Science + Business Media: *J. Phys. II France*, Budding of membranes induced by intramembrane domains, 2, 1992, 1825–1840. Lipowsky, R.)

shape of membranes and vesicles. Indeed, the line tension of the domain boundaries can induce new types of shape transformations such as domain-induced budding, displayed in Figures 5.32 and 5.3. The latter process was first predicted theoretically (Lipowsky, 1992, 1993; Jülicher and Lipowsky, 1993) and then confirmed experimentally by optical microscopy of giant vesicles (Baumgart et al., 2003, 2005; Bacia et al., 2005; Dimova et al., 2007; Semrau et al., 2008).

At the beginnings of the 1990s, it was rather difficult to find experimental evidence for the coexistence of two fluid phases in membranes. This situation has now changed completely because many ternary lipid mixtures have been identified which exhibit two coexisting fluid phases, a liquid-ordered (Lo) and a liquid-disordered (Ld) phase. These lipid mixtures, which consist of a saturated lipid such as sphingomyelin, an unsaturated phospholipid, and cholesterol, form vesicles with several intramembrane domains. The intense experimental study of these mixtures was triggered by the proposal (Simons and Ikonen, 1997) that biological membranes contain intramembrane domains or rafts that are rich in sphingomyelin and cholesterol. In order to directly visualize the different domains formed in lipid vesicles, it was also crucial to find appropriate fluorescent probes that have a preference for one of the two fluid phases (Korlach et al., 1999; Dietrich et al., 2001; Veatch and Keller, 2003; Baumgart et al., 2003).

In this section, we will review the morphologies of multi-domain membranes and vesicles. We will consider multi-component membranes that consist of lipids and proteins and form two coexisting membrane phases, both of which are in a fluid state. Thus, the intramembrane domains could be pure lipid domains but they could also contain membrane proteins that participate in the phase separation. In the next subsection, the process of domain-induced budding as depicted in Figure 5.32 will be discussed. Second, the shape functional for two-domain vesicles will be described in some detail. The morphologies of these vesicles involve again closed membrane necks which are now governed by the interplay between the spontaneous curvatures of the two types of domains and the line tension of the

domain boundary. In addition, the Gaussian curvature moduli of the two membrane domains also affect the vesicle shape and determine the relative position of domain boundary and membrane neck. If the two domains differ in their bending rigidities, this rigidity difference can stabilize multi-domain vesicles with more than two domains and thus truncate the phase separation process. Such multi-domain vesicles undergo morphological transitions which involve changes of both the vesicle shape and the domain pattern (Gutleider et al., 2009; Hu et al., 2011). Finally, in Section 7.6, we will address the interplay between membrane phase separation and ambience-induced segmentation which acts to confine the phase separation to single membrane segments. The experimental methods to identify two coexisting fluid phases within the membranes of GUVs are reviewed in Chapter 18 of this book.

This section is supplemented by two appendices: Appendix 5.F on the matching conditions and curvature discontinuities along domain boundaries; and Appendix 5.G which discusses the interplay of segmentation and phase separation for two-component membranes.

5.8.1 BUDDING OF INTRAMEMBRANE DOMAINS

To be specific, let us consider a single Ld domain embedded in a larger Lo matrix as shown in Figure 5.32. Because the two phases differ in their molecular composition, they will also differ in their curvature-elastic parameters. First, the Ld phase is more flexible than the Lo phase. Second, the two phases will, in general, have different spontaneous curvatures. One mechanism that generates such a difference in preferred curvature is provided by adsorbate molecules with different affinities to the two phases. In addition, the domain boundary contributes a line (free) energy that is proportional to its length; the corresponding free energy per length defines the line tension λ (Lipowsky, 1992, 1993).

To simplify the notation, the Lo and Ld phases will now be denoted by the letters a and b . The Lo- or a -phase has the bending rigidity κ_a and the spontaneous curvature m_a . Likewise, the Ld- or b -domain has the bending rigidity κ_b and the spontaneous curvature m_b . We will first ignore possible contributions from the Gaussian curvature moduli which will be discussed further below.

In order to focus on the b -domain, let us further assume that the a -matrix is weakly curved and that its spontaneous curvature m_a can be ignored. After nucleation, the b -domain is weakly curved as well, see state (1) in Figure 5.32. The domain area A_b then grows by diffusion-limited aggregation. For a circular domain, the domain has the radius $L_b = \sqrt{A_b / \pi}$ which implies the domain boundary length $2\pi L_b$. The domain energy is then given by

$$E_{(1)} = 2\pi L_b \lambda + 2A_b \kappa_b m_b^2 \quad (5.266)$$

where the first term represents the line energy of the domain boundary and the second term the bending energy of the flat b -domain with spontaneous curvature m_b . If we transform the flat domain into a spherical bud connected to the a -matrix by a narrow membrane neck, see state (3) in Figure 5.32, we get essentially rid of the line energy. We now assume that the budding

process is sufficiently fast and that we may ignore changes in the domain area A_b during this process. The bud then has the radius $R_b = \frac{1}{2}L_b$ and the energy

$$E_{(3)} = 8\pi\kappa_b(1 - R_b |m_b|)^2. \quad (5.267)$$

Budding is energetically favored for $E_{(3)} - E_{(1)} < 0$ or (Lipowsky, 1992)

$$L_b = 2R_b > \frac{4\xi_b}{1 + 4\xi_b |m_b|} \equiv L_{b,1} \quad (5.268)$$

(bud energetically favored)

with the invagination length

$$\xi_b \equiv \kappa_b / \lambda \quad (5.269)$$

This simple argument shows that the competition between bending and line tension leads to two regimes for the bud size, depending on the relative size of the invagination length ξ_b and the spontaneous curvature m_b . If the spontaneous curvature m_b is small compared to the inverse invagination length $1/\xi_b = \lambda/\kappa_b$, the budding process is dominated by the line tension, and the bud radius $R_b \approx 4\xi_b$. On the other hand, if the spontaneous curvature m_b is large, the budding process is dominated by this curvature and $R_b \sim 1/|m_b|$.

The argument just described ignores the stability of the closed neck between the b -bud and the weakly curved a -matrix. As discussed further below, such a neck is stable if

$$L_b = 2R_b > \frac{4\xi_b}{1 + 2\xi_b |m_b|} \equiv L_{b,2} \quad (\text{stability of closed neck}). \quad (5.270)$$

Comparison of the two criteria Eqs 5.268 and 5.270 indicates that the budding transition at $L_b = L_{b,1}$ occurs before the closed neck of the bud becomes stable at $L_b = L_{b,2} > L_{b,1}$. This conclusion is corroborated by systematic energy minimization calculations (Jülicher and Lipowsky, 1993, 1996) as described next.

5.8.2 THEORY OF TWO-DOMAIN VESICLES

When a vesicle membrane undergoes phase separation into two coexisting phases a and b , it will initially form many small a - and/or small b -domains which will then coarsen into larger domains.¹³ In this subsection, we will consider the simplest situation in which the completion of this coarsening process leads to one large a -domain coexisting with one large b -domain. Further below, we will also discuss the possibility that the coarsening process is truncated and leads to an equilibrium state of a multi-domain vesicle with more than two domains.

Geometry and energetics of two-domain vesicles

Now, consider a vesicle of volume V that is bounded by a membrane with one a domain and one b domain. We can then decompose the vesicle shape S into three components: the shapes S_a and S_b of the two domains as well as the shape S_{ab} of the ab domain

¹³ We focus here on the nucleation regime close to the binodal line of the membrane phase diagram. Further away from this line, the multi-component membrane phase separates via spinodal decomposition for which the description in terms of sharp domain boundaries does not apply.

boundary. The a and b domains have the surface areas A_a and A_b , respectively. The total area of the vesicle membrane is then given by

$$A = A_a + A_b = \mathcal{A}\{S_a\} + \mathcal{A}\{S_b\} \quad (5.271)$$

where $\mathcal{A}\{\cdot\}$ denotes the area functional as before. The ab domain boundary with shape S_{ab} has a certain length, $\mathcal{L}\{S_{ab}\} = L_{ab}$ where $\mathcal{L}\{\cdot\}$ denotes the length functional.

The energy of a two-domain vesicle can be decomposed into several contributions: the curvature energy of the a domain, the curvature energy of the b domain, and the line energy of the ab domain boundary. As for a GUV with a uniform or single-domain membrane, the curvature energies can be further decomposed into bending and Gaussian curvature contributions. The energy functional of the two-domain vesicle then has the form

$$\mathcal{E}_{2\text{Do}}\{S\} = \mathcal{E}_{\text{bc}}\{S_a\} + \mathcal{E}_{\text{bc}}\{S_b\} + \mathcal{E}_G\{S_a, S_b\} + \lambda \mathcal{L}\{S_{ab}\}. \quad (5.272)$$

The last term on the right hand side of this equation represents the contribution of the domain boundary which is proportional to the line tension λ (Lipowsky, 1992). Any stable domain pattern implies that the line tension λ has to be positive as will be assumed in the following. The energy functional

$$\mathcal{E}_G\{S_a, S_b\} \equiv \kappa_{Ga} \int dA_a G + \kappa_{Gb} \int dA_b G \quad (5.273)$$

represents the combined Gaussian curvature terms of both domains and depends on the Gaussian curvature moduli κ_{Ga} and κ_{Gb} of the a - and b -domains. Finally, the bending energy functionals $\mathcal{E}_{\text{bc}}\{S_a\}$ and $\mathcal{E}_{\text{bc}}\{S_b\}$ have the form

$$\mathcal{E}_{\text{bc}}\{S_a\} = 2\kappa_a \int dA_a (M - m_a)^2 \quad \text{and} \quad \mathcal{E}_{\text{bc}}\{S_b\} = 2\kappa_b \int dA_b (M - m_b)^2 \quad (5.274)$$

which generalizes the spontaneous curvature model for a uniform membrane to the case of two different domains. These energy functionals depend on the bending rigidities κ_a and κ_b as well as on the spontaneous curvatures m_a and m_b .

Shape functional for two-domain vesicles

The equilibrium shapes of a two-domain vesicle are obtained by minimizing the energy functional Eq. 5.272 for a certain volume $V = \mathcal{V}\{S\}$ and for certain areas A_a and A_b of the a - and b -domains. These three constraints can be taken into account by three Lagrange multipliers ΔP , Σ_a , and Σ_b . As a consequence, the shape functional of the two-domain vesicle has the form

$$\mathcal{F}_{2\text{Do}}\{S\} = -\Delta P \mathcal{V}\{S\} + \Sigma_a \mathcal{A}\{S_a\} + \Sigma_b \mathcal{A}\{S_b\} + \mathcal{E}_{2\text{Do}}\{S\}. \quad (5.275)$$

So far, a systematic minimization of this functional has been performed for axisymmetric vesicles using the shooting method (Jülicher and Lipowsky, 1993, 1996) and, to some extent, by numerical minimization of discretized membranes (Gutleider et al., 2009; Hu et al., 2011). In these numerical studies, the

spontaneous curvatures were taken to be relatively small. The same energy functional has also been used to calculate doubly-periodic bicontinuous shapes corresponding to “lattices of passages” (Gózdź and Gompper 1998).

Gaussian curvature energies

The energy functional of a two-domain vesicle contains the Gaussian curvature term $\mathcal{E}_G\{S_a, S_b\}$ as given by Eq. 5.273. If the two Gaussian curvature moduli κ_{Ga} and κ_{Gb} are equal, this term does not depend on the shape but only on the topology of the vesicle and is then given by

$$\mathcal{E}_G\{S_a, S_b\} = 2\pi\chi\kappa_G \quad \text{for } \kappa_{Ga} = \kappa_{Gb} = \kappa_G \quad (5.276)$$

where χ denotes the Euler characteristic of the whole vesicle, see Appendix 5.B. In the following, we will consider two-domain vesicles that have a spherical topology characterized by $\chi = 2$.

If the Gaussian curvature moduli of the a - and b -phases are different, however, the Gaussian curvature terms also make a shape-dependent contribution. Indeed, the Gaussian curvature term in Eq. 5.273 then becomes (Jülicher and Lipowsky, 1993, 1996)

$$\mathcal{E}_G\{S_a, S_b\} = -\Delta\kappa_G \oint d/C_g + 2\pi(\kappa_{Ga} + \kappa_{Gb}). \quad (5.277)$$

with the difference

$$\Delta\kappa_G \equiv \kappa_{Ga} - \kappa_{Gb} \quad (5.278)$$

of the Gaussian curvature moduli. The first term on the right hand side of Eq. 5.277 is proportional to this difference $\Delta\kappa_G$ and to the line integral of the geodesic curvature C_g along the domain boundary. To obtain the correct sign of this term, the orientation of the line element $d\ell$ has to be chosen in such a way that the line integral moves around the b -domain in a clockwise manner when one looks down onto this domain from the exterior solution. The line integral along the domain boundary implies that the first term on the right hand side of Eq. 5.277 depends on the shape S_{ab} of the domain boundary. In contrast, the second term on the right hand side of Eq. 5.277 does not depend on the morphology of the vesicle but reflects its spherical topology. For $\kappa_{Ga} = \kappa_{Gb} = \kappa_G$, the first term vanishes and the second term reduces to $4\pi\kappa_G$ as in Eq. 5.276 with $\chi = 2$.

Euler-Lagrange or local shape equations

The first variation of the shape functional $\mathcal{F}_{2\text{Do}}\{S\}$ as given by Eq. 5.275 leads to two Euler-Lagrange equations for the (local) mean curvature M and the (local) Gaussian curvature G within the membrane domains with shapes S_a and S_b . These equations have the form

$$\Delta P = 2\hat{\Sigma}_i M - 2\kappa_i \nabla_{\text{LB}}^2 M - 4\kappa_i m_i M^2 - 4\kappa_i [M - m_i][M^2 - G] \quad (5.279)$$

with $i = a, b$, the total membrane tensions

$$\hat{\Sigma}_i \equiv \Sigma_i + 2\kappa_i m_i^2, \quad (5.280)$$

and the Laplace-Beltrami operator ∇_{LB}^2 , generalizing the Euler-Lagrange Eq. 5.25 for a uniform membrane. When the two types

of domains form spherical segments, the terms proportional to $M^2 - G$ vanish and we obtain two quadratic equations for the corresponding constant mean curvatures $M = M_a$ and $M = M_b$. Each of these quadratic equations can have up to two solutions which implies that the two-domain vesicles can form coexisting spherical segments with up to four different mean curvatures. One example is a two-domain vesicle with three closed membrane necks: one neck connects two membrane segment of a phase, one neck two membrane segments of b phase, and the third neck connects the a domain with the b domain. The latter neck is governed by a neck condition that includes the line tension of the domain boundary, see further below.

Matching conditions along the domain boundary

In addition to the two Euler-Lagrange Eqs 5.279, we need to impose appropriate matching conditions along the boundary between the two membrane domains. In the theoretical description considered here, we ignore the width of the ab domain boundary.¹⁴ This simplification is justified when the linear size of the a and b domain is large compared to the boundary width, a condition that is usually fulfilled for the optically resolvable membrane domains of giant vesicles. Because we ignore the width of the domain boundary, the bending rigidity and the spontaneous curvature change abruptly as we cross this boundary. Nevertheless, we can still impose the physical requirement that the shapes of the two membrane domains meet “smoothly” along the domain boundary, i.e., that these shapes have a common tangent along this boundary, as explicitly shown for axisymmetric vesicle shapes (Jülicher and Lipowsky, 1996).

Even for axisymmetric vesicle shapes with smooth contours, the matching conditions turn out to be somewhat complex. Indeed, these matching conditions can lead to discontinuities along the domain boundary, both for the curvature and for the mechanical tension. For an axisymmetric vesicle, one of the principal curvatures, say C_1 , is provided by the contour curvature. As described in Appendix 5.F, the contour curvature C_1 attains, in general, two different values C_{1b} and C_{1a} when we approach the domain boundary from the b and a domain, respectively. Defining the mean curvatures $M_a(s_1)$ and $M_b(s_1)$ at the a - and b -sides of the domain boundary, see Appendix 5.F, the curvature discontinuity can be written in the concise form

$$\kappa_a[M_a(s_1) - m_a] - \kappa_b[M_b(s_1) - m_b] = \frac{1}{2}(\kappa_{Gb} - \kappa_{Ga})C_2(s_1) \quad (5.281)$$

where $C_2(s_1)$ is the second principal curvature which is continuous across the domain boundary.

The curvature discontinuity also affects the difference $\Sigma_a - \Sigma_b$ of the mechanical tensions within the two membrane domains. In order to describe this tension difference, we use the parametrization of axisymmetric shapes as shown in Figure 5.33. Because of axisymmetry, the shape is determined by a one-dimensional

¹⁴ The width of the domain boundary is set by the correlation length for the compositional fluctuations. Far away from a critical demixing (or consolute) point, this correlation length will be comparable to the size of the lipid head groups while it becomes large compared to molecular length scales close to a critical point.

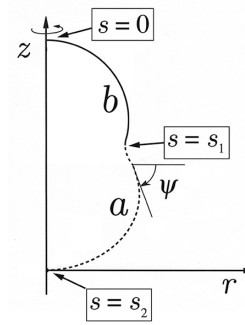


Figure 5.33 Contour of an axisymmetric vesicle with two domains, a (broken line) and b (full line). The contour is parametrized by the arc length s , the interval $0 \leq s < s_1$ corresponds to the b -domain and the interval $s_1 < s \leq s_2$ to the a -domain. The circular domain boundary is located at $s = s_1$. The shape of the contour is described by the radial coordinate $r = r(s)$ and the tilt angle $\psi = \psi(s)$ which varies from $\psi(s = 0) = 0$ at the north pole to $\psi(s = s_2) = \pi$ at the south pole.

contour which can be parametrized by the radial coordinate $r = r(s)$ and the tilt angle $\psi = \psi(s)$, both of which depend on the arc length s of the contour, see Appendix 5.F. The domain boundary is located at $s = s_1$ and the tension difference $\Sigma_a - \Sigma_b$ depends on the radius $r_1 \equiv r(s_1)$ of the circular domain boundary and the tilt angle $\psi_1 \equiv \psi(s_1)$ at this boundary. The tension difference then has the form

$$\Sigma_a - \Sigma_b = \lambda \frac{\cos \psi_1}{r_1} + \Delta_\Sigma \quad (5.282)$$

with Δ_Σ as given by the expression Eq. 5.17. The latter expression involves several terms and depends on the contour curvatures $C_{1a}(s_1)$ and $C_{1b}(s_1)$ and on the second principal curvature $C_2(s_1) = \sin \psi_1 / r_1$ at the domain boundary. If both membrane domains have identical curvature-elastic properties, the additional term Δ_Σ vanishes and we are left with the balance between the line tension λ and the mechanical tensions Σ_a and Σ_b within the two membrane domains. Finally, if the line tension λ vanishes as well, the mechanical tension within the a -domain is equal to the mechanical tension within the b -domain. The equality $\Sigma_a = \Sigma_b$ also holds for two domains with identical curvature-elastic properties if the radius $r_1 = r(s_1)$ of the domain boundary is a local minimum of $r(s)$ as in Figure 5.33, corresponding to the tilt angle $\psi_1 = \psi(s_1) = \pi/2$ and $\cos(\psi_1) = 0$. The latter situation applies to two membrane domains that have the same Gaussian curvature modulus, $\kappa_{Gb} = \kappa_{Ga}$, but is, in general, not valid for $\kappa_{Gb} \neq \kappa_{Ga}$, see last subsection of Section 5.8.3.

Parameters of two-domain vesicles

The morphology of two-domain vesicles depends on three geometric parameters, the vesicle volume V as well as on the partial areas A_a and A_b . Using again the vesicle size $R_{ve} = \sqrt{A/4\pi}$ as the basic length scale, we are left with two dimensionless parameters, the reduced volume $v \sim V/A^{3/2}$ with $A = A_a + A_b$ and $0 \leq v \leq 1$ as well as the area fraction

$$x_b \equiv \frac{A_b}{A_a + A_b} = \frac{A_b}{A} \quad (5.283)$$

of the b -domain with $0 \leq x_b \leq 1$. The area fraction x_a of the a -domain is then given by $x_a = 1 - x_b$.

In addition, the morphology of two-domain vesicles depends on six curvature-elastic parameters: the spontaneous curvatures m_a and m_b , the bending rigidities κ_a and κ_b , the difference $\kappa_{Ga} - \kappa_{Gb}$ of the Gaussian curvature moduli, and the line tension λ . Using the bending rigidity κ_b as the basic energy scale, we obtain five dimensionless parameters: the dimensionless curvatures

$$\bar{m}_a \equiv m_a R_{ve} \quad \text{and} \quad \bar{m}_b \equiv m_b R_{ve}, \quad (5.284)$$

the rigidity ratios

$$\rho_\kappa \equiv \frac{\kappa_a}{\kappa_b} \quad \text{and} \quad \rho_G \equiv \frac{\Delta\kappa_G}{\kappa_b} = \frac{\kappa_{Ga} - \kappa_{Gb}}{\kappa_b}, \quad (5.285)$$

as well as the dimensionless line tension

$$\bar{\lambda} \equiv \frac{\lambda R_{ve}}{\kappa_b}. \quad (5.286)$$

The bending rigidity ratio ρ_κ is expected to be of order one. If we again identify the b - and the a -domains with the Ld and Lo phases of three-component lipid bilayers, the value $\rho_\kappa \simeq 4.5$ has been measured for a certain tie line within the two-phase coexistence region (Heinrich et al., 2010). The rigidity ratio ρ_G is also expected to be of order one. Two groups (Baumgart et al., 2005; Semrau et al., 2008) have compared the experimentally observed shapes of two-domain vesicles with those calculated from the theory reviewed here and developed in (Jülicher and Lipowsky, 1993, 1996). As a result, these groups obtained the estimates $\rho_G \simeq 3.9$ (Baumgart et al., 2005) and $1.1 \leq \rho_G \leq 2.5$ (Semrau et al., 2008).

An order of magnitude estimate of the line tension leads to the value $\lambda \simeq 10^{-11}$ N or 10 pN (Lipowsky, 1992). For the ternary lipid mixtures studied in (Baumgart et al., 2003, 2005; Semrau et al., 2008), the line tensions deduced from the experiments varied between 10^{-12} and 10^{-14} N, reflecting the vicinity of critical demixing points in these mixtures. For giant vesicles with a size R_{ve} between 10 and 50 μm , the dimensionless line tension $\bar{\lambda}$ then varies within the range $1 \lesssim \bar{\lambda} \lesssim 500$.

5.8.3 DOMAIN-INDUCED BUDDING OF VESICLES

The shape functional $\mathcal{F}_{2D_0}\{\mathcal{S}\}$ in Eq. 5.275 has been minimized in order to determine the equilibrium morphologies within the subspace of axisymmetric shapes (Jülicher and Lipowsky, 1993, 1996). As discussed in the previous subsection, these shapes depend on seven dimensionless parameters, two geometric and five material parameters. In order to illustrate the equilibrium morphologies of two-domain shapes, the next subsection describes the dependence of domain-induced budding on the volume-to-area volume v and on the line tension $\bar{\lambda}$, keeping all other parameters fixed. We will see that closed membrane necks play again a prominent role. The closure and the stability of these necks is governed by generalized neck conditions that depend on the line tension.

Budding controlled by osmotic conditions

We now consider a two-domain vesicle with area fraction $x_b = 0.1$, corresponding to a relatively small b -domain, and study the shape of this vesicle as a function of volume-to-area ratio v and line tension $\bar{\lambda}$. In order to reduce the dimension of the parameter space, the a - and b -domain are taken to have the same bending rigidity, $\kappa_a = \kappa_b$, and zero spontaneous curvatures, $m_a = m_b = 0$. Furthermore, we will also assume that the difference $\Delta\kappa_G$ between the Gaussian curvature moduli is small and can be ignored. We are then left with a 2-dimensional $(v, \bar{\lambda})$ -section across the 7-dimensional parameter space. The corresponding morphology diagram is shown in Figure 5.34a.

This diagram contains two lines of limit shapes, L_{ss} and L_{ps} . The limit shapes L_{ss} have volume-to-area ratio $v = v_* = 0.885$ and line tension $\bar{\lambda} > \bar{\lambda}_* = 8.43$. These shapes consist of two spheres, a smaller b -sphere and a larger a -sphere that are connected by a closed neck. The domain boundary is located within this neck and has, thus, zero length. The a -sphere has radius $R_a = \sqrt{A_a / 4\pi}$ and mean curvature $M_a = 1/R_a$ while the b -sphere has radius $R_b = \sqrt{A_b / 4\pi}$ and mean curvature $M_b = 1/R_b$. Therefore, the geometry of the limit shapes L_{ss} is completely determined by the partial areas A_a and A_b . When we inflate one of the limit shapes L_{ss} , thereby increasing the

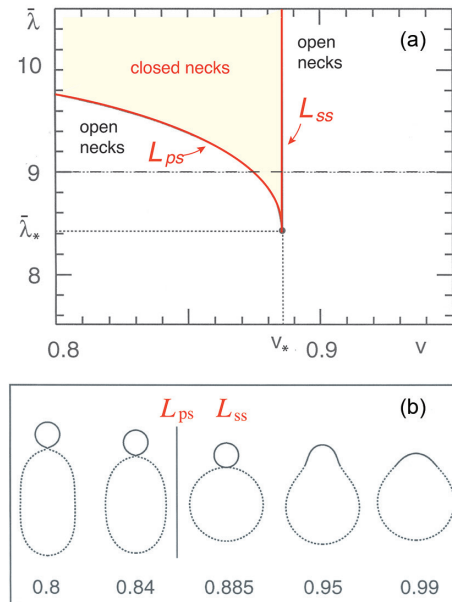


Figure 5.34 (a) Morphology diagram for two-domain vesicles as a function of reduced volume v and line tension $\bar{\lambda}$ and (b) Shapes of two-domain vesicles for $\bar{\lambda} = 9$ and variable v (bottom row), corresponding to the horizontal dashed line in (a). The b -domain covers the area fraction $x_b = 0.1$; both domains are taken to have the same bending rigidity and the same Gaussian curvature modulus as well as zero spontaneous curvatures. The limit shapes L_{ss} consist of two spheres, a larger sphere formed by the a -domain and a smaller sphere formed by the b -domain. The limit shapes L_{ps} consist of an a -prolate and a b -sphere. In (a), the two lines of limit shapes meet at the point $(v, \bar{\lambda}) = (v_*, \bar{\lambda}_*) = (0.885, 8.43)$. As we deflate a vesicle for $\bar{\lambda} > \bar{\lambda}_*$, we first reach the limit shape L_{ss} , at which the open neck closes, move across the shaded region (yellow) of persistent shapes with closed necks, and eventually reach the limit shape L_{ps} , at which the neck starts to open again. (Reproduced from Jülicher, F. and Lipowsky, R. *Phys. Rev. E*, 53, 2670–2683, 1996.)

volume-to-area ratio to $v > v_*$, the neck opens up and the domain boundary acquires a nonzero length.

The limit shapes L_{ps} are located at $v_{ps}(\bar{\lambda}) < v_*$ and again restricted to $\bar{\lambda} > \bar{\lambda}^*$, see Figure 5.34a. The latter shapes consist of an a -prolate and a b -sphere. The b -sphere of the limit shape L_{ps} is identical with the b -sphere of the limit shape L_{ss} and, thus, has the same radius $R_b = \sqrt{A_b / 4\pi}$. This b -sphere is connected to the pole of the a -prolate via a closed neck, and the domain boundary is again located within this neck. At its pole, the a -prolate has the mean curvature

$$M_a = \frac{\lambda}{2\kappa_b} - M_b = \frac{\lambda}{2\kappa_b} - \sqrt{4\pi/A_b}. \quad (5.287)$$

The latter relation represents an example for the neck closure condition of domain-induced budding, see further below. When we deflate one of the limit shapes L_{ps} , thereby decreasing the volume-to-area ratio to $v < v_{ps}$, the neck opens up and the domain boundary acquires a nonzero length.

Inspection of Figure 5.34a shows that the two lines of limit shapes, L_{ps} and L_{ss} , enclose an intermediate parameter regime in which all two-domain shapes have a closed neck. Now, assume that we move across this regime by inflation, thereby increasing the parameter v for fixed value of the line tension $\bar{\lambda} > \bar{\lambda}^*$. We start with a shape that has a volume-to-area ratio $v < v_{ps}(\bar{\lambda})$ and a slightly open neck, see Figure 5.34b. As we reach the limit shape L_{ps} by inflation, the neck closes and the two mean curvatures M_a and M_b adjacent to this neck fulfill the neck closure condition in Eq. 5.287. Further inflation does not affect the b -sphere but increases the volume of the a -prolate, thereby producing different persistent shapes Φ_{ps} with a closed neck. The volume of the a -prolate increases until it is transformed into an a -sphere. During this transformation, the mean curvature M_a at the pole of the a -prolate decreases continuously until it reaches the limiting value $M_a = \sqrt{4\pi/A_a}$ of the a -sphere. After this transformation, the two-domain vesicle forms the limit shape L_{ss} . Because the line tension forces the domain boundary to be located within the neck, a further increase in the vesicle volume necessarily leads to an open neck.

Neck closure and closed neck conditions

The $(v, \bar{\lambda})$ -diagram discussed in the previous subsection, see Figure 5.34a, contains a large parameter region for which the shape of the two-domain vesicle involves a closed membrane neck. This abundance of necks is also obtained for other choices of the area fraction x_b , different values of the bending rigidities κ_a and κ_b , and nonzero values of the spontaneous curvatures m_a and m_b . In all of these cases, the domain boundary is again located within the neck provided the difference $\Delta\kappa_G$ of the Gaussian curvature moduli is small and can be neglected. Such ab necks that completely eliminate the domain boundary will now be considered in more detail.

Out-buds

If the b -domain forms an out-bud as in Figure 5.34b, the closed ab -neck is stable if the mean curvatures M_a and M_b of the a - and b -segments adjacent to the neck satisfy the relation (Jülicher and Lipowsky, 1993, 1996)

$$\kappa_a(M_a - m_a) + \kappa_b(M_b - m_b) \leq \frac{1}{2}\lambda \quad \text{for } \kappa_{Ga} = \kappa_{Gb}. \quad (5.288)$$

The equality sign of this relation provides the neck closure condition for the limit shapes, the inequality sign the closed neck condition. The relation in Eq. 5.288 for a domain-induced out-bud has been confirmed by numerical energy minimization for a large number of different parameter values. This relation can also be derived by parametrizing the shape of the two-domain vesicle in terms of membrane segments with constant mean curvature, compare Section Stability of closed necks. Recently, the neck closure condition corresponding to the equality sign in Eq. 5.288 has been shown to apply to non-axisymmetric shapes as well (Yang et al., 2017).

One should note that the matching condition along the domain boundary no longer applies when we reach a limit shape with a closed neck for which the domain boundary has zero length. Indeed, consider the simplest case of two membrane domains that have the same curvature-elastic parameters. In the latter case, the matching condition in Eq. 5.281 has the simple form $M_a = M_b$, corresponding to a continuous variation of the mean curvature across the domain boundary. In contrast, the limit shape is characterized by the neck closure condition in Eq. 5.288 which reduces to $M_a = \frac{\lambda}{2\kappa_b} - M_b$ when the two domains have the same curvature-elastic parameters. If we combined the latter relation with $M_a = M_b$, we would conclude that $M_a = M_b = \frac{\lambda}{4\kappa_b}$ which is, however, inconsistent with $M_b = \sqrt{4\pi/A_b}$ as in Eq. 5.287. The same conclusion follows also by inspection of the limit shape L_{ps} in Figure 5.34 which clearly shows that $M_a \neq M_b$.

In-buds

If the b -domain forms an in-bud with a closed ab -neck, this neck is stable if (Lipowsky, 2014b)

$$\kappa_a(M_a - m_a) + \kappa_b(M_b - m_b) \geq -\frac{1}{2}\lambda \quad \text{for } \kappa_{Ga} = \kappa_{Gb}. \quad (5.289)$$

This relation can again be derived by an appropriate hemisphere-unduloid parametrization of the vesicle shape or, alternatively, by changing the sign of all curvatures that appear in Eq. 5.288. Because the line tension of the domain boundary is necessarily positive, the right hand side of the inequality in Eq. 5.289 is always negative.

Special parameter values

It is instructive to consider some special cases of the neck closure condition corresponding to the equality in Eqs 5.288 and 5.289. If the a - and b -domains have the same lipid composition and, thus, the same curvature-elastic parameters, the line tension λ vanishes and the neck closure condition becomes $M_a + M_b = 2m$, corresponding to the neck closure relations Eqs 5.52 and 5.53 for a uniform membrane. For a weakly curved a -segment, a spherical b -bud then has the radius

$$R_b = \frac{1}{|M_b|} \approx \frac{1}{2|m|} \quad (\text{uniform membrane, weakly curved } a\text{-segment}). \quad (5.290)$$

Another simple case is provided by a weakly curved a -membrane characterized by a small spontaneous curvature $|m_a| \ll |m_b|$. In this case, the b -domain forms a spherical bud with radius

$$R_b = \frac{1}{|M_b|} \approx \frac{1}{|m_b + \lambda / (2\kappa_b)|} \quad (\text{weakly curved } a\text{-membrane, small } |m_a|). \quad (5.291)$$

Thus, depending on the relative size of the spontaneous curvature $|m_b|$ and the reduced line tension $\lambda/(2\kappa_b)$, the bud size may be dominated by spontaneous curvature or by line tension. For some ternary lipid mixtures, the measured line tension was found to be of the order of 10^{-12} N (Baumgart et al., 2005; Semrau et al., 2008). The bending rigidity κ_b has a typical value of the order of 10^{-19} J. Thus, in these systems, the inverse length scale $\lambda/(2\kappa_b) \simeq 1/(200\text{nm})$ which implies that the bud size is dominated by line tension with $R_b \approx 2\kappa_b/\lambda$ for $|m_b| \ll 1/(200\text{ nm})$ and governed by spontaneous curvature with $R_b \approx 1/|m_b|$ for $|m_b| \gg 1/(200\text{ nm})$.

Effect of Gaussian curvature moduli

In the previous subsection, it was tacitly assumed that the difference $\Delta\kappa_G = \kappa_{Ga} - \kappa_{Gb}$ between the Gaussian curvature moduli of the a and b domain can be ignored. This simplification will be valid as long as $\Delta\kappa_G$ is small compared to the bending rigidities κ_a and κ_b . For larger values of $\Delta\kappa_G$, this difference has a significant effect on the location of the domain boundary, see Figure 5.35.

For an axisymmetric shape as shown in the top figure of Figure 5.35, the shape contour can be parametrized by the arc length s , the radial coordinate r , and the angle ψ between the normal vector and the symmetry axis, see Figure 5.33. The Gaussian curvature contribution in Eq. 5.277 can then be expressed in terms of the tilt angle $\psi_1 = \psi(s_1)$ at the domain boundary and becomes (Jülicher and Lipowsky, 1993, 1996)

$$E_G\{S_a, S_b\} = 2\pi(\kappa_{Ga} - \kappa_{Gb})\cos(\psi_1) \equiv E_G(\psi_1). \quad (5.292)$$

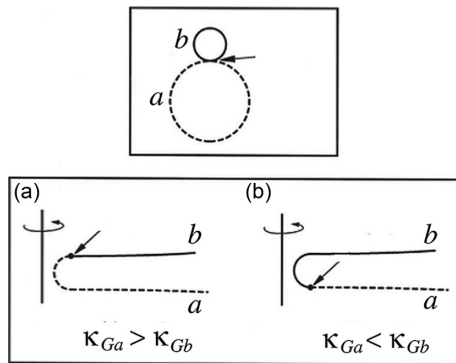


Figure 5.35 (Top) Side view of a vesicle that consists of a large a domain and a small b bud. The two domains are connected by a membrane neck which contains the ab domain boundary (arrow); (Bottom) More detailed view of the neck region which shows that the domain boundary position (arrows) depends on the relative size of the Gaussian curvature moduli κ_{Ga} and κ_{Gb} of the a and b domains. For $\kappa_{Ga} > \kappa_{Gb}$, the domain boundary is shifted towards the b bud. For $\kappa_{Ga} < \kappa_{Gb}$, this boundary is displaced towards the a domain. In both cases (a) and (b), the domain boundary is shifted out of the neck towards the domain with the smaller κ_G -value, and the neck is then formed by the domain with the larger Gaussian curvature modulus (Jülicher and Lipowsky, 1993, 1996). Such shifts of the domain boundaries have been experimentally observed by (Baumgart et al., 2005; Semrau et al., 2008). (Reproduced from Jülicher, F. and Lipowsky, R., *Phys. Rev. E*, 53, 2670–2683, 1996.)

If the domain boundary is located in the neck, i.e., at the closest point of the shape contour to the symmetry axis, the angle $\psi_1 = \pi/2$ and the energy term $E_G(\psi_1) = 0$.

Depending on the sign of $\kappa_{Ga} - \kappa_{Gb}$, the energy term E_G becomes negative as the domain boundary moves out of the neck towards the b or towards the a domain. If $\kappa_{Ga} > \kappa_{Gb}$, this term becomes negative for $\psi_1 > \pi/2$ which implies that the domain boundary prefers to move up towards the b domain as in Figure 5.35a. On the other hand, if $\kappa_{Ga} < \kappa_{Gb}$, E_G becomes negative for $\psi_1 < \pi/2$ which implies that the domain boundary prefers to move down towards the a domain, see Figure 5.35b. In both cases, the neck is then formed by the domain with the larger Gaussian curvature modulus.

The actual displacement of the domain boundary is limited by the line tension. Indeed, as the domain boundary moves out of the neck, the energy gain $|E_G(\psi_1)|$ arising from the Gaussian curvature terms is bounded by

$$|E_G(\psi_1)| \leq 2\pi |\kappa_{Ga} - \kappa_{Gb}| \quad \text{for any value of } \psi_1 \quad (5.293)$$

whereas the line energy of the domain boundary increases monotonically with the length of this boundary.

Such displacements of the domain boundaries away from the neck have indeed been observed experimentally for two-domain vesicles formed by ternary lipid mixtures (Baumgart et al., 2005; Semrau et al., 2008). Based on the observed location of the domain boundaries, the difference $\Delta\kappa_G = \kappa_{Ga} - \kappa_{Gb}$ in the Gaussian curvature moduli has been estimated to be $\Delta\kappa_G \simeq 3.9 \times 10^{-19}$ J in (Baumgart et al., 2005) and 3×10^{-19} J in (Semrau et al., 2008). So far, these values which are of the same order of magnitude as the bending rigidities represent the only experimentally deduced information about the Gaussian curvature moduli of lipid bilayers.

5.8.4 STABLE MULTI-DOMAIN PATTERNS

When we quench a vesicle membrane from the one-phase into the two-phase region, the phase separation process within the membrane starts with the formation of many small domains which then grow and merge into larger domains. Domain growth by coalescence, which is driven by the reduction in the line energy of the domain boundaries, has been observed both in computer simulations (Kumar et al., 2001) and in giant vesicle experiments (Veatch and Keller, 2003). If the line tension is sufficiently large, the coarsening process will often lead to complete phase separation and to two large membrane domains as studied in the previous subsections. However, if the two lipid phases differ in their bending rigidity, a multi-domain pattern with more than two domains can be energetically more favorable (Gutleider et al., 2009; Hu et al., 2011). Some examples with 1 + 3 and 1 + 4 domains are displayed in Figure 5.36. Inspection of these figures shows that the more rigid a -domains are only weakly curved whereas the more flexible b -domains form the more strongly curved membrane segments. A reduction in the number of b -domains would reduce the line energy of these domains but, at the same time, increase the bending energy of the vesicle, and the bending energy increase outweighs the line energy reduction.

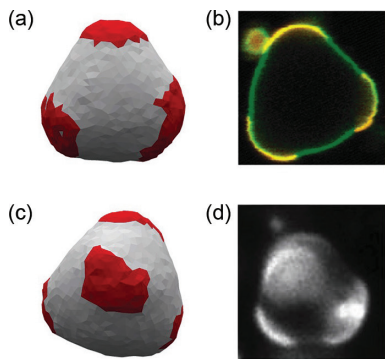


Figure 5.36 Multi-domain vesicles with two membrane domains that differ in their bending rigidities: (a, c) Snapshots from Monte Carlo simulations with (a) three and (c) four domains of the b phase (red) within a single domain of a phase (white); and (b, d) Corresponding images obtained by optical microscopy (Veatch and Keller, 2003; Gudheti et al., 2007). The a phase corresponds to the more rigid liquid-ordered phase, which forms a single, multiply-connected and weakly curved domain, whereas the b phase represents the more flexible liquid-disordered phase which forms three or four disconnected and more strongly curved domains. (Hu, J. et al., *Soft Matter*, 7, 6092–6102, 2011. Reproduced by permission of The Royal Society of Chemistry.)

The shape energy of multi-domain vesicles with N_a and N_b domains is obtained by summing up the bending and Gaussian curvature energies over all $N_a + N_b$ domains and the line energies over all domain boundaries. The minimization of this shape energy has been performed both by solving the corresponding shape equations assuming certain symmetries of the domain patterns (Gutleider et al., 2009) and by Monte Carlo simulations (Hu et al., 2011). As a result, the multi-domain vesicles are found to undergo new types of morphological transformations at which both the vesicle shape and the domain pattern are changed in a discontinuous manner. Presumably the simplest way to explore these morphological transitions is by changing the vesicle volume via osmotic deflation or inflation as illustrated in Figure 5.37.

Each vesicle morphology shown in Figure 5.37 is characterized by a different spatial symmetry: both with respect to the vesicle shape and with respect to the domain pattern. Therefore, all transitions that can be observed between these different morphologies are discontinuous and exhibit hysteresis. As we deflate the vesicle for fixed area fraction $x_b = A_b/(A_a + A_b)$, we can encounter the sequence of vesicle morphologies I_1, I_2, I_3, I_4 , and II_1 displayed in Figure 5.37b. The corresponding transitions $I_N \rightarrow I_{N+1}$ involve the fission of N into $(N + 1)$ b -domains. Such a fission process has to overcome an energy barrier that involves longer domain boundaries and, thus, an increased line energy. In contrast, during inflation, the reverse transitions $I_{N+1} \rightarrow I_N$ lead to a reduction in the number of b -domains and are thus facilitated by the line tension. Therefore, it should be easier to experimentally observe these morphological transitions during inflation processes.

5.8.5 MEMBRANE PHASE SEPARATION AND AMBIENCE-INDUCED SEGMENTATION

As explained in Section 7.6 and illustrated in Figure 5.31, membranes are often exposed to different local environments which act to enrich or deplete certain molecular components of the membranes. As a result, the membranes are partitioned into

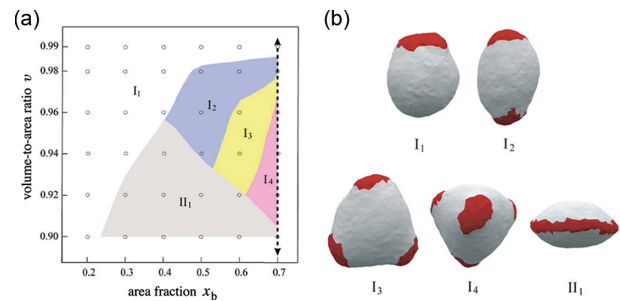


Figure 5.37 Morphological transitions of multi-domain vesicles that simultaneously change the vesicle shape and the domain pattern. (a) Morphology diagram as a function of area fraction x_b of the b -domains and volume-to-area ratio or reduced volume v . The diagram exhibits five different morphologies, labeled by I_1, I_2, I_3, I_4 , and II_1 and depicted in (b). The dashed vertical line at $x_b = 0.7$ indicates a possible deflation/inflation trajectory; and (b) Sequence of vesicle morphologies and morphological transitions that the vesicle explores as we move along the dashed vertical line in (a). For each morphology, the white domain corresponds to the more rigid a or Lo phase, the red domains to the more flexible b or Ld phase. The multi-domain vesicle follows the sequence $I_1 \rightarrow I_2 \rightarrow I_3 \rightarrow I_4 \rightarrow II_1$ during deflation and the reverse sequence during inflation. All transitions $I_1 \leftrightarrow I_2 \leftrightarrow I_3 \leftrightarrow I_4 \leftrightarrow II_1$ break a spatial symmetry. Therefore, all of these transitions are discontinuous and exhibit hysteresis. The transitions from $I_{N+1} \rightarrow I_N$, as induced by inflation, are facilitated by the line tension and should thus be easier to observe experimentally. (Hu, J. et al., *Soft Matter* 7, 6092–6102, 2011. Reproduced by permission of The Royal Society of Chemistry.)

several segments that can differ in their molecular composition. The interplay between this ambience-induced segmentation and membrane phase separation has some interesting consequences as shown theoretically for membranes consisting of two molecular components, see Appendix 5.G (Rouhiparkouhi et al., 2013; Lipowsky et al., 2013). First, the phase separation within the multi-component membrane is always spatially confined to a single segment as illustrated in Figure 5.38. Second, when the membrane is partitioned into K different membrane segments, we encounter K separate coexistence regions as we vary the membrane composition and/or the temperature. Third, the size of the coexistence regions, i.e., the range of compositions that exhibits two-phase coexistence, shrinks with increasing K . These generic properties have direct consequences for cell membranes.

The environment of a cell membrane is rather heterogeneous and the molecular interactions experienced by the different

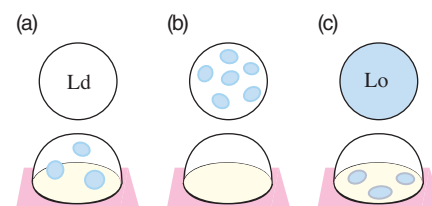


Figure 5.38 Multi-component vesicles with three different compositions. The top row displays the non-adhering vesicles with compositions that belong to (a) the liquid-disordered phase Ld (white), (b) the two-phase coexistence region, and (c) the liquid-ordered phase Lo (blue). The bottom row displays the same vesicles now adhering to a rigid surface or solid support. In the adhering state, membrane phase separation and domain formation can occur either in the bound or in the unbound segment but not in both segments simultaneously.

molecular components of the membrane change on nanoscopic scales. When we focus on the interactions with the cytoskeleton, we can distinguish at least two types of membrane segments, contact segments that interact with the cytoskeletal proteins and noncontact segments that do not experience such interactions (Sako and Kusumi, 1994; Saxton and Jacobson, 1997; Fujiwara et al., 2002; Kusumi et al., 2005). In addition, different contact segments are, in general, exposed to cytoskeletal structures that differ in their molecular composition of actin-binding proteins (Skau and Kovar, 2010; Michelot and Drubin, 2011) and non-contact segments involve additional supramolecular structures such as the protein scaffolds formed during clathrin-dependent endocytosis that have a lifetime in the range between 20 and 80s (Loerke et al., 2009; Cureton et al., 2012).

Thus, cell membranes are expected to be partitioned into many distinct membrane segments that are exposed to different local environments. If lipid phase domains form in such a cell membrane, this domain formation is necessarily restricted to one of the membrane segments and, thus, hard to detect (Lipowsky, 2014b). In the limiting case in which the environmental heterogeneities act as long-lived random fields on the cellular membranes, these heterogeneities would completely destroy the two-phase coexistence region, in analogy to the Ising model with random fields (Binder, 1983; Aizenman and Wehr, 1989; Fischer and Vink, 2011). This view is in agreement with experimental observation on membrane phase separation in giant plasma membrane vesicles (Baumgart et al., 2007; Veatch et al., 2008) because the latter vesicles have no cytoskeleton.

In contrast to lipid phase domains, the formation of intramembrane domains via the clustering of membrane proteins is frequently observed *in vivo*. One example is provided by clathrin-dependent endocytosis which can be understood as a domain-induced budding process that is governed by the membrane's spontaneous curvature. When the endocytic vesicles contain nanoparticles or other types of cargo, the uptake of this cargo becomes maximal at a certain, optimal cargo size (Agudo-Canalejo and Lipowsky, 2015a) as experimentally observed for the uptake of gold nanoparticles by HeLa cells (Chithrani et al., 2006; Chithrani and Chan, 2007) and discussed in more detail in Chapter 8 of this book. In general, protein-rich membrane domains or membrane domains induced by an extended protein coat should always undergo domain-induced budding as long as the lipid-protein domains remain in a fluid state. Recent examples are domain-induced budding processes arising from the clustering of Shiga toxin (Pezeshkian et al., 2016) and from the sequential adsorption of two types of ESCRT proteins (Avalos-Padilla et al., 2018).

5.9 WETTING OF MEMBRANES BY AQUEOUS DROPLETS

Aqueous two-phase systems, also called aqueous biphasic systems, have been used for a long time in biochemical analysis and biotechnology and are intimately related to water-in-water emulsions (Albertsson, 1986; Helfrich et al., 2002; Esquena, 2016). One prominent example are PEG-dextran solutions that undergo aqueous phase separation when the weight fractions of the polymers

exceed a few percent. The corresponding interfacial tensions are ultralow, of the order of 10^{-6} – 10^{-4} N/m, reflecting the vicinity of a critical demixing point in the phase diagram (Scholten et al., 2002; Liu et al., 2012; Atefi et al., 2014; de Freitas et al., 2016). The corresponding phase diagram is displayed in Figure 5.39 based on the experimental data in (Liu et al., 2012). As explained in the following section, aqueous two-phase systems and water-in-water emulsions also provide insight into the wetting behavior of membranes and vesicles. The experimental procedures used to encapsulate aqueous two-phase systems by GUVs are reviewed in Chapter 29 of this book.

In the experimental studies of phase separation of PEG-dextran solutions within GUVs, (Li et al., 2011; Liu et al., 2016) the GUV membranes were observed to form many nanotubes. More precisely, such tubes were formed by the membrane segments in contact with the PEG-rich aqueous phase. Thus, deflation of the PEG-dextran solutions led simultaneously to

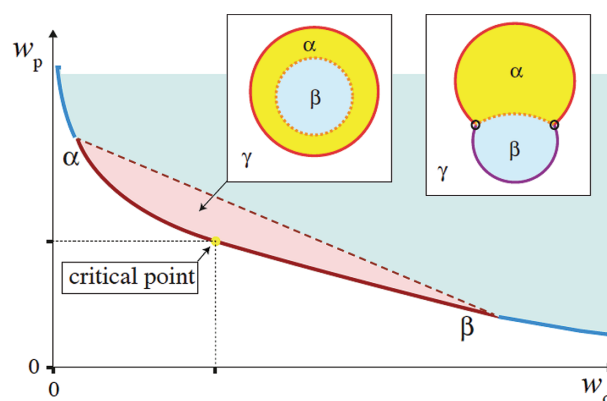


Figure 5.39 Phase diagram and membrane wetting behavior of aqueous PEG-dextran solutions as a function of the weight fractions w_p and w_d for PEG and dextran as determined experimentally in (Liu et al., 2012). For low weight fractions, the polymer mixture forms a spatially uniform aqueous phase corresponding to the one-phase region (white) in the phase diagram. The coexistence region of the PEG-rich phase α and the dextran-rich phase β contains two subregions, a complete wetting region (pink) close to the critical point and a partial wetting region (turquoise) further away from it. In the pink subregion, the membrane is completely wetted by the PEG-rich phase α which encloses the dextran-rich phase β . The corresponding wetting morphology is depicted in the left inset: the outer leaflet of the uniform vesicle membrane (red) is in contact with the exterior phase γ , the inner leaflet with the interior phase α but not with the interior phase β (gravitational effects arising from the different mass densities of the two phases have been ignored). In the turquoise subregion, the membrane is partially wetted by both phases as shown in the right inset: both interior phases α and β are now in contact with the vesicle membrane and induce two distinct membrane segments (red and purple). Within the phase diagram, the boundary between the complete and partial wetting subregions is provided by a certain tie line (red dashed line), the precise location of which depends on the lipid composition of the membrane. Along this tie line, the system undergoes a complete-to-partial wetting transition. The dashed tie-line partitions the binodal line into two line segments (red and blue). If one approaches the red segment of the binodal line from the one-phase region, a wetting layer of the α phase starts to form at the membrane and becomes mesoscopically thick as one reaches this line segment. No such layer is formed along the blue segment of the binodal line.

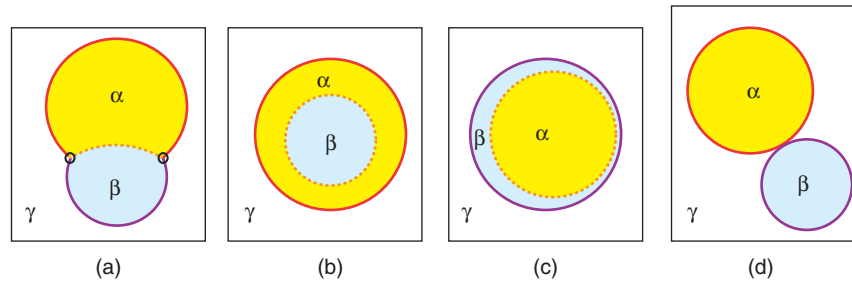


Figure 5.40 In-wetting morphologies arising from phase separation into two aqueous phases, α (yellow) and β (blue), within a giant vesicle. The vesicle is surrounded by the bulk liquid γ (white) which plays the role of an inert spectator phase. Red and purple segments of the vesicle membrane are in contact with the α and β droplets, respectively. The $\alpha\beta$ interfaces are depicted as dashed orange lines: (a) Partial wetting of the vesicle membrane by both the α and the β phase. This morphology involves a three-phase contact line (black circles). On the micrometer scale, the vesicle shape exhibits a kink along this contact line which directly reveals the capillary forces acting onto the vesicle membrane; (b) Complete wetting of the membrane by the α phase; (c) Complete wetting by the β phase; and (d) Special morphology for which the α and the β droplet are separated by a closed membrane neck. The latter morphology, which resembles complete wetting by the γ phase, is only possible if the membrane has a certain minimal area $A = A_{2sp}$ to enclose both spherical droplets completely, see Eq. 5.294.

both wetting and tubulation of the GUVs. However, wetting and tubulation should be regarded as two distinct and independent processes. First, nanotubes can be formed in the absence of aqueous phase separation as predicted theoretically for uniform membranes, see Section 5.6, and observed experimentally (Liu et al., 2016) for GUVs exposed to asymmetric PEG solutions without dextran. Second, membrane wetting is expected to always generate some spontaneous curvature but tubulation can only occur if the spontaneous curvature is sufficiently large compared to the inverse vesicle size as explained in Section 5.6. In the following subsections, we will first focus on wetting and ignore the possibility of tube formation. The additional aspects related to spontaneous tubulation will be addressed in a later subsection.

This section is supplemented by two Appendices: Appendix 5.H on wetting of two membraneless droplets and Appendix 5.I on out-wetting of membranes and vesicles by droplets that originate from the exterior solution.

5.9.1 DISTINCT IN-WETTING MORPHOLOGIES

Wetting phenomena arise in aqueous systems with three separate aqueous phases that will be denoted by α , β , and γ . In the presence of a GUV membrane, which separates the aqueous solution into an interior and exterior compartment, only two of these phases, say α and β , will be in chemical equilibrium and able to form two coexisting phases. We can then distinguish two different cases, out-wetting and in-wetting, depending on whether these coexisting phases are formed within the exterior or interior compartment. For out-wetting, the exterior solution undergoes aqueous phase separation into α and β droplets while the interior solution forms a spatially uniform γ phase. The γ phase does not participate in the wetting process and, thus, represents an inert spectator phase. For in-wetting, the interior solution separates into α and β droplets while the exterior solution forms a spatially uniform γ phase which again plays the role of an inert spectator phase.

In order to simplify the following discussion, I will focus in this section on the case of in-wetting. The case of out-wetting is considered in Appendix 5.I. In-wetting has been studied experimentally for PEG-dextran solutions, using two different methods to induce the phase separation within the GUVs: temperature

changes (Helfrich et al., 2002; Long et al., 2008) and osmotic deflation (Li et al., 2008, 2011; Kusumaatmaja et al., 2009; Liu et al., 2016; Dimova and Lipowsky, 2016). After the phase separation has been completed, the vesicle contains two aqueous droplets consisting of the PEG-rich phase α and the dextran-rich phase β , which are both separated from the exterior phase γ by the GUV membrane.

In general, an aqueous solution with three distinct aqueous phases α , β and γ can form three different liquid-liquid interfaces, an $\alpha\beta$, an $\alpha\gamma$, and a $\beta\gamma$ interface. When the interior aqueous solution within the GUV undergoes aqueous phase separation as considered here, the membrane is partitioned into an $\alpha\gamma$ and a $\beta\gamma$ membrane segment. In principle, one can then distinguish four wetting morphologies: a partial wetting morphology which is characterized by a three-phase contact line and three distinct morphologies of complete wetting as depicted in Figure 5.40.

For the PEG-dextran solutions, complete wetting of the membrane by the β phase as in Figure 5.40c has not been observed. Complete wetting of the membrane by the PEG-rich phase α as in Figure 5.40b was observed close to the critical point of the PEG-dextran mixture, see pink region in Figure 5.39. Partial wetting as in Figure 5.40a was found further away from the critical point, see turquoise region in Figure 5.39. Deflation of the partial wetting morphologies should eventually lead to complete wetting of the $\alpha\beta$ interface by the γ phase, see Figure 5.40d. In the latter case, the GUV membrane consists of three segments: an $\alpha\gamma$ segment around the α droplet, a $\beta\gamma$ segment around the β droplet, and a membrane neck (or nanotube) connecting the $\alpha\gamma$ with the $\beta\gamma$ segment. The latter morphology is not possible if the volume-to-area ratio of the GUV is too large. Indeed, if the α and β droplets have the volumes V_α and V_β , they cannot be completely enclosed by the vesicle membrane if the membrane area A is too small and satisfies the inequality¹⁵

$$A < A_{2sp} \equiv (4\pi/9)^{1/3} (V_\alpha^{2/3} + V_\beta^{2/3}). \quad (5.294)$$



¹⁵ If the vesicle membrane forms nanotubes, the area A corresponds to the apparent area of the mother vesicle.

In the following, I will first focus on systems that fulfill the geometric constraint Eq. 5.294 and thus cannot attain the limit shape with $A = A_{2sp}$ in Figure 5.40d. The latter morphology will be discussed in Section 5.9.8 further below.

In the phase diagram of Figure 5.39, the complete and partial wetting subregions are separated by a certain tie line, at which the system undergoes a complete-to-partial wetting transition. The precise location of this tie line depends on the lipid composition of the membranes. So far, three compositions have been studied: binary lipid mixtures consisting of DOPC and GM1 (Li et al., 2008, 2011) as well as ternary mixtures containing DOPC, dipalmytoyl phosphatidyl choline (DPPC) and cholesterol (Liu et al., 2016). In general, the wetting transition along this tie line can be continuous or discontinuous depending on the manner in which the contact angle vanishes as we approach the transition from the partial wetting regime. So far, the experimental data do not allow us to draw firm conclusions about the continuous or discontinuous nature of the transition.

A particularly interesting class of water-in-water droplets is provided by membraneless organelles and biomolecular condensates that have been discovered *in vivo* and are enriched in intrinsically disordered proteins such as FUS (Brangwynne et al., 2009). It has been recently shown that a FUS-rich droplet in contact with a lipid vesicle can attain three different wetting morphologies depending on the salt concentration in the exterior solution (Knorr et al., under review). First, the droplet may form a thin wetting layer that spreads over the whole vesicle membrane, corresponding to complete wetting by the FUS-rich phase. Second, the droplet may have a limited contact area with the vesicle membrane and can then be characterized by apparent contact angles. Third, the droplet may also avoid the contact with the membrane corresponding to dewetting of the FUS-rich phase.

5.9.2 FLUID-ELASTIC MOLDING OF MEMBRANES

The distinction between dewetting, partial wetting, and complete wetting as described in the previous subsection emphasizes the different morphologies of an aqueous droplet in contact with a vesicle membrane. Alternatively, we may also focus on the response of the membrane to such a droplet. This response reflects the fluid-elastic molding mechanisms by which the droplet shapes the membranes. These mechanisms involve the adhesion of the droplets to the membranes, the capillary forces that the $\alpha\beta$ interface exerts onto the membrane, as well as the bilayer asymmetry and curvature generation arising from the different aqueous phases in contact with the two membrane leaflets. For a large bilayer asymmetry and low membrane tension, the membrane forms nanobuds and nanotubes as observed for vesicle membranes in contact with PEG-dextran solutions (Li et al., 2011; Lipowsky, 2013; Liu et al., 2016).

The different molding mechanisms are governed by different fluid-elastic parameters. First of all, the contact areas between the different aqueous phases and the GUV membrane can be characterized by different adhesive strengths, $W_{\alpha\gamma}$ and $W_{\beta\gamma}$, which represent the adhesion free energies of the $\alpha\gamma$ and $\beta\gamma$ segments per unit area. If the α droplets are attracted towards the membrane, in a background of β phase, the corresponding affinity contrast $W_{\alpha\gamma} - W_{\beta\gamma}$ is negative. In such a situation, the α droplet tries

to increase its contact area $A_{\alpha\gamma}$ with the membrane. However, an increase of the contact area $A_{\alpha\gamma}$ for fixed volume V_α usually implies an increase in the area $A_{\alpha\beta}$ of the $\alpha\beta$ interface and, thus, of the interfacial free energy $A_{\alpha\beta}\Sigma_{\alpha\beta}$ which is proportional to the interfacial tension $\Sigma_{\alpha\beta}$.

On the other hand, the α droplet can simultaneously increase the contact area $A_{\alpha\gamma}$ with the membrane and decrease the area $A_{\alpha\beta}$ of the $\alpha\beta$ interface when it is partially or completely engulfed by the membrane. Complete engulfment of the α droplet as depicted in Figure 5.40d is only possible if the membrane area A is sufficiently large and satisfies $A \geq A_{2sp}$ with the area threshold A_{2sp} as in Eq. 5.294. In general, complete engulfment of a liquid droplet by a vesicle membrane requires some area reservoir or, equivalently, a sufficiently small lateral stress Σ acting within the membrane. Vice versa, a large lateral stress as generated, e.g., by osmotic inflation reduces the contact area for partial wetting and suppresses engulfment.

The interfacial tension $\Sigma_{\alpha\beta}$ of an aqueous two-phase system or water-in-water emulsion can be very small and only of the order of 10^{-6} – 10^{-5} N/m. In spite of these ultra-low tension values, the resulting capillary forces generate strong shape deformations of the vesicle membrane along the three-phase contact line. Indeed, when viewed with conventional optical resolution, the membrane shape exhibits an apparent kink along this contact line as schematically depicted in Figures 5.40a and 5.49a for partial in- and out-wetting, respectively.

Finally, both for in- and for out-wetting, the two leaflets of the different membrane segments are exposed to different aqueous solutions which implies that the membrane segments acquire a certain spontaneous curvature. For a sufficiently large spontaneous curvature, the membrane segment forms nanobuds and nanotubes as observed for giant vesicles in contact with phase-separated PEG-dextran solutions (Li et al., 2011; Lipowsky, 2013; Liu et al., 2016). In the latter case, the spontaneous curvature was generated by PEG adsorption which implies that the nanobuds and nanotubes were formed by the membrane segments $\alpha\gamma$ in contact with the PEG-rich phase, reflecting the more negative adhesive strength $W_{\alpha\gamma}$ of these segments.

5.9.3 THEORY OF VESICLE-DROPLET SYSTEMS

Basic assumptions about the composition of the vesicle membrane

As previously mentioned, multicomponent membranes exposed to two different aqueous solutions are partitioned into two segments that will, in general, differ in their molecular compositions. These different compositions reflect the different molecular interactions between the membrane molecules and the two aqueous phases. Membrane segmentation can also arise via two alternative mechanisms, (i) phase separation within the membrane as discussed in the previous Section 5.8 and (ii) curvature sorting, i.e., the preference of some membrane molecules for highly curved membrane segments.

In the present section, we consider membrane compositions that belong to the one-phase region when the vesicle membrane is exposed to a uniform aqueous environment provided by any of the three liquid phases α , β , and γ . Furthermore, to simplify

the following discussion, we will assume that curvature sorting is negligible and can be ignored.¹⁶ In such a situation, the different molecular compositions of the $\alpha\gamma$ and $\beta\gamma$ membrane segments are determined by the different molecular interactions of the membrane molecules with the two distinct aqueous phases, molecular interactions that will be described by the corresponding adhesion free energies.

Geometry of in-wetting morphologies

The in-wetting morphologies in Figure 5.40 involve one α and one β droplet enclosed by the vesicle membrane. It will be useful to decompose the corresponding shape S into several components. First, we define the shapes S_α and S_β of the two droplets with volumes

$$V_\alpha = \mathcal{V}\{S_\alpha\} \quad \text{and} \quad V_\beta = \mathcal{V}\{S_\beta\}. \quad (5.295)$$

The total volume of the vesicle is then given by

$$V = V_\alpha + V_\beta. \quad (5.296)$$

These volumes can be considered to be constant at constant temperature and fixed osmotic conditions. The two droplets are bounded by three surface segments: the $\alpha\beta$ interface between the α and the β droplet as well as two membrane segments, the $\alpha\gamma$ segment in contact with the α droplet and the $\beta\gamma$ segment exposed to the β droplet. The shapes of these three surfaces will be denoted by $S_{\alpha\beta}$, $S_{\alpha\gamma}$, and $S_{\beta\gamma}$, respectively. Their surface areas are then given by

$$A_{\alpha\beta} = \mathcal{A}\{S_{\alpha\beta}\}, \quad A_{\alpha\gamma} = \mathcal{A}\{S_{\alpha\gamma}\}, \quad \text{and} \quad A_{\beta\gamma} = \mathcal{A}\{S_{\beta\gamma}\}. \quad (5.297)$$

All three surface segments meet along the three-phase contact line which has the shape $S_{\alpha\beta\gamma}$ and the length

$$L_{\alpha\beta\gamma} = \mathcal{L}\{S_{\alpha\beta\gamma}\} \quad (5.298)$$

where $L\{\cdot\}$ is the length functional as before.

The $\alpha\beta$ interface can adapt its area $A_{\alpha\beta}$ to changes in the droplet and membrane morphologies. As before, the total membrane area A will be taken to be constant at constant temperature. The vesicle-droplet system is then characterized by three geometric constraints as provided by the volumes V_α and V_β of the two droplets as well as the total membrane area A . In order to determine the morphology of the vesicle-droplet system, we will minimize the (free) energy of the system, taking these three constraints into account.

Different energetic contributions

The three surface segments and the contact line make different contributions to the total (free) energy of the vesicle-droplet system. One contribution arises from the interfacial tension $\Sigma_{\alpha\beta}$

of the interface between the two liquid phases α and β . The latter contribution is proportional to the interfacial area $A_{\alpha\beta}$ and given by

$$\Sigma_{\alpha\beta} A_{\alpha\beta} = \Sigma_{\alpha\beta} \mathcal{A}\{S_{\alpha\beta}\}. \quad (5.299)$$

The curvature elasticity of each membrane segment $j\gamma$ with $j = \alpha$ or β makes two contributions, a bending energy that depends on the bending rigidity $\kappa_{j\gamma}$ and the spontaneous curvature $m_{j\gamma}$, as well as a contribution from the Gaussian curvature modulus $\kappa_{G,j\gamma}$. In close analogy to the bending energy of a two-domain vesicle, see Eq. 5.274, the bending energy functional of a partially wetted membrane has the form

$$\mathcal{E}_{bc}^{\text{in}}\{S_{\alpha\gamma}, S_{\beta\gamma}\} = \mathcal{E}_{\alpha\gamma}^{\text{in}}\{S_{\alpha\gamma}\} + \mathcal{E}_{\beta\gamma}^{\text{in}}\{S_{\beta\gamma}\} \quad (5.300)$$

with

$$\mathcal{E}_{j\gamma}^{\text{in}}\{S_{j\gamma}\} = 2\kappa_{j\gamma} \int dA_{j\gamma} (M - m_{j\gamma})^2 \quad \text{for } j = \alpha \text{ or } \beta \quad (5.301)$$

which depends on the (local) mean curvature M of the membrane. In addition, the Gaussian curvature energy functional is given by

$$\mathcal{E}_G\{S_{\alpha\beta\gamma}\} = (\kappa_{G,\alpha\gamma} - \kappa_{G,\beta\gamma}) \oint d\ell C_g + 2\pi(\kappa_{G,\alpha\gamma} + \kappa_{G,\beta\gamma}), \quad (5.302)$$

where the first term involves the line integral over the geodesic curvature C_g along the three-phase contact line as follows from the Gauss-Bonnet theorem, see the analogous expression for two-domain vesicles in Eq. 5.277. To obtain the correct sign of this term, the orientation of the line element $d\ell$ has to be chosen in such a way that the $\alpha\gamma$ segment is surrounded in a clockwise manner when one looks down onto this segment from the exterior phase γ . We will again focus on membrane compositions with (at least) one molecular species, such as cholesterol, that undergoes frequent flip-flops between the two leaflets. We can then ignore additional bending energy terms arising from area-difference elasticity as described by Eqs 5.63 and 5.64. Furthermore, as emphasized at the beginning of the present section, we will also assume that this multi-component membrane has no tendency to phase separate and has a laterally uniform composition when exposed to spatially uniform aqueous environments.

In addition, the molecular interactions between the aqueous droplets and the membrane lead to two additional contributions, the adhesion free energies of the droplets and the free energy of the three-phase contact line. The latter contribution is proportional to the length $L_{\alpha\beta\gamma}$ of the contact line and given by

$$\lambda_{co} L_{\alpha\beta\gamma} = \lambda_{co} \mathcal{L}\{S_{\alpha\beta\gamma}\} \quad (5.303)$$

with the contact line tension λ_{co} . The latter line tension can be positive or negative in contrast to the line tension λ of a domain boundary, which must be positive to ensure the stability of the intramembrane domains. Finally, the adhesion free energies will now be discussed in some detail.

¹⁶ In general, curvature sorting should be limited to highly curved membrane segments. For in-wetting morphologies as considered here, high curvatures can be present along the three-phase contact line. In addition, one type of membrane segment may form nanotubes (Li et al., 2011; Liu et al., 2016) which represent highly curved membrane segments as well.

Adhesion free energies of droplets

In order to determine the adhesion free energies of the droplets in contact with the vesicle membrane, we denote the outer and inner leaflet of the bilayer membrane by the subscript “ol” and “il,” respectively, and view the leaflet-water interfaces as “walls” with different interfacial tensions, depending on whether they are exposed to the α or to the β phase.

To each shape S of the wetting morphology depicted in Figure 5.40a, we can define a reference system with the same shape but with both the α and β droplet replaced by γ phase. The intermolecular interactions between the leaflets and the adjacent γ phases then lead to the interfacial tensions $\Sigma_{ol,\gamma}$ and $\Sigma_{il,\gamma}$ of the corresponding leaflet-water interfaces and the combined interfacial free energy functional of both leaflet-water interfaces has the form

$$\mathcal{T}_{\gamma\gamma}\{S_{\alpha\gamma}, S_{\beta\gamma}\} = (\Sigma_{ol,\gamma} + \Sigma_{il,\gamma})(\mathcal{A}\{S_{\alpha\gamma}\} + \mathcal{A}\{S_{\beta\gamma}\}). \quad (5.304)$$

On the length scale of several nanometers, we should be able to ignore the dependence of the interfacial tensions on the interfacial curvatures which implies that both leaflet-water interfaces are governed by the same interfacial tension

$$\Sigma_{l\gamma} \equiv \Sigma_{ol,\gamma} = \Sigma_{il,\gamma} \quad (5.305)$$

corresponding to the leaflet-water interfaces of a planar bilayer membrane.

If we now go back to the wetting morphology in Figure 5.40a, the interfacial free energy of the leaflet-water interfaces becomes

$$\mathcal{T}_{\alpha\beta}\{S_{\alpha\gamma}, S_{\beta\gamma}\} = (\Sigma_{l\alpha} + \Sigma_{l\gamma})\mathcal{A}\{S_{\alpha\gamma}\} + (\Sigma_{l\beta} + \Sigma_{l\gamma})\mathcal{A}\{S_{\beta\gamma}\}. \quad (5.306)$$

The adhesion free energy functional \mathcal{E}_{ad} of the α and the β droplet in contact with one of the bilayer leaflets is then defined by

$$\mathcal{E}_{ad}\{S_{\alpha\gamma}, S_{\beta\gamma}\} \equiv \mathcal{T}_{\alpha\beta} - \mathcal{T}_{\gamma\gamma} = W_{\alpha\gamma}\mathcal{A}\{S_{\alpha\gamma}\} + W_{\beta\gamma}\mathcal{A}\{S_{\beta\gamma}\} \quad (5.307)$$

with the adhesion free energies per unit area, $W_{\alpha\gamma}$ and $W_{\beta\gamma}$, given by (Lipowsky, 2018a)

$$W_{\alpha\gamma} \equiv \Sigma_{l\alpha} - \Sigma_{l\gamma} \quad \text{and} \quad W_{\beta\gamma} \equiv \Sigma_{l\beta} - \Sigma_{l\gamma} \quad (5.308)$$

for the α and β droplet in contact with the inner bilayer leaflet. Thus, the system can be characterized by two adhesive strengths, $W_{\alpha\gamma}$ and $W_{\beta\gamma}$, in close analogy to (i) the adhesive strength W between a membrane and a substrate surface as discussed in Section 5.7 and to (ii) the adhesion of nanoparticles as described in Chapter 8 of this book. When the leaflet prefers the α phase over the γ phase, the adhesive strength $W_{\alpha\gamma} < 0$. Likewise, when the leaflet prefers the β phase over the γ phase, $W_{\beta\gamma} < 0$. The adhesive strength $W_{j\gamma}$ also represents the reversible work that has to be expended per unit area to replace the γ phase by the phase j with $j = \alpha, \beta$. In addition, we can also compare the adhesion of the α and β droplets to one of the leaflets without any reference to the γ phase. Thus, the reversible work per unit area to replace a droplet of β phase in contact with a leaflet by α phase is given by

$$W_{\alpha\beta} \equiv \Sigma_{l\alpha} - \Sigma_{l\beta} = W_{\alpha\gamma} - W_{\beta\gamma} \quad (5.309)$$

which is negative if the leaflet prefers the α phase over the β phase.

Energy functional for in-wetting

Now, let us collect the different terms described previously. As a result, we obtain the energy functional

$$\mathcal{E}_{2Dr}^{in}\{S\} \equiv \Sigma_{\alpha\beta}\mathcal{A}\{S_{\alpha\beta}\} + \mathcal{E}_{bc}^{in}\{S_{\alpha\gamma}, S_{\beta\gamma}\} + \mathcal{E}_{ad}\{S_{\alpha\gamma}, S_{\beta\gamma}\} + \mathcal{E}_{\alpha\beta\gamma}\{S_{\alpha\beta\gamma}\} \quad (5.310)$$

with the contact line contribution

$$\mathcal{E}_{\alpha\beta\gamma}\{S_{\alpha\beta\gamma}\} = \mathcal{E}_G\{S_{\alpha\beta\gamma}\} + \lambda_{co}\mathcal{L}\{S_{\alpha\beta\gamma}\}. \quad (5.311)$$

The subscript 2Dr stands for “two droplets” and the superscript “in” indicates that the energy functional \mathcal{E}^{in} corresponds to in-wetting and should be distinguished from out-wetting. In fact, the only energy contribution that is different for in- and out-wetting is the one that arises from the bending energy $\mathcal{E}_{bc}^{in}\{S\}$ of the two membrane segments, as described by Eq. 5.300, because the spontaneous curvatures change sign when we swap the α and β phases with the γ phase.

Shape functional for in-wetting

In addition to the different energetic contributions of the vesicle-droplet system, we have to take the constraints on the membrane area A and the droplet volumes V_α and V_β into account. The constraint on the membrane area A is implemented by the Lagrange multiplier Σ which can be identified with the lateral stress that acts to stretch (or compress) the membrane as explicitly shown for uniform membranes in Appendix 5.D. In addition, we have to enforce certain values for the volumes V_α and V_β of the α and β droplets. These volumes are determined by the pressures P_α , P_β , and P_γ within the three liquid phases α , β , and γ or, more precisely, by the pressure differences $P_\alpha - P_\gamma$ and $P_\beta - P_\gamma$. We are then led to study the stationary shapes (minima, maxima, and saddle points) of the shape functional

$$\mathcal{F}_{2Dr}^{in}\{S\} = (P_\gamma - P_\alpha)\mathcal{V}\{S_\alpha\} + (P_\gamma - P_\beta)\mathcal{V}\{S_\beta\} + \Sigma\mathcal{A}\{S\} + \mathcal{E}_{2Dr}^{in}\{S\} \quad (5.312)$$

where the last term $\mathcal{E}_{2Dr}^{in}\{S\}$ represents the energy functional for in-wetting as given by Eq. 5.310. Both the pressure differences $P_\gamma - P_\alpha$ and $P_\gamma - P_\beta$ as well as the lateral stress Σ will be used as Lagrange multipliers to fulfill the geometric constraints that the droplet volumes V_α and V_β as well as the total membrane area A have certain prescribed values.

Terms proportional to individual segment areas

The shape functional as given by Eq. 5.312 contains the term $\Sigma\mathcal{A}\{S\}$ which depends on the lateral membrane stress Σ and the adhesion term $\mathcal{E}_{ad}\{S\}$ as given by Eq. 5.307 which depends on the adhesive strengths of the two aqueous phases. When we combine these two terms, we obtain

$$\Sigma\mathcal{A}\{S\} + \mathcal{E}_{ad}\{S\} = \Sigma_{\alpha\gamma}\mathcal{A}\{S_{\alpha\gamma}\} + \Sigma_{\beta\gamma}\mathcal{A}\{S_{\beta\gamma}\} \quad (5.313)$$

with the mechanical segment tensions (Lipowsky, 2018a)

$$\Sigma_{\alpha\gamma} \equiv \Sigma + W_{\alpha\gamma} \text{ and } \Sigma_{\beta\gamma} \equiv \Sigma + W_{\beta\gamma}. \quad (5.314)$$

Thus, each segment tension $\Sigma_{j\gamma}$ depends both on the lateral membrane stress Σ and on the adhesive strength $W_{j\gamma}$. Individual vesicles from a given vesicle preparation are usually characterized by different Σ -values corresponding to different membrane areas and vesicle shapes. In contrast, the adhesive strength $W_{j\gamma}$ is determined by the molecular interactions across the leaflet-water interfaces and should have the same value for all GUVs from the same batch, assuming that their membranes have the same lipid-protein composition and are exposed to aqueous solutions with the same solute composition. As a consequence, the difference

$$\Sigma_{\alpha\gamma} - \Sigma_{\beta\gamma} = W_{\alpha\gamma} - W_{\beta\gamma} = W_{\alpha\beta} \quad (5.315)$$

of the two segment tensions is only determined by the adhesive strengths and should also have the same value for all GUVs from the same batch.

5.9.4 SHAPE EQUATIONS AND MATCHING CONDITIONS

Shape equations for membrane segments

The first variation of the shape functional in Eq. 5.312 leads to two Euler-Lagrange or shape equations for the two membrane segments $\alpha\gamma$ and $\beta\gamma$, in close analogy to the shape Eqs 5.279 for two-domain vesicles. Indeed, the shape equations for the two membrane segments have the form

$$P_j - P_\gamma = 2\hat{\Sigma}_{j\gamma} M - 2\kappa_{j\gamma} \nabla_{LB}^2 M - 4\kappa_{j\gamma} m_{j\gamma} M^2 - 4\kappa_{j\gamma} [M - m_{j\gamma}] [M^2 - G] \quad (5.316)$$

with $j = \alpha, \beta$ and the total segment tensions

$$\hat{\Sigma}_{j\gamma} \equiv \Sigma_{j\gamma} + \sigma_{j\gamma} = \Sigma + W_{j\gamma} + \sigma_{j\gamma} \quad (5.317)$$

which include the spontaneous segment tensions

$$\sigma_{j\gamma} \equiv 2\kappa_{j\gamma} m_{j\gamma}^2. \quad (5.318)$$

As before, the ∇_{LB}^2 symbol represents the Laplace-Beltrami operator, see Eq. 5.24, and G is the (local) Gaussian curvature. For the partial in-wetting morphologies depicted in Figure 5.40a, the pressure differences $P_\alpha - P_\gamma$ and $P_\beta - P_\gamma$ are positive.

Boundary or matching conditions for axisymmetric shapes

In addition to the shape equations for the two membrane segments, the first variation of the shape functional also leads to certain boundary or matching conditions for the two segments along the contact line. For axisymmetric vesicles as depicted in Figure 5.41, these matching conditions can be obtained by generalizing the corresponding conditions for two-domain vesicles as discussed in Section 5.8 and Appendix 5.F. Indeed, the

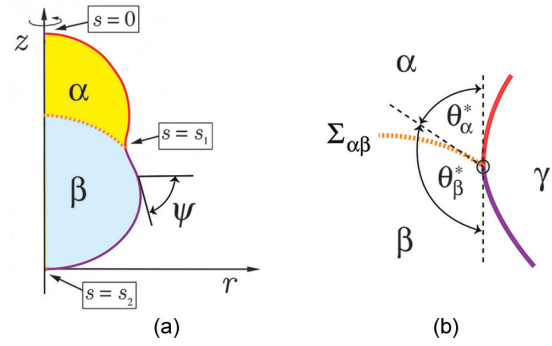


Figure 5.41 (a) Axisymmetric shape corresponding to partial in-wetting: As in Figure 5.33, the 2-dimensional shape of the membrane is uniquely determined by the 1-dimensional shape contour (red-purple) in the (r, z) -plane defined by the coordinate z along the symmetry axis and the radial coordinate r . The shape contour is parametrized by its arc length s , with the north and south pole of the vesicle being located at $s = 0$ and $s = s_2$, respectively, and the contact line at $s = s_1$. The angle ψ describes the tilt of the tangent vector at the shape contour from the horizontal r -direction; and (b) The $\alpha\gamma$ segment (red) and the $\beta\gamma$ segment (purple) meet at the contact line with a common tangent. The angles between this tangent and the tangent to the $\alpha\beta$ interface (dashed orange) represent the intrinsic contact angles θ_α^* and θ_β^* with $\theta_\alpha^* + \theta_\beta^* = \pi$.

axisymmetric shape shown in Figure 5.41 is quite similar to the one in Figure 5.33, the only difference is the presence of the two droplets α and β as well as the $\alpha\beta$ interface between these droplets. In Figure 5.41, the symmetry axis is again chosen to be the z -axis and the shape contour is again parametrized in terms of the arc length s , the radial coordinate $r = r(s)$, and the tilt angle $\psi = \psi(s)$. We can now directly use the matching conditions described in Appendix 5.F.1 if we substitute the domain indices b and a with the segment indices $\alpha\gamma$ and $\beta\gamma$, respectively.

The first variation of the shape functional with respect to the variable $\psi(s_1)$ is obtained by using the substitution $a \rightarrow \beta\gamma$ and $b \rightarrow \alpha\gamma$ in Eqs 5.2 and 5.3 which leads to the curvature discontinuity

$$\kappa_{\beta\gamma} C_1(s_1 + \varepsilon) - \kappa_{\alpha\gamma} C_1(s_1 - \varepsilon) = \delta\kappa C_2(s_1) + 2\kappa_{\beta\gamma} m_{\beta\gamma} - 2\kappa_{\alpha\gamma} m_{\alpha\gamma} \quad (5.319)$$

of the contour curvature C_1 along the three-phase contact line with the parameter

$$\delta\kappa \equiv \kappa_{\alpha\gamma} - \kappa_{\beta\gamma} + \kappa_{G,\alpha\gamma} - \kappa_{G,\beta\gamma}. \quad (5.320)$$

Note that the individual contour curvatures $C_1(s_1 + \varepsilon)$ and $C_1(s_1 - \varepsilon)$ are usually quite large compared to the orthogonal curvature $C_2(s_1)$ that satisfies $C_2(s_1) = \sin\psi(s_1) / r(s_1) \leq 1 / r(s_1)$. The discontinuity $C_1(s_1 + \varepsilon) - C_1(s_1 - \varepsilon)$ of the contour curvature vanishes if the two membrane segments have the same curvature-elastic properties, i.e., the same spontaneous curvature, bending rigidity, and Gaussian curvature modulus. The latter situation has been studied in (Kusumaatmaja et al., 2009) with the additional simplification that both membrane segments have zero spontaneous curvatures, i.e., $m_{\alpha\gamma} = m_{\beta\gamma} = 0$.

Balance between interfacial and segment tensions

A second boundary or matching condition is obtained from the first variation of the shape functional with respect to the variable $r_1 \equiv r(s_1)$ which represents the radius of the contact line. The resulting condition can be obtained from Eq. 5.F16, supplemented by one additional term arising from the interfacial tension $\Sigma_{\alpha\beta}$. We then obtain the balance condition (Lipowsky, 2018a)

$$\Sigma_{\beta\gamma} - \Sigma_{\alpha\gamma} = \Sigma_{\alpha\beta} \cos\theta_\alpha^* + \lambda_{co} \frac{\cos\psi_1}{r_1} + \Delta_{\Sigma,co} \quad (5.321)$$

with the intrinsic contact angle θ_α^* and the tilt angle $\psi_1 \equiv \psi(s_1)$, see Figure 5.41. The last term in Eq. 5.321 has the explicit form

$$\Delta_{\Sigma,co} = \frac{1}{2}\kappa_{\beta\gamma}Q_{\beta\gamma}(s_1 + \varepsilon) - \frac{1}{2}\kappa_{\alpha\gamma}Q_{\alpha\gamma}(s_1 - \varepsilon) \quad (5.322)$$

with the curvature-dependent terms

$$Q_{j\gamma}(s) \equiv C_1^2(s) - [C_2(s) - 2m_{j\gamma}]^2 \quad \text{for } j = \alpha, \beta. \quad (5.323)$$

These relations describe the balance between the capillary forces arising from the interfacial tension $\Sigma_{\alpha\beta}$, the tensions $\Sigma_{\beta\gamma}$ and $\Sigma_{\alpha\gamma}$ of the two membrane segments, and the line tension λ_{co} . The additional term $\Delta_{\Sigma,co}$ in Eq. 5.321 arises from the different curvature-elastic properties of the two membrane segments. Indeed, the term $\Delta_{\Sigma,co}$ vanishes if the two membrane segments have the same curvature-elastic properties. In the latter case, the force balance condition Eqs 5.321 simplifies and becomes

$$\Sigma_{\beta\gamma} - \Sigma_{\alpha\gamma} = W_{\beta\gamma} - W_{\alpha\gamma} = \Sigma_{\alpha\beta} \cos\theta_\alpha^* + \lambda_{co} \frac{\cos\psi_1}{r_1} \quad (5.324)$$

which depends on the difference of the two adhesive strengths $W_{\beta\gamma}$ and $W_{\alpha\gamma}$, the interfacial tension $\Sigma_{\alpha\beta}$, and the contact line tension λ_{co} . Thus, if the vesicle membrane continued to have laterally uniform curvature-elastic properties even when it is partially wetted by the two aqueous droplets, the force balance along the contact line as described by Eq. 5.324 would involve neither the bending rigidity nor the spontaneous curvature of the

membrane. For GUVs, the radius r_1 of the contact line is typically of the order of many micrometers. In such a situation, the term proportional to the line tension λ_{co} in (5.324) can be neglected which implies that the intrinsic contact angle θ_α^* depends only on two material parameters, the difference $W_{\beta\gamma} - W_{\alpha\gamma}$ of the two adhesive strengths and the interfacial tension $\Sigma_{\alpha\beta}$ of the water-water interface.

If the two membrane segments have different spontaneous curvatures but the same bending rigidities κ and the same Gaussian curvature moduli, the additional term $\Delta_{\Sigma,co}$ becomes

$$\Delta_{\Sigma,co} = 4\kappa[m_{\beta\gamma} - m_{\alpha\gamma}][M(s_1 - \varepsilon) - m_{\alpha\gamma}] \quad (5.325)$$

with the mean curvature $M = \frac{1}{2}(C_1 + C_2)$ which satisfies, for $\kappa_{\alpha\gamma} = \kappa_{\beta\gamma} = \kappa$ and $\kappa_{G,\alpha\gamma} = \kappa_{G,\beta\gamma}$, the matching condition

$$M(s_1 + \varepsilon) - m_{\beta\gamma} = M(s_1 - \varepsilon) - m_{\alpha\gamma} \quad (5.326)$$

along the contact line as follows from Eq. 5.319. Thus, the discontinuity in the mean curvature, $M(s_1 + \varepsilon) - M(s_1 - \varepsilon)$, is now equal to the difference in the spontaneous curvatures, $m_{\beta\gamma} - m_{\alpha\gamma}$, and the additional term $\Delta_{\Sigma,co}$ is proportional to this discontinuity.

At present, both the curvature discontinuities and the additional term $\Delta_{\Sigma,co}$ that enters the force balance relation (5.321) cannot be used to analyze the shapes of GUVs because the local membrane curvatures along the contact line have not been resolved by optical microscopy. Therefore, these matching conditions will not be further pursued in the following. On the other hand, the experimental observations revealed one universal feature of the partial wetting morphologies for GUVs, namely that the shapes of the two membrane segments are very well described by spherical caps which is a direct consequence of the capillary forces exerted by the $\alpha\beta$ interface onto the vesicle membrane. Because the $\alpha\beta$ interface necessarily forms a spherical cap as follows from the classical Laplace equation, the partial wetting morphologies consist of three surface segments that form three spherical caps and meet along the three-phase contact line, as displayed in Figure 5.42.

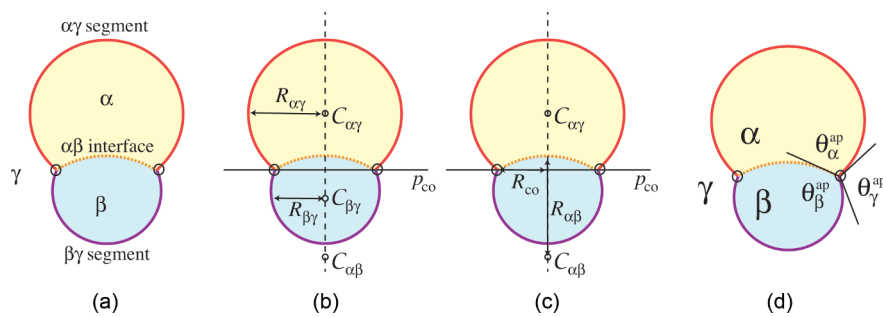


Figure 5.42 Cross-section of partial in-wetting morphology as observed experimentally: (a) Three spherical surface segments corresponding to the $\alpha\beta$ interface (dotted orange line) and to the two membrane segments $\alpha\gamma$ (red) and $\beta\gamma$ (purple). These three spherical caps meet along an apparent contact line (black circles); (b, c) The three-spherical-cap shape is determined by the curvature radii $R_{\alpha\gamma}$, $R_{\beta\gamma}$, and $R_{\alpha\beta}$ of the three spherical caps as well as by the contact line radius R_{co} . The three centers $C_{\alpha\gamma}$, $C_{\beta\gamma}$, and $C_{\alpha\beta}$ of the three spherical caps are located on the rotational symmetry axis (vertical dashed line). In order to obtain a unique shape, we also need to specify the locations of these cap centers relative to the contact line plane p_{co} (full horizontal line), see main text; and (d) At the contact line, the tangent planes to the three spherical surface segments define the three apparent contact angles θ_α^{ap} , θ_β^{ap} , and θ_γ^{ap} with $\theta_\alpha^{ap} + \theta_\beta^{ap} + \theta_\gamma^{ap} = 2\pi$. (From Lipowsky, R. *J. Phys. Chem. B*, 122, 3572–3586, 2018a.)

5.9.5 THREE-SPHERICAL-CAP SHAPES

Geometric relations for three spherical caps

From the optical microscopy images, we can directly deduce the curvature radii of the three spherical caps which will be denoted by $R_{\alpha\beta}$, $R_{\alpha\gamma}$, and $R_{\beta\gamma}$, respectively, see Figure 5.42b, c, and the centers of the spherical caps by $C_{\alpha\gamma}$, $C_{\beta\gamma}$, and $C_{\alpha\beta}$. We will again use the sign convention that all radii are always taken to be positive. Because the three spherical caps meet along the apparent contact line, the three cap centers $C_{\alpha\gamma}$, $C_{\beta\gamma}$, and $C_{\alpha\beta}$ are necessarily colinear. The straight line through these centers represents the axis of rotational symmetry for the three-spherical-cap shape corresponding to the vertical dashed line in Figure 5.42b,c. To obtain a certain three-spherical-cap shape, we also need to specify the radius R_{co} of the apparent contact line in addition to the curvature radii, see Figure 5.42c. In fact, the four length scales $R_{\alpha\beta}$, $R_{\alpha\gamma}$, $R_{\beta\gamma}$, and R_{co} are not quite sufficient to uniquely define the three-spherical-cap shape because we still need to specify (i) whether the two cap centers $C_{\alpha\gamma}$ and $C_{\beta\gamma}$ of the two membrane segments are located above or below the apparent contact line plane p_{co} as depicted by the horizontal full line in Figure 5.42b,c; and (ii) whether the cap center $C_{\alpha\beta}$ of the liquid-liquid interface is above or below this contact line plane corresponding to an $\alpha\beta$ interface that bulges towards the β or towards the α droplet.

For the example shown in Figure 5.42, the cap centers $C_{\alpha\gamma}$ and $C_{\beta\gamma}$ are located above and below the apparent contact line plane p_{co} , respectively. This location of the two cap centers implies that both membrane segments form spherical caps with an equator (or “belly”). In addition, the center $C_{\alpha\beta}$ of the $\alpha\beta$ interface is located below the plane p_{co} which implies that the $\alpha\beta$ interface bulges towards the α droplet corresponding to a pressure P_β in the β droplet that exceeds the pressure P_α in the α droplet. Keeping the four length scales fixed as well as the locations of the two cap centers $C_{\alpha\gamma}$ and $C_{\beta\gamma}$, we may also place the center $C_{\alpha\beta}$ above the contact line plane p_{co} which then leads to an $\alpha\beta$ interface that bulges towards the β droplet corresponding to $P_\alpha > P_\beta$.

We now introduce the sign convention that the mean curvature $M_{\alpha\beta}$ of the $\alpha\beta$ interface is *positive*, i.e.,

$$M_{\alpha\beta} = \frac{1}{R_{\alpha\beta}} > 0 \quad \text{for} \quad P_\alpha > P_\beta \quad (5.327)$$

and *negative* with

$$M_{\alpha\beta} = -\frac{1}{R_{\alpha\beta}} < 0 \quad \text{for} \quad P_\beta > P_\alpha. \quad (5.328)$$

With this sign convention, the classical Laplace equation for the $\alpha\beta$ interface assumes the form

$$P_\alpha - P_\beta = 2\Sigma_{\alpha\beta}M_{\alpha\beta} = \pm \frac{2\Sigma_{\alpha\beta}}{R_{\alpha\beta}} \quad (5.329)$$

where the plus and minus sign applies to $P_\alpha > P_\beta$ and $P_\beta > P_\alpha$, respectively.

Family of three-spherical-cap shapes with geometric constraints

As previously mentioned, the vesicle-droplet systems are characterized by three geometric constraints as provided by the droplet volumes V_α and V_β as well as by the total membrane area A . These three quantities can be expressed in terms of the four radii $R_{\alpha\beta}$, $R_{\alpha\gamma}$, $R_{\beta\gamma}$, and R_{co} which leads to three equations between the four radii. The solution of these three equations may be parametrized in terms of V_α , V_β , A , and a suitable reaction coordinate such as the apparent contact line radius R_{co} . As a result of this reparametrization, we obtain a one-parameter family of three-spherical-cap shapes that fulfill all three geometric constraints.

Apparent contact angles

Another set of geometric quantities that can be directly deduced from the optical microscopy images are the apparent contact angles $\theta_\alpha^{\text{ap}}$, θ_β^{ap} , and $\theta_\gamma^{\text{ap}}$, with $\theta_\alpha^{\text{ap}} + \theta_\beta^{\text{ap}} + \theta_\gamma^{\text{ap}} = 2\pi$ introduced in Figure 5.42d. The sines of these angles can be expressed in terms of the three curvature radii and the apparent contact line radius R_{co} . In general, one has to distinguish several cases depending on the relative locations of the cap centers $C_{\alpha\gamma}$, $C_{\beta\gamma}$, and $C_{\alpha\beta}$ with respect to the contact line plane p_{co} . When these cap centers have the relative locations as in Figure 5.42b,c, corresponding to $P_\beta > P_\alpha$, we obtain the explicit relationships (Lipowsky, 2018a)

$$\sin \theta_\alpha^{\text{ap}} = \frac{R_{co}}{R_{\alpha\beta}R_{\alpha\gamma}} \left(\sqrt{R_{\alpha\beta}^2 - R_{co}^2} + \sqrt{R_{\alpha\gamma}^2 - R_{co}^2} \right), \quad (5.330)$$

$$\sin \theta_\beta^{\text{ap}} = \frac{R_{co}}{R_{\alpha\beta}R_{\beta\gamma}} \left(\sqrt{R_{\alpha\beta}^2 - R_{co}^2} - \sqrt{R_{\beta\gamma}^2 - R_{co}^2} \right), \quad (5.331)$$

with $R_{\alpha\beta} \geq R_{\beta\gamma}$ and

$$\sin \theta_\gamma^{\text{ap}} = \frac{R_{co}}{R_{\alpha\gamma}R_{\beta\gamma}} \left(\sqrt{R_{\alpha\gamma}^2 - R_{co}^2} + \sqrt{R_{\beta\gamma}^2 - R_{co}^2} \right). \quad (5.332)$$

If the two cap centers $C_{\alpha\gamma}$ and $C_{\beta\gamma}$ have the same locations as in Figure 5.42 but the cap center $C_{\alpha\beta}$ is moved to a location above the contact line plane p_{co} , corresponding to $P_\alpha > P_\beta$, these relations assume the slightly modified form

$$\sin \theta_\alpha^{\text{ap}} = \frac{R_{co}}{R_{\alpha\beta}R_{\alpha\gamma}} \left(\sqrt{R_{\alpha\beta}^2 - R_{co}^2} - \sqrt{R_{\alpha\gamma}^2 - R_{co}^2} \right) \quad (5.333)$$

with $R_{\alpha\beta} \geq R_{\alpha\gamma}$,

$$\sin \theta_\beta^{\text{ap}} = \frac{R_{co}}{R_{\alpha\beta}R_{\beta\gamma}} \left(\sqrt{R_{\alpha\beta}^2 - R_{co}^2} + \sqrt{R_{\beta\gamma}^2 - R_{co}^2} \right), \quad (5.334)$$

and

$$\sin \theta_\gamma^{\text{ap}} = \frac{R_{co}}{R_{\alpha\gamma}R_{\beta\gamma}} \left(\sqrt{R_{\alpha\gamma}^2 - R_{co}^2} + \sqrt{R_{\beta\gamma}^2 - R_{co}^2} \right). \quad (5.335)$$

The latter expression is identical with Eq. 5.332 but the first two expressions differ from Eqs 5.330 and 5.331 in the signs before the second square root.

These explicit relations between the sines of the apparent contact angles and the four radii directly demonstrate that the apparent contact angles are determined by the size and shape of the GUVs. In particular, all three angles change when we vary the apparent contact line radius R_{co} .

Angle-curvature relationship

Finally, using some trigonometric relations, it is not difficult to show that the curvature radii and the apparent contact angles satisfy the relation

$$\mp \frac{\sin \theta_\gamma^{\text{ap}}}{R_{\alpha\beta}} = \frac{\sin \theta_\alpha^{\text{ap}}}{R_{\beta\gamma}} - \frac{\sin \theta_\beta^{\text{ap}}}{R_{\alpha\gamma}} \quad (5.336)$$

where the minus and plus sign applies to an $\alpha\beta$ interface that bulges towards the α and the β droplet, respectively. The equalities in Eq. 5.336, which do not depend on the apparent contact line radius R_{co} , may be used to estimate the accuracy of the measured values for the curvature radii and apparent contact angles. When expressed in terms of the mean curvatures, the purely geometric relation (5.336) becomes

$$M_{\alpha\beta} \sin \theta_\gamma^{\text{ap}} = M_{\alpha\gamma} \sin \theta_\beta^{\text{ap}} - M_{\beta\gamma} \sin \theta_\alpha^{\text{ap}}. \quad (5.337)$$

Shape equations for spherical caps

When the membrane segments $\alpha\gamma$ and $\beta\gamma$ assume spherical cap shapes, the shape Eqs 5.316 assume the simplified form

$$P_j - P_\gamma = 2\hat{\Sigma}_{j\gamma} M_{j\gamma} - 4\kappa_{j\gamma} m_{j\gamma} M_{j\gamma}^2 \quad \text{with } j = \alpha, \beta \quad (5.338)$$

with the total segment tensions $\hat{\Sigma}_{j\gamma} \equiv \Sigma_{j\gamma} + \sigma_{j\gamma} = \Sigma + W_{j\gamma} + \sigma_{j\gamma}$ as in Eq. 5.317 and the spontaneous segment tensions $\sigma_{j\gamma} = 2\kappa_{j\gamma} m_{j\gamma}^2$ as in Eq. 5.318. The shape Eqs 5.338 can be rewritten in the more compact form

$$P_j - P_\gamma = 2\Sigma_{j\gamma}^{\text{eff}} M_{j\gamma} \quad \text{with } j = \alpha, \beta \quad (5.339)$$

with the effective tensions

$$\Sigma_{j\gamma}^{\text{eff}} \equiv \hat{\Sigma}_{j\gamma} - 2\kappa_{j\gamma} m_{j\gamma} M_{j\gamma} = \Sigma_{j\gamma} + \sigma_{j\gamma} - 2\kappa_{j\gamma} m_{j\gamma} M_{j\gamma} \quad (5.340)$$

which depend on the mean curvatures $M_{j\gamma}$. Note that these shape equations now determine the *constant* mean curvatures $M_{\alpha\gamma}$ and $M_{\beta\gamma}$ of the two spherical membrane segments. Because both mean curvatures are necessarily positive, a positive value of $P_j - P_\gamma$ implies a positive value of the effective tension $\Sigma_{j\gamma}^{\text{eff}}$.

A linear combination of the Laplace Eq. 5.329 for the $\alpha\beta$ interface and the shape Eqs 5.339 for the two membrane segments can be used to eliminate the three pressure differences. As a result, we obtain the relation

$$\Sigma_{\alpha\beta} M_{\alpha\beta} = \Sigma_{\alpha\gamma}^{\text{eff}} M_{\alpha\gamma} - \Sigma_{\beta\gamma}^{\text{eff}} M_{\beta\gamma} \quad (5.341)$$

between the interfacial tension $\Sigma_{\alpha\beta}$ and the effective tensions $\Sigma_{\alpha\gamma}^{\text{eff}}$ and $\Sigma_{\beta\gamma}^{\text{eff}}$ experienced by the two membrane segments.

Relationship between tensions and angles

Using a combination of the geometric relation, Eq. 5.337, and the curvature-tension relation, Eq. 5.341, we can now eliminate the mean curvature $M_{\alpha\beta}$ of the $\alpha\beta$ interface which leads to the relationship (Lipowsky, 2018a)

$$M_{\alpha\gamma} \left(\frac{\Sigma_{\alpha\gamma}^{\text{eff}}}{\Sigma_{\alpha\beta}} - \frac{\sin \theta_\beta^{\text{ap}}}{\sin \theta_\gamma^{\text{ap}}} \right) = M_{\beta\gamma} \left(\frac{\Sigma_{\beta\gamma}^{\text{eff}}}{\Sigma_{\alpha\beta}} - \frac{\sin \theta_\alpha^{\text{ap}}}{\sin \theta_\gamma^{\text{ap}}} \right) \quad (5.342)$$

between the effective tensions, the apparent contact angles, and the mean curvatures of the $\alpha\gamma$ and $\beta\gamma$ membrane segments. It is important to note that the derivation of Eq. 5.342 was based (i) on the purely geometric relation, Eq. 5.337, which applies to three spherical caps that intersect along the apparent contact line and (ii) on the shape equations for the spherical membrane segments and the $\alpha\beta$ interface. In particular, this derivation did not make any assumptions about the mechanical balance of the interfacial and membrane tensions along the apparent contact line.

The relationship in Eq. 5.342 is reminiscent of the relation as given by Eq. 5.H7 in Appendix 5.H which applies to two membraneless droplets adhering to each other within a bulk liquid without a vesicle. The latter relation depends only on the contact angles and on the interfacial tensions, both of which represent material parameters. In contrast, the relationship in Eq. 5.342 for partial in-wetting of GUVs depends on several geometry-dependent parameters: (i) Explicitly on the mean curvatures $M_{\alpha\gamma} = 1/R_{\alpha\gamma}$ and $M_{\beta\gamma} = 1/R_{\beta\gamma}$ of the two membrane segments; (ii) Implicitly on these two curvatures via the effective tensions $\Sigma_{\alpha\gamma}^{\text{eff}}$ and $\Sigma_{\beta\gamma}^{\text{eff}}$; and (iii) On the apparent contact angles which are determined by the three-spherical-cap geometry as described in Eqs 5.330 to 5.332 for $P_\beta > P_\alpha$ and in Eqs 5.333 to 5.335 for $P_\alpha > P_\beta$.¹⁷

Parameter dependencies

On the other hand, many of the parameters that enter Eq. 5.342 can be determined experimentally. The interfacial tension $\Sigma_{\alpha\beta}$ represents a material parameter that can be obtained via experimental studies of macroscopic $\alpha\beta$ interfaces as demonstrated for PEG-dextran solutions in (Liu et al., 2012). In addition, the apparent contact angles and the mean curvatures can be obtained, for each vesicle-droplet couple, from optical microscopy experiments. It is less obvious how to determine the parameter combinations that enter the effective membrane tensions $\Sigma_{j\gamma}^{\text{eff}}$ as given by Eq. 5.340. These parameter combinations are the total segment tensions $\hat{\Sigma}_{j\gamma} = \Sigma + W_{j\gamma} + 2\kappa_{j\gamma} m_{j\gamma}^2$ as defined by Eq 5.317 and the combinations $\kappa_{j\gamma} m_{j\gamma}$ with $j = \alpha$ or β . Without prior knowledge about the bending rigidities and the spontaneous curvatures, these four parameter combinations should be regarded as unknowns that enter the relationship in Eq. 5.342 in a linear fashion. In order to determine four unknowns, we need four linearly independent equations.

¹⁷ In both cases, the cap centers $C_{\alpha\gamma}$ and $C_{\beta\gamma}$ are located on different sides of the contact line plane p_{co} . Slightly different relations apply if these two cap centers are located on the same side of p_{co} which implies that one of the membrane segments attains a spherical cap without an equator.

To obtain such a set of equations, we might want to apply the relationship in Eq. 5.342 to four different vesicle-droplet couples as obtained from the same vesicle batch or the same preparation protocol. The four couples should then have the same composition of the vesicle membrane and the same composition of the different aqueous phases. As a consequence, all four vesicle-droplet couples should be characterized by the same interfacial tension $\Sigma_{\alpha\beta}$, the same adhesive strengths $W_{j\gamma}$, the same spontaneous curvatures $m_{j\gamma}$, and the same bending rigidities $\kappa_{j\gamma}$ because all of these quantities represent material parameters. However, the total segment tensions also include the overall lateral stress Σ that does *not* represent a material parameter but depends on the vesicle geometry and, thus, will vary from vesicle to vesicle even within the same batch. Therefore, if we applied the relationship in Eq. 5.342 to four different vesicle-droplet couples, the corresponding total segment tensions would involve four different stresses. As a consequence, each additional vesicle-droplet system would introduce one additional unknown as provided by the lateral stress experienced by the corresponding vesicle membrane.

To address this difficulty, two strategies can be pursued. First, we could consider GUVs with low lateral stresses Σ that fulfill the condition

$$|\Sigma| \ll W_{j\gamma} + 2\kappa_{j\gamma} m_{j\gamma}^2 \quad \text{for } j = \alpha \text{ or } \beta. \quad (5.343)$$

We could then ignore these stresses and estimate the total segment tensions by their asymptotic behavior

$$\hat{\Sigma}_{j\gamma} \approx W_{j\gamma} + 2\kappa_{j\gamma} m_{j\gamma}^2. \quad (5.344)$$

In the latter case, the total segment tensions would have the same values for all vesicle-droplet couples from the same batch. On the one hand, one would expect intuitively that the lateral stresses can be strongly reduced by osmotic deflation of the GUVs. On the other hand, the inequality in Eq. 5.343 involves two terms that may have different signs: the spontaneous tension $2\kappa_{j\gamma} m_{j\gamma}^2$ is always positive but the affinity strength $W_{j\gamma}$ will be negative when the membranes prefers the j phase over the γ phase. These two terms could cancel each other to a large extent, implying that the lateral stress must become ultralow in order to fulfill the inequality in Eq. 5.343.

A second strategy that does not involve any assumption about the magnitude of the lateral stress Σ is to consider several droplets adhering to the same vesicle. This strategy is described in the next paragraph.

Several droplets adhering to the same GUV

Thus, consider a situation in which several α droplets adhere to the interior leaflet of the same GUV membrane. These droplets coexist with one large β droplet inside the GUV. The different α droplets are labeled by $n = 1, 2, \dots, N$. The vesicle membrane is then partitioned into $N + 1$ segments labeled by $n\gamma$ and $\beta\gamma$. The different $n\gamma$ segments experience the effective membrane tensions

$$\Sigma_{\alpha\gamma}^{(n)} = \Sigma + W_{\alpha\gamma} + \sigma_{\alpha\gamma} - 2\kappa_{\alpha\gamma} m_{\alpha\gamma} M_{\alpha\gamma}^{(n)} \quad (5.345)$$

where all parameters on the right hand side are independent of n apart from the mean curvatures $M_{\alpha\gamma}^{(n)}$ of the $n\gamma$ segments. For such a geometry, we obtain N relationships of the form

$$M_{\alpha\gamma}^{(n)} \left(\frac{\Sigma_{\alpha\gamma}^{(n)}}{\Sigma_{\alpha\beta}} - \frac{\sin \theta_{\beta}^{(n)}}{\sin \theta_{\gamma}^{(n)}} \right) = M_{\beta\gamma} \left(\frac{\Sigma_{\beta\gamma}^{\text{eff}}}{\Sigma_{\alpha\beta}} - \frac{\sin \theta_{\alpha}^{(n)}}{\sin \theta_{\gamma}^{(n)}} \right) \quad (5.346)$$

with $n = 1, 2, \dots, N$. This set of equations can be rewritten in the form

$$\Upsilon_{\alpha\gamma}^{(n)} \equiv M_{\alpha\gamma}^{(n)} \left(\frac{\Sigma_{\alpha\gamma}^{(n)}}{\Sigma_{\alpha\beta}} - \frac{\sin \theta_{\beta}^{(n)}}{\sin \theta_{\gamma}^{(n)}} \right) + M_{\beta\gamma} \frac{\sin \theta_{\alpha}^{(n)}}{\sin \theta_{\gamma}^{(n)}} = M_{\beta\gamma} \frac{\Sigma_{\beta\gamma}^{\text{eff}}}{\Sigma_{\alpha\beta}} \quad (5.347)$$

where the last term is independent of the droplet label n . We then conclude that (Lipowsky, 2018a)

$$\Upsilon_{\alpha\gamma}^{(1)} = \Upsilon_{\alpha\gamma}^{(2)} = \dots = \Upsilon_{\alpha\gamma}^{(N)}. \quad (5.348)$$

Therefore, from three different $n\gamma$ segments with three distinct mean curvatures $M_{\alpha\gamma}^{(n)}$ and, thus, three distinct expressions $\Upsilon_{\alpha\gamma}^{(n)}$, we obtain two linearly independent equations from which can deduce the two parameter combinations $(\Sigma + W_{\alpha\gamma} + \sigma_{\alpha\gamma})/\Sigma_{\alpha\beta}$ and $\kappa_{\alpha\gamma} m_{\alpha\gamma}/\Sigma_{\alpha\beta}$ for any value of Σ .

5.9.6 SHAPE FUNCTIONAL FOR THREE SPHERICAL CAPS

So far, we did not consider the force balance along the apparent contact line of the three spherical cap segments. We now address this force balance using a somewhat different approach. We start from the energy functional $\mathcal{E}_{2\text{Dr}}^{\text{in}}\{\mathcal{S}\}$ and the shape functional $\mathcal{F}_{2\text{Dr}}^{\text{in}}\{\mathcal{S}\}$ as given by Eqs 5.310 and 5.312 and apply these functionals to the three-spherical-cap shapes $\mathcal{S} = \mathcal{S}^{\text{sc}}$ which include the spherical cap shapes $\mathcal{S}_{\alpha\gamma}^{\text{sc}}$ and $\mathcal{S}_{\beta\gamma}^{\text{sc}}$ of the two membrane segments. The energy functional $\mathcal{E}_{2\text{Dr}}^{\text{in}}\{\mathcal{S}\}$ then assumes the form

$$\mathcal{E}_{2\text{Dr}}^{\text{in}}\{\mathcal{S}^{\text{sc}}\} = E^{\text{in}}(R_{\alpha\beta}, R_{\alpha\gamma}, R_{\beta\gamma}, R_{\text{co}}) \quad (5.349)$$

where the energy E^{in} represents an explicit function of the four variables $R_{\alpha\beta}$, $R_{\alpha\gamma}$, $R_{\beta\gamma}$, and R_{co} . The contributions from the Gaussian curvature energies and from the line tension are confined to the true contact line which is embedded in a highly curved membrane segment. These latter segment is lost when we use the three-spherical-cap approximation and replace the true by the apparent contact line. Therefore, we will now ignore these two energetic contributions. The energy function E^{in} then has the form

$$E^{\text{in}} = \sum_{j=\alpha,\beta} E_{j\gamma}^{\text{in}} \quad \text{with } E_{j\gamma}^{\text{in}} = W_{j\gamma} A_{j\gamma} + E_{j\gamma}^{\text{in,be}} \quad (5.350)$$

which consists of the adhesion free energies $W_{j\gamma} A_{j\gamma}$ and the bending energy contributions

$$E_{j\gamma}^{\text{in,be}} \equiv 2\kappa_{j\gamma} A_{j\gamma} (M_{j\gamma} - m_{j\gamma})^2 \quad (5.351)$$

with $j = \alpha$ or β and constant mean curvatures $M_{j\gamma} = 1/R_{j\gamma}$.

Likewise, when we apply the shape functional in Eq. 5.312 to the three-spherical-cap shape S^{sc} , the resulting expression

$$\mathcal{F}^{in}\{S^{sc}\} = F^{in}(R_{\alpha\beta}, R_{\alpha\gamma}, R_{\beta\gamma}, R_{co}) \quad (5.352)$$

also becomes an explicit function F^{in} of the four radii. This function has the form

$$F^{in} = (P_\gamma - P_\alpha)V_\alpha + (P_\gamma - P_\beta)V_\beta + \Sigma(A_{\alpha\gamma} + A_{\beta\gamma}) + E^{in} \quad (5.353)$$

with the energy function E^{in} as given by Eq. 5.350. It will be convenient to rewrite this shape function according to

$$F^{in} = (P_\gamma - P_\alpha)V_\alpha + (P_\gamma - P_\beta)V_\beta + \Delta F^{in} \quad (5.354)$$

with

$$\Delta F^{in} \equiv \Sigma_{\alpha\beta}A_{\alpha\beta} + \Sigma_{\alpha\gamma}A_{\alpha\gamma} + \Sigma_{\beta\gamma}A_{\beta\gamma} + \sum_{j=\alpha,\beta} E_{j\gamma,be}^{in} \quad (5.355)$$

and the mechanical segment tensions $\Sigma_{j\gamma} = \Sigma + W_{j\gamma}$ as defined in Eq. 5.314.

In order to obtain a self-consistent description, we will now consider two limiting cases corresponding to small spontaneous curvatures and small bending energies as well as large spontaneous curvatures and large spontaneous tensions.

Small spontaneous curvatures and small bending energies

For membrane segment $j\gamma$, the regime of small spontaneous curvature will be defined by

$$(1 - |\eta|)M_{j\gamma} \leq m_{j\gamma} \leq (1 + |\eta|)M_{j\gamma} \quad (\text{small curvature } m_{j\gamma}) \quad (5.356)$$

with a dimensionless coefficient $|\eta| > 0$ of order one. For these $m_{j\gamma}$ -values, the segment's bending energy $E_{j\gamma,be}^{in}$ satisfies the inequality

$$E_{j\gamma,be}^{in} = 2\kappa_{j\gamma}(M_{j\gamma} - m_{j\gamma})^2 A_{j\gamma} \leq 2\kappa_{j\gamma} |\eta|^2 M_{j\gamma}^2 A_{j\gamma}. \quad (5.357)$$

In terms of the curvature radius $R_{j\gamma}$ of membrane segment $j\gamma$, we obtain the squared mean curvature $M_{j\gamma}^2 = R_{j\gamma}^{-2}$ and the segment area

$$A_{j\gamma} = 4\pi\zeta_{j\gamma}R_{j\gamma}^2 \quad \text{with} \quad \zeta_{j\gamma} \equiv \frac{A_{j\gamma}}{4\pi R_{j\gamma}^2} \quad (5.358)$$

which implies the inequality

$$E_{j\gamma,be}^{in} \leq 8\pi\kappa_{j\gamma} |\eta|^2 \zeta_{j\gamma} \quad \text{with} \quad 0 < \zeta_{j\gamma} < 1 \quad (5.359)$$

for the bending energy of the $j\gamma$ segment.

The small bending energy regime for the $j\gamma$ segment will now be defined by the condition that this energy is small compared to the interfacial free energy $\Sigma_{\alpha\beta}A_{\alpha\beta}$, i.e., by the condition

$$E_{j\gamma,be}^{in} \ll \Sigma_{\alpha\beta}A_{\alpha\beta} \quad (\text{small bending energy } E_{j\gamma,be}^{in}). \quad (5.360)$$

Using the two inequalities in Eq. 5.359, the condition in Eq. 5.360 can be fulfilled by

$$E_{j\gamma,be}^{in} \leq 8\pi\kappa_{j\gamma} |\eta|^2 \ll \Sigma_{\alpha\beta}A_{\alpha\beta} \quad (5.361)$$

or

$$A_{\alpha\beta} \gg 8\pi |\eta|^2 \frac{\kappa_{j\gamma}}{\Sigma_{\alpha\beta}} \quad (5.362)$$

with the dimensionless coefficient $|\eta|$ of order one, see Eq. 5.356.¹⁸

Thus, if the spontaneous curvature $m_{j\gamma}$ is small and satisfies the inequalities in Eq. 5.356 and if the interfacial area $A_{j\gamma}$ is large and satisfies the inequality in Eq. 5.362, we can ignore the bending energy $E_{j\gamma,be}^{in}$ of the membrane segment $j\gamma$ compared to the interfacial free energy $\Sigma_{\alpha\beta}A_{\alpha\beta}$. The energy contribution from this segment, see Eq. 5.350, then has the simple form

$$E_{j\gamma}^{in} \approx W_{j\gamma}A_{j\gamma}, \quad (5.363)$$

i.e., this contribution is dominated by the adhesion free energy between the membrane and the α or β droplet.

Large spontaneous curvatures and spontaneous tensions

For segment $j\gamma$, the regime of large spontaneous curvatures is defined by

$$|m_{j\gamma}| \gg |M_{j\gamma}| \quad (\text{regime of large } m_{j\gamma}). \quad (5.364)$$

In the latter regime, the bending energy $E_{j\gamma,be}^{in}$ of the $j\gamma$ segment becomes

$$E_{j\gamma,be}^{in} \approx 2\kappa_{j\gamma}m_{j\gamma}^2 A_{j\gamma} = \sigma_{j\gamma}A_{j\gamma} \quad (5.365)$$

with the spontaneous tension $\sigma_{j\gamma}$ which implies the contribution

$$E_{j\gamma}^{in} \approx (W_{j\gamma} + \sigma_{j\gamma})A_{j\gamma} \quad (5.366)$$

of the $j\gamma$ segment to the energy function E^{in} in Eq. 5.350.

Shape functions for special parameter regimes

If both segments belong to the small spontaneous curvature and small bending energy regime, the shape function ΔF^{in} as given by Eq. 5.355 simplifies and becomes $\Delta F^{in} = \Delta F_{s+s}^{in}$ with the area-dependent shape function

$$\Delta F_{s+s}^{in} \equiv \Sigma_{\alpha\beta}A_{\alpha\beta} + \Sigma_{\alpha\gamma}A_{\alpha\gamma} + \Sigma_{\beta\gamma}A_{\beta\gamma} \quad (\text{small + small regime}) \quad (5.367)$$

which depends on the mechanical segment tensions $\Sigma_{\alpha\gamma}$ and $\Sigma_{\beta\gamma}$. On the other hand, if both membrane segments belong to the

¹⁸ The numerical value of $|\eta|$ was taken to be $|\eta| = 3/2$ in (Lipowsky, 2018a).

large spontaneous curvature regime, we obtain the shape function $\Delta F_{l+}^{\text{in}} = \Delta F_{l+}^{\text{in}}$ with

$$\Delta F_{l+}^{\text{in}} \equiv \Sigma_{\alpha\beta} A_{\alpha\beta} + \hat{\Sigma}_{\alpha\gamma} A_{\alpha\gamma} + \hat{\Sigma}_{\beta\gamma} A_{\beta\gamma} \quad (\text{large + large regime}). \quad (5.368)$$

with the total segment tensions $\hat{\Sigma}_{j\gamma} = \Sigma_{j\gamma} + \sigma_{j\gamma} = \Sigma + W_{j\gamma} + 2\kappa_{j\gamma} m_{j\gamma}^2$ as in Eq. 5.317.

Finally, if one membrane segment, say $\alpha\gamma$, has a large spontaneous curvature whereas the other membrane segment, $\beta\gamma$, has a small spontaneous curvature, the shape function becomes $\Delta F_{l+s}^{\text{in}} = \Delta F_{l+s}^{\text{in}}$ with

$$\Delta F_{l+s}^{\text{in}} \equiv \Sigma_{\alpha\beta} A_{\alpha\beta} + \hat{\Sigma}_{\alpha\gamma} A_{\alpha\gamma} + \Sigma_{\beta\gamma} A_{\beta\gamma} \quad (\text{large + small regime}). \quad (5.369)$$

Note that we can obtain the shape function for the small-small regime from the shape function for the large-large regime by putting the spontaneous curvatures $m_{j\gamma}$ and, thus, the spontaneous segment tensions $\sigma_{j\gamma}$ equal to zero for both segments which implies that the total segment tensions $\hat{\Sigma}_{j\gamma}$ reduce to the mechanical segment tensions $\Sigma_{j\gamma}$. Likewise, we obtain the shape function for the large-small regime from the shape function of the large-large regime by putting the spontaneous tension $\sigma_{\beta\gamma}$ of the $\beta\gamma$ membrane segment equal to zero which leads to $\hat{\Sigma}_{\beta\gamma} = \Sigma_{\beta\gamma}$.

5.9.7 FORCE BALANCE ALONG APPARENT CONTACT LINE

Constrained energy minimization within the subspace of three-spherical-cap shapes then implies the four stationarity conditions (Lipowsky, 2018a)

$$\frac{\partial F^{\text{in}}}{\partial R_{\alpha\beta}} = 0, \quad \frac{\partial F^{\text{in}}}{\partial R_{\alpha\gamma}} = 0, \quad \frac{\partial F^{\text{in}}}{\partial R_{\beta\gamma}} = 0, \quad \text{and} \quad \frac{\partial F^{\text{in}}}{\partial R_{\text{co}}} = 0. \quad (5.370)$$

It is not difficult to show that the first condition $\partial F^{\text{in}}/\partial R_{\alpha\beta} = 0$ is equivalent to the classical Laplace Eq. 5.329 for the curvature radius $R_{\alpha\beta}$ of the $\alpha\beta$ interface. We should also require that the two stationarity relations $\partial F^{\text{in}}/\partial R_{\alpha\gamma} = 0$ and $\partial F^{\text{in}}/\partial R_{\beta\gamma} = 0$ lead back to the shape Eqs 5.339 for the curvature radii $R_{\alpha\gamma}$ and $R_{\beta\gamma}$ of the two membrane segments. The latter requirement is, however, not fulfilled in general but only for certain regions of the parameter space.

These special parameter regions include the small-small, large-large, and large-small regimes described in the previous subsection and defined by the shape functions ΔF^{in} in Eqs 5.367 to 5.369. All of these shape functions have the same form as the shape function ΔF_o for two membraneless droplets as given by Eq 5.H12 in Appendix 5.H when we substitute the interfacial tensions $\Sigma_{\alpha\gamma}$ and $\Sigma_{\beta\gamma}$ of the membraneless droplets by the mechanical or total tensions of the membrane segments. Using the same substitution in the force balance Eq. 5.H9 for membraneless droplets, we obtain the corresponding force balance conditions for the membrane-enclosed droplets.

As explained above, we can recover the small-small regime from the large-large regime by putting the spontaneous tensions of the two membrane segments equal to zero. Likewise, we can recover the large-small regime from the large-large regime by putting the spontaneous tension $\sigma_{\beta\gamma}$ equal to zero. Therefore, it is sufficient to consider the substitution in the force balance Eq. 5.H9 for the large-large regime. In the latter case, the interfacial tensions $\Sigma_{\alpha\gamma}$ and $\Sigma_{\beta\gamma}$ in Eq. 5.H9 for membraneless droplets have to be substituted by the total segment tensions $\hat{\Sigma}_{\alpha\gamma}$ and $\hat{\Sigma}_{\beta\gamma}$, respectively. As a result, we obtain the force balance conditions

$$\frac{\Sigma_{\alpha\beta}}{\sin \theta_{\gamma}^{\text{ap}}} = \frac{\hat{\Sigma}_{\alpha\gamma}}{\sin \theta_{\beta}^{\text{ap}}} = \frac{\hat{\Sigma}_{\beta\gamma}}{\sin \theta_{\alpha}^{\text{ap}}} \quad (\text{large-large regime}) \quad (5.371)$$

between the $\alpha\beta$ interface and the two membrane segments along the apparent contact line. These conditions are equivalent to the two linearly independent relationships

$$\frac{\hat{\Sigma}_{\alpha\gamma}}{\Sigma_{\alpha\beta}} = \frac{\sin \theta_{\beta}^{\text{ap}}}{\sin \theta_{\gamma}^{\text{ap}}} \quad \text{and} \quad \frac{\hat{\Sigma}_{\beta\gamma}}{\Sigma_{\alpha\beta}} = \frac{\sin \theta_{\alpha}^{\text{ap}}}{\sin \theta_{\gamma}^{\text{ap}}} \quad (\text{large-large regime}) \quad (5.372)$$

between the tensions and the contact angles (Lipowsky, 2013, 2014b). The force balance as given by Eq. 5.371 represents the law of sines for a triangle with the three sides $\Sigma_{\alpha\beta}$, $\hat{\Sigma}_{\alpha\gamma}$, and $\hat{\Sigma}_{\beta\gamma}$ as displayed in Figure 5.43b. For membraneless droplets, the corresponding triangle is displayed in Figure 5.48.

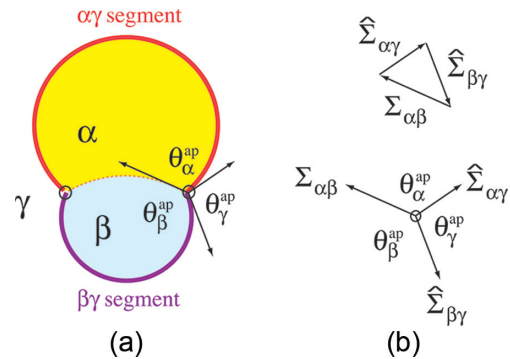


Figure 5.43 Force balance along the apparent contact line for small and large spontaneous curvatures: (a) Partial in-wetting morphology of vesicle (red, purple) enclosing two aqueous droplets of α (yellow) and β (blue) phase immersed in the exterior liquid γ (white). As in Figure 5.42, the membrane segments $\alpha\gamma$ (red) and $\beta\gamma$ (purple) form spherical caps that meet the $\alpha\beta$ interface (broken orange) along the apparent contact line (small black circles) where the three surface segments form the apparent contact angles $\theta_{\alpha}^{\text{ap}}$, $\theta_{\beta}^{\text{ap}}$, and $\theta_{\gamma}^{\text{ap}}$; and (b) Force balance between the interfacial tension $\Sigma_{\alpha\beta}$ as well as the total tensions $\hat{\Sigma}_{\alpha\gamma}$ and $\hat{\Sigma}_{\beta\gamma}$ of the two membrane segments as defined by Eq. 5.317. The three tensions form a triangle which implies the relations in Eqs 5.371 and 5.372 (Lipowsky, 2013, 2018a). The latter relations can be explicitly derived for three parameter regimes: (i) if both spontaneous curvatures are large as defined by Eq. 5.364, (ii) if both spontaneous curvatures are small and the interfacial area $A_{\alpha\beta}$ is sufficiently large as in Eqs 5.356 and 5.362, which implies $\hat{\Sigma}_{j\gamma} \approx \Sigma_{j\gamma}$; and (iii) for one small and one large spontaneous curvature.

Essentially the same force balance conditions apply to the small-small and large-small regimes. If the $\beta\gamma$ membrane segment belongs to the regime of small spontaneous curvature and small bending energy, the corresponding force balance conditions are obtained from those in Eqs 5.371 and 5.372 by replacing the total segment tension $\hat{\Sigma}_{\beta\gamma} = \Sigma_{\beta\gamma} + \sigma_{\beta\gamma}$ by the mechanical segment tension $\Sigma_{\beta\gamma}$. Likewise, the conditions for the small-small regime are obtained by replacing the total segment tensions $\hat{\Sigma}_{j\gamma}$ of both segments by the mechanical segment tensions $\Sigma_{j\gamma}$.

Difference of total segment tensions

Subtracting the two force balance relations in Eq. 5.372 from each other, we obtain the difference

$$\frac{\hat{\Sigma}_{\beta\gamma} - \hat{\Sigma}_{\alpha\gamma}}{\Sigma_{\alpha\beta}} = \frac{W_{\beta\gamma} - W_{\alpha\gamma} + \sigma_{\beta\gamma} - \sigma_{\alpha\gamma}}{\Sigma_{\alpha\beta}} = \Xi(\theta_{\alpha}^{\text{ap}}, \theta_{\beta}^{\text{ap}}, \theta_{\gamma}^{\text{ap}}) \quad (5.373)$$

with the function

$$\Xi(x, y, z) = \frac{\sin x - \sin y}{\sin z}, \quad (5.374)$$

as in Eq. 5.H19. Note that the overall lateral stress Σ , which depends on the vesicle geometry, drops out from the difference $\hat{\Sigma}_{\beta\gamma} - \hat{\Sigma}_{\alpha\gamma}$. As a consequence, Eq. 5.373 provides a relation between the apparent contact angles $\theta_{\alpha}^{\text{ap}}$, $\theta_{\beta}^{\text{ap}}$, and $\theta_{\gamma}^{\text{ap}}$, the adhesive strengths $W_{\alpha\gamma}$ and $W_{\beta\gamma}$, and the spontaneous tensions $\sigma_{\alpha\gamma}$ and $\sigma_{\beta\gamma}$, i.e., between the apparent contact angles and material parameters. As shown in Appendix 5.H.4, the function $\Xi(\theta_{\alpha}^{\text{ap}}, \theta_{\beta}^{\text{ap}}, \theta_{\gamma}^{\text{ap}})$ satisfies the inequalities

$$-1 \leq \Xi(\theta_{\alpha}^{\text{ap}}, \theta_{\beta}^{\text{ap}}, \theta_{\gamma}^{\text{ap}}) \leq +1 \quad (5.375)$$

as follows from the triangle inequalities for the triangle in Figure 5.43b. The upper bound $\Xi = +1$ is obtained for the apparent contact angles $\theta_{\alpha}^{\text{ap}} = 0$ and $\theta_{\beta}^{\text{ap}} = \theta_{\gamma}^{\text{ap}} = \pi$, corresponding to complete wetting of the membrane by the α phase as in Figure 5.40b. The lower bound $\Xi = -1$ is obtained for the angles $\theta_{\beta}^{\text{ap}} = 0$ and $\theta_{\alpha}^{\text{ap}} = \theta_{\gamma}^{\text{ap}} = \pi$, corresponding to complete wetting of the membrane by the β phase as shown in Figure 5.40c.

Relation between apparent and intrinsic contact angles

For some special parameter regions, we can also obtain a simple relation between the apparent contact angles in Figure 5.42 and the intrinsic contact angle in Figure 5.41. We now consider two membrane segments that have essentially the same curvature-elastic properties which implies the simplified force balance

$$\Sigma_{\beta\gamma} - \Sigma_{\alpha\gamma} = \Sigma_{\alpha\beta} \cos \theta_{\alpha}^* \quad (5.376)$$

along the true contact line as described by Eq. 5.324 where we assumed a large contact line radius and ignored the term proportional to the line tension λ_{co} . Two membrane segments with the

same curvature-elastic properties have the same spontaneous tensions. Therefore, the difference $\Sigma_{\beta\gamma} - \Sigma_{\alpha\gamma}$ between the mechanical tensions of the two segments is equal to the difference $\hat{\Sigma}_{\beta\gamma} - \hat{\Sigma}_{\alpha\gamma}$ between the total segment tensions. For small or large spontaneous curvatures, we then obtain

$$\Sigma_{\beta\gamma} - \Sigma_{\alpha\gamma} = \hat{\Sigma}_{\beta\gamma} - \hat{\Sigma}_{\alpha\gamma} = \Sigma_{\alpha\beta} \frac{\sin \theta_{\alpha}^{\text{ap}}}{\sin \theta_{\gamma}^{\text{ap}}} - \Sigma_{\alpha\beta} \frac{\sin \theta_{\beta}^{\text{ap}}}{\sin \theta_{\gamma}^{\text{ap}}} \quad (5.377)$$

where the second equality follows from Eq. 5.372. A combination of Eq. 5.377 with Eq. 5.376 then leads to the relation

$$\cos \theta_{\alpha}^* = \frac{\sin \theta_{\alpha}^{\text{ap}} - \sin \theta_{\beta}^{\text{ap}}}{\sin \theta_{\gamma}^{\text{ap}}} \quad (5.378)$$

between the intrinsic contact angle θ_{α}^* that is not accessible to conventional optical microscopy and the apparent contact angles that can be obtained from the microscopy images.

In (Kusumaatmaja et al., 2009), the relation in Eq. 5.378 was originally derived for the special case of vanishing spontaneous curvatures for both membrane segments, i.e., $m_{\alpha\gamma} = m_{\beta\gamma} = 0$, and was then used to analyze the shapes of vesicles that enclosed one PEG-rich and one dextran-rich droplet. Even though the apparent contact angles of these vesicles were quite different, the relation in Eq. 5.378 led to a fairly constant value for the intrinsic contact angle θ_{α}^* . Later experiments revealed, however, that the spontaneous curvatures $m_{\alpha\gamma}$ must be quite large because the $\alpha\gamma$ membrane segments in contact with the PEG-rich phase formed nanotubes, see Figures 5.4 and 5.21 corresponding to a spontaneous curvature of about $1/(125 \text{ nm})$ for the Ld phase and $1/(600 \text{ nm})$ for the Lo phase. (Li et al., 2011; Liu et al., 2016) Furthermore, the experimental data as well as molecular dynamics simulations provided strong evidence that this large spontaneous curvature was generated by asymmetric adsorption of PEG molecules. Therefore, it is tempting to assume that the spontaneous curvature $m_{\beta\gamma}$ of the $\beta\gamma$ membrane segments in contact with the dextran-rich phase was comparatively small. A small value of $m_{\beta\gamma}$ and a large value of $m_{\alpha\gamma}$ would justify the use of Eq 5.372 to describe the force balance along the apparent contact line but it would not justify the use of Eq. 5.376 to describe the force balance along the true contact line because the latter equation is based on the assumption that both membrane segments have essentially the same spontaneous curvature. On the other hand, if we assumed that the spontaneous curvature $m_{\beta\gamma}$ is large as well and comparable to $m_{\alpha\gamma}$, we could justify the use of both Eqs 5.372 and 5.376. Therefore, it would be rather valuable to determine the spontaneous curvature $m_{\beta\gamma}$ in an independent manner, e.g., by studying GUVs that are completely filled with the dextran-rich phase, corresponding to a point in the aqueous phase diagram of Figure 5.39 that is located on the binodal line between the partial wetting regime of the two-phase coexistence region and the uniform phase at high dextran concentrations, see lower blue segment of the binodal in Figure 5.39. Deflation of such a GUV will lead to budding for small spontaneous curvatures as in Section 5.5 or to tubulation for large spontaneous curvatures as in Section 5.6.

Membrane nanotubes for partial and complete wetting

As shown in Figure 5.39, the phase diagram of aqueous PEG-dextran solutions exhibits a two-phase coexistence region with both a complete wetting regime close to the critical point and a partial wetting regime further away from this point. The two wetting regimes are separated by a certain tie line corresponding to the dashed straight line in Figure 5.39. For complete wetting, the whole GUV membrane is exposed to the PEG-rich phase whereas, for partial wetting, only the $\alpha\gamma$ membrane is in contact with this aqueous phase. Therefore, in the complete and partial wetting regime, nanotubes were formed by the whole GUV membrane and the $\alpha\gamma$ membrane segment, respectively. Furthermore, for complete wetting, the tubes stayed away from the $\alpha\beta$ interface whereas they accumulated on this interface for partial wetting. In the latter case, the adhesion of the tubes to the $\alpha\beta$ interface lowers the (free) energy of the vesicle-droplet system as shown in (Liu et al., 2016). Each tube that adheres to the $\alpha\beta$ interface is in contact with both the α and the β phase and, thus, forms both an $\alpha\gamma$ and a $\beta\gamma$ membrane segment separated by a contact line parallel to the long tube axis. Along these microscopic contact lines, the angle between the $\alpha\beta$ interface and the $\alpha\gamma$ tube segments is again given by the intrinsic contact angle θ_α^* with the same local geometry as depicted in Fig. 5.41b, because the γ phase within the tubes is identical with the exterior aqueous phase.

If the $\alpha\gamma$ membrane segment forms nanotubes, the segment tension $\Sigma_{\alpha\gamma} = \Sigma + W_{\alpha\gamma}$ is small compared to the spontaneous tension $\sigma_{\alpha\gamma}$ of this segment (Lipowsky, 2013) as follows from the mechanical equilibrium between the highly curved tubes and the weakly curved spherical $\alpha\gamma$ segments, see the detailed discussion of this aspect in Section 5.6. The corresponding tension-angle relationship in Eq. 5.372 then assumes the simplified form

$$\frac{\sigma_{\alpha\gamma}}{\Sigma_{\alpha\beta}} = \frac{2\kappa_{\alpha\gamma}m_{\alpha\gamma}^2}{\Sigma_{\alpha\beta}} \approx \frac{\sin\theta_\beta^{\text{ap}}}{\sin\theta_\gamma^{\text{ap}}} \quad (\text{tubulated } \alpha\gamma \text{ segments}) \quad (5.379)$$

which can be used to estimate the spontaneous curvature $m_{\alpha\gamma}$ from the apparent contact angles (Liu et al., 2016).

5.9.8 TWO-DROPLET VESICLES WITH CLOSED NECKS

For partial in-wetting, the vesicle membrane is in contact with two enclosed droplets, as displayed in Figure 5.43a. When we deflate such a two-droplet vesicle, it can decrease its interfacial energy by reducing the area $A_{\alpha\beta}$ of the $\alpha\beta$ interface. The corresponding energy gain is governed by $\Delta A_{\alpha\beta}\Sigma_{\alpha\beta}$ where $\Delta A_{\alpha\beta}$ is the change in interfacial area. Such a morphological change is, in fact, rather likely unless one of the membrane segments has a sufficiently large spontaneous curvature to form nanobuds and nanotubes. If the $\alpha\gamma$ segment forms nanotubes, for example, the energy gain is $\Delta A_{\alpha\gamma}\sigma_{\alpha\gamma}$ with the area $\Delta A_{\alpha\gamma}$ stored in the nanotubes and the spontaneous tension $\sigma_{\alpha\gamma} = 2\kappa_{\alpha\gamma}m_{\alpha\gamma}^2$. So, we expect that osmotic deflation of a partially wetted vesicle leads to a reduction of the interfacial area whenever $\sigma_{\alpha\gamma} \ll \Sigma_{\alpha\beta}$. This competition between different morphological pathways is more systematically described in Appendix 5.J for the special case of two-droplet vesicles with up-down symmetry.

Thus, in the absence of bud and tube formation, the area of the $\alpha\beta$ interface will eventually shrink to zero and the vesicle membrane will then form a closed membrane neck around this point-like interface as in Figure 5.40d. For such a morphology, which looks like the limit shape L^{pea} in Figure 5.15a but involves two different interior solutions α and β , the vesicle membrane has the area $A = A_{2\text{sp}} \propto V_\alpha^{2/3} + V_\beta^{2/3}$, which is determined by the volumes V_α and V_β of the two spherical droplets as in Eq. 5.294.

As described in Section 5.8.3 on domain-induced budding, spherical buds with closed necks are also formed by two-domain vesicles arising from lipid phase separation within multi-component membranes. Compared to such two-domain vesicles, the closed neck of a two-droplet vesicle is further stabilized by the formation of the $\alpha\beta$ interface during neck opening. If we assume an axisymmetric neck and ignore a possible difference of the Gaussian curvature moduli $\kappa_{G,\alpha\gamma}$ and $\kappa_{G,\beta\gamma}$, the contact line is located within the membrane neck and the contact line radius r_1 is equal to the neck radius R_{ne} . Furthermore, because of the assumed axisymmetry, the neck-spanning $\alpha\beta$ interface has the shape of a spherical cap that meets the membrane along the circular contact line with the intrinsic contact angle θ_α^* of the α droplet, see Figure 5.41b. The free energy of the membrane neck then includes the interfacial free energy

$$\Sigma_{\alpha\beta}A_{\alpha\beta} = \frac{2\pi}{1 + \sin\theta_\alpha^*} \Sigma_{\alpha\beta}R_{\text{ne}}^2 \quad (5.380)$$

which grows quadratically with increasing neck radius R_{ne} . The bending energy of the vesicle membrane that consists of two membrane segments and forms an open neck of radius R_{ne} can be obtained from the corresponding expression for two-domain vesicles as derived in (Jülicher and Lipowsky, 1996). Adding the free energy of the contact line, we then obtain

$$E_{\text{be}}(R_{\text{ne}}) + 2\pi R_{\text{ne}}\lambda_{\text{co}} \approx E_{\text{be}}(R_{\text{ne}} = 0) - 4\pi E_1 R_{\text{ne}} \quad \text{for small } R_{\text{ne}} \quad (5.381)$$

with

$$E_1 \equiv \kappa_{\alpha\gamma}(M_{\alpha\gamma} - m_{\alpha\gamma}) + \kappa_{\beta\gamma}(M_{\beta\gamma} - m_{\beta\gamma}) - \frac{1}{2}\lambda_{\text{co}}. \quad (5.382)$$

The closure of the neck and the stability of the closed neck are governed by the behavior of the combined free energy $\Sigma_{\alpha\beta}A_{\alpha\beta} + E_{\text{be}}(R_{\text{ne}}) + 2\pi R_{\text{ne}}\lambda_{\text{co}}$ for small R_{ne} . In the latter limit, the leading term is provided by the E_1 -term in (5.381) because the interfacial free energy $\Sigma_{\alpha\beta}A_{\alpha\beta} \sim R_{\text{ne}}^2$. Therefore, we obtain the stability criterion $E_1 \leq 0$ which is equivalent to

$$\kappa_{\beta\gamma}(M_{\beta\gamma} - m_{\beta\gamma}) + \kappa_{\alpha\gamma}(M_{\alpha\gamma} - m_{\alpha\gamma}) \leq \frac{1}{2}\lambda_{\text{co}} \quad (\kappa_{G,\beta\gamma} \simeq \kappa_{G,\alpha\gamma}). \quad (5.383)$$

The equality in Eq (5.383) describes the neck closure condition for limit shapes obtained from vesicle shapes with open necks whereas the inequality describes the stability of closed necks. Because the additional term arising from the $\alpha\beta$ interface is irrelevant in the limit of small neck radius R_{ne} ,

the stability criterion in Eq. 5.383 has the same form as the corresponding criterion for two-domain vesicles as given by Eq. 5.288 with the line tension λ of the domain boundary replaced by the line tension λ_{co} of the three-phase contact line. It is important to note, however, that the stability condition in Eq. 5.383 has been obtained under the implicit assumption that the membrane neck is axisymmetric. The latter assumption is justified for a positive value of the contact line tension λ_{co} but may not apply to a negative value of λ_{co} . Indeed, recent molecular simulations have shown that a negative contact line tension can lead to a spontaneous symmetry breaking of the rotational symmetry and to a tight-lipped contact line (Satarifard et al., 2018).

5.9.9 NUCLEATION OF NANODROPLETS AT MEMBRANES

In general, phase separation in liquid mixtures may proceed via nucleation and growth of small droplets or via spinodal decomposition. In the nucleation regime, the droplets are formed by the minority phase and have to overcome a certain free energy barrier in order to grow. This barrier is reduced if a droplet is nucleated at an adhesive surface. For a rigid surface as provided by a tense membrane, the barrier reduction depends primarily on the contact angle of the droplet. For a flexible and deformable membrane, as considered here, the barrier may be further reduced by the elastic response of the membrane which can adapt its shape and composition to the molecular interactions with the droplet.

As in the previous subsections, we focus on phase separation of the interior aqueous solution into two coexisting liquid phases, α and β . For complete wetting of the vesicle membrane by the α phase, the intrinsic contact angle θ_{α}^* vanishes which implies that the phase separation starts via the formation of a thin α layer at the inner leaflet of the vesicle membrane, see pink subregion in Figure 5.39. For partial wetting, on the other hand, the intrinsic

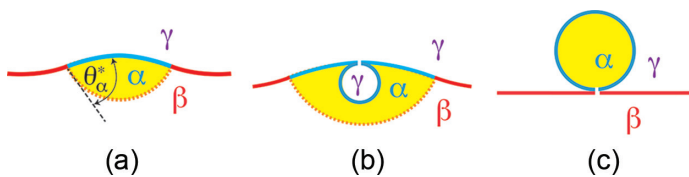


Figure 5.44 In-wetting: Nucleation and growth of an aqueous nanodroplet (yellow) consisting of α phase in contact with an aqueous β phase and the inner leaflet of a weakly curved vesicle membrane (blue/red) that separates the α and β phases from the exterior aqueous phase γ . The contact line with the $\alpha\beta$ interface (broken orange) divides the membrane into two segments, an $\alpha\gamma$ segment (blue) and a $\beta\gamma$ segment (red). Both segments are exposed to asymmetric aqueous environments which act to induce spontaneous curvatures $m_{\alpha\gamma}$ and $m_{\beta\gamma}$. Here, we focus on the case $m_{\beta\gamma} \approx 0$ and $|m_{\alpha\gamma}| \gg m_{\beta\gamma}$: (a) Initially, the $\alpha\beta$ interface has the shape of a spherical cap and forms the intrinsic contact angle θ_{α}^* with the adjacent $\alpha\gamma$ segment (blue) of the membrane; (b) For negative values of $m_{\alpha\gamma}$, the $\alpha\gamma$ membrane segment prefers to form a spherical in-bud that is filled with exterior γ phase. The closure and stability of the in-bud's neck depends only on $m_{\alpha\gamma}$; and (c) For positive values of $m_{\alpha\gamma}$, the $\alpha\gamma$ membrane segment prefers to engulf the α droplet, in particular if the volume of the droplet matches the preferred bud size. Complete engulfment leads to a closed membrane neck that replaces the $\alpha\beta$ interface, thereby eliminating the contribution of this interface to the system's free energy.

contact angle θ_{α}^* is finite, and the phase separation within the nucleation regime starts with nanodroplets of α phase that are formed at the inner membrane leaflet as shown in Figure 5.44a.

For such a small droplet, the intrinsic contact angle will be affected by the tension λ_{co} of the contact line, see Eqs 5.321 and 5.324. This contact line tension can be positive or negative, in contrast to the line tension of domain boundaries which is always positive. In fact, recent molecular simulation indicate that the contact line tension λ_{co} can be negative (Satarifard et al., 2018) which implies that it acts to decrease the contact angle θ_{α}^* of small droplets compared to larger ones.

After an α droplet as in Figure 5.44a has been formed, the $\alpha\gamma$ segment of the membrane in contact with this droplet is exposed to an asymmetric environment and can acquire an appreciable spontaneous curvature $m_{\alpha\gamma}$. In order to simplify the following discussion, let us assume that the spontaneous curvature $m_{\alpha\gamma}$ is large compared to the spontaneous curvature $m_{\beta\gamma}$ of the $\beta\gamma$ segment and that the latter curvature is small and can be ignored.

If the spontaneous curvature $m_{\alpha\gamma}$ is *negative* as in the case of PEG-dextran solutions that undergo phase separation within the vesicle interior, the membrane prefers to curve towards the inner leaflet and to form a spherical in-bud of radius R_{γ} that is filled with the exterior γ phase as in Figure 5.44b. As shown in this figure, all membrane segments adjacent to the closed neck are formed by the $\alpha\gamma$ membrane with spontaneous curvature $m_{\alpha\gamma}$. The membrane neck is then characterized by the condition $0 > M_{\text{ne}} = \frac{1}{2}(M_1 + M_2) \geq m_{\alpha\gamma}$ where M_1 and $M_2 = -1/R_{\gamma}$ are the mean curvatures of the two membrane segments 1 and 2 on the two sides of the neck. Because these two membrane segments have the same curvature-elastic properties, this stability condition is identical with Eq. 5.57 for uniform membranes, see also Figure 5.14(d–f) in Section 4.6. Inspection of Figure 5.44b reveals that the in-bud displaces some volume of α phase and *increases* the area of the $\alpha\beta$ interface which implies that the α droplet has to reach a sufficiently large volume before the in-bud becomes energetically favorable. After such an in-bud has been formed, the bud radius increases until the spherical shape becomes unstable and transforms into a short necklace-like tube as displayed in Figure 5.23.

On the other hand, if the droplet-induced curvature $m_{\alpha\gamma}$ is *positive*, the $\alpha\gamma$ membrane segment prefers to curve towards the outer leaflet of the vesicle membrane and to form a spherical out-bud of radius R_{α} that is filled with α phase as in Figure 5.44c. As shown in the latter panel, the two membrane segments adjacent to the neck of the out-bud are now provided by the $\alpha\gamma$ and the $\beta\gamma$ segments which have, in general, different spontaneous curvatures $m_{\alpha\gamma}$ and $m_{\beta\gamma}$. The formation of the out-bud reduces the free energy of the membrane-droplet system by (i) adapting the mean curvature of the $\alpha\gamma$ segment to its spontaneous curvature $m_{\alpha\gamma}$ and (ii) replacing the $\alpha\beta$ interface by a closed membrane neck which implies a strong reduction of the interfacial free energy. The corresponding neck condition is given by Eq. 5.383 if both membrane segments have essentially the same Gaussian curvature modulus, $\kappa_{G,\beta\gamma} \approx \kappa_{G,\alpha\gamma}$. If the Gaussian curvature moduli are different, the vesicles may still form closed membrane necks but the domain boundaries are then shifted away from these necks and, thus, have a finite length, compare Figure 5.35.

5.10 TOPOLOGICAL CHANGES OF MEMBRANES

In the previous sections, we focused on processes that do not change the topology of the membranes. Now, let us briefly consider two important topology-transforming processes, membrane fusion and membrane fission (or scission). During membrane fusion, two separate membranes are combined into a single one; during fission, a single membrane is divided up into two separate ones. These processes are ubiquitous in eukaryotic cells: Both the outer cell membrane and the inner membranes of organelles act (i) as donor membranes that continuously produce vesicles via budding and fission and (ii) as acceptor membranes that integrate such vesicles via adhesion and fusion. One example for fission is provided by the closure of autophagosomes which are double-membrane organelles (Knorr et al., 2012, 2015).

5.10.1 FREE ENERGY LANDSCAPES

It is instructive to consider the free energy landscapes for fusion and fission as schematically depicted in Figure 5.45. Fusion is exergonic, if the free energy G_2 of the 2-vesicle state exceeds the free energy G_1 of the 1-vesicle state. In the opposite case with $G_1 > G_2$, fission is exergonic. Exergonic fusion or fission processes occur spontaneously but the kinetics of these processes is governed by the free energy barriers Δ between the 1-vesicle and the 2-vesicle state, see Figure 5.45. Because these barriers are typically large compared to $k_B T$, even exergonic fusion and fission processes will be rather slow unless coupled to other molecular processes that act to reduce these barriers. Indeed, in the living cell, the fusion and fission of biomembranes is controlled by membrane-bound proteins such as SNAREs and dynamin as

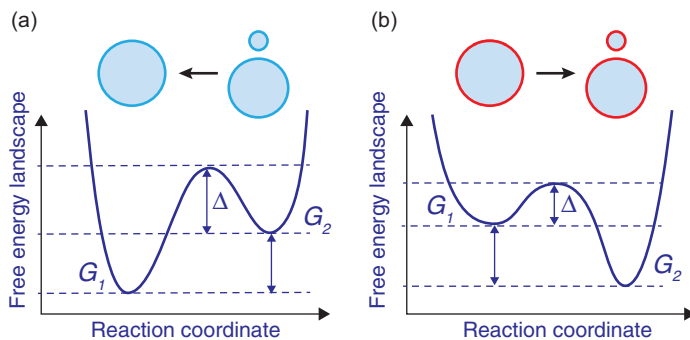


Figure 5.45 Free energy landscapes for membrane fusion and fission (or scission): (a) Schematic landscape for an exergonic fusion process. In this case, the free energy G_2 of the 2-vesicle state exceeds the free energy G_1 of the 1-vesicle state; and (b) Schematic landscape for an exergonic fission process. In the latter case the free energy G_1 of the 1-vesicle state is larger than the free energy G_2 of the 2-vesicle state. The cartoons (top row) show a 1-vesicle state on the left and a 2-vesicle state on the right; both states have the same membrane area. The small vesicle of the 2-vesicle state has the radius R_{ss} which is much smaller than the radius of the large vesicle. The blue membranes in (a) have a spontaneous curvature with magnitude $|m| \ll 1/R_{ss}$, whereas the red membranes in (b) have a large spontaneous curvature with $m \simeq 1/(2R_{ss})$. In both (a) and (b), the free energy difference $G_2 - G_1$ determines the direction in which the processes can proceed spontaneously (black arrows) while the kinetics of these processes is governed by the free energy barriers Δ .

will be discussed in later chapters of this book. It should also be emphasized that the free energy landscape may involve several barriers as has been observed in molecular dynamics simulations of tension-induced fusion (Graffmüller et al., 2007, 2009).

Dependence on spontaneous curvature

The free energy difference $G_2 - G_1$ between the 2-vesicle and the 1-vesicle state can be estimated if one ignores energetic contributions arising from changes in volume and focuses on changes in curvature energy (Lipowsky, 2013). Because of the topological changes, we need to take the Gaussian curvature and the associated Gaussian curvature modulus κ_G into account. (Helfrich, 1973) Stability arguments indicate that $-2 < \kappa_G/\kappa < 0$ (Helfrich and Harbich, 1987). For the following considerations, it will be sufficient to use the rough estimate $\kappa_G \simeq -\kappa$ which is consistent with both experimental (Derzhanski et al., 1978; Lorenzen et al., 1986) and simulation (Hu et al., 2012) studies. A small spherical vesicle that is cleaved off from a donor membrane then changes the total curvature energy by a certain amount that can be used to estimate the free energy difference $G_2 - G_1$. It is important to note, however, that this change in curvature energy depends strongly on the magnitude of the spontaneous curvature.

5.10.2 EXERGONIC FUSION FOR SMALL m

Let us consider a 1-vesicle state corresponding to a spherical GUV that acts as the donor membrane and a 2-vesicle state obtained from this GUV by cleaving off a much smaller spherical vesicle, see top row of Figure 5.45. Both states have the same membrane area. The small vesicle of the 2-vesicle state has the radius R_{ss} which is taken to be much smaller than the radius of the GUV. We may then ignore any constraints on the vesicle volumes and assume that the large vesicle of the 2-vesicle state has a spherical shape as well. If the GUV membrane is uniform and the magnitude $|m|$ of its spontaneous curvature is much smaller than the inverse size, $1/R_{ss}$, of the small vesicle, the free energy difference between the 2-vesicle and 1-vesicle state is *positive* and given by

$$G_2 - G_1 = 8\pi\kappa + 4\pi\kappa_G \simeq +4\pi\kappa \quad \text{for } |m| \ll 1/R_{ss} \quad (5.384)$$

where the estimate $\kappa_G \simeq -\kappa$ has been used. In this case, the fission process is endergonic whereas the fusion process is exergonic, see the corresponding free energy landscape in Figure 5.45a. For the typical rigidity value $\kappa \simeq 20k_B T$, the relation Eq. 5.384 leads to the fairly large free energy difference $G_2 - G_1 \simeq +250k_B T$!

5.10.3 EXERGONIC FISSION FOR LARGE m

On the other hand, if the magnitude $|m|$ of the spontaneous curvature is large, the GUV can form a small spherical bud with radius $R_{ss} \simeq 1/(2|m|)$ as in Figure 5.45b as follows from the closed neck condition for the corresponding limit shapes L^{pea} and L^{sto} as discussed in Section 5.5.2. If this bud is cleaved off, the free energy difference between the resulting 2-vesicle state and the initial 1-vesicle state is now *negative* and given by

$$\begin{aligned} G_2 - G_1 &= 8\pi\kappa(1 - 2R_{ss}|m|) \\ &+ 4\pi\kappa_G \simeq 4\pi\kappa_G \simeq -4\pi\kappa \quad (5.385) \\ &\text{for } R_{ss} \simeq 1/(2|m|). \end{aligned}$$

In the latter case, the fission process is exergonic and the fusion process is endergonic, corresponding to a free energy landscape as in Figure 5.45b. Now, the free energy difference $G_2 - G_1 \simeq -250k_B T$ for a typical value $\kappa \simeq 20k_B T$ of the bending rigidity.

Biological membranes often form intramembrane domains with an appreciable spontaneous curvature m_{do} . One example for this latter case is provided by clathrin-dependent endocytosis which leads to membrane domains with a spontaneous curvature $m_{do} \simeq -1/(40\text{nm})$ (Agudo-Canalejo and Lipowsky, 2015a). Now, consider a GUV with a small membrane domain that has an appreciable spontaneous curvature m_{do} whereas the spontaneous curvature of the remaining GUV membrane is again negligible. The membrane domain can then form a small spherical bud of size $R_{ss} = 1/|m_{do}|$ as follows from the closed neck condition for domain-induced budding, see Eq. 5.291. If the latter bud is cleaved off, the free energy difference between the resulting 2-vesicle state and the initial 1-vesicle state is again negative and has the form

$$G_2 - G_1 = 8\pi\kappa(1 - 2R_{ss}|m_{do}|) + 4\pi\kappa_G - 4\pi \frac{\lambda}{|m_{do}|} \simeq -12\pi\kappa - 4\pi \frac{\lambda}{|m_{do}|} \quad (5.386)$$

where λ denotes the line tension of the domain boundary. Because this line tension has to be positive, the fission of a domain-induced bud is an exergonic process that leads to an even larger free energy gain $|G_2 - G_1| > 12\pi\kappa \gtrsim 750k_B T$ for bending rigidity $\kappa \simeq 20k_B T$.

5.11 SUMMARY AND OUTLOOK

This chapter addressed the multi-responsive behavior of giant vesicles from a theoretical point of view. Because the vesicle membranes are fluid, they can respond to external perturbation by remodeling both their shape and their local membrane composition. Two curvature-elastic parameters that play a prominent role in the whole chapter are the spontaneous curvature m , which provides a quantitative measure for bilayer asymmetry (Section 3.5), and the spontaneous tension $\sigma = 2\kappa m^2$, which provides the intrinsic tension scale of curvature elasticity (Section 5.4.2). If molecular flip-flops between the two leaflets of the bilayer membrane can be ignored, the spontaneous curvature becomes an effective spontaneous curvature m_{eff} that contains both a local and a non-local contribution, the latter arising from area-difference-elasticity, see Eqs 5.66 and 5.67.

All biomembranes are asymmetric in the sense that the two leaflets have different lipid compositions (Fadeel and Xue, 2009) and that the membrane proteins have a preferred orientation related to their biological function. It is important to realize that both lipids and membrane proteins as well as adsorbed solutes and anchored macromolecules can contribute to the spontaneous curvature as illustrated by the examples in Box 5.1. In fact, the framework of curvature elasticity as reviewed here applies to giant vesicles irrespective of the chemical nature of the molecular membrane components as long as the vesicle membranes are in a fluid state. Thus, these vesicles may be built up from different lipid components, membrane proteins, or other amphiphilic molecules such as diblock copolymers.

The shapes and shape transformations of membranes with laterally uniform curvature-elastic properties are governed by two dimensionless parameters, the volume-to-area ratio (or reduced volume) v and the spontaneous curvature $\bar{m} = R_{vc}m$. These two parameters can be controlled by changes in the osmotic conditions and by one of the curvature-generating mechanisms in Box 5.1. The resulting shape transformations often lead to budding and tubulation processes, which create nanobuds and nanotubes as described in Sections 5.5 and 5.6. The buds and tubes represent additional membrane compartments that are still connected to the mother vesicle via closed or narrow membrane necks. These necks are a direct consequence of curvature elasticity (Section 5.4.6, Figure 5.14) and can be used to deduce the spontaneous curvature from the GUV morphology as described in Box 5.2. The latter deduction is based on the local stability conditions for closed necks as given by Eqs 5.60 and 5.61 which relate the neck curvature to the spontaneous curvature. In the absence of flip-flops, one obtains the generalized stability conditions in Eqs 5.68 and 5.69. Sufficiently large values of m_{eff} lead to the cleavage of the membrane neck and thus to complete membrane fission, see Section 5.5.4.

In cell biology, the closure and cleavage of such membrane necks represents an essential step for many processes such as endo- and exocytosis, the secretion of giant plasma membrane vesicles (or “blebs”) (Scott, 1976; Baumgart et al., 2007; Veatch et al., 2008; Keller et al., 2009) and outer membrane vesicles (Kulp and Kuehn, 2010; Schertzer and Whiteley, 2012) from eukaryotic and prokaryotic cells, as well as cytokinesis during cell division.

When a GUV undergoes spontaneous tubulation, the total membrane tension is dominated by the spontaneous tension as described by Eqs 5.193 and 5.215 for necklace-like and cylindrical nanotubes, respectively. Because the spontaneous tension is a material parameter, tubulated vesicles behave, to a large extent, like liquid droplets with a variable surface area and with an effective interfacial tension that is provided by the spontaneous tension σ . This droplet-like behavior, which reflects the area reservoir that the nanotubes provide for the mother vesicle, leads to an increased robustness against mechanical perturbations as has been recently demonstrated by micropipette aspiration and cycles of osmotic deflation and inflation (Bhatia et al., 2018).

Membrane nanotubes are also formed within eukaryotic cells and provide ubiquitous structural elements of many membrane-bound organelles such as the endoplasmic reticulum, the Golgi, the endosomal network, and mitochondria (Marchi et al., 2014; van Weering and Cullen, 2014; Weststrate et al., 2015). These intracellular nanotubes are used for molecular sorting, signaling, and transport. Intercellular (or “tunneling”) nanotubes formed by the plasma membranes of two or more cells provide long-distance connections for cell-cell communication, intercellular transport, and virus infections (Wang and Gerdes, 2015; He et al., 2010; Sowinski et al., 2008). It seems rather plausible to assume that these tubes are also generated by spontaneous curvature and/or locally applied forces but the relative importance of these two tubulation mechanisms remains to be elucidated.

Additional shape transformations of membranes and vesicles can be induced by adhesive surfaces as described in Section 5.7. The onset of adhesion is governed by the simple stability relation in Eq. 5.236 which depends on the adhesion length $R_W = \sqrt{2\kappa/|W|}$. This length can vary over several orders of magnitude as illustrated by the membrane-particle couples in Table 5.2. Analogous stability relations play an important role for the engulfment of nanoparticles by membranes as described in Chapter 8 of this book.

The adhesion of a vesicle to a rigid substrate or solid support leads to the segmentation of the vesicle membrane into a bound and unbound membrane segment. For multi-component vesicle membranes, these two segments can differ in their molecular composition and thus in their curvature-elastic properties when the vesicle membrane contains several molecular components, as explained in Section 7.6. Therefore, the adhesion of multi-component membranes provides a relatively simple example for ambience-induced segmentation. This kind of segmentation plays an important role for the adhesion of nanoparticles by membrane-anchored receptors (Agudo-Canalejo and Lipowsky, 2015a), see the more detailed discussion in Chapter 8 of this book.

Multi-component membranes can undergo phase separation into two fluid phases, a process that is now firmly established for a variety of three-component membranes as discussed in Section 2.4 and at the beginning of Section 5.8. Membrane phase separation leads to multi-domain vesicles, the shape of which is governed by the interplay between the curvature-elastic properties of the intramembrane domains and the line tension of the domain boundaries. One prominent example for this interplay is domain-induced budding, see Figure 5.32 and Section 5.8.3. Another example is provided by transformations between different patterns of intramembrane domains, which are coupled to drastic shape changes of the vesicles as illustrated in Figure 5.37.

Membrane phase separation of multi-component vesicles is strongly affected by ambience-induced segmentation of the vesicle membranes as explained in Section 5.8.5. Indeed, if the membrane is partitioned into several segments that differ in their molecular composition, membrane phase separation is only possible in one of the segments but not in several segments simultaneously. Because cellular membranes are exposed to rather heterogeneous environments, the associated segmentation acts to suppress the formation of intramembrane domains within such membranes. The latter mechanism explains the difficulty to detect lipid phase separation *in vivo*, in contrast to the large intramembrane domains frequently observed in multi-component lipid membranes.

Another interesting example for ambience-induced segmentation is provided by membranes and vesicles exposed to aqueous two-phase systems or water-in-water emulsions as described in Section 5.9. To simplify the discussion, Section 5.9 focused on aqueous phase separation within the GUVs which leads to the in-wetting morphologies displayed in Figure 5.40. Out-wetting morphologies arising from phase separation of the exterior aqueous solution are addressed in Appendix 5.I. For partial in-wetting as shown in Figure 5.40a, the interface between the two aqueous phases α and β exerts capillary forces onto the GUV membrane along the three-phase contact line. On the micrometer scale,

these forces lead to apparent kinks of the membrane shapes. This response of the membranes to the capillary forces is quite remarkable because the interfacial tension of the $\alpha\beta$ interface is ultralow, of the order of 10^{-6} – 10^{-4} N/m, reflecting the vicinity of a critical demixing point in the aqueous phase diagram.

However, the apparent kink of the membrane shape should not persist to the nanoscale because such a kink would imply a very large bending energy of the GUV membrane. Therefore, when viewed on the nanometer scale, the membrane should be smoothly curved, which implies the existence of an intrinsic contact angle as depicted in Figure 5.41. This angle is related to the difference of the segment tensions as given by the force balance Eq. 5.321. The latter equation also depends on the local curvatures of the two membrane segments at the contact line. At present, these curvatures cannot be determined experimentally which implies that the force balance Eq. 5.321 cannot be scrutinized by experiment.

On the other hand, the optical micrographs of the GUV shape showed that the two membrane segments in contact with the α and β droplets form spherical caps to a very good approximation. The extrapolation of these spherical cap shapes defines an apparent contact line and apparent contact angles as shown in Figures 5.42 and 5.43. The spherical cap geometry leads to the simplified shape Eqs 5.338 which imply the general relationship in Eq. 5.342. The latter relationship depends on the effective tensions and curvature radii of the two membrane segments as well as on the interfacial tension and the apparent contact angles. This relationship can be used to obtain the curvature-elastic parameters of the membrane segments from the observed wetting morphology.

For certain regions of the parameter space corresponding to small and large spontaneous curvatures, a simplified set of tension-angle relationships can be derived for the force balance along the apparent contact lines. For small spontaneous curvatures as defined by Eq. 5.356, the bending energies can be neglected compared to the interfacial free energy of the $\alpha\beta$ interface if the interfacial area $A_{\alpha\beta}$ is sufficiently large and satisfies the inequality in Eq. 5.362. In this parameter regime, we obtain the relationships in Eqs 5.371 and 5.372 which relate the total membrane tensions and the interfacial tension to the apparent contact angles, corresponding to the force triangle in Figure 5.43b. The same relationships apply to large spontaneous curvatures for which the bending energy is dominated by the spontaneous tension and behaves as in Eq. 5.365. If one of the membrane segments forms membrane nanotubes, one can ignore the mechanical tension within this segment compared to its spontaneous tension and use the simpler relationship in Eq. 5.379 to estimate the spontaneous curvature of the tubulated segment.

In the context of synthetic biology, GUVs are very attractive as possible microcompartments for the bottom-up assembly of artificial protocells (Walde et al., 2010; Fenz and Sengupta, 2012; Schwille, 2015; Weiss et al., 2018). One practical problem that has impeded research in this direction is the limited robustness of GUVs against mechanical perturbations. Very recently, this limitation has been overcome by two different strategies. One strategy is based on the formation of GUVs within emulsion droplets that support and stabilize the GUVs (Weiss et al., 2018), see also

Chapter 30 of this book. The other strategy uses the special properties of tubulated GUVs as discussed in Section 5.6. The nanotubes increase the robustness of the giant vesicles by providing a membrane reservoir for the mother vesicles which can then adapt their surface area to avoid membrane rupture (Bhatia et al., 2018). In the latter study, the increased robustness has already been demonstrated by micropipette experiments and by repeated cycles of osmotic deflation and inflation. Giant vesicles with membrane nanotubes will also tolerate other mechanical perturbations, arising, e.g., from the adhesion and engulfment of microparticles, in close analogy to cellular uptake via phagocytosis and pinocytosis, or in response to constriction forces that can lead to membrane fission and the formation of smaller membrane compartments. The latter process of artificial cytokinesis is an important objective for the bottom-up assembly of artificial protocells. Thus, both droplet-stabilized and tubulated GUVs provide new and promising modules for the bottom-up assembly of such artificial protocells.

ACKNOWLEDGMENTS

I thank all my collaborators for enjoyable and fruitful interactions and Jaime Agudo-Canalejo and Rumiana Dimova for detailed comments on earlier versions of this manuscript.

APPENDICES

5.A BRIEF EXCURSION INTO DIFFERENTIAL GEOMETRY

Any membrane shape S can be described in terms of two surface coordinates $\underline{s} \equiv (s^1, s^2)$ and a vector-valued function $\vec{X} = \vec{X}(\underline{s})$ that maps the surface coordinates into three-dimensional space (see, e.g., do Carmo, 1976). At any point P of the membrane surface, the tangent vectors \vec{X}_i with $i = 1, 2$ and the normal vector \hat{n} are then given by

$$\vec{X}_i = \frac{\partial \vec{X}}{\partial s^i} \quad \text{and} \quad \hat{n} = \frac{\vec{X}_1 \times \vec{X}_2}{|\vec{X}_1 \times \vec{X}_2|} \quad (5.A1)$$

where the symbol \times denotes the vector product in three-dimensional space. The three vectors \vec{X}_1 , \vec{X}_2 , and \hat{n} represent a right-handed trihedron at any point P of the membrane surface. Note that the normal vector \hat{n} is a unit vector which is orthogonal to the plane spanned by the two tangent vectors. In general, the tangent vectors \vec{X}_1 and \vec{X}_2 are neither unit vectors nor orthogonal to each other. These tangent vectors define the metric tensor

$$g_{ij} = \vec{X}_i \cdot \vec{X}_j, \quad (5.A2)$$

where the symbol \cdot denotes the scalar product. As we move along the membrane surface, the normal vector \hat{n} is tilted and this tilt can be expressed in terms of the tangent vectors because the normal vector is a unit vector with $\hat{n} \cdot \hat{n} = 1$ and $\frac{\partial \hat{n}}{\partial s^i} \cdot \hat{n} = 0$. The tilt of the normal vector then defines the curvature tensor b_i^j via

$$\frac{\partial \hat{n}}{\partial s^i} = -b_i^j \vec{X}_j \equiv -b_i^1 \vec{X}_1 - b_i^2 \vec{X}_2 \quad (5.A3)$$

where the second equation explains the summation over the repeated index j . The principal curvatures C_1 and C_2 discussed in Section 3.2 are the eigenvalues of the curvature tensor $-b_i^j$. This definition of the principal curvatures implies that a sphere is characterized by the principal curvatures $C_1 = C_2 > 0$.¹⁹ Using the definition of the normal vector in Eq. 5.A1, we can express the first derivatives $\frac{\partial \hat{n}}{\partial s^i}$ of the normal vector via the second derivatives $\frac{\partial^2 \vec{X}}{\partial s^i \partial s^j}$ of the vector-valued function $\vec{X}(\underline{s})$. Therefore, in order to define the principal curvatures at a certain point on the membrane surface, the components of the vector $\vec{X}(\underline{s})$ that describes the membrane shape in the vicinity of this point must be sufficiently smooth and twice differentiable with respect to the surface coordinates s^i .

5.B TOPOLOGY OF VESICLES

Giant vesicles that do not experience external forces or constraints form closed membrane surfaces without pores or edges. In general, the topology of such a surface can be characterized by two related integers: (i) the number of handles, also known as the genus g of the surface, and (ii) the Euler characteristic $\chi = 2 - 2g$. For any segmentation or partitioning of the membrane surface in terms of (curved) polygons, the Euler characteristic χ is equal to the number of polygons minus the number of edges plus the number of corners.

Three surfaces with genus $g = 0, 1$, and 2 are displayed in Figure 5.46: A surface with $g = 0$ and $\chi = 2$ is topologically equivalent to a sphere, a doughnut or torus is characterized by $g = 1$ and $\chi = 0$, and the Lawson surface with two handles has genus $g = 2$ and Euler characteristic $\chi = -2$. Furthermore, a set of several such surfaces has an Euler characteristic that is equal to the sum of the individual Euler characteristics.

Thus, a set of n spheres has the Euler characteristics $\chi = 2n$.

For a closed membrane surface without bilayer edges, the Gauss-Bonnet theorem implies that the integrated Gaussian curvature is given by $\int dA G = 2\pi\chi = 2\pi(2 - 2g)$ as in Eq. 5.10. On the other hand, if the membrane surface has pores (or holes) that are bounded by bilayer edges, each edge makes a contribution to the integrated Gaussian curvature as given by

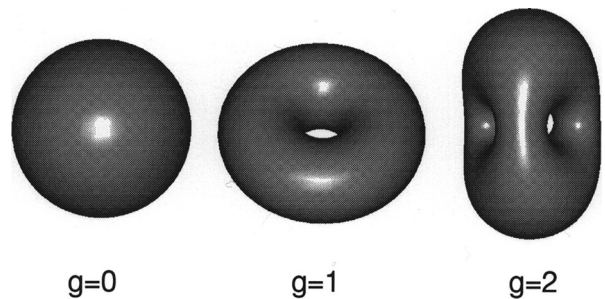


Figure 5.46 A sphere has no handle and genus $g = 0$; a torus has one handle and genus $g = 1$; the Lawson surface on the right has two handles and genus $g = 2$. The genus is a topological invariant and does not change for arbitrary shape deformations as long as we do not rupture or porate the surface.

¹⁹ Most text books on differential geometry take the principal curvatures to be the eigenvalues of b_i^j instead of $-b_i^j$. This conventional choice leads to $C_1 = C_2 < 0$ for a sphere.

$$\int dAG = -\oint dl C_g + 2\pi \quad (5.B1)$$

which depends on the line integral of the geodesic curvature C_g along the bilayer edge. In general, each bilayer edge will also contribute an edge energy which is proportional to the length of the edge.

Vesicles of genus $g = 2$ as illustrated by the rightmost shape in Figure 5.46 can undergo thermally excited shape transformations that correspond to conformal transformations of the vesicle shape, for which the vesicle volume, the membrane area, and the integrated mean curvature of the vesicle remain constant. This conformal diffusion in shape space was first predicted theoretically (Jülicher et al., 1993) and subsequently confirmed experimentally (Michalet and Bensimon, 1995).

5.C HIGHLY CURVED MEMBRANE SEGMENTS

5.C.1 HIGHER ORDER CURVATURE TERMS

As explained in Section 5.4.1, the spontaneous curvature model as defined by the curvature energy functional in Eq. 5.11 is obtained from a small curvature expansion up to second order in the principal curvatures C_1 and C_2 and ignores terms of higher order in these curvatures. These higher-order terms have the general form

$$\mathcal{E}_{\text{cu}}^{p,q} \equiv \int dA \kappa_{p,q} [C_1^p C_2^q + C_2^p C_1^q] \quad \text{with } p+q \geq 3. \quad (5.C1)$$

A somewhat different classification using symmetry arguments has been given by (Mitov, 1978).

A rough estimate for the magnitude of these terms can be obtained by dimensional analysis. The elastic parameter $\kappa_{p,q}$ has the dimension of energy multiplied by length to the power $p+q-2$. If we take the bending rigidity κ as the basic energy scale and the membrane thickness ℓ_{me} as the basic molecular length, we obtain $\kappa_{p,q} \sim \kappa \ell_{\text{me}}^{p+q-2}$. On the other hand, a vesicle with membrane area A has the overall size $R_{\text{ve}} = \sqrt{A/(4\pi)}$. Therefore, dimensional analysis implies that the higher-order terms behave as

$$\mathcal{E}_{\text{cu}}^{p,q} \sim \kappa (R_{\text{ve}}/\ell_{\text{me}})^{2-(p+q)} \quad (5.C2)$$

and decay to zero, in the limit of large $R_{\text{ve}}/\ell_{\text{me}}$, provided $p+q \geq 3$.

The estimate in Eq. 5.C2 indicates that, for $R_{\text{ve}} \gtrsim 5\ell_{\text{me}} \simeq 20$ nm, all higher-order terms with $p+q \geq 4$ should be negligible compared to the second-order terms of the spontaneous curvature model as given by Eq. 5.11. On the other hand, third-order terms with $p+q=3$ could make a significant contribution for $5\ell_{\text{me}} \lesssim R_{\text{ve}} \lesssim 20\ell_{\text{me}} \simeq 80$ nm. The latter terms have the general form $C_1^3 + C_2^3$ and $C_1^2 C_2 + C_2^2 C_1$ and involve the additional elastic parameters $\kappa_{3,0}$ and $\kappa_{2,1}$.

The same conclusion applies to small spherical buds with radius R_{bud} and narrow cylindrical tubes with radius R_{tu} . Thus, all higher-order terms should be negligible for $R_{\text{bud}} \gtrsim 80$ nm and $R_{\text{tu}} \gtrsim 80$ nm but third-order terms could make a significant contributions for smaller values of R_{bud} or R_{tu} . In order to study the

latter contributions in a systematic manner, molecular simulations should be rather useful.

5.C.2 MEMBRANE NECKS AS CURVATURE DEFECTS

As described in Section 5.4.6, closed membrane necks arise as limit shapes from the smooth solutions of the Euler-Lagrange or local shape equation. As the neck closes and the neck radius R_{ne} goes to zero, the adjacent membrane segment becomes highly curved because the curvature $1/R_{\text{ne}}$ diverges. This divergence is truncated because the membrane curvature cannot exceed the inverse membrane thickness $1/\ell_{\text{me}}$.

Taking the molecular structure of the bilayer membrane into account, this structure should be strongly perturbed in the vicinity of a closed neck and this perturbed molecular structure might lead to a finite “defect energy” δE_{ne} of the neck. A simple estimate of this latter energy can be obtained as follows. As explained in Section 5.3.1, curvature as a continuum concept emerges for membrane patches with a lateral dimension, say ℓ , that is about twice the membrane thickness. If we assume that the neck strongly perturbs the bilayer structure of a membrane patch of area ℓ^2 , we obtain the estimate

$$\delta \bar{E}_{\text{ne}} \equiv \frac{\delta E_{\text{ne}}}{8\pi\kappa} = \frac{\ell^2}{4\pi} [M_{\text{ne}} - m]^2 \quad (5.C3)$$

which behaves as

$$\delta \bar{E}_{\text{ne}} \approx \frac{m^2 \ell^2}{4\pi} \quad \text{for large } |m| \gg |M_{\text{ne}}|. \quad (5.C4)$$

This neck energy should be compared with the bending energy $\bar{E}_{\text{be}}(R_2) = (1 - mR_2)^2$ of a spherical bud with radius R_2 . Bud and neck then have the combined energy

$$\bar{E}_{\text{be}} + \delta \bar{E}_{\text{ne}} \approx m^2 R_2^2 \left(1 + \frac{\ell^2}{4\pi R_2^2} \right) \quad \text{for large } |m| \gg |M_{\text{ne}}|. \quad (5.C5)$$

Thus, if we take $\ell \simeq 8$ nm, the correction term arising from the putative defect energy of the neck can be safely ignored for buds with radius $R_2 \gtrsim 40$ nm. In order to obtain a reliable estimate for smaller buds, molecular simulations should again be quite useful.

5.D MECHANICAL TENSION OF MEMBRANES

In this appendix, we consider vesicles with compressible membranes and determine their equilibrium shapes by minimizing the combined bending and stretching energy with respect to membrane area for fixed vesicle volume.

5.D.1 MECHANICAL TENSION AND STRETCHING ENERGY

In the absence of external forces or constraints, a bilayer membrane attains a certain optimal area A_{opt} , which corresponds to the optimal packing of its molecules. The membrane experiences a tension, Σ_{st} , when its area A is stretched and deviates from the optimal value A_{opt} . This stretch tension can be expressed as

$$\Sigma_{\text{st}}(A) = K_A \frac{A - A_{\text{opt}}}{A_{\text{opt}}} \quad (5.D1)$$

up to first order in $A - A_{\text{opt}}$, which defines the area compressibility modulus K_A . The stretch tension Σ_{st} must be smaller than the tension of rupture, Σ_{rup} . For lipid bilayers, the rupture tension Σ_{rup} is about two orders of magnitude smaller than the area compressibility modulus K_A and of the order of a few mN/m.

The work of stretching or compression, starting from the initial area $A = A_{\text{opt}}$, defines the stretching energy

$$E_{\text{st}}(A) = \int_{A_{\text{opt}}}^A dx \Sigma_{\text{st}}(x) = \frac{1}{2} K_A \frac{(A - A_{\text{opt}})^2}{A_{\text{opt}}}. \quad (5.D2)$$

For an arbitrary vesicle shape S , we define the stretching energy functional via

$$\mathcal{E}_{\text{st}}\{S\} \equiv E_{\text{st}}(\mathcal{A}\{S\}). \quad (5.D3)$$

5.D.2 COMBINED BENDING AND STRETCHING ENERGY

The total elastic energy of a compressible membrane, which consists of its combined bending and stretching energy, is now equal to

$$\mathcal{E}_{\text{el}}\{S\} \equiv \mathcal{E}_{\text{bc}}\{S\} + \mathcal{E}_{\text{st}}\{S\}. \quad (5.D4)$$

The corresponding shape functional has the form

$$\mathcal{F}_{\text{el}}\{S\} = -\Delta P \mathcal{V}\{S\} + \mathcal{E}_{\text{bc}}\{S\} + \mathcal{E}_{\text{st}}\{S\} \quad (5.D5)$$

where the pressure difference ΔP is used, as before, as a Lagrange multiplier to ensure that $\mathcal{V}\{S\} = V$.

5.D.3 TWO-STEP MINIMIZATION PROCEDURE

The minimization of the shape functional Eq. 5.D5 can be performed in two steps:

- (i) First, we minimize the shape functional Eq. 5.22 for the spontaneous curvature model using the Lagrange multiplier tension Σ to enforce the membrane area $\mathcal{A}\{S\} = A$. As a result, we obtain the bending energy function

$$E_{\text{bc}}(V, A; \kappa, m, j) = \mathcal{E}_{\text{bc}}\{S^j\} \quad (5.D6)$$

as in Eq. 5.28, which represents the membrane's bending energy as a function of volume V and membrane area A along a branch of (meta)stable equilibrium shapes S^j . In general, we expect to find several branches of such shapes as illustrated in Figure 5.12 for vanishing spontaneous curvature, $m = 0$.

- (ii) Second, we minimize the combined elastic energy functional $\mathcal{E}_{\text{el}} = \mathcal{E}_{\text{bc}} + \mathcal{E}_{\text{st}}$ with respect to membrane area A for fixed volume V . Because the stretching energy is an explicit function of the membrane area, we can replace the minimization of the elastic energy functional \mathcal{E}_{el} by the minimization of the elastic energy function

$$\begin{aligned} E_{\text{el}}(V, A) &\equiv E_{\text{bc}}(V, A) + E_{\text{st}}(A) \\ &= E_{\text{bc}}(V, A) + \frac{1}{2} K_A \frac{(A - A_{\text{opt}})^2}{A_{\text{opt}}}. \end{aligned} \quad (5.D7)$$

The relation $(dE_{\text{el}}(V, A)/dA)_V = 0$ then determines the equilibrium value $A = A^{\text{eq}}$ of the membrane area via

$$K_A \frac{A^{\text{eq}} - A_{\text{opt}}}{A_{\text{opt}}} = - \left(\frac{dE_{\text{bc}}(V, A^{\text{eq}})}{dA^{\text{eq}}} \right)_V. \quad (5.D8)$$

In this way, the minimization of the combination of bending and stretching energy has been reduced to the minimization of the bending energy functional alone, which determines the bending energy E_{bc} as a function of V and A .

5.D.4 MECHANICAL TENSION

The relation as given by Eq. 5.D8 has a very simple physical interpretation. By definition, the left hand side of Eq. 5.D8 is equal to the stretch tension Σ_{st} , see Eq. 5.D1, whereas the right hand side of this equation corresponds to the relationship Eq. 5.32 which expresses the Lagrange multiplier tension Σ as the derivative of the bending energy with respect to membrane area A . Therefore, the relation Eq. 5.D8 is equivalent to

$$\Sigma_{\text{st}} = K_A \frac{A^{\text{eq}} - A_{\text{opt}}}{A_{\text{opt}}} = - \left(\frac{dE_{\text{bc}}(V, A^{\text{eq}})}{dA^{\text{eq}}} \right)_V = \Sigma \quad (5.D9)$$

which reveals that the Lagrange multiplier tension Σ is, in fact, identical with the stretch tension Σ_{st} . The identity Eq. 5.D9 is not restricted to a specific form of the bending energy but holds for any such energy, when minimized for fixed vesicle volume and fixed membrane area. An analogous equation also holds for the bilayer coupling model (Svetina and Zeks, 1989), in which the bending energy function E_{bc} depends on the volume V , membrane area A , as well as total mean curvature $I_M = \int dA M$, and the partial derivative on the right hand side of Eq. 5.D9 has to be taken at constant volume V and constant total mean curvature I_M .

5.E DIFFERENT VARIANTS OF CURVATURE MODELS

In this appendix, we will consider three variants of the curvature model: the spontaneous curvature (SC) model as studied in the main text, the bilayer coupling model, and the area-difference-elasticity model. Two general results will be shown explicitly: (i) all three models lead to the same stationary shapes of vesicles; and (ii) all stationary shapes of the area-difference-elasticity model are also stationary shapes of the spontaneous curvature model with an effective spontaneous curvature m_{eff} .

As in the main text, all functionals will be denoted by calligraphic letters. Thus, we again consider the geometric functionals $\mathcal{V}\{S\}$, $\mathcal{A}\{S\}$, $\Delta\mathcal{A}\{S\}$, and $\mathcal{I}_M\{S\}$ and denote their values for the stationary shapes $S = S^{\text{st}}$ by V , A , ΔA , and I_M .

5.E.1 BILAYER COUPLING (BC) MODEL

For the sake of clarity, it is convenient to start with the bilayer coupling (BC) model which is defined by the bending energy functional

$$\mathcal{E}_{\text{BC}}\{S\} \equiv 2\kappa \int dA M^2. \quad (5.E1)$$

In this model, one considers vesicle shapes with fixed volume V , fixed area A , and integrated mean curvature I_M where the latter quantity is proportional to area difference ΔA between the two leaflets of the bilayer membrane. The stationary shapes S_{BC}^{st} of this model follow from the first variation of the shape functional

$$\mathcal{F}_{BC}\{S\} = -P_{BC}\mathcal{V}\{S\} + \Sigma_{BC}\mathcal{A}\{S\} + Q_{BC}\mathcal{I}_M\{S\} + \mathcal{E}_{BC}\{S\}. \quad (5.E2)$$

The stationary shapes S_{BC}^{st} again form several branches labeled by j . The stationary shapes on branch j will be denoted by S_{BC}^j . The energies of these stationary shapes defines the energy functions as given by

$$E_{BC}(V, A, I_M; j) = \mathcal{E}_{BC}\{S_{BC}^j\} \quad (5.E3)$$

along the branch j . Interpreting the relation between the energy functional \mathcal{E}_{BC} and the shape functional \mathcal{F}_{BC} as a Legendre transformation, we obtain the relations

$$P_{BC} = \left(\frac{dE_{BC}}{dV} \right)_{A, I_M}, \quad \Sigma_{BC} = - \left(\frac{dE_{BC}}{dA} \right)_{V, I_M}, \quad (5.E4)$$

and

$$Q_{BC} = - \left(\frac{dE_{BC}}{dI_M} \right)_{V, A} \quad (5.E5)$$

for the three Lagrange multipliers P_{BC} , Σ_{BC} , and Q_{BC} .

The spontaneous curvature (SC) model studied in the main text is defined by the energy functional

$$\mathcal{E}_{SC}\{S\} \equiv \mathcal{E}_{bc}\{S\} = \mathcal{E}_{BC}\{S\} - 4\kappa m \mathcal{I}_M\{S\} + 2\kappa m^2 \mathcal{A}\{S\}. \quad (5.E6)$$

In this model, one considers vesicle shapes with fixed volume V and fixed area A . The stationary shapes S_{SC}^{st} of this model follow from the first variation of the shape functional

$$\mathcal{F}_{SC}\{S\} = -P_{SC}\mathcal{V}\{S\} + \Sigma_{SC}\mathcal{A}\{S\} + \mathcal{E}_{SC}\{S\} \quad (5.E7)$$

with $P_{SC} \equiv \Delta P$.

5.E.1.1 Identical stationary shapes in BC and SC models

A direct comparison of the two shape functionals \mathcal{F}_{BC} and \mathcal{F}_{SC} in Eqs 5.E2 and 5.E7 shows that these shape functionals are identical provided one chooses

$$P_{BC} = P_{SC}, \quad \Sigma_{BC} = \Sigma_{SC} + 2\kappa m^2, \quad \text{and} \quad Q_{BC} = -4\kappa m. \quad (5.E8)$$

or

$$P_{SC} = P_{BC}, \quad \Sigma_{SC} = \Sigma_{BC} - \frac{Q_{BC}^2}{8\kappa} \quad \text{and} \quad m = -\frac{Q_{BC}}{4\kappa}. \quad (5.E9)$$

As a consequence, the Euler-Lagrange equations of the two models are also identical. The Euler-Lagrange equation of the SC model has the form

$$P_{SC} = 2\Sigma_{SC}M - 2\kappa\nabla_{LB}^2M - 4\kappa(M-m)[M(M+m)-G] \quad (5.E10)$$

as given by Eq. 5.23 with $P_{SC} \equiv \Delta P$ and $\Sigma_{SC} \equiv \Sigma$. The Euler-Lagrange equation of the BC model is obtained from Eq. 5.E10 by the parameter mapping Eq. 5.E9. Therefore, the stationary shapes of the SC model are also stationary shapes of the BC model and *vice versa* when we map the parameters of the two models according to Eq. 5.E8 or Eq. 5.E9, and we can identify the stationary shapes for each branch j , i.e., $S_{SC}^j = S_{BC}^j$, as well as the associated limit shapes.

5.E.2 AREA-DIFFERENCE-ELASTICITY MODEL

The bending energy functional of the area-difference-elasticity model as given by Eq. 5.63 can be rewritten in the form

$$\mathcal{E}_{ADE}\{S\} = \mathcal{E}_{BC}\{S\} - 4\kappa m \mathcal{I}\{S\} + 2\kappa m^2 \mathcal{A}\{S\} + \mathcal{D}_{ADE}\{S\} \quad (5.E11)$$

with the nonlocal bending energy term $\mathcal{D}_{ADE}\{S\}$ as in Eq. 5.64.

In the area-difference-elasticity model, one again considers vesicle shapes with fixed volume V and fixed area A . In order to deal with the nonlocal character of $\mathcal{D}_{ADE}\{S\}$, it is useful to use a two-step variational procedure (Miao et al., 1994). In the first step, we determine the stationary shapes of Eq. 5.E11 for fixed volume V , fixed area A , and fixed integrated mean curvature I_M . These shapes are obtained from the first variation of the shape functional

$$\tilde{\mathcal{F}}_{ADE}\{S\} = -P\mathcal{V}\{S\} + \tilde{\Sigma}_{ADE}\mathcal{A}\{S\} + \tilde{Q}_{ADE}\mathcal{I}_M\{S\} + \mathcal{E}_{ADE}\{S\}. \quad (5.E12)$$

For fixed area A and fixed integrated mean curvature I_M , the energy functional in Eq. 5.E11 reduces to $\mathcal{E}_{ADE}\{S\} = \mathcal{E}_{BC}\{S\} + \text{const.}$

Therefore, the stationary shapes S_{ADE}^j of the ADE model for the given values of V , A , and I_M are identical with the stationary shapes S_{BC}^j of the BC model for the same values of V , A , and I_M and, thus, fulfill the same Euler-Lagrange equation as given by Eq. 5.E10 with the parameter mapping as in Eq. 5.E9. The energy function

$$\tilde{E}_{ADE}(V, A, I_M; j) = \mathcal{E}_{ADE}\{S_{ADE}^j\} \quad (5.E13)$$

is then equal to

$$\tilde{E}_{ADE} = E_{BC}(V, A, I_M; j) - 4\kappa m I_M + 2\kappa m^2 A + 2\pi\kappa\Delta \frac{(I_M - I_{M,0})^2}{A}. \quad (5.E14)$$

Furthermore, the Lagrange multiplier \tilde{Q}_{ADE} in Eq. 5.E12 fulfills the relation

$$\tilde{Q}_{ADE} = - \left(\frac{d\tilde{E}_{ADE}}{dI_M} \right)_{V, A} = Q_{BC} + 4\kappa m - 4\pi\kappa\Delta \frac{I_M - I_{M,0}}{A} \quad (5.E15)$$

with Q_{BC} as in Eq. 5.E5).

In the second step of the variational procedure, we determine the values of the integrated mean curvature I_M that lead to extrema of the energy function \tilde{E}_{ADE} for fixed volume V and fixed area A . These extrema follow from the condition

$$\left(\frac{d\tilde{E}_{\text{ADE}}}{dI_M} \right)_{V,A} = 0. \quad (5.E16)$$

Inserting this condition into Eq. 5.E15, we obtain the identity

$$Q_{\text{BC}} = -4\kappa m + 4\pi\kappa_{\Delta} \frac{I_M - I_{M,0}}{A}. \quad (5.E17)$$

Finally, we use the relation between Q_{BC} and the spontaneous curvature as given by Eq. 5.E8 with $m \equiv m_{\text{eff}}$. As a result, we obtain the expression Eq. 5.66 for the effective spontaneous curvature m_{eff} of the equivalent spontaneous curvature model.

5.F DISCONTINUITIES ALONG DOMAIN BOUNDARIES

This appendix, which supplements Section 5.8 on multi-domain membranes and vesicles, describes the matching conditions for the domain shapes along a domain boundary in some detail. Even for axisymmetric vesicle shapes with smooth contours, these matching conditions turn out to be somewhat complex. Indeed, these matching conditions imply discontinuities along the domain boundary, both for the curvature and for the mechanical tension. In order to describe these discontinuities, we parametrize the contour of the axisymmetric shape by its arc length s starting from the north pole of the shape. We could then use cylindrical coordinates, r and z , to describe the vesicle shape but it is more convenient to use the coordinate r and the tilt angle ψ ,²⁰ see Figure 5.33.

For an axisymmetric shape as in Figure 5.33, the two principal curvatures are given by

$$C_1 = \frac{d\psi}{ds} \equiv \dot{\psi} \quad \text{and} \quad C_2 = \frac{\sin\psi}{r} \quad (5.F1)$$

where C_1 represents the curvature of the shape contour. The second principal curvature C_2 is continuous at the domain boundary with $s = s_1$ because both the tilt angle $\psi(s)$ and the coordinate $r(s)$ are continuous at this s -value. In contrast, the contour curvature C_1 can change discontinuously at the domain boundary.

5.F.1 CURVATURE DISCONTINUITIES

This discontinuity follows from the matching condition (Jülicher and Lipowsky, 1996)

$$\kappa_a \dot{\psi}(s_1 + \varepsilon) - \kappa_b \dot{\psi}(s_1 - \varepsilon) = \delta\kappa C_2(s_1) + 2\kappa_a m_a - 2\kappa_b m_b \quad (5.F2)$$

with

$$\delta\kappa \equiv \kappa_b - \kappa_a + \kappa_{G_b} - \kappa_{G_a}. \quad (5.F3)$$

We now introduce the notation

$$C_{1a}(s_1) \equiv \dot{\psi}(s_1 + \varepsilon) \quad \text{and} \quad C_{1b}(s_1) \equiv \dot{\psi}(s_1 - \varepsilon) \quad (5.F4)$$

for the contour curvatures and

$$M_a(s_1) \equiv \frac{1}{2}[C_{1a}(s_1) + C_2(s_1)] \quad \text{and} \quad (5.F5)$$

$$M_b(s_1) \equiv \frac{1}{2}[C_{1b}(s_1) + C_2(s_1)]$$

for the mean curvatures at the two sides of the domain boundary. Using this notation, the matching condition Eq. 5.F2 can be rewritten as

$$\kappa_a [M_a(s_1) - m_a] - \kappa_b [M_b(s_1) - m_b] = \frac{1}{2}(\kappa_{G_b} - \kappa_{G_a})C_2(s_1). \quad (5.F6)$$

The above matching conditions imply the discontinuity

$$C_{1a}(s_1) - C_{1b}(s_1) = \dot{\psi}(s_1 + \varepsilon) - \dot{\psi}(s_1 - \varepsilon) = \Delta_1 \quad (5.F7)$$

of the contour curvature C_1 with

$$\Delta_1 \equiv \frac{\kappa_b - \kappa_a}{\kappa_a} C_{1b}(s_1) + \frac{\delta\kappa}{\kappa_a} C_2(s_1) + 2 \frac{\kappa_a m_a - \kappa_b m_b}{\kappa_a} \quad (5.F8)$$

as follows from Eq. 5.F2. Note that the discontinuity Δ_1 depends (i) on the contour curvature $C_{1b}(s_1)$ along the b -side of the domain boundary and (ii) on the second principal curvature $C_2(s_1)$ at this boundary. Rearranging the terms in Eq. 5.F7, we obtain the discontinuity

$$M_a(s_1) - M_b(s_1) = \frac{1}{2}\Delta_1 \quad (5.F9)$$

of the mean curvature M . Note also that the curvature discontinuities as described by Eqs 5.F7 and 5.F9 depend only on *local* properties of the vesicle shape close to the domain boundary.

The matching conditions for the curvatures simplify when we consider two membrane domains for which some of the curvature-elastic parameters are identical. If both membrane domains have the same Gaussian curvature modulus, the expression Eq. 5.F8 becomes

$$\Delta_1 = 2 \frac{\kappa_b - \kappa_a}{\kappa_a} M_{1b} + 2 \frac{\kappa_a m_a - \kappa_b m_b}{\kappa_a} \quad (\kappa_{G_b} = \kappa_{G_a}) \quad (5.F10)$$

and the matching condition Eq. 5.F6 attains the simple and concise form

$$\kappa_a [M_a(s_1) - m_a] = \kappa_b [M_b(s_1) - m_b] \quad (\kappa_{G_b} = \kappa_{G_a}). \quad (5.F11)$$

If both domains have the same Gaussian curvature modulus and the same bending rigidity, the discontinuity Δ_1 becomes

$$\Delta_1 = 2(m_a - m_b) \quad (\kappa_{G_b} = \kappa_{G_a} \text{ and } \kappa_b = \kappa_a). \quad (5.F12)$$

In this case, the curvature discontinuity is independent of the principal curvatures at the domain boundary and proportional to the difference $m_b - m_a$ of the spontaneous curvatures. Using the matching condition in the form Eq. 5.F11, we also obtain

²⁰ The two variables ψ and r satisfy the relation $\frac{dr}{ds} = \cos\psi$, a condition that is incorporated into the variational calculation by a Lagrange parameter function (Seifert et al., 1991; Jülicher and Lipowsky, 1996).

$$M_b(s_1) - m_b = M_a(s_1) - m_a \quad \text{for } \kappa_{Gb} = \kappa_{Ga} \text{ and } \kappa_b = \kappa_a. \quad (5.F13) \quad \text{and}$$

Therefore, the deviation of the mean curvature from the spontaneous curvature is continuous across the domain boundary if the two membrane domains have the same Gaussian curvature modulus and the same bending rigidity. Likewise, the discontinuity simplifies to

$$\Delta_1 = 2 \frac{\kappa_b - \kappa_a}{\kappa_a} [M_b(s_1) - m] \quad \text{for } m_b = m_a = m \text{ and } \kappa_{Gb} = \kappa_{Ga}. \quad (5.F14)$$

In the latter case, the curvature discontinuity is proportional to the difference $\kappa_b - \kappa_a$ of the bending rigidities and to the deviation $M_b(s_1) - m$ of the mean curvature $M_b(s_1)$ along the b -side of the domain boundary from the spontaneous curvature m . Finally, the curvature discontinuity Δ_1 vanishes if both membrane domains have the same curvature-elastic properties, i.e.,

$$\Delta_1 = 0 \quad \text{for } m_b = m_a, \kappa_b = \kappa_a, \text{ and } \kappa_{Gb} = \kappa_{Ga}. \quad (5.F15)$$

5.F.2 DIFFERENCE BETWEEN MECHANICAL TENSIONS

The discontinuity Δ_1 of the contour curvature C_1 at the domain boundary also affects the difference $\Sigma_b - \Sigma_a$ of the mechanical tensions within the two membrane domains. Using the results of (Jülicher and Lipowsky, 1996), one finds the tension difference

$$\Sigma_a - \Sigma_b = \lambda \frac{\cos \Psi(s_1)}{r(s_1)} + \Delta_\Sigma \quad (5.F16)$$

with

$$\Delta_\Sigma \equiv \frac{1}{2} \kappa_a Q_a(s_1) - \frac{1}{2} \kappa_b Q_b(s_1) \quad (5.F17)$$

and

$$Q_j(s_1) \equiv C_{1j}^2(s_1) - [C_2(s_1) - 2m_j]^2 \quad \text{for } j = a, b. \quad (5.F18)$$

It follows from the relations in Eqs 5.F2, 5.F3, and 5.F6 that the curvature discontinuities along the domain boundary depend on the difference $\kappa_{Gb} - \kappa_{Ga}$ of the Gaussian curvature moduli. Therefore, the expression Eq. 5.F17 for Δ_Σ implicitly depends on $\kappa_{Gb} - \kappa_{Ga}$ as well.

Inspection of the expression Eq. 5.F17 shows that Δ_Σ contains only two shape-independent terms as given by the spontaneous tensions $\sigma_j = 2\kappa_j m_j^2$ with $j = a, b$. Thus, we can decompose the expression Eq. 5.F17 according to

$$\Delta_\Sigma = -2\kappa_a m_a^2 + 2\kappa_b m_b^2 + \Delta_S = -\sigma_a + \sigma_b + \Delta_S \quad (5.F19)$$

with

$$\Delta_S \equiv \frac{1}{2} \kappa_a \tilde{Q}_a(s_1) - \frac{1}{2} \kappa_b \tilde{Q}_b(s_1) \quad (5.F20)$$

$$\tilde{Q}_j(s_1) = C_{1j}^2(s_1) - C_2^2(s_1) + 4C_2(s_1)m_j. \quad (5.F21)$$

The tension difference in Eq. 5.F16 can then be rewritten as

$$\hat{\Sigma}_a - \hat{\Sigma}_b = \lambda \frac{\cos \Psi(s_1)}{r(s_1)} + \Delta_S. \quad (5.F22)$$

If both membrane domains have the same bending rigidity κ and the same Gaussian curvature modulus, the quantities Δ_Σ and Δ_S become

$$\Delta_\Sigma = 2\kappa(m_a - m_b)[M_a(s_1) - m_a + M_b(s_1) - m_b] \quad (5.F23)$$

$(\kappa_b = \kappa_a, \text{ and } \kappa_{Gb} = \kappa_{Ga})$

and

$$\Delta_S = 2\kappa(m_a - m_b)[M_a(s_1) + M_b(s_1)] \quad (5.F24)$$

$(\kappa_b = \kappa_a, \text{ and } \kappa_{Gb} = \kappa_{Ga}).$

Note that $M_b(s_1) - m_b = M_a(s_1) - m_a$ according to Eq. 5.F13 for two domains with the same bending rigidity and the same Gaussian curvature modulus. Finally, if all curvature-elastic parameters of the two membrane domains are identical, the contour curvature is continuous across the domain boundary, see Eq. 5.F15, which implies $C_{1b}(s_1) = C_{1a}(s_1)$, $Q_b(s_1) = Q_a(s_1)$, and

$$\Delta_\Sigma = \Delta_S = 0 \quad \text{for } m_b = m_a, \kappa_b = \kappa_a, \text{ and } \kappa_{Gb} = \kappa_{Ga}. \quad (5.F25)$$

Therefore, in this case, the balance between the mechanical membrane tensions Σ_a and Σ_b within the two domains and the line tension γ of the domain boundary is described by

$$\Sigma_a - \Sigma_b = \lambda \frac{\cos \Psi(s_1)}{r(s_1)} \quad \text{for } m_b = m_a, \kappa_b = \kappa_a, \text{ and } \kappa_{Gb} = \kappa_{Ga}. \quad (5.F26)$$

The minimization of the energy functional Eq. 5.272 also implies a third matching condition that describes a jump in $\tilde{\psi}$, i.e., in the first derivative of the contour curvature $C_1 = \tilde{\psi}$ with respect to the arc length s .²¹

5.G SEGMENTATION AND PHASE SEPARATION OF TWO-COMPONENT MEMBRANES

The interplay of ambience-induced segmentation and phase separation of membranes has been theoretically studied in some detail for membranes with two lipid components, say l_a and l_b (Rouhiparkouhi et al., 2013; Lipowsky et al., 2013). If the membranes contains more than two components, we can single out one special component, denote this component by l_a , and combine all

²¹ In order to derive this third matching condition, it is useful to start from the shape equation for $\tilde{\psi}$ within the two domains, see Eq. (A.13) in (Jülicher and Lipowsky, 1996), from which one can determine the quantity $\kappa_a \tilde{\psi}(s_1 + \varepsilon) - \kappa_b \tilde{\psi}(s_1 - \varepsilon)$. The latter quantity depends only on *local* properties of the vesicle shape close to the domain boundary.

other components into an effective second component l_b , thereby mapping a multi-component membrane onto a two-component one. To simplify the following discussion, we will ignore differences in the molecular areas of the two lipid components and take both molecular areas to be equal to A_l . If the membrane contains N_{l_a} lipids l_a and N_{l_b} lipids l_b , the total membrane area A is then given by

$$A = \frac{1}{2}(N_{l_a} + N_{l_b})A_l \quad (5.G1)$$

where the factor 1/2 takes into account that the bilayer membrane consists of two leaflets.

The membrane is exposed to K local environments that differ in their molecular compositions and thus partition the membrane into several segments distinguished by the superscript $[k]$ with $k = 1, 2, \dots, K$ as in Figure 5.31. The total membrane area A is then partitioned into the segmental areas $A^{[k]}$ with

$$A = A^{[1]} + A^{[2]} + \dots + A^{[K]}. \quad (5.G2)$$

Furthermore, the total number of l_a and l_b molecules contained in segment $[k]$ is fixed and equal to $A^{[k]}/A_l$. Therefore, when one molecule diffuses from segment $[k]$ to a neighboring segment $[k']$, another molecule must diffuse from segment $[k']$ to segment $[k]$.

When a lipid molecule l_a or l_b is located in segment $[k]$, the molecular interactions with the adjacent environment $[k]$ lead to the interaction energies $U_{l_a}^{[k]}$ and $U_{l_b}^{[k]}$, respectively, where effectively attractive interactions are described by negative values $U_{l_a}^{[k]} < 0$ and $U_{l_b}^{[k]} < 0$. The enrichment or depletion of the two lipid species adjacent to environment $[k]$ is then determined by the relative affinity

$$\Delta U^{[k]} = U_{l_a}^{[k]} - U_{l_b}^{[k]} \quad \text{within segment}[k], \quad (5.G3)$$

which is negative if environment $[k]$ prefers the l_a lipids and positive if this environment prefers the l_b lipids.

For a homogeneous environment with interaction energies $U_{l_a}^{[k]} = 0$ and $U_{l_b}^{[k]} = 0$, the two lipid species have the chemical potentials μ_{l_a} and μ_{l_b} . These chemical potentials are not independent because the lipid numbers N_{l_a} and N_{l_b} are related via Eq. 5.G1. The membrane system is then described by the semigrand canonical ensemble with the relative chemical potential (Lipowsky et al., 2013)

$$\Delta\mu \equiv \mu_{l_a} - \mu_{l_b}. \quad (5.G4)$$

Within this statistical ensemble, the phase transition occurs along the line

$$\Delta\mu = \Delta\mu^*(T) \quad \text{for } T_t < T < T_c \quad (5.G5)$$

in the $(\Delta\mu, T)$ plane where T_t and T_c are the temperatures of the triple point and the critical demixing point, respectively. The function $\Delta\mu^*(T)$ is obtained from the free energy in the semigrand canonical ensemble and depends on all parameters that describe the interactions between the lipid components (Lipowsky et al., 2013).

When the membrane is now partitioned into several segments by the different local environments, the chemical potentials are shifted by the interaction energies $U_{l_a}^{[k]}$ and $U_{l_b}^{[k]}$. Each segment $[k]$ is now characterized by the relative chemical potential

$$\Delta\mu^{[k]} \equiv \mu_{l_a} + U_{l_a}^{[k]} - (\mu_{l_b} + U_{l_b}^{[k]}) = \Delta\mu + \Delta U^{[k]}, \quad (5.G6)$$

which is equal to the relative chemical potential of the homogeneous system shifted by the relative affinity $\Delta U^{[k]}$. As a consequence, each segment $[k]$ undergoes a phase transition along the line

$$\Delta\mu^{[k]} = \Delta\mu + \Delta U^{[k]} = \Delta\mu^*(T) + \Delta U^{[k]} \quad \text{for } T_t < T < T_c, \quad (5.G7)$$

and the membrane consisting of K segments exhibits K phase transitions as shown in Figure 5.47. The transition lines for segment $[k + 1]$ and segment $[k]$ are separated by

$$\Delta\mu^{[k+1]} - \Delta\mu^{[k]} = U^{[k+1]} - U^{[k]} \equiv \Delta U_k \quad (5.G8)$$

with the affinity contrast ΔU_k between segment $[k + 1]$ and segment $[k]$.

In the canonical ensemble, the relative chemical potential $\Delta\mu$ is replaced by the mole fraction X_{l_a} of the l_a lipids with $0 \leq X_{l_a} \leq 1$. Each transition line within the $(\Delta\mu, T)$ phase diagram as displayed in Figure 5.47 is then mapped onto a coexistence region within the (X_{l_a}, T) phase diagram. Because the resulting K coexistence regions have to be accommodated, at each temperature T , within the interval $0 \leq X_{l_a} \leq 1$, the average width of a single coexistence region is necessarily smaller than $1/K$ and therefore decreases monotonically with increasing number K of distinct local environments.

5.H WETTING OF TWO MEMBRANELESS DROPLETS

Wetting of a vesicle membrane, arising from the aqueous phase separation within the vesicle, leads to two aqueous droplets enclosed by this membrane as depicted in the insets of

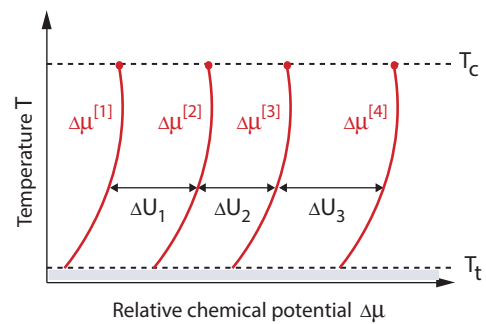


Figure 5.47 Phase diagram for a two-component membrane exposed to $K = 4$ different environments as a function of relative chemical potential $\Delta\mu$ and temperature T with $T_t < T \leq T_c$. Segment $[k]$ undergoes a phase transition along the demixing line $\Delta\mu = \Delta\mu^{[k]}$ as given by Eq. 5.G7. The demixing lines $\Delta\mu^{[k+1]}$ and $\Delta\mu^{[k]}$ are separated by the affinity contrast ΔU_k between segment $[k + 1]$ and segment $[k]$ as in Eq. 5.G8. Each demixing line has a critical point at $T = T_c$.

Figure 5.39. This appendix describes the analogous but somewhat simpler situation corresponding to the wetting of two droplets in the *absence* of the membrane. The two droplets consist of the two liquid phases α and β and are completely immersed into the bulk liquid phase γ , see **Figure 5.48**. The latter wetting system will now be discussed in some detail to reveal the similarities and differences compared to the wetting of membranes, see **Section 9.3**.

5.H.1 SPHERICAL GEOMETRY AND CONTACT ANGLES

The two droplets in **Figure 5.48** consist of two aqueous phases, α and β , which are immersed into a third liquid phase γ . The geometry of such a droplet pair involves three interfaces: the $\alpha\gamma$ interface between the α droplet and the exterior γ phase; the $\beta\gamma$ interface between the β droplet and the γ phase; and the $\alpha\beta$ interface between the α and the β droplets. All three interfaces form spherical segments that meet at the three-phase contact line as shown in **Figure 5.48a**. The curvature radii of the three spherical radii are denoted by $R_{\alpha\gamma}$, $R_{\beta\gamma}$, and $R_{\alpha\beta}$ which are all taken to be positive.²² Along the contact line, the tangent planes of the three interfaces form the three contact angles θ_α , θ_β , and θ_γ with $\theta_\alpha + \theta_\beta + \theta_\gamma = 2\pi$, see **Figure 5.48b**. It is not difficult to show that the shape consisting of three spherical segments implies the geometric relation

$$\pm \frac{\sin \theta_\gamma}{R_{\alpha\beta}} = \frac{\sin \theta_\alpha}{R_{\beta\gamma}} - \frac{\sin \theta_\beta}{R_{\alpha\gamma}} \quad (5.H1)$$

or

$$\pm \frac{1}{R_{\alpha\beta}} = \frac{\sin \theta_\alpha / \sin \theta_\gamma}{R_{\beta\gamma}} - \frac{\sin \theta_\beta / \sin \theta_\gamma}{R_{\alpha\gamma}} \quad (5.H2)$$

where the plus and minus sign corresponds to an $\alpha\beta$ interface that bulges towards the α and the β phase, respectively. Thus,

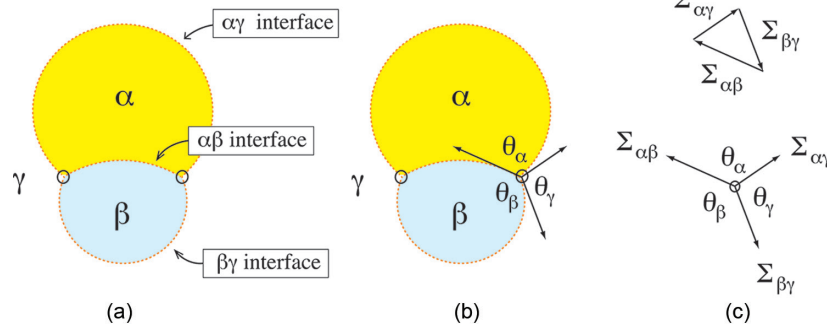


Figure 5.48 (a) Partial wetting of an α droplet (yellow) and a β droplet (blue) immersed in the liquid bulk phase γ (white). The two droplets are bounded by the $\alpha\gamma$, $\alpha\beta$, and $\beta\gamma$ interfaces. All three interfaces form spherical segments that meet at the three-phase contact line (small black circles); (b) Along the contact line, the tangent planes of the three interfaces form the three contact angles θ_α , θ_β , and θ_γ with $\theta_\alpha + \theta_\beta + \theta_\gamma = 2\pi$; and (c) The interfacial tensions $\Sigma_{\alpha\beta}$, $\Sigma_{\alpha\gamma}$, and $\Sigma_{\beta\gamma}$ pull at the contact line in the directions of the three tangent planes. In mechanical equilibrium, the three tensions must balance and add up to zero which implies that they form the sides of a triangle (upper panel) which is known as Neumann's triangle.

²² Note that the $\alpha\beta$ interface may bulge towards the α phase as in **Figure 5.48a** or towards the β phase depending on the relative magnitude of the pressures within the α and β phases.

the plus sign applies, in particular, to the geometry displayed in **Figure 48a,b**.

5.H.2 MECHANICAL EQUILIBRIUM BETWEEN INTERFACES

To proceed, let us consider the balance between the Laplace pressures and the interfacial tensions $\Sigma_{\alpha\gamma}$, $\Sigma_{\beta\gamma}$, and $\Sigma_{\alpha\beta}$ of the three interfaces. The mean curvatures $M_{\alpha\gamma} = 1/R_{\alpha\gamma}$ and $M_{\beta\gamma} = 1/R_{\beta\gamma}$ of the $\alpha\gamma$ and $\beta\gamma$ interfaces satisfy the two Laplace equations

$$\Delta P_{i\gamma} \equiv P_i - P_\gamma = 2\Sigma_{i\gamma} M_{i\gamma} = 2\Sigma_{i\gamma}/R_{i\gamma} > 0 \text{ for } i = \alpha, \beta. \quad (5.H3)$$

These equations are also valid when the two droplets are not in contact with each other and form two separate spheres immersed into the γ phase. For the partial wetting geometry, on the other hand, the mean curvature $M_{\alpha\beta} = \pm 1/R_{\alpha\beta}$ of the $\alpha\beta$ interface satisfies another Laplace equation as given by

$$P_\beta - P_\alpha = 2\Sigma_{\alpha\beta} M_{\alpha\beta} = \pm 2\Sigma_{\alpha\beta}/R_{\alpha\beta}. \quad (5.H4)$$

As before, the plus and minus sign corresponds to an $\alpha\beta$ interface that bulges towards the α and β phase, respectively. The pressure differences can be eliminated by a combination of all three Laplace equations which leads to the relationship

$$\pm \frac{\Sigma_{\alpha\beta}}{R_{\alpha\beta}} = \frac{\Sigma_{\beta\gamma}}{R_{\beta\gamma}} - \frac{\Sigma_{\alpha\gamma}}{R_{\alpha\gamma}} \quad (5.H5)$$

or

$$\pm \frac{1}{R_{\alpha\beta}} = \frac{\Sigma_{\beta\gamma} / \Sigma_{\alpha\beta}}{R_{\beta\gamma}} - \frac{\Sigma_{\alpha\gamma} / \Sigma_{\alpha\beta}}{R_{\alpha\gamma}}. \quad (5.H6)$$

between the three interfacial tensions.

5.H.3 INTERFACIAL TENSIONS FROM CONTACT ANGLES

If we combine the relationship Eq. 5.H6 between the three tensions with the purely geometric relation Eq. 5.H2, we obtain

$$\frac{1}{R_{\alpha\gamma}} \left(\frac{\Sigma_{\alpha\gamma}}{\Sigma_{\alpha\beta}} - \frac{\sin\theta_\beta}{\sin\theta_\gamma} \right) = \frac{1}{R_{\beta\gamma}} \left(\frac{\Sigma_{\beta\gamma}}{\Sigma_{\alpha\beta}} - \frac{\sin\theta_\alpha}{\sin\theta_\gamma} \right). \quad (5.H7)$$

Both the interfacial tensions and the contact angles are material parameters that do not depend on the droplet geometry, provided the droplets are sufficiently large and we can ignore the contact line tension. As a consequence, the relation (5.7) can only hold for arbitrary values of the radii $R_{\alpha\gamma}$ and $R_{\beta\gamma}$, if the terms in the two parentheses vanish separately. Therefore, we conclude that

$$\frac{\Sigma_{\alpha\gamma}}{\Sigma_{\alpha\beta}} = \frac{\sin\theta_\beta}{\sin\theta_\gamma} \quad \text{and} \quad \frac{\Sigma_{\beta\gamma}}{\Sigma_{\alpha\beta}} = \frac{\sin\theta_\alpha}{\sin\theta_\gamma} \quad (5.H8)$$

which relate the interfacial tensions to the contact angles. It is interesting to note that the derivation of Eq. 5.H8 was based (i) on the purely geometric relation Eq. 5.H2 for three spherical caps and (ii) on the Laplace Eqs 5.H3 and 5.H4 for the mechanical equilibrium of the spherical cap segments of the three interfaces away from the contact line. On the other hand, the relationships Eq. 5.H8 can also be derived from the force balance between the three interfacial tensions at the contact line. Indeed, in mechanical equilibrium, the three tensions must add up to zero which implies that these tensions form the sides of a triangle as shown in the upper panel of Figure 5.48c. In the literature on capillary forces, this triangle is known as Neumann’s triangle (Rowlinson and Widom, 1989). The law of sines for triangles then leads to the equalities

$$\frac{\Sigma_{\alpha\beta}}{\sin\theta_\gamma} = \frac{\Sigma_{\alpha\gamma}}{\sin\theta_\beta} = \frac{\Sigma_{\beta\gamma}}{\sin\theta_\alpha} \quad (5.H9)$$

which are equivalent to the relations Eq. 5.H8.

It is instructive to rederive the force balance conditions as described by Eqs 5.8 or by the equivalent Eqs 5.9 using a variational approach. To do so, we start from the parametrization of the three-spherical-cap geometry in terms of the four radii $R_{\alpha\beta}$, $R_{\alpha\gamma}$, $R_{\beta\gamma}$, and R_{co} as described in Section 9.5.1 and consider the (free) energy of the three interfaces which has the form

$$E_o(R_{\alpha\beta}, R_{\alpha\gamma}, R_{\beta\gamma}, R_{co}) = \Sigma_{\alpha\beta} A_{\alpha\beta} + \Sigma_{\alpha\gamma} A_{\alpha\gamma} + \Sigma_{\beta\gamma} A_{\beta\gamma}. \quad (5.H10)$$

The three interfacial areas can be written as explicit functions of the four radii. To minimize this energy function for fixed droplet volumes V_α and V_β , we define the shape function

$$F_o(R_{\alpha\beta}, R_{\alpha\gamma}, R_{\beta\gamma}, R_{co}) \equiv (P_\gamma - P_\alpha)V_\alpha + (P_\gamma - P_\beta)V_\beta + \Delta F_o \quad (5.H11)$$

with

$$\Delta F_o \equiv E_o = \Sigma_{\alpha\beta} A_{\alpha\beta} + \Sigma_{\alpha\gamma} A_{\alpha\gamma} + \Sigma_{\beta\gamma} A_{\beta\gamma} \quad (5.H12)$$

where the two droplet volumes V_α and V_β are again explicit functions of the four radii. The stationary three-spherical-cap shapes are then obtained from

$$\frac{\partial F_o}{\partial R_{\alpha\beta}} = 0, \quad \frac{\partial F_o}{\partial R_{\alpha\gamma}} = 0, \quad \frac{\partial F_o}{\partial R_{\beta\gamma}} = 0, \quad \text{and} \quad \frac{\partial F_o}{\partial R_{co}} = 0. \quad (5.H13)$$

From these stationarity conditions, we recover the three Laplace Eqs 5.3 and 5.4 as well as the force balance Eqs 5.8 along the contact line.

5.H.4 TRIANGLE RELATIONS FOR INTERFACIAL TENSIONS

Inspection of Figure 5.48c shows that the three contact angles are the exterior angles of the triangle formed by the three tensions. So far, it has been tacitly assumed that all three contact angles are neither zero nor equal to π . In fact, as one of the contact angle goes to zero, the two other angles must approach the limiting value π . In this limit, the interface of two phases is *completely* wet by the third phase. As an example, consider complete wetting of the $\beta\gamma$ interface by the α phase. In the latter case, the contact angle L_1^\dagger and the two other contact angles have the values $\theta_\beta = \theta_\gamma = \pi$. The α phase then forms a thin wetting layer between the β and the γ phases. In such a situation, one side of the tension triangle becomes equal to the sum of the two other sides and the triangle collapses.

For any triangle, the length of a given side must be smaller than or equal to the sum of the lengths of the two other sides. For the tension triangle in Figure 5.48c, the corresponding triangle relations are given by

$$\Sigma_{\alpha\gamma} \leq \Sigma_{\beta\gamma} + \Sigma_{\alpha\beta}, \quad \Sigma_{\beta\gamma} \leq \Sigma_{\alpha\gamma} + \Sigma_{\alpha\beta} \quad \text{and} \quad \Sigma_{\alpha\beta} \leq \Sigma_{\alpha\gamma} + \Sigma_{\beta\gamma}. \quad (5.H14)$$

It will be instructive to rewrite these relations in a somewhat redundant manner as given by

$$-\Sigma_{\alpha\beta} \leq \Sigma_{\beta\gamma} - \Sigma_{\alpha\gamma} \leq +\Sigma_{\alpha\beta}, \quad (5.H15)$$

$$-\Sigma_{\alpha\gamma} \leq \Sigma_{\beta\gamma} - \Sigma_{\alpha\beta} \leq +\Sigma_{\alpha\gamma} \quad (5.H16)$$

and

$$-\Sigma_{\beta\gamma} \leq \Sigma_{\beta\gamma} - \Sigma_{\alpha\gamma} \leq +\Sigma_{\beta\gamma} \quad (5.H17)$$

which provide lower and upper bounds for all tension differences. In fact, multiplying these inequalities by (-1) , we obtain inequalities of the form $-\Sigma_{\alpha\beta} \leq \Sigma_{\alpha\gamma} - \Sigma_{\beta\gamma} \leq +\Sigma_{\alpha\beta}$ etc. Therefore, the difference between any two tensions is larger or equal to (-1) times the third tension and smaller or equal to $(+1)$ times the third tension.

The inequalities in these triangle relations correspond to partial wetting while the equalities correspond to complete wetting.

As an example, consider the bounds for the tension difference $\Sigma_{\beta\gamma} - \Sigma_{\alpha\gamma}$ as given by Eq. 5.H15. Using the relations in Eq. 5.H8, we obtain the expression

$$\frac{\Sigma_{\beta\gamma} - \Sigma_{\alpha\gamma}}{\Sigma_{\alpha\gamma}} = \frac{\sin\theta_\alpha - \sin\theta_\beta}{\sin\theta_\gamma}. \quad (5.H18)$$

It will be convenient to define the function

$$\Xi(x, y, z) \equiv \frac{\sin x - \sin y}{\sin z} \quad (5.H19)$$

Combining the relations Eqs 5.H18 and 5.H15, we obtain the inequalities

$$-1 \leq \Xi(\theta_\alpha, \theta_\beta, \theta_\gamma) \leq +1 \quad (5.H20)$$

for the function Ξ that depends on all three contact angles. The lower bound

$$\Xi(\theta_\alpha = \pi, \theta_\beta = 0, \theta_\gamma = \pi) = -1 \quad (5.H21)$$

describes complete wetting of the $\alpha\gamma$ interface by the β phase whereas the upper bound

$$\Xi(\theta_\alpha = 0, \theta_\beta = \pi, \theta_\gamma = \pi) = +1 \quad (5.H22)$$

corresponds to complete wetting of the $\beta\gamma$ interface by the α phase.

5.1 OUT-WETTING OF MEMBRANES AND VESICLES

In the main text, we focused on in-wetting morphologies of GUVs that arise from aqueous phase separation within the giant vesicles, see Figure 5.40. Wetting of vesicle membranes has also been observed when the vesicles were exposed to PEG-dextran solutions that underwent phase separation outside the GUVs (Li et al., 2012). The aqueous minority phase then forms droplets that can adhere to the vesicle membrane.

5.1.1 OUT-WETTING MORPHOLOGIES

The interaction of the membrane with one such droplet leads to several out-wetting morphologies as shown in Figure 5.49. The morphologies in Figure 5.49a and b have been observed for PEG-dextran solutions (Li et al., 2012). The morphology in Figure 5.49a corresponds to partial wetting of the vesicle membrane by the coexisting liquid phases α and β . This morphology is again characterized by a three-phase contact line that partitions the membrane into two segments. When viewed with optical resolution, the shape contour has an apparent kink at the contact line which should be replaced by a smoothly curved membrane segment when we look at this line with nanoscale resolution.

For partial out-wetting, the $\alpha\beta$ interface partitions the vesicle membrane into an $\gamma\alpha$ segment and a $\gamma\beta$ segment. At first sight, swapping the subscripts γ and α as well as γ and β for out-wetting compared to in-wetting morphologies might seem a bit pedantic but turns out to be important because of the spontaneous curvatures. These curvatures have a sign that is taken to be positive and negative if the membrane prefers to bulge towards the exterior and interior solution, respectively. Therefore, when we swap the interior and exterior solutions, the spontaneous curvature m_{ij} for out-wetting morphologies will differ from the spontaneous curvature $m_{ji} = -m_{ij}$ for in-wetting morphologies.

5.1.2 THEORY OF OUT-WETTING

Geometry of out-wetting morphologies

The out-wetting morphologies in Figure 5.49 involve the spectator phase γ inside the GUV as well as a single β droplet coexisting with the bulk phase α in the exterior solution. The shape S of the vesicle-droplet system can again be decomposed into several components. First, we define the shape S_γ of the interior β droplet, which is identical with the vesicle shape, and the shape S_β of the β droplet. The corresponding droplet volumes are denoted by

$$V_\gamma = \mathcal{V}\{S_\gamma\} \quad \text{and} \quad V_\beta = \mathcal{V}\{S_\beta\}. \quad (5.11)$$

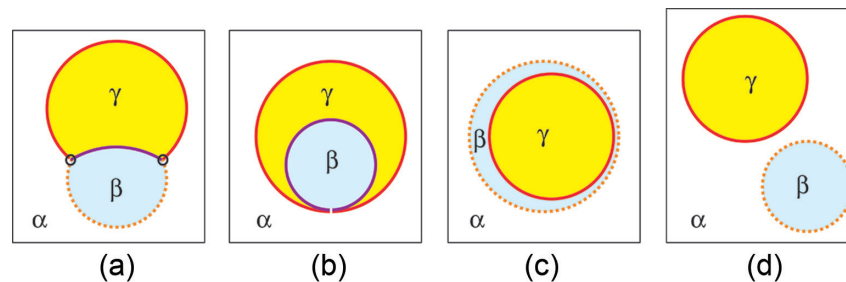


Figure 5.49 Out-wetting morphologies of giant vesicles arising from phase separation of the exterior solution into two aqueous phases, α (white) and β (blue). The vesicle is filled with the aqueous spectator phase γ . (yellow) The $\alpha\beta$ interfaces are depicted as dashed orange lines, the membrane segments in contact with the α and β droplets as red and purple lines, respectively: (a) Partial wetting of the vesicle membrane by α and β as observed on the micrometer scale. The apparent kink at the contact line (black circles) reveals the capillary forces that the $\alpha\beta$ interface exerts onto the vesicle membrane; (b) Special morphology for which the β droplet and the bulk phase α are separated by a closed membrane neck. This morphology resembles complete wetting by the γ phase and required a sufficiently small reduced volume v of the vesicle; (c) Complete wetting of the membrane by the β phase; and (d) Complete wetting by the α phase which leads to the release of the β droplet from the vesicle.

The vesicle volume is now identical with the volume of the γ droplet, i.e., $V = V_\gamma$. These volumes can be considered to be constant at constant temperature and fixed osmotic conditions. The two droplets are bounded by three surface segments: the $\alpha\beta$ interface between the β droplet and the aqueous bulk phase α as well as two membrane segments, the $\gamma\alpha$ segment in contact with the α phase and the $\beta\gamma$ segment exposed to the β droplet. The shapes of these three surfaces will be denoted by $S_{\alpha\beta}$, $S_{\gamma\alpha}$ and $S_{\beta\gamma}$, respectively, with surface areas

$$A_{\alpha\beta} = \mathcal{A}\{S_{\alpha\beta}\}, \quad A_{\gamma\alpha} = \mathcal{A}\{S_{\gamma\alpha}\}, \quad \text{and} \quad A_{\beta\gamma} = \mathcal{A}\{S_{\beta\gamma}\}. \quad (5.12)$$

The total surface area A of the vesicle membrane is then given by

$$A = A_{\gamma\alpha} + A_{\beta\gamma}. \quad (5.13)$$

All three surface segments meet along the three-phase contact line which has the shape $S_{\alpha\beta\gamma}$ and the length

$$L_{\alpha\beta\gamma} = \mathcal{L}\{S_{\alpha\beta\gamma}\}. \quad (5.14)$$

The $\alpha\beta$ interface can adapt its area $A_{\alpha\beta}$ to changes in the droplet and membrane morphologies. As before, the total membrane area A will be taken to be constant at constant temperature. The vesicle-droplet system is then characterized by three geometric constraints as provided by the volumes V_γ and V_β of the two droplets as well as the total membrane area A . In order to determine the morphology of the vesicle-droplet system, we will minimize the (free) energy of the system, taking these three constraints into account.

Adhesion free energies

The adhesion free energy per unit contact area between the outer leaflet of the vesicle membrane and the aqueous bulk phase α will be denoted by $W_{\gamma\alpha}$. Likewise, the adhesive strength $W_{\gamma\beta}$ describes the adhesion free energy per unit contact area between the outer leaflet of the vesicle membrane and the β droplet. The adhesion free energy of the vesicle-droplet system then has the form

$$E_{\text{ad}} = W_{\gamma\alpha} A_{\gamma\alpha} + W_{\gamma\beta} A_{\beta\gamma} \quad (5.15)$$

corresponding to the adhesion free energy functional

$$\mathcal{E}_{\text{ad}}\{S_{\gamma\alpha}, S_{\beta\gamma}\} = W_{\gamma\alpha} \mathcal{A}\{S_{\gamma\alpha}\} + W_{\gamma\beta} \mathcal{A}\{S_{\beta\gamma}\}. \quad (5.16)$$

We ignore any curvature-dependence of the adhesive strengths $W_{\gamma\alpha}$ and $W_{\gamma\beta}$ which leads to the identities

$$W_{\gamma\alpha} = W_{\alpha\gamma} \quad \text{and} \quad W_{\gamma\beta} = W_{\beta\gamma}, \quad (5.17)$$

i.e., the adhesive strengths $W_{\gamma\alpha}$ and $W_{\gamma\beta}$ for out-wetting are identical with the adhesive strengths $W_{\alpha\gamma}$ and $W_{\beta\gamma}$ for in-wetting as defined in Eq. 5.308. Therefore, the adhesion free energy functional for out-wetting has the same form as for in-wetting.

Mechanical, spontaneous, and total segment tensions

The adhesive strengths $W_{\gamma\alpha}$ and $W_{\gamma\beta}$ contribute to the mechanical tensions

$$\Sigma_{\gamma\alpha} = \Sigma + W_{\gamma\alpha} \quad \text{and} \quad \Sigma_{\gamma\beta} = \Sigma + W_{\gamma\beta} \quad (5.18)$$

of the two membrane segments where Σ is again the overall stress of the vesicle membrane arising from the constraint on the total membrane area. If the two segments have a spontaneous curvature, the weakly curved segments experience the spontaneous tension

$$\sigma_{\gamma\alpha} = 2\kappa_{\gamma\alpha} m_{\gamma\alpha}^2 \quad \text{and} \quad \sigma_{\gamma\beta} = 2\kappa_{\gamma\beta} m_{\gamma\beta}^2. \quad (5.19)$$

The mechanical and the spontaneous segment tensions add up to the total segment tensions

$$\hat{\Sigma}_{\gamma\alpha} = \Sigma_{\gamma\alpha} + \sigma_{\gamma\alpha} \quad \text{and} \quad \hat{\Sigma}_{\gamma\beta} = \Sigma_{\gamma\beta} + \sigma_{\gamma\beta} \quad (5.110)$$

which enter the shape equations for the two membrane segments $\gamma\alpha$ and $\beta\gamma$.

Shape functional for out-wetting

In close analogy to Eq. 5.312 for in-wetting, the shape functional for out-wetting has the form

$$\mathcal{F}_{2\text{Dr}}^{\text{out}}\{S\} = (P_\alpha - P_\gamma)\mathcal{V}\{S_\gamma\} + (P_\alpha - P_\beta)\mathcal{V}\{S_\beta\} + \Sigma\mathcal{A}\{S\} + \mathcal{E}_{2\text{Dr}}^{\text{out}}\{S\} \quad (5.111)$$

with the energy functional

$$\mathcal{E}_{2\text{Dr}}^{\text{out}}\{S\} \equiv \Sigma_{\alpha\beta}\mathcal{A}\{S_{\alpha\beta}\} + \mathcal{E}_{\text{bc}}^{\text{out}}\{S_{\gamma\alpha}, S_{\beta\gamma}\} + \mathcal{E}_{\text{ad}}\{S_{\gamma\alpha}, S_{\beta\gamma}\} + \mathcal{E}_{\alpha\beta\gamma}\{S_{\alpha\beta\gamma}\}. \quad (5.112)$$

Compared to the energy functional for in-wetting, the energy functional for out-wetting differs only in the bending energy functional which has the form

$$\mathcal{E}_{\text{bc}}^{\text{out}}\{S_{\gamma\alpha}, S_{\beta\gamma}\} = \sum_{j=\alpha,\beta} 2\kappa_{\gamma j} \int dA_{\gamma j} (M - m_{\gamma j})^2 \quad (5.113)$$

for out-wetting. As mentioned, the spontaneous curvatures $m_{\gamma j}$ for out-wetting and $m_{j\gamma}$ for in-wetting are different and related by

$$m_{\gamma j} = -m_{j\gamma}. \quad (5.114)$$

In contrast, the bending rigidities $\kappa_{\gamma j}$ for out-wetting are identical with the bending rigidities $\kappa_{j\gamma}$ for in-wetting.

5.1.3 THREE-SPHERICAL-CAP SHAPES

The out-wetting morphologies observed experimentally are well-described by three-spherical-cap shapes as depicted in Figure 5.49. The $\alpha\beta$ interface always forms a spherical cap with mean curvature $M_{\alpha\beta} = 1/R_{\alpha\beta} > 0$. Furthermore, when viewed on the micrometer scale as in Figure 5.49a, the two membrane segments $\gamma\alpha$ and $\beta\gamma$ also form two spherical caps with mean curvatures $M_{\gamma\alpha} = 1/R_{\gamma\alpha} > 0$ and $M_{\beta\gamma} = \pm 1/R_{\beta\gamma}$. These mean curvatures are governed by the shape equations

$$P_\gamma - P_j = 2\Sigma_{\gamma j}^{\text{eff}} M_{\gamma j} \quad \text{with } j = \alpha, \beta \quad (5.115)$$

with the effective, curvature-dependent tensions

$$\Sigma_{\gamma j}^{\text{eff}} \equiv \Sigma + W_{\gamma j} + \sigma_{\gamma j} - 2\kappa_{\gamma j} m_{\gamma j} M_{\gamma j} \quad (5.116)$$

of the two membrane segments $\gamma\alpha$ and $\gamma\beta$. Because the mean curvature $M_{\gamma\alpha}$ of the membrane segment $\gamma\alpha$ in contact with the bulk phase α is necessarily positive, the effective tension $\Sigma_{\gamma\alpha}^{\text{eff}}$ has the same sign as the pressure difference $P_\gamma - P_\alpha$. In contrast, the mean curvature $M_{\gamma\beta}$ of the membrane segment in contact with the β droplet may be positive or negative which implies that the effective tension $\Sigma_{\gamma\beta}^{\text{eff}}$ need not have the same sign as the pressure difference $P_\gamma - P_\beta$.

In addition, we introduce three apparent contact angles $\theta_\gamma^{\text{ap}}$, θ_β^{ap} , and $\theta_\alpha^{\text{ap}}$ that open up towards the three liquid phases γ , β , and α . The tension-angle-curvature relationship for partial out-wetting is then given by

$$M_{\gamma\alpha} \left(\frac{\Sigma_{\gamma\alpha}^{\text{eff}}}{\Sigma_{\alpha\beta}} - \frac{\sin \theta_\beta^{\text{ap}}}{\sin \theta_\gamma^{\text{ap}}} \right) = M_{\gamma\beta} \left(\frac{\Sigma_{\gamma\beta}^{\text{eff}}}{\Sigma_{\alpha\beta}} - \frac{\sin \theta_\alpha^{\text{ap}}}{\sin \theta_\gamma^{\text{ap}}} \right). \quad (5.117)$$

In contrast to in-wetting, the mean curvature $M_{\gamma\beta}$ of the $\gamma\beta$ membrane segment can now be negative corresponding to a $\gamma\beta$ segment that bulges towards the γ phase within the vesicle.

If several β droplets adhere to the exterior leaflet of a single GUV, we obtain several $\gamma\beta$ segments which we can distinguish by the label $n = 1, 2, \dots, N$. These $\gamma\beta$ segments have the mean curvatures $M_{\gamma\beta}^{(n)}$ and experience the effective tensions $\Sigma_{\gamma\beta}^{(n)}$. We then obtain the relations $\Upsilon_{\gamma\beta}^{(1)} = \Upsilon_{\gamma\beta}^{(2)} = \dots = \Upsilon_{\gamma\beta}^{(N)}$ with

$$\Upsilon_{\gamma\beta}^{(n)} \equiv M_{\gamma\alpha} \frac{\sin \theta_\beta^{(n)}}{\sin \theta_\gamma^{(n)}} + M_{\gamma\beta}^{(n)} \left(\frac{\Sigma_{\gamma\beta}^{(n)}}{\Sigma_{\alpha\beta}} - \frac{\sin \theta_\alpha^{(n)}}{\sin \theta_\gamma^{(n)}} \right), \quad (5.118)$$

in close analogy to the relations as given by Eqs 5.347 and 5.348 for in-wetting. Thus, from three different $\gamma\beta$ segments with three distinct mean curvatures $M_{\gamma\beta}^{(n)}$, we can obtain the two parameter combinations $(\Sigma + W_{\gamma\beta} + \sigma_{\gamma\beta})/\Sigma_{\alpha\beta}$ and $\kappa_{\gamma\beta} m_{\gamma\beta}/\Sigma_{\alpha\beta}$ that determine the tension ratios $\Sigma_{\gamma\beta}^{(n)}/\Sigma_{\alpha\beta}$.

5.1.4 FORCE BALANCE ALONG APPARENT CONTACT LINE

In order to describe the force balance between the two membrane segments and the $\alpha\beta$ interface in a self-consistent manner, we consider again special parameter regimes in close analogy to the force balance for in-wetting morphologies. Thus, we can distinguish small-small, large-large, and large-small regimes for out-wetting as well.

Special parameter regimes

The relationships between the effective tensions and apparent contact angles as given by Eqs. 5.17 and 5.18 depend on the mean curvatures of the different membrane segments. We can again

derive curvature-independent relationships if we consider membrane segments characterized by small spontaneous curvatures and small bending energies or large spontaneous curvatures and large spontaneous tensions. The corresponding shape function has the form

$$F^{\text{out}} = (P_\alpha - P_\gamma)V_\gamma + (P_\alpha - P_\beta)V_\beta + \Delta F^{\text{out}} \quad (5.119)$$

where the area-dependent shape function ΔF^{out} is somewhat different for the different regimes. If both membrane segments have large spontaneous curvatures, the area-dependent shape function ΔF^{out} has the form

$$\Delta F_{l+s}^{\text{out}} = \Sigma_{\alpha\beta} A_{\alpha\beta} + \hat{\Sigma}_{\gamma\alpha} A_{\gamma\alpha} + \hat{\Sigma}_{\gamma\beta} A_{\gamma\beta} \quad (5.120)$$

for large-large regime.

Likewise, we obtain $\Delta F^{\text{out}} = \Delta F_{l+s}^{\text{out}}$ with

$$\Delta F_{l+s}^{\text{out}} = \Sigma_{\alpha\beta} A_{\alpha\beta} + \Sigma_{\gamma\alpha} A_{\gamma\alpha} + \Sigma_{\gamma\beta} A_{\gamma\beta} \quad (5.121)$$

for small-small regime.

and $\Delta F^{\text{out}} = \Delta F_{s+s}^{\text{out}}$ with

$$\Delta F_{s+s}^{\text{out}} = \Sigma_{\alpha\beta} A_{\alpha\beta} + \Sigma_{\gamma\alpha} A_{\gamma\alpha} + \Sigma_{\gamma\beta} A_{\gamma\beta} \quad (5.122)$$

for small-small regime.

Comparison with the area-dependent shape functions for in-wetting as given by Eqs 5.367–5.369 shows that, in all three regimes, the area-dependent shape function ΔF^{out} for out-wetting is identical with the shape function ΔF^{in} for in-wetting when we replace the segment labels $\gamma\alpha$ and $\gamma\beta$ by the segment labels $\alpha\gamma$ and $\beta\gamma$.

Force balance relations

Minimization of the shape function ΔF^{out} with respect to the four curvature radii $R_{\gamma\alpha}$, $R_{\gamma\beta}$, and $R_{\alpha\beta}$ as well as with respect to the contact line radius R_{co} leads to the shape equations for the three spherical caps as well as to the force balance relations

$$\frac{\hat{\Sigma}_{\gamma\alpha}}{\Sigma_{\alpha\beta}} = \frac{\sin \theta_\beta^{\text{ap}}}{\sin \theta_\gamma^{\text{ap}}} \quad \text{and} \quad \frac{\hat{\Sigma}_{\gamma\beta}}{\Sigma_{\alpha\beta}} = \frac{\sin \theta_\alpha^{\text{ap}}}{\sin \theta_\gamma^{\text{ap}}}. \quad (5.123)$$

More precisely, the latter relations describe the force balance along the apparent contact line if both membrane segments $\gamma\alpha$ and $\gamma\beta$ belong to the large spontaneous curvature regime. If the $\gamma\alpha$ segment belongs to the small spontaneous curvature and small bending energy regime, the total segment tension $\hat{\Sigma}_{\gamma\alpha}$ in Eq. 5.123 is replaced by the mechanical segment tension $\Sigma_{\gamma\alpha}$. Likewise, if the $\gamma\beta$ segment belongs to the latter regime, the total segment tension $\hat{\Sigma}_{\gamma\beta}$ is replaced by the mechanical segment $\Sigma_{\gamma\beta}$.

5.2 SYMMETRIC TWO-DROPLET VESICLES

In this appendix, we address the deflation of two-droplet vesicles that belong to the partial in-wetting regime as illustrated in Figure 5.40a. When such a vesicle is osmotically deflated, it may

follow two distinct morphological pathways. The first pathway leads to the engulfment of both droplets by the membrane as in [Figure 5.40d](#). The second pathway leads to the formation of many nanobuds and nanotubes as in [Figure 5.21](#). In order to discuss the competition between these two morphological pathways, it is instructive to consider a simplified case corresponding to two-droplet vesicles with an up-down symmetry.

Up-down symmetric geometry and fluid-elastic parameters

Such a two-droplet vesicle contains one α and one β droplet, both of which have the same volume $V_\alpha = V_\beta \equiv V_1$. The two droplets are separated by a planar $\alpha\beta$ interface, corresponding to apparent contact angles $\theta_\alpha^{\text{ap}} = \theta_\beta^{\text{ap}}$. Likewise, the two membrane segments $\alpha\gamma$ and $\beta\gamma$ in contact with the α and β phase have the same areas $A_{\alpha\gamma} = A_{\beta\gamma} \equiv A_1$. Therefore, the vesicle volume V and the membrane area A are given by

$$V = V_\alpha + V_\beta = 2V_1 \text{ and } A = A_{\alpha\gamma} + A_{\beta\gamma} = 2A_1. \quad (5.J1)$$

Before deflation, the initial shape of the vesicle is taken to be a sphere with volume

$$V_{\text{ini}} = \frac{4\pi}{3} R_{\text{vc}}^3 \text{ with } R_{\text{vc}} = \sqrt{A / (4\pi)} \quad (5.J2)$$

which implies the reduced volume $v = v_{\text{ini}} = 1$.

In order to preserve the up-down symmetry during deflation, the two phases α and β and the two membrane segments $\alpha\gamma$ and $\beta\gamma$ are taken to have the same fluid-elastic parameters. Thus, both phases adhere to the membrane with the same adhesive strength $W_{\alpha\gamma} = W_{\beta\gamma} \equiv W$, and both membrane segments are characterized by the same bending rigidity $\kappa_{\alpha\gamma} = \kappa_{\beta\gamma} \equiv \kappa$ and the same spontaneous curvature $m_{\alpha\gamma} = m_{\beta\gamma} \equiv m$.

Regime of small spontaneous curvatures

First, consider the case of a small spontaneous curvature with $|m| \ll 1/R_{\text{vc}}$. The free energy E_{ini} of the initial spherical shape is then given by

$$E_{\text{ini}} \approx \Sigma_{\alpha\beta} A_{\alpha\beta} + 8\pi\kappa \text{ with } A_{\alpha\beta} = A / 4 \text{ (small } |m| \text{)}. \quad (5.J3)$$

Because both droplets have the same adhesive strength, the adhesion free energy WA does not depend on the shape of the vesicle and thus plays no role when we compare different vesicle morphologies.

For small $|m|$, the vesicle membrane cannot form any stable nanobuds or nanotubes and osmotic deflation from the initial volume V_{ini} to the volume

$$V_{\text{eng}} \equiv V_{\text{ini}} / \sqrt{2} \quad (5.J4)$$

leads to the engulfment of both droplets as in [Figure 5.40d](#). Each droplet forms a sphere which is enclosed by the corresponding membrane segment. The two spherical segments are connected by a closed membrane neck which replaces the $\alpha\beta$ interface. Therefore,

the free energy E_{eng} of this two-sphere shape does not involve any contribution from the interfacial tension $\Sigma_{\alpha\beta}$ and has the form

$$E_{\text{eng}} \approx 16\pi\kappa \text{ (small } |m| \text{)}. \quad (5.J5)$$

arising from the bending energy of two spherical membrane segments.

The two-sphere shape without an $\alpha\beta$ interface has a lower free energy than the initial one-sphere shape if $E_{\text{eng}} - E_{\text{ini}} < 0$ which implies the inequalities

$$\Sigma_{\alpha\beta} > \frac{8\pi\kappa}{A} \text{ or } A > \frac{8\pi\kappa}{\Sigma_{\alpha\beta}} \quad (5.J6)$$

for the interfacial tension and the membrane area. Therefore, for small $|m|$, deflation of the initial spherical vesicle leads to the two-sphere morphology without an $\alpha\beta$ interface for sufficiently large interfacial tension $\Sigma_{\alpha\beta}$ or sufficiently large membrane area A .

Regime of large spontaneous curvatures

For large spontaneous curvatures with $|m| \gg 1/R_{\text{vc}}$, the initial spherical vesicle with volume $V = V_{\text{ini}}$ has the free energy

$$E_{\text{ini}} \approx \left(\frac{1}{4}\Sigma_{\alpha\beta} + \sigma\right)A \text{ (large } |m| \text{)} \quad (5.J7)$$

which depends on the spontaneous tension $\sigma = 2\kappa m^2$.

When we deflate this vesicle to obtain the smaller volume $V_{\text{eng}} = V_{\text{ini}} / \sqrt{2}$, the vesicle membrane may again engulf the two droplets completely, thereby replacing the $\alpha\beta$ interface by a closed membrane neck. The free energy E_{eng} of the latter shape is now given by

$$E_{\text{eng}} \approx \sigma A \text{ (large } |m| \text{)} \quad (5.J8)$$

which is smaller than E_{ini} . Therefore, the first morphological pathway which eliminates the $\alpha\beta$ interface always reduces the free energy of the vesicle-droplet system.

However, for large $|m|$, the deflated vesicle can also form nanobuds and nanotubes. To simplify the following discussion, the buds and tubes are built up from zero-energy spherules with radius $R_2 = 1/|m|$ as described in [Sections 5.5](#) and [5.6](#). As a result of this second morphological pathway, the membrane forms a spherical mother vesicle with radius R_{mv} and N spherules of radius $1/|m|$ which are connected by closed membrane necks. The volume V_{tub} of this shape is given by

$$V_{\text{tub}} = \frac{4\pi}{3} R_{\text{mv}}^3 \pm \frac{4\pi}{3} \frac{N}{|m|^3} \quad (5.J9)$$

where the plus and minus sign corresponds to out- and in-spherules, respectively, and the conserved membrane area A can be decomposed according to

$$A = 4\pi R_{\text{mv}}^2 + 4\pi \frac{N}{m^2}. \quad (5.J10)$$

In order to compare the two morphological pathways of engulfment and tubulation, we now consider the same deflation depth in both cases corresponding to $V_{\text{tub}} = V_{\text{eng}} = V_{\text{ini}} / \sqrt{2}$ as in Eq 5.J4. The latter equality implies

$$\frac{4\pi}{3} R_{\text{mv}}^3 \pm \frac{4\pi}{3} \frac{N}{|m|^3} = \frac{4\pi}{3} \frac{R_{\text{vc}}^3}{\sqrt{2}}. \quad (5.J11)$$

In addition, the conservation of the membrane area leads to

$$A = 4\pi R_{\text{vc}}^2 = 4\pi R_{\text{mv}}^2 + \Delta A \quad (5.J12)$$

with the excess area

$$\Delta A = 4\pi \frac{N}{\bar{m}^2} \quad (5.J13)$$

stored in the nanobuds and nanotubes. Thus, the area fraction φ stored in the N spherules is given by

$$\varphi \equiv \frac{\Delta A}{A} = \frac{N}{\bar{m}^2}. \quad (5.J14)$$

When expressed in terms of the dimensionless radius

$$r_{\text{mv}} \equiv R_{\text{mv}}/R_{\text{vc}} \quad (5.J15)$$

and the dimensionless spontaneous curvature $\bar{m} = mR_{\text{vc}}$, the two relationships in Eqs 5.11 and 5.12 attain the form

$$r_{\text{mv}}^3 \pm \frac{\varphi}{|\bar{m}|} = \frac{1}{\sqrt{2}} \quad \text{and} \quad r_{\text{mv}}^2 + \varphi = 1. \quad (5.J16)$$

These two equations determine the two unknown variables r_{mv} and φ in terms of \bar{m} . The solutions of these two equations have the asymptotic behavior

$$\varphi = \frac{N}{\bar{m}^2} \approx \frac{2}{3} \frac{\sqrt{2}-1}{\sqrt{2}} = 0.195 \quad (5.J17)$$

and

$$r_{\text{mv}} = \sqrt{1-\varphi} \approx 0.897 \quad \text{for large } |\bar{m}|. \quad (5.J18)$$

The asymptotic behavior for the area fraction $\varphi = N / \bar{m}^2$ also follows from Eq. 5.171 with $\nu = 1/\sqrt{2}$.

Because the spherules with radius $R_2 = 1/|m|$ do not contribute to the bending energy of the vesicle membrane, the tubulated vesicle has the free energy

$$E_{\text{tub}} \approx \Sigma_{\alpha\beta} \pi R_{\text{mv}}^2 + \sigma 4\pi R_{\text{mv}}^2 = \left(\frac{1}{4}\Sigma_{\alpha\beta} + \sigma\right)(A - \Delta A) \quad (5.J19)$$

which implies

$$E_{\text{tub}} - E_{\text{ini}} = -\left(\frac{1}{4}\Sigma_{\alpha\beta} + \sigma\right)\Delta A < 0 \quad (\text{large } |m|) \quad (5.J20)$$

as follows from the expression for E_{ini} in Eq. 5.J7. Therefore, the second morphological pathway induced by deflation also reduces the free energy of the vesicle-droplet system.

What remains to be done is to compare the free energies E_{tub} and E_{eng} , both of which are smaller than E_{ini} . Using Eqs 5.8 and 5.19, we obtain the free energy difference

$$E_{\text{tub}} - E_{\text{eng}} = \frac{1}{4}\Sigma_{\alpha\beta} A - \left(\frac{1}{4}\Sigma_{\alpha\beta} + \sigma\right)\Delta A. \quad (5.J21)$$

which is negative if

$$\varphi = \frac{\Delta A}{A} > \frac{\Sigma_{\alpha\beta}}{4\sigma + \Sigma_{\alpha\beta}} \quad (5.J22)$$

or

$$\sigma > \frac{1-\varphi}{4\varphi} \Sigma_{\alpha\beta}. \quad (5.J23)$$

Furthermore, the area fraction φ (as in Eq. 5.J23) attains the constant value $\frac{2}{3} \frac{\sqrt{2}-1}{\sqrt{2}} = 0.195$ for large $|m|$ as in Eq. 5.J17. Using this asymptotic behavior, we find that

$$E_{\text{tub}} < E_{\text{eng}} \quad \text{for} \quad \frac{\sigma}{\Sigma_{\alpha\beta}} > \frac{1+\sqrt{2}}{4(2-\sqrt{2})} = 1.030 \quad (\text{large } |m|). \quad (5.J24)$$

Therefore, the free energy E_{tub} of the tubulated vesicle is lower than the free energy E_{eng} of the vesicle with two completely engulfed droplets if the spontaneous tension σ is large compared to the interfacial tension $\Sigma_{\alpha\beta}$.

Spatial location of zero-energy spherules

In the previous discussion, we did not have to specify the spatial location of the spherules which may be attached to the two membrane segments or to other spherules within necklace-like tubes. Indeed, because the spherules have zero bending energy, the free energy E_{tub} depends only on the number N of the spherules but not on their spatial locations. In particular, for equal adhesive strengths $W_{\alpha\gamma} = W_{\beta\gamma}$ as considered above, an arbitrary number of N_{α} spherules can be in contact with the α phase which implies that $N_{\beta} = N - N_{\alpha}$ spherules are in contact with the β phase, extending the morphological complexity discussed in Section 5.6.4.

This degeneracy is, however, lifted if the adhesive strength $W_{\alpha\gamma}$ of the α droplet differs from the adhesive strength $W_{\beta\gamma}$ of the β droplet. If the α droplet is more adhesive than the β droplet, corresponding to $W_{\alpha\gamma} < W_{\beta\gamma}$, a spherule in contact with the α phase gains the adhesion free energy $(W_{\alpha\gamma} - W_{\beta\gamma})4\pi|m|^2$ compared to a spherule in contact with the β phase. Therefore, if both membrane segments are still characterized by the same fluid-elastic parameters, the morphology with the lowest free energy is provided by N spherules that are all in contact with the α phase for $W_{\alpha\gamma} < W_{\beta\gamma}$.

GLOSSARY OF SYMBOLS

Symbols for membrane geometry and topology

A	membrane area
$\mathcal{A}\{S\}$	area functional of vesicle shape S
A_{bo}	membrane area bound to rigid substrate surface
ΔA	area difference between two leaflets of bilayer membrane
C_1, C_2	two principal curvatures of membrane surface
c	Euler characteristic, $\chi = 2 - 2g$
g	topological genus of vesicle, i.e., number of handles
G	determinant of metric tensor g_{ij}
g_{ij}	metric tensor, $g_{ij} = \vec{X}_i \cdot \vec{X}_j$
h_i^j	curvature tensor
G	Gaussian curvature of membrane surface, $G = C_1 C_2$
l_M	integrated mean curvature, $l_M = \int dA M$
$\mathcal{I}_M\{S\}$	integrated mean curvature functional of membrane shape S
l_{me}	membrane thickness
M	mean curvature of membrane surface, $M = \frac{1}{2}(C_1 + C_2)$
M_1, M_2	mean curvature of two segments adjacent to a closed neck
M_{ne}	(effective) neck curvature, $M_{ne} = \frac{1}{2}(M_1 + M_2)$
\bar{M}_{ne}	dimensionless neck curvature, $\bar{M}_{ne} = M_{ne} R_{ve}$
\hat{n}	unit vector normal to membrane surface
ψ	tilt angle along the contour of an axisymmetric vesicle shape
r	radial coordinate for the contour of an axisymmetric vesicle shape
R_{cy}	radius of cylindrical membrane segment
R_{ne}	radius of membrane neck
R_{sp}	radius of spherical membrane segment
R_{ve}	vesicle size, $R_{ve} = \sqrt{A/(4\pi)}$, used as basic length scale
S	shape of vesicle
\underline{s}	two-dimensional surface coordinates, $\underline{s} \equiv (s^1, s^2)$, of membrane shape
\vec{X}	vector-valued function $\vec{X} = \vec{X}(\underline{s})$ in three dimensions
\vec{X}_i	two tangent vectors to membrane surface, $\vec{X}_i = \partial \vec{X} / \partial s^i$
V	volume of vesicle
$\mathcal{V}\{S\}$	volume functional of vesicle shape S
v	volume-to-area ratio or reduced volume, $v = 6\sqrt{\pi} V / A^{3/2}$

Symbols for curvature models of uniform membranes

A_{opt}	optimal membrane area corresponding to optimal molecular packing
E_{be}	bending energy
\bar{E}_{be}	dimensionless bending energy, $\bar{E}_{be} = E_{be} / (8\pi\kappa)$
$\mathcal{E}_{be}\{S\}$	bending energy functional of vesicle shape S
$\bar{\mathcal{E}}_{be}\{S\}$	dimensionless bending energy functional, $\bar{\mathcal{E}}_{be} = \mathcal{E}_{be} / (8\pi\kappa)$
$\mathcal{E}_{cu}\{S\}$	curvature energy functional of vesicle shape S

f	locally applied pulling force acting on a small membrane segment
f_{eff}^{in}	effective constriction force acting on the neck of an in-bud
f_{eff}^{out}	effective constriction force acting on the neck of an out-bud
$f_{ex} > 0$	pulling force pointing towards the exterior vesicle compartment
$f_{in} < 0$	pulling force pointing towards the interior vesicle compartment
f_m^{in}, f_m^{out}	constriction forces generated by spontaneous curvature
F	shape energy, $F = -\Delta PV + \Sigma A + E_{be}$
$\mathcal{F}\{S\}$	shape functional of vesicle shape S
$l_{M,0}$	integrated mean curvature of vesicle shape with an optimal area difference
κ	bending rigidity of membrane, used as basic energy scale
κ_Δ	second bending rigidity for area difference elasticity
κ_G	Gaussian curvature modulus
K_A	area compressibility modulus
λ_{ed}	line tension of bilayer edge
m	spontaneous curvature of bilayer membrane
\bar{m}	dimensionless spontaneous curvature, $\bar{m} = m R_{ve}$
m_{com}	composite curvature, $m_{com} = m + f / (4\pi\kappa)$
m_{eff}	effective spontaneous curvature, $m_{eff} = m + m_{nlo}$
m_{nlo}	nonlocal spontaneous curvature
P_{in}	osmotic pressure within interior compartment
P_{ex}	osmotic pressure within exterior compartment
ΔP	osmotic pressure difference across the membrane, $\Delta P = P_{in} - P_{ex}$
S^{st}	stationary shape, i.e., stationary solution of the Euler-Lagrange equation
σ	spontaneous tension, $\sigma = 2\kappa m^2$
Σ	mechanical membrane tension
$\hat{\Sigma}$	total membrane tension, $\hat{\Sigma} = \Sigma + \sigma$

Symbols for spheres and tubules (Sections 5.5 and 5.6)

B_\star^+	bifurcation point for $(1+N)$ -sphere vesicle at $(\bar{m}, v) = (\bar{m}_\star^+, v_\star^+)$
B_\diamond^+	bifurcation point for $(1+N)$ -sphere vesicle at $(\bar{m}, v) = (\bar{m}_\diamond^+, v_\diamond^+)$
L^{pea}	limit shape of two-sphere vesicle with $m > 0$
L^{sto}	limit shape of two-sphere vesicle with $m < 0$
L^{out}	limit shape of two-sphere vesicle consisting of two equal spheres
L^{in}	limit shape of two-sphere vesicle consisting of two nested spheres with equal radius
L_\star^+	limit shape of $(1+N)$ -sphere vesicle at B_\star^+ with balanced volume, $v_1 = Nv_2$
L_1^+	limit shape of $(1+N)$ -sphere vesicle dominated by r_1 -sphere, $v_1 > Nv_2$
L_2^+	limit shape of $(1+N)$ -sphere vesicle dominated by r_2 -spheres, $v_1 < Nv_2$

L_{\diamond}^+	limit shape of $(1+N)$ -sphere vesicle at B_{\diamond}^+ with $v_1 = v_2$
$L_{=}^+$	limit shape of $(1+N)$ -sphere vesicle consisting of $(1+N)$ equal spheres
$L_{[N]}^{\text{in}}$	limit shape with in-necklaces containing N small spheres
$L_{[N]}^{\text{out}}$	limit shape with out-necklaces containing N small spheres
\bar{m}_*^+	\bar{m} -value of bifurcation point B_*^+ , $\bar{m}_*^+ = \frac{1}{2}(1+N)^{1/3}3^{3/2}$
\bar{m}_{12}^+	\bar{m} -value of bifurcation point B_{\diamond}^+ , $\bar{m}_{\diamond}^+ = \sqrt{1+N}$
\bar{M}_{12}	(effective) neck curvature of 12-neck of necklace-like tube
\bar{M}_{22}	(effective) neck curvature of 22-neck of necklace-like tube
N	number of r_2 -spheres for $(1+N)$ -sphere vesicles and necklace-like tubes
Φ^{pea}	persistent two-sphere vesicle with $m > 0$
Φ_*^+	persistent $(1+N)$ -spheres, same geometry as L_*^+ shape but with $\bar{m} > \bar{m}_*^+$
Φ_1^+	persistent $(1+N)$ -spheres, same geometries as L_1^+ shapes but with larger \bar{m} -values
Φ_2^+	persistent $(1+N)$ -spheres, same geometries as L_2^+ shapes but with larger \bar{m} -values
r_1, r_2	dimensionless radii of two-sphere vesicle, $r_i = R_i/R_{\text{ve}}$
R_{cy}	radius of cylindrical membrane segment
R_{pip}	radius of cylindrical pipette
R_{sp}	radius of spherical membrane segment
R_1, R_2	two radii of two-sphere shape
ρ_1	volume fraction of large r_1 -sphere, $\rho_1 = v_1 / (Nv_2)$
ρ_2	volume fraction of N small r_2 -spheres, $\rho_2 = Nv_2 / v_1 = 1 / \rho_1$
σ	spontaneous tension, $\sigma = 2\kappa m^2$
Σ	mechanical membrane tension
Σ_{asp}	aspiration tension as given by Eq. 5.210
$\hat{\Sigma}$	total membrane tension, $\hat{\Sigma} = \Sigma + \sigma$
Θ^{in}	two-sphere vesicle with an in-bud, unspecified neck condition
Θ^{out}	two-sphere vesicle with an out-bud, unspecified neck condition
v_1	dimensionless volume of single r_1 -sphere, $v_1 = r_1^3$
v_2	dimensionless volume of single r_2 -sphere, $v_2 = r_2^3$
v_*^+	v -value of bifurcation point B_*^+ , $v_*^+ = 2 / (1+N)^{1/3}3^{3/2}$
v_{\diamond}^+	v -value of bifurcation point B_{\diamond}^+ , $v_{\diamond}^+ = 1 / \sqrt{1+N}$
v_{co}^+	smallest possible volume of $(1+N)$ -sphere vesicle with mutual contacts of out-buds
v^{pea}	volume of limit shape L^{pea}
v^{sto}	volume of limit shape L^{sto}
$v_{=}^{\text{out}}$	volume of limit shape $L_{=}^{\text{out}}$ consisting of two equal spheres
$v_{[N]}^{\text{in}}$	volume of limit shape $L_{[N]}^{\text{in}}$ with in-necklaces of total length N
$v_{[N]}^{\text{out}}$	volume of limit shape $L_{[N]}^{\text{out}}$ with out-necklaces of total length N
Z^{in}	vesicle shape with one in-bud that has radius $r_2 = 1/ \bar{m} $ and zero bending energy

Z_N^{in}	vesicle shape with N in-buds that have radius $r_2 = 1/ \bar{m} $ and zero bending energy
Z^{out}	vesicle shape with one out-bud that has radius $r_2 = 1/\bar{m}$ and zero bending energy
Z_N^{out}	vesicle shape with N out-buds that have radius $r_2 = 1/\bar{m}$ and zero bending energy

Symbols for adhesion of vesicles (Section 5.7)

A_{bo}	area of bound membrane segment adhering to the substrate surface
A_{un}	area of unbound membrane segment not in contact with the surface
$C_{\parallel\text{co}}$	membrane curvature parallel to the contact line
$C_{\perp\text{co}}$	membrane curvature perpendicular to the contact line
E_{ad}	adhesion (free) energy
\mathcal{E}_{ad}	adhesion (free) energy functional
\mathcal{E}_{AV}	energy functional of adhering vesicle
$f_{\text{W}}^{\text{in}}, f_{\text{W}}^{\text{out}}$	effective constriction forces generated by adhesion
\mathcal{F}_{AV}	shape functional of adhering vesicle
l_1, l_2	two lipid species
M_{bo}	mean curvature of membrane segment bound to adhesive surface
M_{co}	contact mean curvature of unbound membrane segment
R_{be}	radius of spherical bead
$R_{\parallel\text{co}}$	membrane's curvature radius parallel to the contact line
$R_{\perp\text{co}}$	membrane's curvature radius perpendicular to the contact line
R_{W}	adhesion length, $R_{\text{W}} = \sqrt{2\kappa/ W }$
S_{bo}	shape of bound membrane segment in contact with the adhesive surface
S_{un}	shape of unbound membrane segment not in contact with the adhesive surface
θ_{eff}	effective contact angle of adhering vesicle for strong adhesion
$ W $	adhesion free energy density or adhesive strength
$ w $	dimensionless adhesive strength, $ w = W R_{\text{ve}}^2 / \kappa$

Symbols for multi-domain vesicles (Section 5.8)

a, b	indices for different membrane phases
A_a, A_b	area of intramembrane domain formed by membrane phases a and b
$\Delta\kappa_{\text{G}}$	difference in Gaussian curvature moduli, $\Delta\kappa_{\text{G}} = \kappa_{\text{Ga}} - \kappa_{\text{Gb}}$
κ_a, κ_b	bending rigidities of a - and b -domains
$\kappa_{\text{Ga}}, \kappa_{\text{Gb}}$	Gaussian curvature moduli of a - and b -domains
$\mathcal{L}\{\cdot\}$	length functional
L_{ab}	length of ab domain boundary, $L_{ab} = \mathcal{L}\{S_{ab}\}$
Ld, Lo	liquid-disordered and liquid-ordered phase of lipid mixtures
λ	line tension of domain boundary between intramembrane domains

$\bar{\lambda}$	dimensionless line tension, $\bar{\lambda} = \lambda R_{ve}/\kappa_b$
m_a, m_b	spontaneous curvatures of a and b domain
\bar{m}_a, \bar{m}_b	dimensionless spontaneous curvatures, $\bar{m}_a = m_a R_{ve}$
M_a	mean curvature of a -domain adjacent to closed neck
M_b	mean curvature of b -domain adjacent to closed neck
$M_a(s_1)$	mean curvature of a -domain along domain boundary of axisymmetric shape
$M_b(s_1)$	mean curvature of b -domain along domain boundary of axisymmetric shape
S_a, S_b	shapes of intramembrane domains consisting of membrane phases a and b
S_{ab}	shape of domain boundary between a and b domain
s_1	value of arc length s at the domain boundary of axisymmetric shape
Σ_a, Σ_b	mechanical membrane tensions in the a and b domains
x_a, x_b	area fractions of two-domain vesicles, $x_a = A_a/A$ and $x_b = A_b/A$

Symbols for wetting of membranes (Section 5.9)

α, β, γ	indices for different aqueous phases
$\alpha\beta$	index for interface between α and β phase
$\alpha\gamma$	index for membrane segment between α droplet and external phase γ
$\beta\gamma$	index for membrane segment between β droplet and external phase γ
\mathcal{E}_{ad}	adhesion free energy arising from the membrane-droplet interactions
$j\gamma$	index for $j\gamma$ membrane segment with $j = \alpha$ or β
$\kappa_{j\gamma}$	bending rigidity of $j\gamma$ membrane segment
λ_{co}	line tension of contact line
$m_{j\gamma}$	spontaneous curvature of $j\gamma$ membrane segment
$M_{j\gamma}$	mean curvature of $j\gamma$ membrane segment, three-spherical cap shape
r_1	radius of true contact line
$R_{\alpha\beta}$	curvature radius of the ab interface, three-spherical-cap shape
$R_{j\gamma}$	curvature radius of $j\gamma$ membrane segment, three-spherical-cap shape
R_{co}	radius of apparent contact line
$\sigma_{j\gamma}$	spontaneous tension of $j\gamma$ segment, $\sigma_{\alpha\gamma} = 2\kappa_{\alpha\gamma}m_{\alpha\gamma}^2$
Σ	overall lateral stress, Lagrange multiplier for the total membrane area
$\Sigma_{\alpha\beta}$	interfacial tension of $\alpha\beta$ interface
$\Sigma_{j\gamma}$	mechanical tension of $j\gamma$ segment, $\Sigma_{j\gamma} = \Sigma + W_{j\gamma}$
$\Sigma_{j\gamma}^{eff}$	effective membrane tension of $j\gamma$ segment, $\Sigma_{j\gamma}^{eff} = \hat{\Sigma}_{j\gamma} - 2\kappa_{j\gamma}m_{j\gamma}M_{j\gamma}$
$\hat{\Sigma}_{j\gamma}$	total membrane tension of $j\gamma$ segment, $\hat{\Sigma}_{j\gamma} = \Sigma_{j\gamma} + \sigma_{j\gamma}$

$\theta_{\alpha}^{ap}, \theta_{\beta}^{ap}, \theta_{\gamma}^{ap}$	apparent contact angles which depend on the vesicle geometry
θ_{α}^*	intrinsic contact angle between $\alpha\gamma$ membrane segment and $\alpha\beta$ interface
θ_{β}^*	intrinsic contact angle between $\beta\gamma$ membrane segment and $\alpha\beta$ interface
$\mathcal{T}_{\alpha\gamma}$	free energy of leaflet-water interfaces for partial in-wetting morphology
$\mathcal{T}_{\gamma\gamma}$	free energy of leaflet-water interfaces in contact with γ phase only
V_{α}, V_{β}	volumes of droplets formed by aqueous α and β phase
$W_{\alpha\gamma}$	adhesion (free) energy density of α phase replacing γ phase
$W_{\beta\gamma}$	adhesion (free) energy density of β phase replacing γ phase

REFERENCES

Agudo-Canalejo J, Lipowsky R (2015a) Critical particle sizes for the engulfment of nanoparticles by membranes and vesicles with bilayer asymmetry. *ACS Nano*, 9:3704–3720.

Agudo-Canalejo J, Lipowsky R (2015b) Adhesive nanoparticles as local probes of membrane curvature. *Nano Lett.*, 15:7168–7173.

Agudo-Canalejo J, Lipowsky R (2016) Stabilization of membrane necks by adhesive particles, substrate surfaces, and constriction forces. *Soft Matter*, 12:8155–8166.

Agudo-Canalejo J, Lipowsky R (2017) Uniform and janus-like nanoparticles in contact with vesicles: Energy landscapes and curvature-induced forces. *Soft Matter*, 13:2155–2173.

Agudo-Canalejo J, Lipowsky R (in preparation) Strong influence of spontaneous curvature on vesicle adhesion.

Aizenman M, Wehr J (1989) Rounding of first-order phase transitions in systems with quenched disorder. *Phys. Rev. Lett.*, 62:2503–2506.

Albertsson PA (1986) *Partition of Cell Particles and Macromolecules: Separation and Purification of Biomolecules, Cell Organelles Membranes, and Cells in Aqueous Polymer Two-Phase Systems and Their Use in Biochemical Analysis and Biotechnology*. 3 edition, New York: John Wiley & sons.

Almeida PFF, Vaz WLC (1995) Lateral diffusion in membranes. In Lipowsky R, Sackmann E (Eds.), *Structure and Dynamics of Membranes, Vol. 1A of Handbook of Biological Physics*. Amsterdam, the Netherlands: Elsevier.

Anderson TH, Min Y, Weirich KL, Zeng H, Fygenson D, Israelachvili JN (2009) Formation of supported bilayers on silica substrates. *Langmuir*, 25:6997–7005.

Atefi E, J. Adinin Mann J, Tavara H (2014) Ultralow interfacial tensions of aqueous two-phase systems measured using drop shape. *Langmuir*, 30:9691–9699.

Aureli M, Mauri L, Ciampa MG, Prinetti A, Toffano G, Secchieri C, Sonnino S (2016) GM1 Ganglioside: Past studies and future potential. *Mol. Neurobiol.*, 53:1824–1842.

Avalos-Padilla Y, Knorr RL, Javier-Reyna R, Garca-Rivera G, Lipowsky R, Dimova R, Orozco E (2018) The conserved ESCRT-III machinery participates in the phagocytosis of *Entamoeba histolytica*. *Front. Cell. Infect. Microbiol.*, 8:53. doi:10.3389/fcimb.2018.00053.

Bacia K, Schwille P, Kurzchalia T (2005) Sterol structure determines the separation of phases and the curvature of the liquid-ordered phase in model membranes. *PNAS*, 102:3272–3277.

- Bancroft WD (1913) The theory of emulsification. *V. J. Phys. Chem.*, 17:501–519.
- Bancroft W, Tucker C (1927) Gibbs on emulsification. *J. Phys. Chem.*, 31:1681–1692.
- Bangham A, Horne R (1964) Negative staining of phospholipids and their structural modification by surface-active agents as observed in the electron microscope. *J. Mol. Biol.*, 8:660–668.
- Baumgart T, Das S, Webb WW, Jenkins JT (2005) Membrane elasticity in giant vesicles with fluid phase coexistence. *Biophys. J.*, 89:1067–1080.
- Baumgart T, Graber ZT, Shi Z (2017) Cations induce shape remodeling of negatively charged phospholipid membranes. *PCCP*, 19:15285–15295.
- Baumgart T, Hammond AT, Sengupta P, Hess ST, Holowka DA, Baird BA, Webb WW (2007) Large-scale fluid/fluid phase separation of proteins and lipids in giant plasma membrane vesicles. *PNAS*, 104:3165–3170.
- Baumgart T, Hess S, Webb W (2003) Imaging coexisting fluid domains in biomembrane models coupling curvature and line tension. *Nature*, 425:821–824.
- Berndl K (1990) *Formen Von Vesikeln Diplomarbeit*, Ludwig-Maximilians-Universität München.
- Berndl K, Käs J, Lipowsky R, Sackmann E, Seifert U (1990) Shape transformations of giant vesicles: Extreme sensitivity to bilayer asymmetry. *Europhys. Lett.*, 13:659–664.
- Bhatia T, Agudo-Canalejo J, Dimova R, Lipowsky R (2018) Membrane nanotubes increase the robustness of giant vesicles. *ACS Nano*, 12:4478–4485.
- Bhatia T, Dimova R, Lipowsky R in preparation Morphological complexity of giant vesicles exposed to asymmetric sugar solutions.
- Binder K (1983) Random-field induced interface widths in Ising systems. *Z. Phys. B*, 50:343–352.
- Brangwynne CP, Eckmann CR, Courson DS, Rybarska A, Hoeghe C, Gharakhani J, Jülicher F, Hyman AA (2009) Germline P granules are liquid droplets that localize by controlled dissolution/condensation. *Science*, 324:1729–1732.
- Breidenich M, Netz R, Lipowsky R (2000) The shape of polymer-decorated membranes. *Europhys. Lett.*, 49:431–437.
- Breidenich M, Netz R, Lipowsky R (2001) Adsorption of polymers anchored to membranes. *Europ. Phys. J. E*, 5:403–414.
- Breidenich M, Netz R, Lipowsky R (2005) The influence of non-anchored polymers on the curvature of vesicles. *Mol. Phys.*, 103:3160–3183.
- Brüning BA, Prévost S, Stehle R, Steitz R, Falus P, Farago B, Hellweg T (2014) Bilayer undulation dynamics in unilamellar phospholipid vesicles: Effect of temperature, cholesterol and trehalose. *Biochim. Biophys. Acta*, 1838:2412–2419.
- Canham P (1970) The minimum energy of bending as a possible explanation of the biconcave shape of the human red blood cell. *J. Theoret. Biol.*, 26:61–81.
- Cevc G, Marsh D (1987) *Phospholipid Bilayers: Physical Principles and Models*, New York: John Wiley & Sons.
- Chithrani BD, Chan WCW (2007) Elucidating the mechanism of cellular uptake and removal of protein-coated gold nanoparticles of different sizes and shapes. *Nano Lett.*, 7:1542–1550.
- Chithrani BD, Ghazani AA, Chan WCW (2006) Determining the size and shape dependence of gold nanoparticle uptake into mammalian cells. *Nano Lett.*, 6:662–668.
- Collins MD, Keller SL (2008) Tuning lipid mixtures to induce or suppress domain formation across leaflets of unsupported asymmetric bilayers. *PNAS*, 105:124–128.
- Cureton DK, Harbison CE, Parrish CR, Kirchhausen T (2012) Limited transferrin receptor clustering allows rapid diffusion of canine parvovirus into clathrin endocytic structures. *J. Virol.*, 86:5330–5340.
- Dalmédico A (1991) Sophie Germain. *Sci. Am.*, 265:117–122.
- Dasgupta R, Dimova R (2014) Inward and outward membrane tubes pulled from giant vesicles. *J. Phys. D: Appl. Phys.*, 47:282001.
- Dasgupta R, Miettinen M, Fricke N, Lipowsky R, Dimova R (2018) The glycolipid GM1 reshapes asymmetric biomembranes and giant vesicles by curvature generation. *Proc. Nat. Acad. Sci. USA*, 115:5756–5761.
- David JH, Clair JJ, Juhasz J (2009) Phase equilibria in DOPC/DPPC-d62/Cholesterol mixtures. *Biophys. J.*, 96:521–539.
- de Freitas RA, Nicolai T, Chassenieux C, Benyahia L (2016) Stabilization of water-in-water emulsions by polysaccharide-coated protein particles. *Langmuir*, 32:1227–1232.
- Derzhanski A, Petrov AG, Mitov MD (1978) Molecular asymmetry and saddle-splay elasticity in lipid bilayers. *Ann. Phys.*, 3:297.
- Deserno M (2004) Elastic deformation of a fluid membrane upon colloid binding. *Phys. Rev. E*, 69:031903.
- Deserno M, Müller MM, Guven J (2007) Contact lines for fluid surface adhesion. *Phys. Rev. E*, 76:011605.
- Deuling H, Helfrich W (1976) The curvature elasticity of fluid membranes: A catalogue of vesicle shapes. *J. Physique*, 37:1335–1345.
- Devaux P, McConnell HM (1972) Lateral diffusion in spin-labeled phosphatidylcholine multilayers. *JACS*, 94:4475–4481.
- Dietrich C, Bagatolli L, Volovyk Z, Thompson N, Levi M, Jacobson K, Gratton E (2001) Lipid rafts reconstituted in model membranes. *Biotopology*, 8:1417–1428.
- Dimova R, Aranda S, Bezlyepkina N, Nikolov V, Riske K, Lipowsky R (2006) A practical guide to giant vesicles: Probing the membrane nanoregime via optical microscopy. *J. Phys. Cond. Mat.*, 18:S1151–S1176.
- Dimova R, Lipowsky R (2016) Giant vesicles exposed to aqueous two-phase systems: Membrane wetting, budding processes, and spontaneous tubulation. *Adv. Mater. Interf.*, 4:1600451.
- Dimova R, Riske KA, Aranda S, Bezlyepkina N, Knorr RL, Lipowsky R (2007) Giant vesicles in electric fields. *Soft Matter*, 3:817–827.
- do Carmo M (1976) *Differential Geometry of Curves and Surfaces*. Englewood Cliffs: Upper Saddle River, NJ.
- Döbereiner HG, Evans E, Kraus M, Seifert U, Wortis M (1997) Mapping vesicle shapes into the phase diagram: A comparison of experiment and theory. *Phys. Rev. E*, 55:4458–4474.
- Döbereiner HG, Selchow O, Lipowsky R (1999) Spontaneous curvature of asymmetric bilayer membranes. *Eur. Biophys. J.*, 28:174–178.
- Eggeling C, Ringemann C, Medda R, Schwarzmann G, Sandhoff K, Polyakova S, Belov VN, Hein B, von Middendorff C, Schönle A, Hell SW (2009) Direct observation of the nanoscale dynamics of membrane lipids in a living cell. *Nature*, 457:1159–1162.
- Esquena J (2016) Water-in-water (W/W) emulsions. *Curr. Opin. Colloid Interface Sci.*, 25:109–119.
- Evans E (1974) Bending resistance and chemically induced moments in membrane bilayers. *Biophys. J.*, 14:923–931.
- Evans E, Needham D (1987) Physical properties of surfactant bilayer membranes: Thermal transitions, elasticity, rigidity, cohesion, and colloidal interactions. *J. Phys. Chem.*, 91:4219–4228.
- Ewers H, Römer W, Smith AE, Bacia K, Dmitrieff S, Chai W, Mancini R et al., (2010) GM1 structure determines SV40-induced membrane invagination and infection. *Nature Cell Biol.*, 12:11–18.
- Fadeel B, Xue D (2009) The ins and outs of phospholipid asymmetry in the plasma membrane: Roles in health and disease. *Crit. Rev. Biochem. Mol. Biol.*, 44:264–77.
- Farsad K, Ringstad N, Takei K, Floyd SR, Rose K, Camilli PD (2001) Generation of high curvature membranes mediated by direct endophilin bilayer interactions. *J. Cell Biol.*, 155:193–200.
- Fenz SF, Sengupta K (2012) Giant vesicles as cell models. *Integr. Biol.*, 4:982–995.

- Fischer T, Vink RLC (2011) Domain formation in membranes with quenched protein obstacles: Lateral heterogeneity and the connection to universality classes. *J. Chem. Phys.*, 134:055106.
- Ford MGJ, Mills IG, Peter BJ, Vallis Y, Praefcke GJK, Evans PR, McMahon HT (2002) Curvature of clathrin-coated pits driven by epsin. *Nature*, 419:361–366.
- Fourcade B, Miao L, Rao M, Wortis M, Zia R (1994) Scaling analysis of narrow necks in curvature models of fluid lipid–bilayer vesicles. *Phys. Rev. E*, 49:5276–5286.
- Frank FC (1958) I. Liquid crystals. on the theory of liquid crystals. *Discuss. Faraday Soc.*, 25:19–28.
- Fujiwara T, Ritchie K, Murakoshi H, Jacobson K, Kusumi A (2002) Phospholipids undergo hop diffusion in compartmentalized cell membrane. *J. Cell Biol.*, 157:1071–1081.
- Garg S, Rühle J, Lüdtke K, Jordan R, Naumann CA (2007) Domain registration in raft-mimicking lipid mixtures studied using polymer- tethered lipid bilayers. *Biophys. J.*, 92:1263–1270.
- Georgiev VN, Grafmüller A, Bléger D, Hecht S, Kunstmann S, Barbirz S, Lipowsky R, Dimova R (2018) Area increase and budding in giant vesicles triggered by light: Behind the scene. *Adv. Sci.*, 5:1800432.
- Ghosh R, Satarifard V, Grafmüller A, Lipowsky R in preparation Adsorption-Induced Budding and Fission of Nanovesicles.
- Goetz R, Gompper G, Lipowsky R (1999) Mobility and elasticity of self-assembled membranes. *Phys. Rev. Lett.*, 82:221–224.
- Goetz R, Lipowsky R (1998) Computer simulations of bilayer membranes: Self-assembly and interfacial tension. *J. Chem. Phys.*, 108:7397–7409.
- Gorter E, Grendel F (1925) On bimolecular layers of lipoids on the chromocytes of the blood. *J. Exp. Med.*, 41:439–443.
- Gózd' W, Gompper G (1998) Composition-driven shape transformations of membranes of complex topology. *Phys. Rev. Lett.*, 80:4213–4216.
- Grafmüller A, Shillcock J, Lipowsky R (2007) Pathway of membrane fusion with two tension-dependent energy barriers. *Phys. Rev. Lett.*, 98:218101.
- Grafmüller A, Shillcock JC, Lipowsky R (2009) The fusion of membranes and vesicles: Pathway and energy barriers form dissipative particle dynamics. *Biophys. J.*, 96:2658–2675.
- Gruhn T, Franke T, Dimova R, Lipowsky R (2007) Novel method for measuring the adhesion energy of vesicles. *Langmuir*, 23:5423–5429.
- Gudheti MV, Mlodzianoski M, Hess ST (2007) Imaging and shape analysis of guvs as model plasma membranes: Effect of Trans dopc on membrane properties. *Biophys. J.*, 93:2011–2023.
- Gutleiderer E, Gruhn T, Lipowsky R (2009) Polymorphohism of vesicles with multi-domain patterns. *Soft Matter*, 5:3303–3311.
- He K, Luo W, Zhang Y, Liu F, Liu D, Xu L, Qin L, Xiong C, Lu Z, Fang X, Zhang Y (2010) Intercellular transportation of quantum dots mediated by membrane nanotubes. *ACS Nano*, 6:3015–3022.
- Heinrich M, Tian A, Esposito C, Baumgart T (2010) Dynamic sorting of lipids and proteins in membrane tubes with a moving phase boundary. *PNAS*, 107:7208–7213.
- Heinrich V, Waugh RE (1996) A piconewton force transducer and its application to measurement of the bending stiffness of phospholipid membranes. *Ann. Biomed. Eng.*, 24:595–605.
- Helfrich M, Mangeney-Slavin L, Long M, Djoko K, Keating C (2002) Aqueous phase separation in giant vesicles. *J. Am. Chem. Soc.*, (JACS) 124:13374–13375.
- Helfrich W (1973) Elastic properties of lipid bilayers: Theory and possible experiments. *Z. Naturforsch.*, 28c:693–703.
- Helfrich W, Harbich W (1987) Equilibrium configurations of fluid membranes. In Meunier J, Langevin D, Boccarda N. (Ed.), *Physics of Amphiphilic Layers, Vol. 21 of Springer Proceedings in Physics*, 58–63. Berlin, Germany: Springer Berlin Heidelberg.
- Hochmuth RM, Wiles HC, Evans EA, McCown JT (1982) Extensional flow of erythrocytemembrane: From cell body to elastic tether. *Biophys. J.*, 39:83–89.
- Hu J, Weikl T, Lipowsky R (2011) Vesicles with multiple membrane domains. *Soft Matter*, 7:6092–6102.
- Hu J, Lipowsky R, Weikl TR (2013) Binding constants of membrane-anchored receptors and ligands depend strongly on the nanoscale roughness of membranes. *Proc. Nat. Acad. Sci. USA*, 110:15283–15288.
- Hu M, Briguglio JJ, Deserno M (2012) Determining the Gaussian curvature modulus of lipid membranes in simulations. *Biophys. J.*, 102:1403–1410.
- Jenkins J (1977) Static equilibrium configurations of a model red blood cell. *J. Math. Biology*, 4:149–169.
- Jensen MH, Morris EJ, Simonsen AC (2007) Domain shapes, coarsening, and random patterns in ternary membranes. *Langmuir*, 23:8135–8141.
- Jülicher F, Lipowsky R (1993) Domain-induced budding of vesicles. *Phys. Rev. Lett.*, 70:2964–2967.
- Jülicher F, Lipowsky R (1996) Shape transformations of inhomogeneous vesicles with intramembrane domains. *Phys. Rev. E*, 53:2670–2683.
- Jülicher F, Seifert U, Lipowsky R (1993) Conformal degeneracy and conformal diffusion of vesicles. *Phys. Rev. Lett.*, 71:452–455.
- Karimi M, Steinkühler S, Roy D, Dasgupta R, Lipowsky R, Dimova R (2018) Asymmetric ionic conditions generate large membrane curvatures. *Nano Lett* 18:7816–7821.
- Keller H, Lorizate M, Schwillle P (2009) PI(4,5)P2 Degradation promotes the formation of cytoskeleton-free model membrane systems. *ChemPhysChem*, 10:2805–2812.
- Kiessling V, Wan C, Tamm LK (2009) Domain coupling in asymmetric lipid bilayers. *Biochim. Biophys. Acta*, 1788:64–71.
- Klotzsch E, Schütz GJ (2013) A critical survey of methods to detect plasma membrane rafts. *Phil. Trans. R. Soc. B*, 368:20120033.
- Knorr RL, Dimova R, Lipowsky R (2012) Curvature of double-membrane organelles generated by changes in membrane size and composition. *PLoS One*, 7:e32753.
- Knorr RL, Franzmann T, Feeney M, Frigerio L, Hyman A, Dimova R, Lipowsky R (under review) Wetting and molding of membranes by biomolecular condensates.
- Knorr RL, Lipowsky R, Dimova R (2015) Autophagosome closure requires membrane scission. *Autophagy*, 11:2134–2137.
- Korlach J, Schwillle P, Webb W, Feigenson G (1999) Characterization of lipid bilayer phases by confocal microscopy and fluorescence correlation spectroscopy. *Proc. Natl. Acad. Sci. USA*, 96:8461–8466.
- Kornberg R, McConnell H (1971) Lateral diffusion of phospholipids in a vesicle membrane. *Proc. Nat. Acad. Sci. USA*, 68:2564–2568.
- Kulp A, Kuehn MJ (2010) Biological functions and biogenesis of secreted bacterial outer membrane vesicles. *Annu. Rev. Microbiol.*, 64:163–184.
- Kumar S, Gompper G, Lipowsky R (2001) Budding dynamics of multi-component membranes. *Phys. Rev. Lett.*, 86:3911–3914.
- Kusumaatmaja H, Li Y, Dimova R, Lipowsky R (2009) Intrinsic contact angle of aqueous phases at membranes and vesicles. *Phys. Rev. Lett.*, 103:238103.
- Kusumi A, Nakada C, Ritchie K, Murase K, Suzuki K, Murakoshi H, Kasai RS, Kondo J, Fujiwara T (2005) Paradigm shift of the plasma membrane concept from the two-dimensional continuum fluid to the partitioned fluid: High-speed single-molecule tracking of membrane molecules. *Annu. Rev. Biophys. Biomol. Struct.*, 34:351–378.
- Li Y, Lipowsky R, Dimova R (2008) Transition from complete to partial wetting within membrane compartments. *JACS*, 130:12252–12253.

- Li Y, Lipowsky R, Dimova R (2011) Membrane nanotubes induced by aqueous phase separation and stabilized by spontaneous curvature. *Proc. Nat. Acad. Sci. USA*, 108:4731–4736.
- Li Y, Kusumaatmaja H, Lipowsky R, Dimova R (2012) Wetting-induced budding of vesicles in contact with several aqueous phases. *J. Phys. Chem. B*, 116:1819–1823.
- Lipowsky R (1991) The conformation of membranes. *Nature*, 349:475–481.
- Lipowsky R (1992) Budding of membranes induced by intramembrane domains. *J. Phys. II France*, 2:1825–1840.
- Lipowsky R (1993) Domain-induced budding of fluid membranes. *Biophys. J.*, 64:1133–1138.
- Lipowsky R (1995) Bending of membranes by anchored polymers. *Europhys. Lett.*, 30:197–202.
- Lipowsky R (2002) Domains and rafts in membranes: Hidden dimensions of selforganization. *J. Biological Phys.*, 28:195–210.
- Lipowsky R (2013) Spontaneous tubulation of membranes and vesicles reveals membrane tension generated by spontaneous curvature. *Faraday Discuss.*, 161:305–331.
- Lipowsky R (2014a) Coupling of bending and stretching deformations in vesicle membranes. *Adv. Colloid Interface Sci.*, 208:14–24.
- Lipowsky R (2014b) Remodeling of membrane compartments: Some consequences of membrane fluidity. *Biol. Chem.*, 395:253–274.
- Lipowsky R (2018a) The response of membranes and vesicles to capillary forces arising from aqueous two-phase systems and water-in-water emulsions. *J. Phys. Chem. B*, 122:3572–3586.
- Lipowsky R (2018b) Curvature elasticity and multi-sphere morphologies. *J. Phys. D: Appl. Phys.*, 51:343001/22–24.
- Lipowsky R, Brinkmann M, Dimova R, Franke T, Kierfeld J, Zhang X (2005) Droplets, bubbles, and vesicles at chemically structured surfaces. *J. Phys. Cond. Mat.*, 17:S537–S558.
- Lipowsky R, Dimova R (2003) Domains in membranes and vesicles. *J. Phys. Cond. Mat.*, 15:S31–S45.
- Lipowsky R, Döbereiner HG (1998) Vesicles in contact with nanoparticles and colloids. *Europhys. Lett.*, 43:219–225.
- Lipowsky R, Rouhiparkouhi T, Discher DE, Weikl TR (2013) Domain formation in cholesterol/phospholipid membranes exposed to adhesive surfaces or environments. *Soft Matter*, 9:8438–8453.
- Lipowsky R, Seifert U (1991) Adhesion of vesicles and membranes. *Mol. Cryst. Liq. Cryst.*, 202:17–25.
- Liu Y, Agudo-Canalejo J, Grafmüller A, Dimova R, Lipowsky R (2016) Patterns of flexible nanotubes formed by liquid-ordered and liquid-disordered membranes. *ACS Nano*, 10:463–474.
- Liu Y, Lipowsky R, Dimova R (2012) Concentration dependence of the interfacial tension for aqueous two-phase polymer solutions of dextran and polyethylene glycol. *Langmuir*, 28:3831–3839.
- Loerke D, Mettlen M, Yarar D, Jaqaman K, Jaqaman H, Danuser G, Schmid SL (2009) Cargo and dynamin regulate clathrin-coated pit maturation. *PLoS Biol.*, 7:e1000057.
- Long MS, Cans AS, Keating CD (2008) Budding and asymmetric protein microcompartmentation in giant vesicles containing two aqueous phases. *JACS*, 130:756–762.
- Lorenzen S, Servuss RM, Helfrich W (1986) Elastic torques about membrane edges: A study of pierced egg lecithin vesicles. *Biophys. J.*, 50:565–572.
- Marchi S, Patergnani S, Pinton P (2014) The endoplasmic reticulum-mitochondria connection: One touch, multiple functions. *Biochim. Biophys. Acta*, 1837:461–469.
- McMahon HT, Gallop JL (2005) Membrane curvature and mechanisms of dynamic cell membrane remodeling. *Nature*, 438:590–596.
- Miao L, Fourcade B, Rao M, Wortis M, Zia R (1991) Equilibrium budding and vesiculation in the curvature model of fluid lipid vesicles. *Phys. Rev. A*, 43:6843–6856.
- Miao L, Seifert U, Wortis M, Döbereiner HG (1994) Budding transitions of fluid-bilayer vesicles: The effect of area-difference elasticity. *Phys. Rev. E*, 49:5389–5407.
- Michalet X, Bensimon D (1995) Observation of stable shapes and conformal diffusion of genus 2 vesicles. *Science*, 269:666–668.
- Michelot A, Drubin DG (2011) Building distinct actin filament networks in a common cytoplasm. *Curr. Biol.*, 21:R560–R569.
- Miettinen M, Lipowsky R (2019) Lipid bilayers with frequent flip-flops have tensionless leaflets. *Nano Lett*, in press.
- Mitov M (1978) Third and fourth order curvature elasticity of lipid bilayers. *Compte Rendues de l'Academie bulgare des Sciences*, 31:513–515.
- Moy VT, Jiao Y, Hillmann T, Lehmann H, Sano T (1999) Adhesion energy of receptor-mediated interaction measured by elastic deformation. *Biophys. J.*, 76:1632–1638.
- Nikolov V, Lipowsky R, Dimova R (2007) Behavior of giant vesicles with anchored DNA molecules. *Biophys. J.*, 92:4356–4368.
- Orth A, Johannes L, Römer W, Steinem C (2012) Creating and modulating microdomains in pore-spanning membranes. *Chem. Phys. Chem.*, 13:108–114.
- Ou-Yang ZC, Helfrich W (1989) Bending energy of vesicle membranes: General expressions for the first, second and third variation of the shape energy and applications to spheres and cylinders. *Phys. Rev. A*, 39:5280–5288.
- Patarala S, Liu Y, Lipowsky R, Dimova R (2014) Effect of cytochrome c on the phase behavior of charged multicomponent lipid membranes. *Biochim. Biophys. Acta*, 1838:2036–2045.
- Peter BJ, Kent HM, Mills IG, Vallis Y, Butler PJG, Evans PR, McMahon HT (2004) BAR domains as sensors of membrane curvature: The amphiphysin BAR structure. *Science*, 303:495–499.
- Pezeshkian W, Gao H, Arumugam S, Becken U, Bassereau P, Florent JC, Ipsen JH, Johannes L, Shillcock JC (2016) Mechanism of shiga toxin clustering on membranes. *ACS Nano*, 11:314–324.
- Riske KA, Bezlyepkina N, Lipowsky R, Dimova R (2006) Electrofusion of model lipid membranes viewed with high temporal resolution. *Biophys. Rev. Lett.*, 1:387–400.
- Robertson JD (1959) The ultrastructure of cell membranes and their derivatives. *Biochem. Soc. Symp.*, 16:3–43.
- Robertson JD (1960) The molecular structure and contact relationships of cell membranes. *Prog. Biophys. Biop. Ch.*, 10:343–418.
- Rouhiparkouhi T, Weikl TR, Discher DE, Lipowsky R (2013) Adhesion-induced phase behavior of two-component membranes and vesicles. *Int. J. Mol. Sci.*, 14:2203–2229.
- Rowlinson J, Widom B (1989) *Molecular Theory of Capillarity*. Oxford: Clarendon Press.
- Rozycki B, Lipowsky R (2015) Spontaneous curvature of bilayer membranes from molecular simulations: Asymmetric lipid densities and asymmetric adsorption. *J. Chem. Phys.*, 142:054101.
- Rózycki B, Lipowsky R (2016) Membrane curvature generated by asymmetric depletion layers of ions, small molecules, and nanoparticles. *J. Chem. Phys.*, 145:074117.
- Sackmann E, Träuble H (1972) Studies of the crystalline-liquid crystalline phase transition of lipid model membranes II: Analysis of electron spin resonance spectra of steroid labels incorporated into lipid membranes. *JACS*, 94:4492–4498.
- Sako Y, Kusumi A (1994) Compartmentalized structure of the plasma membrane for receptor movements as revealed by a nanometer-level motion analysis. *J. Cell Biol.*, 125:1251–1264.
- Satarifard V, Grafmüller A, Lipowsky R (2018) Nanodroplets at membranes create tight-lipped membrane necks via negative line tension. *ACS Nano*, 12:12424–12435.
- Saxton MJ, Jacobson K (1997) Single-particle tracking: Applications to membrane dynamics. *Annu. Rev. Biophys. Biomol. Struct.*, 26:373–399.
- Schengrund CL (2015) Gangliosides: Glycosphingolipids essential for normal neural development and function. *Trends Biochemical Sci.*, 40:397–406.

- Schertzer JW, Whiteley M (2012) A bilayer-couple model of bacterial outer membrane vesicle biogenesis. *MBIO*, 3:e00297–e00311.
- Scholten E, Tuinier R, Tromp RH, Lekkerkerker HNW (2002) Interfacial tension of a decomposed biopolymer mixture. *Langmuir*, 18:2234–2238.
- Schönherr H, Johnson JM, Lenz P, Frank CW, Boxer SG (2004) Vesicle adsorption and lipid bilayer formation on glass studied by atomic force microscopy. *Langmuir*, 20:11600–11606.
- Schwille P (2015) Jump-starting life? Fundamental aspects of synthetic biology. *J. Cell Biol.*, 210:687–690.
- Scott RE (1976) Plasma membrane vesiculation: A new technique for isolation of plasma membranes. *Science*, 194:743–745.
- Seifert U (1997) Configurations of membranes and vesicles. *Adv. Phys.*, 46:13–137.
- Seifert U, Berndl K, Lipowsky R (1991) Shape transformations of vesicles: Phase diagram for spontaneous curvature and bilayer coupling model. *Phys. Rev. A*, 44:1182–1202.
- Seifert U, Lipowsky R (1990) Adhesion of vesicles. *Phys. Rev. A*, 42:4768–4771.
- Semrau S, Idema T, Holtzer L, Schmidt T, Storm C (2008) Accurate determination of elastic parameters for multi-component membranes. *Phys. Rev. Lett.*, 100:088101.
- Simons K, Ikonen E (1997) Functional rafts in cell membranes. *Nature*, 387:569–572.
- Simunovic M, Lee KYC, Bassereau P (2015) Celebrating soft matter's 10th anniversary: Screening of the calcium-induced spontaneous curvature of lipid membranes. *Soft Matter*, 11:5030–5036.
- Singer S, Nicolson G (1972) The fluid mosaic model of the structure of cell membranes. *Science*, 175:720–731.
- Skau CT, Kovar DR (2010) Fimbrin and tropomyosin competition regulates endocytosis and cytokinesis kinetics in fission yeast. *Curr. Biol.*, 20:1415–1422.
- Sorre B, Callan-Jones A, Manzi J, Goud B, Prost J, Bassereau P, Roux A (2012) Nature of curvature coupling of amphiphysin with membranes depends on its bound density. *PNAS*, 109:173–178.
- Sosale N, Rouhparakouhi T, Bradshaw AM, Dimova R, Lipowsky R, Discher DE (2015) Cell rigidity and shape override CD47's "Self" signaling in phagocytosis by hyperactivating Myosin-II. *Blood*, 125:542–552.
- Sowinski S, Jolly C, Berninghausen O, Purbhoo MA, Chauveau A, Köhler K, Oddos S, et al., (2008) Membrane nanotubes physically connect T cells over long distances presenting a novel route for HIV-1 transmission. *Nat. Cell Biol.*, 10:211–219.
- Sreekumari A, Lipowsky R (2018) Lipids with bulky head groups generate large membrane curvatures by small compositional asymmetries. *J. Chem. Phys.*, 149: 084901.
- Steinkühler J, Agudo-Canalejo J, Lipowsky R, Dimova R (2016) Modulating vesicle adhesion by electric fields. *Biophys. J.*, 111:1454–1464.
- Steinkühler J, Rózycki B, Alvey C, Lipowsky R, Weikl TR, Dimova R, Discher DE (2019) Membrane fluctuations and acidosis regulate cooperative binding of "marker of self" CD47 to macrophage receptor SIRP α . *J Cell Sci.*, 132:jcs216770.
- Steinkühler J, Bhatia T, Lipowsky R, Dimova R (in preparation) Giant plasma membrane vesicles with nanotubes exhibit unusual elastic properties.
- Steinkühler J, Knorr R, Zhao Z, Bhatia T, Bartelt S, Wegner S, Dimova R, Lipowsky R (in preparation) Controlled division of cell-sized vesicles by low densities of membrane-bound proteins.
- Svetina S, Zeks B (1989) Membrane bending energy and shape determination of phospholipid vesicles and red blood cells. *Eur. Biophys. J.*, 17:101–111.
- Takei K, Slepnev VI, Haucke V, Camilli PD (1999) Functional partnership between amphiphysin and dynamin in clathrin-mediated endocytosis. *Nat. Cell Biol.*, 1:33–39.
- Tian A, Capraro BR, Esposito C, Baumgart T (2009) Bending stiffness depends on curvature of ternary lipid mixture tubular membranes. *Biophys. J.*, 97:1636–1646.
- Tordeux C, Fournier JB, Galatola P (2002) Analytical characterization of adhering vesicles. *Phys. Rev. E*, 65:041912–1–041912–9.
- Träuble H, Sackmann E (1972) Studies of the crystalline-liquid crystalline phase transition of lipid model membranes III: Structure of a steroid-lecithin system below and above the lipid-phase transition. *JACS*, 94:4499–4510.
- Uppamoochikkal P, Tristram-Nagle S, Nagle JF (2010) Orientation of tie-lines in the phase diagram of DOPC/DPPC/Cholesterol model biomembranes. *Langmuir*, 26:17363–17368.
- van Meer G, Voelker DR, Feigenson GW (2008) Membrane lipids: Where they are and how they behave. *Nature Rev.: Mol. Cell Biol.*, 9:112–124.
- van Weering JRT, Cullen PJ (2014) Membrane-associated cargo recycling by tubule-based endosomal sorting. *Semin. Cell Dev. Biol.*, 31:40–47.
- Veatch SL, Cicuta P, Sengupta P, Honerkamp-Smith A, Holowka D, Baird B (2008) Critical fluctuations in plasma membrane vesicles. *ACS Chem. Biol.*, 3:287–293.
- Veatch SL, Gawrisch K, Keller SL (2006) Closed-loop miscibility gap and quantitative tie-lines in ternary membranes containing diphytanoyl PC. *Biophys. J.*, 90:4428–4436.
- Veatch S, Keller S (2003) Separation of liquid phases in giant vesicles of ternary mixtures of phospholipids and cholesterol. *Biophys. J.*, 85:3074–3083.
- Vequi-Suplicy C, Riske K, Knorr R, Dimova R (2010) Vesicles with charged domains. *Biochim. Biophys. Acta*, 1798:1338–1347.
- Walde P, Cosentino K, Engel H, Stano P (2010) Giant vesicles: Preparations and applications. *ChemBioChem*, 11:848–865.
- Wang Q, Navarro VAS, Peng G, Molinelli E, Goh SL, Judson BL, Rajashankar KR, Sondermann H (2009) Molecular mechanism of membrane constriction and tubulation mediated by the F-BAR protein Pascin/Syndapin. *PNAS*, 106:12700–12705.
- Wang X, Gerdes HH (2015) Transfer of mitochondria via tunneling nanotubes rescues apoptotic PC12 cells. *Cell Death Differ.*, 22:1181–1191.
- Weikl TR, Asfaw M, Krobath H, Rózycki B, Lipowsky R (2009) Adhesion of membranes via receptor–ligand complexes: Domain formation, binding cooperativity, and active processes. *Soft Matter*, 5:3213–3224.
- Weikl TR, Hu J, Xu GK, Lipowsky R (2016) Binding equilibrium and kinetics of membrane-anchored receptors and ligands in cell adhesion: Insights from computational model systems and theory. *Cell. Adh. Migr.*, 10:576–589.
- Weiss M, Frohnmayer JP, Benk LT, Haller B, Janiesch JW, Heitkamp T, Börsch M, et al., (2018) Sequential bottom-up assembly of mechanically stabilized synthetic cells by microfluidics. *Nat. Mater.*, 17:89–95.
- Westrate LM, Lee JE, Prinz WA, Voeltz GK (2015) Form follows function: The importance of endoplasmic reticulum shape. *Annu. Rev. Biochem.* 84:791–811.
- Willmore T (1982) *Total Curvature in Riemannian Geometry*. Chichester, UK: Ellis Horwood.
- Yang P, Du Q, Tu ZC (2017) General neck condition for the limit shape of budding vesicles. *Phys. Rev. E*, 95:042403.